

Ministry of Science and Higher Education of the Russian Federation
ITMO University

ISSN 2220-8054

NANOSYSTEMS:
PHYSICS, CHEMISTRY, MATHEMATICS

2025, volume 16(2)

Наносистемы: физика, химия, математика

2025, том 16, № 2



NANOSYSTEMS:

PHYSICS, CHEMISTRY, MATHEMATICS

ADVISORY BOARD MEMBERS

Chairman: V.N. Vasiliev (*St. Petersburg, Russia*),
V.M. Buznik (*Moscow, Russia*); V.M. Ievlev (*Voronezh, Russia*), P.S. Kop'ev (*St. Petersburg, Russia*), V.N. Parmon (*Novosibirsk, Russia*), A.I. Rusanov (*St. Petersburg, Russia*),

EDITORIAL BOARD

Editor-in-Chief: I.Yu. Popov (*St. Petersburg, Russia*)

Section Co-Editors:

Physics – V.M. Uzdin (*St. Petersburg, Russia*),

Material science – V.V. Gusarov (*St. Petersburg, Russia*); O.V. Al'myasheva (*St. Petersburg, Russia*);

Chemistry – V.K. Ivanov (*Moscow, Russia*),

Mathematics – I.Yu. Popov (*St. Petersburg, Russia*).

Editorial Board Members:

V.M. Adamyan (*Odessa, Ukraine*); A.P. Alodjants (*St. Petersburg, Russia*); S. Bechta (*Stockholm, Sweden*); J. Behrndt (*Graz, Austria*); A. Chatterjee (*Hyderabad, India*); A.V. Chizhov (*Dubna, Russia*); A.N. Enyashin (*Ekaterinburg, Russia*), E.A. Gudilin (*Moscow, Russia*); H. Jónsson (*Reykjavik, Iceland*); A.R. Kaul (*Moscow, Russia*); A.A. Kiselev (*Durham, USA*); Yu.S. Kivshar (*Canberra, Australia*); S.A. Kozlov (*St. Petersburg, Russia*); P.A. Kurasov (*Stockholm, Sweden*); A.V. Lukashin (*Moscow, Russia*); G.P. Miroshnichenko (*St. Petersburg, Russia*); I.Ya. Mittova (*Voronezh, Russia*); H. Najjar (*Monastir, Tunisia*), Nguyen Anh Tien (*Ho Chi Minh, Vietnam*); V.V. Pankov (*Minsk, Belarus*); K. Pankrashkin (*Oldenburg, Germany*); A.V. Ragulya (*Kiev, Ukraine*); V. Rajendran (*Tamil Nadu, India*); A.A. Rempel (*Ekaterinburg, Russia*); A.A. Rogachev (*Minsk, Belarus*); V.Ya. Rudyak (*Novosibirsk, Russia*); H.M. Sedighi (*Ahvaz, Iran*); D Shoikhet (*Karmiel, Israel*); M.N. Smirnova (*Moscow, Russia*); P. Stovicek (*Prague, Czech Republic*); V.M. Talanov (*Novocherkassk, Russia*); A.Ya. Vul' (*St. Petersburg, Russia*); A.V. Yakimansky (*St. Petersburg, Russia*), V.A. Zagrebnoy (*Marseille, France*).

Editors:

I.V. Blinova; A.I. Popov; A.I. Trifanov; E.S. Trifanova (*St. Petersburg, Russia*),

R. Simoneaux (*Philadelphia, Pennsylvania, USA*).

Address: ITMO University, Kronverkskiy pr., 49, St. Petersburg 197101, Russia.

Phone: +7(812)607-02-54, **Journal site:** <http://nanojournal.ifmo.ru/>,

E-mail: nanojournal.ifmo@gmail.com

AIM AND SCOPE

The scope of the journal includes all areas of nano-sciences. Papers devoted to basic problems of physics, chemistry, material science and mathematics inspired by nanosystems investigations are welcomed. Both theoretical and experimental works concerning the properties and behavior of nanosystems, problems of its creation and application, mathematical methods of nanosystem studies are considered.

The journal publishes scientific reviews (up to 30 journal pages), research papers (up to 15 pages) and letters (up to 5 pages). All manuscripts are peer-reviewed. Authors are informed about the referee opinion and the Editorial decision.

CONTENT

MATHEMATICS

- O.Sh. Karshiboev, M.M. Rahmatullaev
The phase transition for the three-state SOS model with one-level competing interactions on the binary tree 134
- N.M. Khatamov, N.N. Malikov
Extremality of Gibbs measures for the DNA-Ising molecule model on the Cayley tree 142
- F.H. Haydarov, R.A. Ilyasova, K.S. Mamayusupov
Pinned gradient measures of SOS model associated with H_A -boundary laws on Cayley trees 154
- M.M. Rakhmatullaev, N.D. Samijonova
Translation-invariant p -adic quasi Gibbs measures for the Potts model with an external field on the Cayley tree 164

PHYSICS

- E.N. Popov, A.I. Trifanov, M.A. Moskalenko, V.A. Reshetov
Quantum coupling between radio modes in a single-atom maser with two resonators 176
- D.V. Pozdnyakov, A.V. Borzdov, V.M. Borzdov
Simulation of a quasi-ballistic quantum-barrier field-effect transistor based on GaAs quantum wire 183
- I.A. Baigunov, Kh.T. Kholmurodov, P.P. Gladyshev
Alcohol dehydrogenase: molecular dynamics study of conformational and orientational behaviour of the enzyme in complex with nad during sorption on the surface of electrode materials using graphite as an example 192
- Khaled Abdulhaq, Mohammad K. Elsaid, Diana Dahliah
Thermal and magnetic properties and density of state of in 3D SnTe (001) surface state under combined exchange and strain effects 199
- V.A. Kurakin, T.N. Kobernik
Understanding the electronic properties of carbon polyprismanes from the sp^3 tight-binding model 209
- R.V. Shalayev, V.N. Varyukhin
Application of carbon nanomaterials in semiconductor electronics 216

S.O. Kasparyan, A.E. Ordabaev, A.V. Bakulin, S.E. Kulkova
Elastic and thermal properties of some ternary β -Ti based alloys 225

CHEMISTRY AND MATERIAL SCIENCE

M.S. Lomakin
Phase formation in the $\text{Na}_2\text{O}-\text{Bi}_2\text{O}_3-\text{Fe}_2\text{O}_3-\text{MoO}_3-(\text{H}_2\text{O})$ system 235

M.N. Nikolaeva, E.M. Ivan'kova, A.N. Bugrov
Conducting properties of single-wall carbon nanotubes in composites based on polystyrene 243

Information for authors 250

In memory of Pavel Pavlovich Fedorov (16.04.1950 – 31.03.2025)



Professor DSc Pavel Pavlovich Fedorov, 74, passed away suddenly on March 31, 2025. He was an outstanding materials scientist, chemical engineer, and inventor of several new optical materials.

Pavel P. Fedorov graduated from M.V. Lomonosov Moscow Institute of Fine Chemical Technology with an MS degree in chemical engineering in 1972, while majoring in chemical technology of rare and trace elements. He successfully defended his PhD. thesis titled "Study of the phase diagrams of $\text{CaF}_2\text{-(Y,Ln)F}_3$ systems and polymorphism of rare earth trifluorides" (1977) and DSc thesis titled "High-temperature chemistry of the condensed state of systems with rare earth

trifluorides as a basis for obtaining new materials" (1991).

After graduation, Pavel P. Fedorov worked at A.V. Shubnikov Institute of Crystallography of the Russian Academy of Sciences from 1972 to 2003, where he advanced from a laboratory assistant to a leading research fellow. In 2000, he attained the rank of full professor of crystallography and crystal physics. From 2003, Prof. Fedorov was affiliated with the A.M. Prokhorov General Physics Institute of the Russian Academy of Sciences, where he served as the head of the laboratory of nanomaterials technology for photonics, head of the nanotechnology department, and chief research fellow until his death.

Prof. Fedorov was well-published, authoring more than 1000 research papers (including 33 reviews) in peer-reviewed journals as well as 5 textbooks. He was also a prolific inventor, being included in 31 patents. Pavel was also well-respected in the scientific community, serving not only as a reviewer for more than 45 international and Russian periodicals but as an editorial board member for several scientific journals. Areas of scientific interest included heterovalent isomorphism in crystals and glasses, thermodynamic theory of morphotropy, phase diagrams, and fluoride laser ceramics. He developed the bifurcation theory for phase diagrams, publishing papers on the prediction and experimental detection of saddle points on melting surfaces of ternary solid solutions as well as generalization of the Tiller criterion for morphological stability of a flat crystallization front.

Pavel was also a valued mentor, functioning as an advisor for more than 30 MS theses, 9 PhD theses, and a scientific consultant for three DSc theses. He

received numerous decorations and honorable citations, but more importantly, Pavel was a keen observer of correctness of scientific data. He always made sure that his published data were correct and would never be the source of subsequent errata.

Pavel had several active interests, including geology, archeology, anthropology, history, philosophy, and poetry. People that knew him were impressed by his extremely positive outlook and optimistic worldview. They will always remember him as a talented scientist, a skilled leader, a patient mentor, and a valued friend.

A. A. Alexandrov, O. K. Alimov, O. V. Almjasheva, A. E. Baranchikov, S. Ch. Batygov, T.B. Bekker, M. A. Borik, I. I. Buchinskaya, V. M. Buznik, E. V. Chernova, M. E. Doroshenko, A. V. Egorysheva, Yu. A. Ermakova, S. A. Filatova, E. A. Garibin, S. V. Garnov, K. S. Gavrichev, T. Yu. Glazunova, V. V. Glushkov, V.V. Gusarov, V. K. Ivanov, N. A. Ivanovskaya, V. A. Kamynin, D. G. Kochiev, A. E. Kokh, K. A. Kokh, N. G. Kononova, V. A. Konyushkin, S. L. Korableva, A. V. Kulebyakin, S. V. Kuznetsov, E. E. Lomonova, A. A. Luginina, V. L. Manomenova, V. A. Myzina, A. N. Nakladov, K.N. Nischev, A. S. Nizamutdinov, A. G. Papashvili, A. I. Popov, P. A. Popov, V. Yu. Proydakova, M. S. Pudovkin, A. A. Pynenkov, E. B. Rudneva, V. V. Semashko R. L. Simoneaux, N. I. Sorokin, V. A. Stasyuk, N. Yu. Tabachkova, V. B. Tsvetkov, S. N. Ushakov, M. A. Uslamina, A. A. Volchek, A. E. Voloshin, V. V. Voronov, D. S. Yasyrkina, A. I. Zagumennyi, R. M. Zakalukin, A. S. Zakharova, E. V. Zharikov.

The phase transition for the three-state SOS model with one-level competing interactions on the binary tree

Obid Sh. Karshiboev^{1,a}, Muzaffar M. Rahmatullaev^{2,3,b}

¹Namangan State University, Namangan, Uzbekistan

²V. I. Romanovskiy Institute of Mathematics, Uzbekistan Academy of Sciences, Tashkent, Uzbekistan

³New Uzbekistan University, Tashkent, Uzbekistan

^aokarshiboevsher@mail.ru, ^bmrahmatullaev@rambler.ru,

Corresponding author: O. Sh. Karshiboev, okarshiboevsher@mail.ru

PACS 82B23, 82B26, 60G70

ABSTRACT In this paper, we consider a three-state solid-on-solid (SOS) model with two competing interactions (nearest-neighbor, one-level next-nearest-neighbor) on the Cayley tree of order two. We show that at some values of the parameters the model exhibits a phase transition. We also prove that for the model under some conditions there is no two-periodic Gibbs measures.

KEYWORDS Cayley tree, Gibbs measure, SOS model, competing interactions

ACKNOWLEDGEMENTS The second author (MMR) thanks the State Grant F-FA-2021-425 of the Republic of Uzbekistan. We thank the referee for the careful reading of the manuscript and especially for a number of suggestions that have improved the paper.

FOR CITATION Karshiboev O.Sh., Rahmatullaev M.M. The phase transition for the three-state SOS model with one-level competing interactions on the binary tree. *Nanosystems: Phys. Chem. Math.*, 2025, **16** (2), 134–141.

1. Introduction

Recent advances in nanoscience and nanotechnology have led to significant interest in extending thermodynamics and statistical mechanics to small systems consisting of a finite number of particles, far below the thermodynamic limit [1, 2]. In nanoscale systems, structural characteristics exhibit dynamic behavior, in contrast to the static equilibrium observed in macroscopic phases. Phase coexistence in these systems is expected to occur over ranges of temperature and pressure rather than at sharp points, as seen in bulk materials. Consequently, the Gibbs phase rule is no longer strictly applicable, and various metastable phases may emerge that have no counterparts in macroscopic systems [3–5]. This introduces challenges in understanding property relations and phase transitions in small (nano) systems. Addressing these challenges requires the development of new working equations for thermodynamics and statistical mechanics tailored to small systems. Notably, the concept of molecular self-assembly—central to bottom-up nanotechnology—relies on phase transition principles, a concept highlighted by Feynman [6].

The solid-on-solid (SOS) model on a Cayley tree was introduced in [7] as a generalization of the Ising model. Since then, significant research has focused on investigating various properties of SOS models on Cayley trees (see, e.g., [8–14]; see also [15] for a comprehensive review).

In this paper, we investigate phase transitions in the three-state SOS model on a Cayley tree of order two with nearest-neighbor and one-level next-nearest-neighbor interactions. Phase transitions are a central topic in statistical mechanics [16]. The existence of the Gibbs measures for a given model defines the occurrence of a phase transition [15–21]. While previous studies [20, 21] have analyzed Gibbs measures for mixed-spin Ising models and continuous spin systems, our work focuses on a three-state SOS model with one-level competing interactions. Unlike [21], which examines translation-invariant measures under an external field, our study explores the impact of one-level next-nearest-neighbor interactions on phase transitions, revealing conditions under which multiple Gibbs measures emerge. For the classical models (Ising and Potts models) of statistical mechanics on Cayley trees within radius three interactions, this problem is well studied (for the Ising model see, e.g., [22–30], for the Potts model see, e.g., [31–34]).

We obtain a functional equation for the model using the self-similarity of the Cayley tree. Here we consider only the one-level next-nearest-neighbor interactions, since studying both one-level and prolonged next-nearest-neighbor interactions simultaneously usually lead to functional equations which are difficult to solve (this happens even for the Ising model, see, e.g., [35]). We prove that at some values of parameters the model possesses multiple Gibbs measures which implies the existence of phase transition. Moreover, imposing restrictions on interactions, we obtain some explicit conditions for which it is possible to establish the uniqueness or, conversely, the nonuniqueness of the Gibbs measures. We

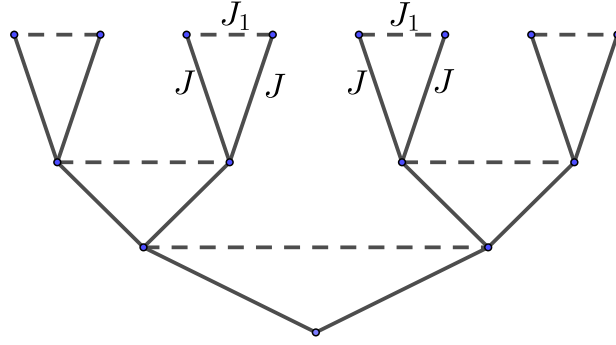


FIG. 1. The Cayley tree of order two with nearest-neighbor (—) and one-level next-nearest-neighbour (- - - -) interactions

also show that under certain conditions, the model does not admit any two-periodic Gibbs measures. We also provide a conjecture on the absence of two-periodic Gibbs measure for the model on the invariant set.

The paper is organized as follows. Section 2 provides definitions of the model, the Cayley tree, and the Gibbs measures. In Section 3, we reformulate the problem of describing limiting Gibbs measures as a system of nonlinear functional equations. Section 4 establishes the existence of phase transitions in the model. Section 5 examines two-periodic Gibbs measures, while Section 6 summarizes the key findings and outlines potential directions for future research.

2. Preliminaries

Cayley tree. The Cayley tree Γ^k of order $k \geq 1$ is an infinite, cycle-free graph that exactly $k + 1$ edges issue from each vertex. We denote by V the set of vertices and by L the set of edges. Two vertices x and y , where $x, y \in V$, are called nearest-neighbor if there exists an edge $l \in L$ connecting them, which is denoted by $l = \langle x, y \rangle$. The distance on this tree, denoted by $d(x, y)$, is defined as the number of nearest-neighbor pairs of the minimal path between the vertices x and y (where a path is a collection of nearest-neighbor pairs, two consecutive pairs sharing at least a given vertex).

For a fixed $x^0 \in V$, called the root, we set

$$W_n(x^0) = \{x \in V \mid d(x, x^0) = n\}, \quad V_n(x^0) = \bigcup_{m=0}^n W_m(x^0)$$

and denote by

$$S(x) = \{y \in W_{n+1}(x^0) : d(x, y) = 1\}, \quad x \in W_n(x^0)$$

the set of *direct successors* of x . We will omit x^0 in the notations W_n , and V_n because x^0 is fixed. For the sake of simplicity, we put $|x| = d(x, x^0)$, $x \in V$. Two vertices $x, y \in V$ are called second nearest-neighbor if $d(x, y) = 2$. The second nearest-neighbor vertices x and y are called prolonged second nearest-neighbors if $|x| \neq |y|$ and is denoted by $> \widetilde{x, y} <$. The second nearest-neighbor vertices $x, y \in V$ that are not prolonged are called one-level next-nearest-neighbors since $|x| = |y|$ and are denoted by $> \overline{x, y} <$.

In this paper, we consider a semi-infinite Cayley Γ^k of order $k \geq 2$, i.e. a cycles-free graph with $(k + 1)$ edges issuing from each vertex except for x^0 and with k edges issuing from the vertex x^0 . According to well known theorems, this can be reconstituted as a Cayley tree [16, 31].

In the SOS model, the spin variables $\sigma(x)$ take values from the set $\Phi = \{0, 1, 2\}$, which is associated with each vertex of the tree Γ^k . The SOS model with nearest-neighbor and one-level next-nearest-neighbor interactions is defined by the following Hamiltonian:

$$H(\sigma) = -J \sum_{\langle x, y \rangle} |\sigma(x) - \sigma(y)| - J_1 \sum_{> \overline{x, y} <} |\sigma(x) - \sigma(y)|, \quad (1)$$

where the sum in the first term ranges all nearest-neighbors, the second sum ranges all one-level next-nearest-neighbors, and $J, J_1 \in \mathbb{R}$ are the coupling constants (see Fig. 1).

3. Recursive Equations

There are multiple approaches to derive the nonlinear functional equations governing the limiting Gibbs measures for lattice models on the Cayley tree. One approach utilizes properties of Markov random fields on Cayley trees (see, e.g., [7]). Another approach relies on recursive equations for partition functions (see, e.g., [31]). Both approaches ultimately yield the same equation (see, e.g., [15]). Since the second approach is more suitable for models with competing interactions, we adopt this approach.

Let Λ be a finite subset of V . We denote by $\sigma(\Lambda)$ the restriction of σ to Λ and let $\bar{\sigma}(V \setminus \Lambda)$ represent a fixed boundary configuration. The total energy of $\sigma(\Lambda)$, given the condition $\bar{\sigma}(V \setminus \Lambda)$, is defined as

$$H(\sigma(\Lambda) | \bar{\sigma}(V \setminus \Lambda)) = -J \sum_{\langle x, y \rangle: x, y \in \Lambda} |\sigma(x) - \sigma(y)| - J_1 \sum_{\langle x, y \rangle: x \in \Lambda, y \notin \Lambda} |\sigma(x) - \sigma(y)|, \quad (2)$$

The partition function $Z_\Lambda(\bar{\sigma}(V \setminus \Lambda))$ over the finite volume Λ with boundary condition $\bar{\sigma}(V \setminus \Lambda)$ is defined as

$$Z_\Lambda(\bar{\sigma}(V \setminus \Lambda)) = \sum_{\sigma(\Lambda) \in \Omega(\Lambda)} \exp(-\beta H_\Lambda(\sigma(\Lambda) | \bar{\sigma}(V \setminus \Lambda))), \quad (3)$$

where $\Omega(\Lambda)$ is the set of all configurations in volume Λ and $\beta = \frac{1}{T}$ is the inverse temperature. Then the conditional Gibbs measure μ_Λ of a configuration $\sigma(\Lambda)$ is defined as

$$\mu_\Lambda(\sigma(\Lambda) | \bar{\sigma}(V \setminus \Lambda)) = \frac{\exp(-\beta H(\sigma(\Lambda) | \bar{\sigma}(V \setminus \Lambda)))}{Z_\Lambda(\bar{\sigma}(V \setminus \Lambda))}.$$

We consider the configuration $\sigma(V_n)$, the partition function Z_{V_n} and conditional Gibbs measure $\mu_\Lambda(\sigma(\Lambda) | \bar{\sigma}(V \setminus \Lambda))$ over the volume V_n . For simplicity, we denote them by σ_n , $Z^{(n)}$ and μ_n , respectively. The partition function $Z^{(n)}$ can be decomposed into the following summands:

$$Z^{(n)} = Z_0^{(n)} + Z_1^{(n)} + Z_2^{(n)}, \quad (4)$$

where

$$Z_i^{(n)} = \sum_{\sigma_n \in \Omega(V_n): \sigma(x^0) = i} \exp(-\beta H_{V_n}(\sigma | \bar{\sigma}(V \setminus V_n))), \quad i = 0, 1, 2. \quad (5)$$

Hereafter, we restrict our analysis to the case $k = 2$.

Denote $\theta = \exp(\beta J)$, $\theta_1 = \exp(\beta J_1)$. Let $S(x^0) = \{x^1, x^2\}$. If $\sigma(x^0) = i$, $\sigma(x^1) = j$ and $\sigma(x^2) = m$, then from (2) and (3), we obtain the following relation

$$Z_i^{(n)} = \sum_{j, m=0}^2 \exp(\beta J |i - j| + \beta J |i - m| + \beta J_1 |j - m|) Z_j^{n-1} Z_m^{(n-1)},$$

so that

$$\begin{aligned} Z_0^{(n)} &= \left[(Z_0^{(n-1)})^2 + 2\theta\theta_1 Z_0^{(n-1)} Z_1^{(n-1)} + 2\theta^2\theta_1^2 Z_0^{(n-1)} Z_2^{(n-1)} \right. \\ &\quad \left. + \theta^2 (Z_1^{(n-1)})^2 + 2\theta^3\theta_1 Z_1^{(n-1)} Z_2^{(n-1)} + \theta^4 (Z_2^{(n-1)})^2 \right], \\ Z_1^{(n)} &= \left[\theta^2 (Z_0^{(n-1)})^2 + 2\theta\theta_1 Z_0^{(n-1)} Z_1^{(n-1)} + 2\theta^2\theta_1^2 Z_0^{(n-1)} Z_2^{(n-1)} \right. \\ &\quad \left. + (Z_1^{(n-1)})^2 + 2\theta\theta_1 Z_1^{(n-1)} Z_2^{(n-1)} + \theta^2 (Z_2^{(n-1)})^2 \right], \\ Z_2^{(n)} &= \left[\theta^4 (Z_0^{(n-1)})^2 + 2\theta^3\theta_1 Z_0^{(n-1)} Z_1^{(n-1)} + 2\theta^2\theta_1^2 Z_0^{(n-1)} Z_2^{(n-1)} \right. \\ &\quad \left. + \theta^2 (Z_1^{(n-1)})^2 + 2\theta\theta_1 Z_1^{(n-1)} Z_2^{(n-1)} + (Z_2^{(n-1)})^2 \right]. \end{aligned}$$

Introducing the notations $u_n(x^0) = \frac{Z_1^{(n)}(x^0)}{Z_0^{(n)}(x^0)}$, $v_n(x^0) = \frac{Z_2^{(n)}(x^0)}{Z_0^{(n)}(x^0)}$, we obtain the following system of recurrent equations:

$$\begin{cases} u_n = \frac{\theta^2 + 2\theta\theta_1 u_{n-1} + 2\theta^2\theta_1^2 v_{n-1} + u_{n-1}^2 + 2\theta\theta_1 u_{n-1} v_{n-1} + \theta^2 v_{n-1}^2}{1 + 2\theta\theta_1 u_{n-1} + 2\theta^2\theta_1^2 v_{n-1} + \theta^2 u_{n-1}^2 + 2\theta^3\theta_1 u_{n-1} v_{n-1} + \theta^4 v_{n-1}^2} \\ v_n = \frac{\theta^4 + 2\theta^3\theta_1 u_{n-1} + 2\theta^2\theta_1^2 v_{n-1} + \theta^2 u_{n-1}^2 + 2\theta\theta_1 u_{n-1} v_{n-1} + v_{n-1}^2}{1 + 2\theta\theta_1 u_{n-1} + 2\theta^2\theta_1^2 v_{n-1} + \theta^2 u_{n-1}^2 + 2\theta^3\theta_1 u_{n-1} v_{n-1} + \theta^4 v_{n-1}^2}. \end{cases} \quad (6)$$

Evidently,

$$u_n(x^0) = \frac{\mu_n(\sigma_n(x^0) = 1)}{\mu_n(\sigma_n(x^0) = 0)}, \quad v_n(x^0) = \frac{\mu_n(\sigma_n(x^0) = 2)}{\mu_n(\sigma_n(x^0) = 0)}.$$

If we can find the limit of $u_n(x^0)$ as n tends to infinity, we will find the ratio for the probability of value 1 to the probability of value 0 at the root for the limiting Gibbs measure. Similarly, if we can find the limit of $v_n(x^0)$ as n tends to infinity, we will find the ratio for the probability of value 2 to the probability of value 0 at the root for the limiting Gibbs measures. Thus, the fixed points of equation (6) describe the translation-invariant limiting Gibbs measure of the model (1).

If $u = \lim_{n \rightarrow \infty} u_n$ and $v = \lim_{n \rightarrow \infty} v_n$ then

$$\begin{cases} u = \frac{\theta^2 + 2\theta\theta_1 u + 2\theta^2\theta_1^2 v + u^2 + 2\theta\theta_1 uv + \theta^2 v^2}{1 + 2\theta\theta_1 u + 2\theta^2\theta_1^2 v + \theta^2 u^2 + 2\theta^3\theta_1 uv + \theta^4 v^2}, \\ v = \frac{\theta^4 + 2\theta^3\theta_1 u + 2\theta^2\theta_1^2 v + \theta^2 u^2 + 2\theta\theta_1 uv + v^2}{1 + 2\theta\theta_1 u + 2\theta^2\theta_1^2 v + \theta^2 u^2 + 2\theta^3\theta_1 uv + \theta^4 v^2}. \end{cases} \quad (7)$$

Remark 1. The system (7) coincides with the classical result for the SOS model (see, e.g., [7, 9]) when $\theta_1 = 1$ ($J_1 = 0$), i.e.

$$\begin{cases} u = \left(\frac{u + \theta v + \theta}{\theta^2 v + \theta u + 1} \right)^2, \\ v = \left(\frac{\theta u + v + \theta^2}{\theta^2 v + \theta u + 1} \right)^2. \end{cases} \quad (8)$$

It is important to note that if there is more than one positive solution for system (7), then there is more than one translation-invariant limiting Gibbs measure corresponding to each solution. We say that a phase transition occurs for the model (1), if system (7) has more than one positive solution.

4. Translation-invariant Gibbs measures

In this section, we investigate phase transitions in the model. We consider dynamical system (6) and study its asymptotic behavior. Let $x = (u, v) \in \mathbb{R}_+^2$. The dynamical system $F : \mathbb{R}_+^2 \rightarrow \mathbb{R}_+^2$ is defined by

$$\begin{cases} u' = \frac{\theta^2 + 2\theta\theta_1 u + 2\theta^2\theta_1^2 v + u^2 + 2\theta\theta_1 uv + \theta^2 v^2}{1 + 2\theta\theta_1 u + 2\theta^2\theta_1^2 v + \theta^2 u^2 + 2\theta^3\theta_1 uv + \theta^4 v^2}, \\ v' = \frac{\theta^4 + 2\theta^3\theta_1 u + 2\theta^2\theta_1^2 v + \theta^2 u^2 + 2\theta\theta_1 uv + v^2}{1 + 2\theta\theta_1 u + 2\theta^2\theta_1^2 v + \theta^2 u^2 + 2\theta^3\theta_1 uv + \theta^4 v^2}. \end{cases} \quad (9)$$

Then recurrent equations (6) can be rewritten as $x^{(n+1)} = F(x^{(n)})$, $n \geq 0$. Recall that the point x is a periodic point of period p if $F^p(x) = x$, where $F^p(x)$ stands for p -fold composition of F into itself, i.e., $F^p(x) = \underbrace{F(F(\dots F(x)))}_{p}$. A

point $x \in \mathbb{R}_+^2$ is called a fixed point for $F : \mathbb{R}_+^2 \rightarrow \mathbb{R}_+^2$ if $F(x) = x$ (see for more details [1, Chapter 1] or [36, Section 1]). To analyze phase transitions in the class of translation-invariant limiting Gibbs measures, it is necessary to characterize the fixed points of the mapping $F(x) = x$. We now describe the solutions of this equation. It follows that the set

$$I = \{x = (u, v) \in \mathbb{R}^2 : v = 1\}. \quad (10)$$

is invariant under the operator F . On the set I , system of equations (7) reduces to

$$u = f(u) \quad (11)$$

where

$$f(u) = f(u, \theta, \theta_1) := \frac{u^2 + 4\theta\theta_1 u + 2\theta^2(\theta_1^2 + 1)}{\theta^2 u^2 + 2\theta\theta_1(\theta^2 + 1)u + \theta^4 + 2\theta^2\theta_1^2 + 1}. \quad (12)$$

It is easy to see that the function $f(u)$ defined in (12) is continuous, bounded with $f(0) > 0$ and $\lim_{u \rightarrow +\infty} f(u) < +\infty$. Moreover, this function is decreasing for $\theta > 1$ and increasing for $\theta < 1$. Thus, it suffices to consider the case $\theta < 1$, since for $\theta > 1$ the equation (11) has a unique positive solution. From properties of the function f , it follows that the function f has at least one fixed point, say, u_* . We have

Theorem 1. Let $\theta < 1$. For the SOS model with one-level second nearest-neighbor interactions on the binary tree on the set I , if the condition $f'(u_*) > 1$, that is,

$$\frac{2(1 - \theta^2) \left(2\theta^3\theta_1^3 + 2\theta^2\theta_1^2 u_* + \theta\theta_1 u_*^2 + \theta^2 u_* + 2\theta\theta_1 + u_* \right)}{\left(2\theta^3\theta_1 u_* + \theta^4 + 2\theta^2\theta_1^2 + \theta^2 u_*^2 + 2\theta\theta_1 u_* + 1 \right)^2} > 1 \quad (13)$$

is satisfied, then there exist three distinct translation-invariant limiting Gibbs measures, i.e., the phase transition occurs.

Proof. When $f'(u_*) > 1$, u_* is unstable. Thus, a small neighborhood $(u_* - \varepsilon, u_* + \varepsilon)$ of u_* exists such that for $u \in (u_* - \varepsilon, u_*)$, $f(u) < u$, and for $(u_*, u_* + \varepsilon)$, $f(u) > u$. Since $f(0) > 0$, there exists a solution between 0 and u_* . Similarly, since $\lim_{u \rightarrow +\infty} f(u) < +\infty$ there is another solution between u_* and $+\infty$. Thus, there exist three solutions. Since there exist a bijection between the solutions of Eq. (11) and the translation-invariant limiting Gibbs measures, it follows that there exist three translation-invariant limiting Gibbs measures, which implies the existence of a phase transition. This completes the proof. \square

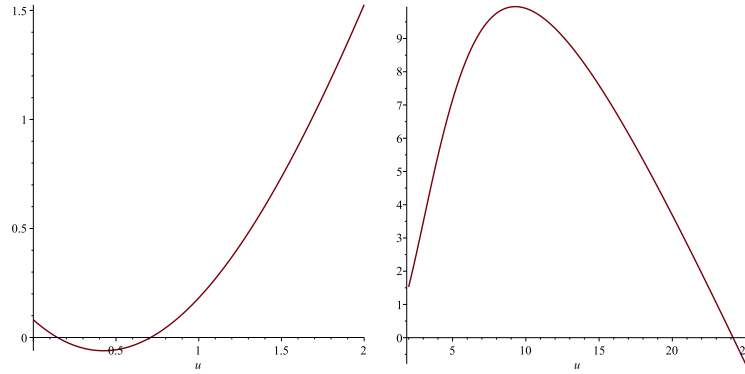


FIG. 2. The plot of $f(u) - u$ when $\theta = 0.2$, $\theta_1 = 0.5$. In this case, the function f has three positive fixed points: ≈ 0.1461 ; 0.7085 ; 24.1453 . The plot of the function is drawn for $u \in [0, 2]$, $u \in [2, 25]$ separately to show all three solutions

Remark 2. Note that the set of parameters which satisfy $f'(u_*) > 1$ is not empty, e.g., see Fig. 2.

Remark 3. In Theorem 1, we find sufficient conditions for Eq. (11) to possess multiple solutions, i.e., there might be multiple solutions for the equation even if $f'(u^*) \leq 1$.

Although solving the equation (11) for both parameters seems to be difficult, we could solve the equation in the case $\theta = \theta_1$. In this case, the equation (11) reads:

$$u^3 + Au^2 + Bu + C = 0, \quad (14)$$

where

$$A = \frac{1}{\theta^2} \left(\theta - \sqrt{\frac{\sqrt{3}-1}{2}} \right) \left(\theta + \sqrt{\frac{\sqrt{3}-1}{2}} \right) \left(\theta^2 + \frac{\sqrt{3}+1}{2} \right),$$

$$B = (\theta - 1)(\theta + 1)(3\theta^2 - 1), \quad C = -2\theta^2(\theta^2 + 1).$$

Note that $\sqrt{\frac{\sqrt{3}-1}{2}} \approx 0.605$ and $\frac{1}{\sqrt{3}} \approx 0.577$. According to the Descartes Rule of Signs (see, e.g., [37], Corollary 1), the equation (14) has at least one positive root and has at most three positive roots. We calculate the discriminant of (14) as in [38]:

$$\Delta'(\theta) := -\Delta(\theta) = 4A^3C - A^2B^2 - 18ABC + 4B^3 + 27C^2. \quad (15)$$

It is known (see [38], Theorem 4.3.8) that if $\Delta' > 0$ then the equation (14) has one real root and two imaginary roots. If $\Delta' = 0$ then the equation (14) has three real roots, at least two of which are equal. If $\Delta' < 0$ then the equation (14) has three distinct real roots. By the Descartes Rule of Signs, in order to have more than one distinct positive solutions, we should necessarily have

$$A < 0, \quad B > 0, \quad \Delta' \leq 0$$

which implies $\theta \leq \theta_c \approx 0.2729$, where θ_c solves the equation

$$100\theta^{14} + 8\theta^{12} + 372\theta^{10} - 56\theta^8 + 357\theta^6 - 155\theta^4 + 23\theta^2 - 1 = 0.$$

Summarizing, we have

Lemma 1. *There exists a unique $\theta_c \approx 0.2729$ such that*

- *If $\theta > \theta_c$ then Eq. (14) has one positive solution $u_1 > 0$*
- *If $\theta = \theta_c$ then Eq. (14) has two positive solutions $u_2 < u_1$*
- *If $\theta < \theta_c$ then Eq. (14) has three positive solutions $u_3 < u_2 < u_1$.*

See Fig. 3

We obtain

Theorem 2. For the SOS model with one-level next-nearest-neighbour interactions on the binary tree under condition $\theta = \theta_1$ on the set I there exists $\theta_c \approx 0.2729$ such that for $\theta \leq \theta_c$ there is a phase transition and for $\theta > \theta_c$ there is no phase transition.

Remark 4. In [9], the model is considered with only nearest neighbor interactions, and the critical value is found to be $\theta_{cr} \approx 0.1414$. We can see that the one-level next-nearest-interaction enlarges the phase transition interval.

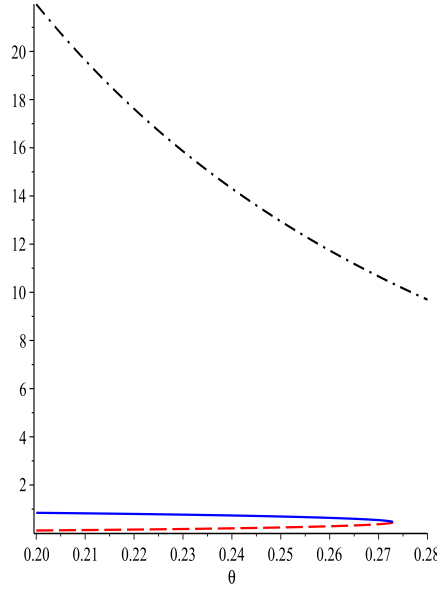


FIG. 3. The graph of functions $u_i = u_i(\theta)$, $i = 1, 2, 3$. Upper curve is u_1 , middle curve is u_2 and lower curve is u_3

5. Two-periodic Gibbs measures

The notion of periodic Gibbs measures is discussed by Sinai [39] and Ganikhodjaev and Rozikov [40]. In this section, we examine periodic solutions of Eq. (6). To describe the 2-periodic Gibbs measures of the model within the set I given in (10), we will analyze the equation $f(f(u)) = u$, where the function f is defined by (12). In this case, the positive roots of the equation

$$\frac{f(f(u)) - u}{f(u) - u} = 0, \tag{16}$$

subject to the condition $f(u) \neq u$, describe the pure two-periodic Gibbs measures. By simplifying above equation, we obtain

$$A u^2 + B u + C = 0 \tag{17}$$

where

$$\begin{aligned} A &:= A(\theta; \theta_1) = \theta^6 + 2\theta^4\theta_1^2 + 2\theta^3\theta_1 + \theta^2 + 2\theta\theta_1 + 1, \\ B &:= B(\theta; \theta_1) = 2\theta^7\theta_1 + 4\theta^5\theta_1^3 + 2\theta^5\theta_1 + 6\theta^4\theta_1^2 + 4\theta^3\theta_1^3 - \theta^4 + 2\theta^3\theta_1 + 10\theta^2\theta_1^2 + 6\theta\theta_1 + 1, \\ C &:= C(\theta; \theta_1) = \theta^8 + 4\theta^6\theta_1 + 4\theta^4\theta_1^4 + 4\theta^5\theta_1 + 8\theta^3\theta_1^3 + 2\theta^4 + 6\theta^2\theta_1^2 + 2\theta^2 + 4\theta\theta_1 + 1. \end{aligned}$$

Note that $A > 0$, $C > 0$ for any $\theta > 0$, $\theta_1 > 0$. According to Descartes' Rule of Signs (see, e.g., [37], Corollary 1) if $B \geq 0$ then the equation (17) does not have any positive solution (see Fig. 4). Thus, we have the following assertion:

Theorem 3. If

$$(\theta, \theta_1) \in \{(\theta, \theta_1) \in \mathbb{R}_+^2 : B \geq 0\}$$

then for the SOS model with one-level next-nearest-neighbour interactions on the binary tree there is no two-periodic (except for translation-invariant) Gibbs measures on the set I (10).

Based on Theorem 3, we now examine the case $B < 0$. If $B < 0$, then Eq. (17) may have two positive solutions. We compute the discriminant of Eq. (17):

$$D := D(\theta; \theta_1) = B^2 - 4AC.$$

It follows that if $B < 0$ and $D \geq 0$, then Eq. (17) has at least one positive solution. However, a computer analysis shows that the set

$$\mathcal{S} = \{(\theta, \theta_1) \in \mathbb{R}_+^2 : D \geq 0, B < 0\}$$

is empty. Summarising, we make

Conjecture 1. The SOS model with one-level next-nearest-neighbor interactions on the binary tree admits no two-periodic Gibbs measures within the set I (10).

Remark 5. a) Note that for the model (1) there might be two-periodic Gibbs measures outside of the set I (10).

b) In the case $\theta = \theta_1$ one can easily see that $B > 0$, thus, there is no two-periodic Gibbs measures.

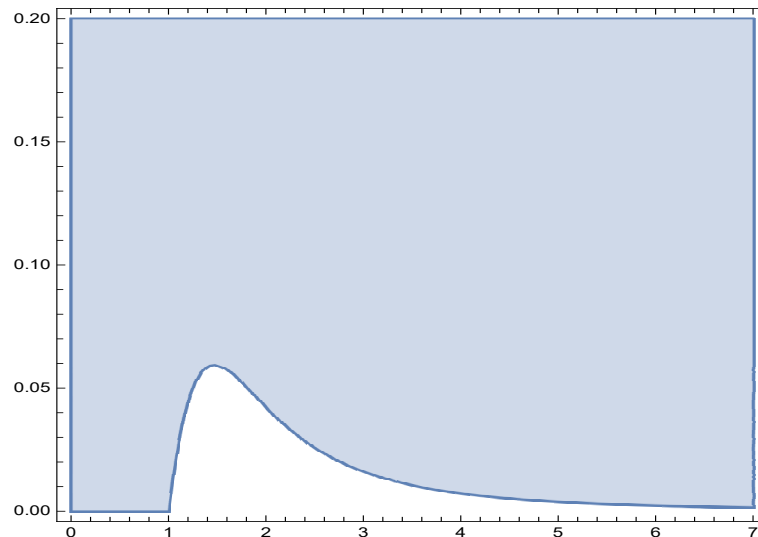


FIG. 4. The plot of $B(\theta, \theta_1)$ for $\theta \in (0, 7)$ and $\theta_1 \in (0, 0.2)$ The shaded area corresponds to $B(\theta, \theta_1) \geq 0$

6. Conclusion

In this paper, we have investigated phase transitions in the three-state solid-on-solid (SOS) model with one-level next-nearest-neighbor interactions on a Cayley tree of order two. Leveraging the self-similarity of the Cayley tree, we have derived a system of nonlinear recursive equations that describe the limiting Gibbs measures of the model. Our analysis revealed that for certain parameter values, the model exhibits multiple Gibbs measures, indicating the existence of a phase transition. Furthermore, we established explicit conditions under which the Gibbs measure is either unique or non-unique.

Additionally, we investigated the existence of two-periodic Gibbs measures and demonstrated that under certain conditions, no such measures exist in the model. We also proposed a conjecture stating the complete absence of two-periodic Gibbs measures on the invariant set. These results enhance our understanding of phase transitions in lattice models with competing interactions, which play a crucial role in statistical mechanics and mathematical physics.

From a broader perspective, our findings have implications for nanoscience, where phase transitions in nanoscale systems often exhibit unique characteristics due to finite-size effects. Studying Gibbs measures in these models provides insight into self-assembly processes and critical phenomena in nanomaterials. Future research may extend this approach to more complex lattice structures, higher-order interactions, or external fields to explore additional phase transition behaviors.

References

- [1] Devaney R.L. *An Introduction to Chaotic Dynamical Systems*. Westview Press, Boulder, 2003, 336 p.
- [2] Esfarjani K., Mansoori G.A. Statistical mechanical modeling and its application to nanosystems. *Handbook of Theoretical and Computational Nanotechnology*, 2006, **2**(14), P. 1–45.
- [3] Hill L. *Thermodynamics of Small Systems*. W.A. Benjamin, New York, 1963.
- [4] Hill T.L. A Different Approach to Nanothermodynamics. *Nano Letters*, 2001, **1**, P. 273–275.
- [5] Mansoori G.A. An Introduction to Nanoscience and Nanotechnology. *Proceedings of the First Conference on Nanotechnology - The Next Industrial Revolution*, 2002, **2**, p. 345.
- [6] Feynman R.P. There's plenty of room at the bottom. *Engineering and Science*, 1960, **5**(23), P. 22–36.
- [7] Rozikov U.A., Suhov Y.M. Gibbs measures for SOS model on a Cayley tree. *Infinite Dimensional Analysis, Quantum Probability and Related Topics*, 2006, **9**(3), P. 471–488.
- [8] Karshiboev O.Sh. Periodic Gibbs measures for the three-state SOS model on a Cayley tree with a translation-invariant external field. *Theor. Math. Phys.*, 2022, **212**, P. 1276–1283.
- [9] Kuelske C., Rozikov U.A. Extremality of translation-invariant phases for a three-state SOS-model on the binary tree. *J. Stat. Phys.*, 2015, **160**, P. 659–680.
- [10] Rahmatullaev M.M., Abraev B.U. Non-translation invariant Gibbs measures of an SOS model on a Cayley tree. *Reports on Mathematical Physics*, 2020, **86**(3), P. 345–360.
- [11] Rahmatullaev M.M., Abraev B.U. On ground states for the SOS model with competing interactions. *Journal of Siberian Federal University*, 2022, **15**(2), P. 1–14.
- [12] Rahmatullaev M.M., Karshiboev O.Sh. Gibbs measures for the three-state SOS model with external field on a Cayley tree. *Positivity*, 2022, **26**(74), P. 1–15.
- [13] Rahmatullaev M.M., Karshiboev O.Sh. Phase transition for the SOS model under inhomogeneous external field on a Cayley tree. *Phase Transitions*, 2022, **95**(12), P. 901–907.
- [14] Rozikov U.A., Shoyusupov Sh.A. Gibbs measures for the SOS model with four states on a Cayley tree. *Theoretical and Mathematical Physics*, 2006, **149**(1), P. 1312–1323.
- [15] Rozikov U.A. *Gibbs Measures on Cayley Trees*. World Scientific, Singapore, 2013, 404 p.
- [16] Georgii H.-O. *Gibbs Measures and Phase Transitions*. W. de Gruyter, Berlin, 1988.

- [17] Eshkabilov Yu.Kh., Haydarov F.H. On positive solutions of the homogeneous Hammerstein integral equation. *Nanosystems: Physics, Chemistry, Mathematics*, 2015, **6**(5), P. 618–627.
- [18] Ganikhodjaev N.N., Rahmatullaev M.M., Abdusalomova M.R. Phase transitions for the “uncle-nephew” model. *Nanosystems: Physics, Chemistry, Mathematics*, 2022, **13**(5), P. 498–502.
- [19] Khatamov N.M. Holliday junctions in the HC Blume-Capel model in “one case” on DNA. *Nanosystems: Physics, Chemistry, Mathematics*, 2021, **12**(5), P. 563–568.
- [20] Mavlonov I.M., Sattarov A.M., Karimova S.A., Haydarov F.H. On solutions to nonlinear integral equation of the Hammerstein type and its applications to Gibbs measures for continuous spin systems. *Nanosystems: Physics, Chemistry, Mathematics*, 2024, **15**(1), P. 23–30.
- [21] Rahmatullaev M.M., Egamov D.O. Translation-invariant Gibbs measures for the mixed spin-1/2 and spin-1 Ising model with an external field on a Cayley tree. *Nanosystems: Physics, Chemistry, Mathematics*, 2024, **15**(5), P. 576–585.
- [22] Ganikhodjaev N. Ising model with competing “uncle-nephew” interactions. *Phase Transitions*, 2016, **89**(12), P. 1196–1202.
- [23] Ganikhodjaev N., Akin H., Uguz S., Temir S. Phase diagram and extreme Gibbs measures of the Ising model on a Cayley tree in the presence of competing binary and ternary interactions. *Phase Transitions*, 2011, **84**(11-12), P. 1045–1063.
- [24] Katsura S., Takizawa M. Bethe lattice and the Bethe approximation. *Progress of Theoretical Physics*, 1974, **51**(1), P. 82–98.
- [25] Mukhamedov F., Rozikov U. On Gibbs Measures of Models with Competing Ternary and Binary Interactions and Corresponding von Neumann Algebras II. *Journal of Statistical Physics*, 2005, **119**, P. 427–446.
- [26] Ostilli M., Mukhamedov F., Mendes J. Phase diagram of an Ising model with competitive interactions on a Husimi tree and its disordered counterpart. *Physica A: Statistical Mechanics and its Applications*, 2008, **387**(12), P. 2777–2792.
- [27] Tragtenberg M.H.R., Yokoi C.S.O. Field behaviour of an Ising model with competing interactions on the Bethe lattice. *Physical Review E*, 1995, **52**(3), P. 2187–2197.
- [28] Vannimenus J. Modulated phase of an Ising system with competing interactions on a Cayley tree. *Z. Phys. B*, 1981, **43**, P. 141–148.
- [29] Yokoi C.S.O., Oliveira M.J., Salinas S.R. Strange attractor in the Ising model with competing interactions on the Cayley tree. *Phys. Rev. Lett.*, 1985, **54**(3), P. 163–166.
- [30] Mukhamedov F., Rozikov U. On Gibbs Measures of Models with Competing Ternary and Binary Interactions and Corresponding von Neumann Algebras. *Journal of Statistical Physics*, 2004, **114**, P. 825–848.
- [31] Ganikhodjaev N.N., Akin H., Temir S. Potts model with two competing binary interactions. *Turkish Journal of Mathematics*, 2007, **31**(3), P. 365–378.
- [32] Ganikhodjaev N., Mukhamedov F., Mendes J.F.F. On the three-state Potts model with competing interactions on the Bethe lattice. *Journal of Statistical Mechanics*, 2006, **08**(1-29), P. P08012.
- [33] Ganikhodjaev N.N., Mukhamedov F., Pah C. H. Phase diagram of the three-state Potts model with next-nearest-neighbor interactions on the Bethe lattice. *Physics Letters A*, 2008, **373**(1), P. 33–38.
- [34] Ganikhodjaev N.N., Temir S., Akin H. Modulated phase of a Potts model with competing binary interactions on a Cayley tree. *J. Stat. Phys.*, 2009, **137**, P. 701–715.
- [35] Ganikhodjaev N.N., Pah C.H., Wahiddin M.R.B. Exact solution of an Ising model with competing interactions on a Cayley tree. *Journal of Physics A: Mathematical and General*, 2003, **36**(15), P. 4283–4289.
- [36] Rozikov U.A. *An introduction to mathematical billiards*. World Scientific, Hackensack, NJ, 2019.
- [37] Prasolov V.V. *Polynomials*. Springer Science and Business Media, 2004, 301 p.
- [38] Leung K.T., Mok I.A.C., Seun S.N. Polynomials and equations. *Hong Kong University Press*, 1992, 250 p.
- [39] Sinai Ya.G. *Theory of phase transitions: rigorous results*. Elsevier, 2014, 159 p.
- [40] Ganikhodjaev N.N., Rozikov U.A. Description of periodic extreme Gibbs measures of some lattice models on the Cayley tree. *Theor. Math. Phys.*, 1997, **111**, P. 480–486.

Submitted 12 September 2024; revised 22 February 2025; accepted 23 February 2025

Information about the authors:

Obid Sh. Karshiboev – Namangan State University, 161, Boburshox str, 160107, Namangan, Uzbekistan; ORCID 0000-0001-6204-4621; okarshiboevsher@mail.ru

Muzaffar M. Rahmatullaev – V. I. Romanovskiy Institute of Mathematics, Uzbekistan Academy of Sciences, 4-b, University str, 100174, Tashkent, Uzbekistan; New Uzbekistan University, 100000, Tashkent, Uzbekistan; ORCID 0000-0003-2987-7714; mrahmatullaev@rambler.ru

Conflict of interest: the authors declare no conflict of interest.

Extremality of Gibbs measures for the DNA-Ising molecule model on the Cayley tree

Nosirjon M. Khatamov^{1,2,a}, Nematulla N. Malikov^{1,b}¹Namangan state university, Namangan, Uzbekistan,²V. I. Romanovskiy Institute of Mathematics, Uzbekistan Academy of Sciences, Tashkent, Uzbekistan^anxatamov@mail.ru, ^bmalikovnematulla24@gmail.comCorresponding author: N. M. Khatamov, nxatamov@mail.ru

PACS 517.98

ABSTRACT We examine a model of a DNA-Ising molecule on a Cayley tree of order $k \geq 2$. For this model, we derive a system of functional equations, where each positive solution corresponds to a Gibbs measure. On the general order Cayley tree, we can solve the model exactly. Specifically, we can find the exact value of the critical temperature T_c for any $k \geq 2$ so that, if $T \geq T_c$, there is a unique translation-invariant Gibbs measure (TIGM), and if $T < T_c$, there are three TIGMs. We determine the model's typical configurations and stationary distributions for high enough and low enough temperatures. The primary attention is focused on the systematic study of the structure of the set of the Gibbs measures. In this paper, we present a non-trivial adaptation of famous techniques, such as the Martinelli-Sinclair-Weitz criterion for determining the extremality of TIGMs and the Kesten-Stigum criterion for determining the non-extremality of TIGMs. One of the important contributions of this paper is the resolution of the extremality versus non-extremality regions for one of the TIGMs on a Cayley tree of the general order. For the other TIGMs, the extremality and non-extremality regions are determined on Cayley trees of orders up to 5.

KEYWORDS DNA, temperature, Cayley tree, Gibbs measure, translation-invariant measures, extreme of measure

ACKNOWLEDGEMENTS The authors express their gratitude to Academician U. A. Rozikov for his suggestions that contributed to improving the readability of the article. We thank the referee for the careful reading of the manuscript and especially for a number of suggestions that have improved the paper. The first author (NMKh) thanks the State Grant F-FA-2021-425 of the Republic of Uzbekistan for financial support.

FOR CITATION Khatamov N.M., Malikov N.N. Extremality of Gibbs measures for the DNA-Ising molecule model on the Cayley tree. *Nanosystems: Phys. Chem. Math.*, 2025, **16** (2), 142–153.

1. Introduction and Definitions

The Ising model is the most basic and widely used phase transition model in statistical physics, and it has a long and significant history. The significance of the statistical theory of the Ising model is described through the fact that it is used to investigate a wide variety of both magnetic and non-magnetic systems.

Translation-invariant, periodic and weakly periodic Gibbs measures for the Ising model on the Cayley tree were researched by U.A. Rozikov, M.M. Rakhmatullaev [1, 2]. In the studies by P.M. Blekher and N.N. Ganikhodzhaev [3], the existence of a continuum number of Gibbs measures was proved.

In the research performed by U.A. Rozikov, D. Gandolfo, J. Ruiz, H. Akin, S. Temur, and F.Kh. Khaydarov, the limit Gibbs measures for the Ising model were investigated using a method based on the theory of Markov random fields and the recurrent equations (see [4–6]).

In recent years, the thermodynamics of certain DNA models has been investigated in the field of statistical physics. For instance, in [7–12], the Holliday junctions of the DNA molecule of the Ising, Potts, and Blume-Capel models on the Cayley tree were studied. In [13], statistical mechanics methods, specifically the theory of Gibbs measures, are employed to analyze the thermodynamic properties of a new model. Using these measures, the phases (states) of the DNA-RNA system are characterized, and the conditions (in temperature) for DNA-RNA renaturation are outlined. The book [14] discusses the latest mathematical results regarding Gibbs measures for the Potts model with q states, focusing on both the integer lattice and Cayley trees. It also demonstrates various applications of the Potts model to real situations such as biology, physics, financial engineering, medicine, sociology, neural networks, and other scientific fields.

It is widely acknowledged that the nucleotide sequence of DNA encodes genetic information [15]. Each DNA molecule consists of a double helix made up of two complementary nucleotide chains connected by base pairs through $G + C$ and $A + T$ bonds. In this context, C stands for cytosine, G for guanine, A for adenine, and T for thymine. Genetic information is replicated by utilizing one DNA strand as a template to synthesize a complementary strand. The genetic

information encoded in an organism's DNA provides the instructions for the synthesis of all the proteins that the organism will produce throughout its life.

The structure of DNA can be analyzed using statistical physics approaches (see [16, 17]), representing a single DNA strand as a stochastic system of interacting bases that exhibit long-range correlations. This analysis reveals a significant link between the structure of the DNA sequence and temperature; for instance, phase transitions in this system can be understood as conformational changes.

It is recognized [2, 18–23] that the set of Gibbs measures constitutes a non-empty, convex, and compact subset within the space of probability measures. Additionally, every Gibbs measure can be represented as an integral of extreme Gibbs measures, a concept referred to as extreme decomposition [18]. As a result, the extreme points play a crucial role in characterizing the entire convex set of Gibbs measures. The extreme disordered phases of lattice models are especially important in the context of information flow theory [2, 24–26]. In this paper, we present a non-trivial adaptation of established methods, such as the Kesten-Stigum criterion [32] for determining the non-extremality of translation-invariant Gibbs measures, and the Martinelli-Sinclair-Weitz method [33] for assessing the extremality of these measures.

The organization of the paper is as follows: Chapter 2 introduces the fundamental definitions from biology and mathematics. In Chapter 3, we formulate a system of functional equations, where each solution characterizes a family of finite-dimensional Gibbs distributions and ensures the existence of a thermodynamic limit for these distributions. Moreover, we investigate the nature of DNA interactions by exploring the properties of Markov chains (with the corresponding Gibbs measures). At extremely high and low temperatures, we derive stationary distributions and typical configurations of the model. In Chapters 4 and 5, we analyze the (non)extremity problem related to the obtained TIGMs.

2. Description of DNA as a Cayley tree

Following [2, 7, 9], we review some definitions.

A Cayley tree Γ^k of order $k \geq 1$ is an infinite tree, which is defined as a graph without cycles, where exactly $k + 1$ edges converge at each vertex. Let $\Gamma^k = (V, L, i)$, where V denotes the set of vertices of Γ^k , L is the set of edges and i is the incidence function that assigns each edge $l \in L$ to its endpoints $x, y \in V$. If $i(l) = \{x, y\}$, x and y are called nearest neighbors, represented as $l = \langle x, y \rangle$. The distance $d(x, y)$, $x, y \in V$ on a Cayley tree is defined as the number of edges in the shortest path connecting x to y :

$$d(x, y) = \min\{d | \exists x = x_0, x_1, \dots, x_{d-1}, x_d = y \in V \text{ such that } \langle x_0, x_1 \rangle, \dots, \langle x_{d-1}, x_d \rangle\}.$$

For a fixed $x^0 \in V$, we define $W_n = \{x \in V \mid d(x, x^0) = n\}$,

$$V_n = \{x \in V \mid d(x, x^0) \leq n\}, \quad L_n = \{l = \langle x, y \rangle \in L \mid x, y \in V_n\}. \quad (1)$$

Let $\mathbb{Z} = \{\dots, -2, -1, 0, 1, 2, \dots\}$. In [27], it was established that the vertices of the Cayley tree can be partitioned into equivalence classes that are indexed by integers, and for each vertex in the m -equivalence class, there is a unique path such that the equivalence class numbers of the successive vertices along this path create an infinite sequence in both directions: $\dots, m - 2, m - 1, m, m + 1, m + 2, \dots$. It is called the \mathbb{Z} -path.

Because each vertex x has its own \mathbb{Z} -path, it is evident that the Cayley tree encompasses an infinite number of (countable) sets of \mathbb{Z} -paths. We define the hierarchy of the Cayley tree of a set of DNA molecules as follows.

Given a configuration σ on the Cayley tree, the presence of countably many \mathbb{Z} -paths implies that there are also countably many distinct DNAs. We define two DNAs as *neighbors* if there is an edge in the Cayley tree such that one endpoint is part of the first DNA and the other endpoint is part of the second DNA. By construction, it is evident that there is a unique edge for every pair of neighboring DNAs. This edge has equivalent endpoints, meaning that both ends belong to the same equivalence class for some $m \in \mathbb{Z}$.

A hierarchy is created by a countable, infinite set of DNA molecules where

- (i) No two DNAs ever intersect,
- (ii) every DNA possesses its own countable set of neighboring DNAs,
- (iii) for any two neighboring DNAs, denoted as D_1 and D_2 , there exists a unique edge $l = l(D_1; D_2) = \langle x, y \rangle$ where $x \sim y$ that connects these DNAs, and
- (iv) The ball V_n intersects only finitely many DNAs for any finite $n \geq 1$.

Model. A configuration $\sigma = \sigma(x)$, $x \in V$ on the vertex set of a Cayley tree is defined as the function σ that assigns a value $\sigma(x) \in \{-1, 1\}$, to each vertex $x \in V$, here -1 and 1 accordingly represents the base pairs $A + T$ and $C + G$. The sets of all configurations on V and V_n are accordingly denoted by Ω and Ω_n . The restriction of a configuration to a \mathbb{Z} -path is termed DNA. This type of problem is discussed in the work [9]. Here, two potentials define the energies of the DNA molecule set's configuration σ : one on the \mathbb{Z} -path and the other off the \mathbb{Z} -path. The DNA molecule's configuration energies σ on the path \mathbb{Z} and outside of it are determined by the same potentials in this work, namely, the Ising model of the configuration energies σ of the DNA molecule set is considered

$$H(\sigma) = J \sum_{\langle x, y \rangle \in L} \sigma(x)\sigma(y), \quad (2)$$

here the vertices of the closest neighbors are indicated by $\langle x, y \rangle$, $J > 0$ is the coupling constant between neighboring DNAs, and $\sigma(x) \in \{-1, 1\}$.

3. Thermodynamics of the DNA molecule system.

We establish a finite-dimensional distribution for the probability measure μ on the set Ω_n of all conceivable configurations on V_n

$$\mu_n(\sigma_n) = Z_n^{-1} \exp\{\beta H_n(\sigma_n) + \sum_{y \in W_n} h_{\sigma(y), y}\}, \quad (3)$$

where Z_n^{-1} is the normalizing coefficient, $\beta = \frac{1}{T}$, $T > 0$ is the temperature,

$$H_n(\sigma_n) = \sum_{\langle x, y \rangle \in L_n} \sigma_n(x) \sigma_n(y)$$

and $\{h_{i,x} \in \mathbb{R}, i = -1, 1, x \in V_n\}$

Remark 1. The quantities $e^{h_{i,x}}$ define the boundary law in the sense of definition 12.10 in [18] (see also [28–30]). In our case, these quantities define the boundary law of the biological DNA system.

We will refer to the probability distributions (3) as consistent if, for all $n \geq 1$ and $\sigma_{n-1} \in \Omega_{n-1}$:

$$\sum_{\omega_n \in \Omega_{W_n}} \mu_n(\sigma_n \vee \omega_n) = \mu_{n-1}(\sigma_{n-1}), \quad (4)$$

where $\sigma_n \vee \omega_n$ is the union of configurations.

For $x \in V_{n-1}$, we define the set $S(x) = \{t \in V_n : \langle x, t \rangle\}$. For $x \in V$, we define x_\downarrow as the unique point in the set $\{y \in V : \langle x, y \rangle\} \setminus S(x)$. It is evident that

$$S(x) \cap \mathbb{Z}\text{-path} = \begin{cases} \{x_0, x_1\} \subset V, & \text{if } \langle x_\downarrow, x \rangle \notin \mathbb{Z}\text{-path}, \\ \{x_1\} \subset V, & \text{if } \langle x_\downarrow, x \rangle \in \mathbb{Z}\text{-path}. \end{cases}$$

We introduce the notation

$$\begin{aligned} S_0(x) &= S(x) \setminus \{x_0, x_1\}, \langle x_\downarrow, x \rangle \notin \mathbb{Z}\text{-path}, \\ S_1(x) &= S(x) \setminus \{x_1\}, \langle x_\downarrow, x \rangle \in \mathbb{Z}\text{-path}. \end{aligned}$$

A specific instance of Theorem 1 from [9] is the following theorem.

Theorem 1. *The probability distributions μ_n in (3) are consistent if and only if the equations*

$$\begin{aligned} z_x &= \frac{\theta^2 \hat{z}_{x_0} + 1}{\hat{z}_{x_0} + \theta^2} \cdot \frac{\theta^2 \hat{z}_{x_1} + 1}{\hat{z}_{x_1} + \theta^2} \prod_{t \in S_0(x)} \frac{\theta^2 z_t + 1}{z_t + \theta^2}, \langle x_\downarrow, x \rangle \notin \mathbb{Z}\text{-path}, \\ \hat{z}_x &= \frac{\theta^2 \hat{z}_{x_1} + 1}{\hat{z}_{x_1} + \theta^2} \prod_{t \in S_1(x)} \frac{\theta^2 z_t + 1}{z_t + \theta^2}, \langle x_\downarrow, x \rangle \in \mathbb{Z}\text{-path}, \end{aligned} \quad (5)$$

holds for any $x \in V \setminus \{x^0\}$. Here

$$\begin{aligned} \theta &= e^{-J\beta}, \\ z_x &= e^{h_{1,x} - h_{-1,x}}, \langle x_\downarrow, x \rangle \notin \mathbb{Z}\text{-path}, \\ \hat{z}_x &= e^{h_{1,x} - h_{-1,x}}, \langle x_\downarrow, x \rangle \in \mathbb{Z}\text{-path}. \end{aligned}$$

Remark 2. The difference between the present paper and [9] is that here the number of parameters is reduced, but the tree order is increased to $k = 2, 3, 4, 5$ and the results are obtained for these cases. At the same time, in these cases, we consider the problem of extremity of Gibbs measures which is a new problem in the set of DNA molecules.

It follows from Theorem 1 that for any set of vectors $\mathbf{z} = \{(z_x, \hat{z}_x)\}$ satisfying the system of functional equations (5), there exists a unique Gibbs measure μ and vice versa. But the analysis of this system of nonlinear functional equations is not easy. In the next subsection, we will find several of its solutions.

Remark 3. The number of solutions of the system (5) depends on the temperature and the interaction parameters θ . If this system has more than one solution, then there is more than one Gibbs measure (i.e., a phase transition occurs in the DNA model).

We find solutions of the system of equations (5) of the form

$$\begin{aligned} z_x &= u, \text{ for all } \langle x_\downarrow, x \rangle \notin \mathbb{Z}\text{-path}, \\ \hat{z}_x &= v, \text{ for all } \langle x_\downarrow, x \rangle \in \mathbb{Z}\text{-path}. \end{aligned}$$

The Gibbs measures corresponding to such solutions are called *translation-invariant*.

From (5), we obtain

$$\begin{aligned} u &= \left(\frac{\theta^2 v + 1}{v + \theta^2} \right)^2 \left(\frac{\theta^2 u + 1}{u + \theta^2} \right)^{k-2}, \\ v &= \left(\frac{\theta^2 v + 1}{v + \theta^2} \right) \left(\frac{\theta^2 u + 1}{u + \theta^2} \right)^{k-1}, \end{aligned} \quad (6)$$

where $u, v > 0$. Clearly, $u = v = 1$ satisfies system (6) for any $k \geq 2$ and $\theta > 0$.

Now, in the general case, we solve the system of equations (6). To do this, we divide the first equation by the second of this system. Then we get

$$\frac{u}{v} = \frac{\theta^2 v + 1}{v + \theta^2} \cdot \frac{u + \theta^2}{\theta^2 u + 1},$$

or

$$(u - v)(\theta^2 uv + \theta^4(u + v) + \theta^2) = 0.$$

The last equation is true if and only if $u = v$. Since $u, v, \theta > 0$, then $\theta^2 uv + \theta^4(u + v) + \theta^2 > 0$.

Therefore, it is sufficient to find a solution to the system of equations (6) in the case $u = v$, i.e.

$$u = \left(\frac{\theta^2 u + 1}{u + \theta^2} \right)^k. \quad (7)$$

Denoting $x = \sqrt[k]{u}$ from (7), we obtain

$$x^{k+1} - \theta^2 x^k + \theta^2 x - 1 = 0. \quad (8)$$

Equation (7) has a solution $x = 1$ regardless of the parameters (θ, k) . Dividing the both parts of (7) by $x - 1$, we obtain

$$x^k - (\theta^2 - 1)(x^{k-1} + x^{k-2} + \dots + x) + 1 = 0. \quad (9)$$

The following lemma gives one the number of solutions of the equation (9):

Lemma 1. [31] For each $k \geq 2$, there exists exactly one critical value of θ , i.e. $\theta_c = \theta_c(k) := \sqrt{\frac{k+1}{k-1}}$, such that

- (1) if $\theta < \theta_c$, then equation (9) does not have a positive solution;
- (2) if $\theta = \theta_c$, then equation (9) has a unique solution $x_1^{(k)} = 1$;
- (3) if $\theta > \theta_c$, then equation (9) has exactly two solutions (both different from 1), denoted as $x_2^{(k)}, x_3^{(k)}$.

Thus, the corresponding solutions (7) are equal to

$$\begin{aligned} 1) & 1 \text{ for } \theta \leq \theta_c, \\ 2) & 1, \left(x_2^{(k)}\right)^k, \left(x_3^{(k)}\right)^k \text{ for } \theta > \theta_c. \end{aligned} \quad (10)$$

For $k \geq 2$, we can prove the following lemma.

Lemma 2. Let $k \geq 2$ and $\theta_{cr} = \sqrt{\frac{k+1}{k-1}}$. Then the following statements hold:

- if $\theta = \exp(-J\beta) \leq \theta_c$, then system (6) has a unique solution

$$\mathbf{z}_1^{(k)} = (u_1^{(k)}, u_1^{(k)}) = (1, 1);$$

- if $\theta > \theta_c$, then system (6) has three solutions

$$\mathbf{z}_1^{(k)} = (u_1^{(k)}, u_1^{(k)}) = (1, 1), \mathbf{z}_2^{(k)} = (u_2^{(k)}, u_2^{(k)}), \mathbf{z}_3^{(k)} = (u_3^{(k)}, u_3^{(k)}),$$

where

$$u_i^{(k)} = \left(x_i^{(k)}\right)^k, i = 2, 3, u_2^{(k)} u_3^{(k)} = 1.$$

Let us denote by $\mu_i^{(k)}$ the Gibbs measures corresponding to the solutions $\mathbf{z}_i^{(k)}$, $i = 1, 2, 3$. Let us define the critical temperature

$$T_c := T_c(k) = \frac{J}{\ln \sqrt{\frac{k-1}{k+1}}}.$$

Thus, summarising, we obtain the following result

Theorem 3. For the DNA-Ising molecule model on the Cayley tree of order $k \geq 2$, the following statements are true:

- 1) if $T \geq T_c$, then there exists a unique translation-invariant Gibbs measure $\mu_1^{(k)}$;

2) if $T < T_c$, then there exist three translation-invariant Gibbs measures $\mu_1^{(k)}, \mu_2^{(k)}, \mu_3^{(k)}$, i.e. a phase transition occurs.

Remark 4. Note that, in comparison with work [9], the exact value of the critical temperature is found here for any $k \geq 2$, and the analysis of the equations in these works is different.

For further discussion, we will need an explicit solution of the system of equations (6), i.e. equation (7).

Equation (7) has the following explicit solutions:

- for $k = 2$ there is a unique solution $u_1^{(2)} = 1$ for $0 < \theta \leq \sqrt{3}$ and there are three positive solutions for $\theta > \sqrt{3}$:

$$u_1^{(2)} = 1, u_{2,3}^{(2)} = \frac{\theta^4 - 2\theta^2 - 1 \pm \sqrt{(\theta^4 - 2\theta^2 - 1)^2 - 4}}{2}. \tag{11}$$

- for $k = 3$ there is a unique solution $u_1^{(3)} = 1$ in the interval $0 < \theta \leq \sqrt{2}$ and there are three positive solutions in the interval $\theta > \sqrt{2}$:

$$u_1^{(3)} = 1, u_{2,3}^{(3)} = \frac{\theta^6 - 3\theta^2 \pm \sqrt{(\theta^6 - 3\theta^2)^2 - 4}}{2}. \tag{12}$$

- for $k = 4$ there is a unique solution $u_1^{(4)} = 1$ in the interval $0 < \theta \leq \sqrt{\frac{5}{3}}$ and for $\theta > \sqrt{\frac{5}{3}}$ there are three positive solutions:

$$u_1^{(4)} = 1, u_{2,3}^{(4)} = \left(\frac{z_1 \pm \sqrt{z_1^2 - 4}}{2} \right)^4, \tag{13}$$

where

$$z_1 = \frac{\theta^2 - 1 + \sqrt{(\theta^2 - 1)^2 + 4(1 + \theta^2)}}{2}.$$

- for $k = 5$ there is a unique solution $u_1^{(5)} = 1$ in the interval $0 < \theta \leq \sqrt{\frac{3}{2}}$ and for $\theta > \sqrt{\frac{3}{2}}$ there are three positive solutions:

$$u_1^{(5)} = 1, u_{2,3}^{(5)} = \left(\frac{z_2 \pm \sqrt{z_2^2 - 4}}{2} \right)^5. \tag{14}$$

where

$$z_2 = \frac{\theta^2 + \sqrt{\theta^4 + 4}}{2}.$$

Markov chains. The transition matrix of a Markov chain (with a given Gibbs measure) is defined as (see [9])

$$\mathbb{P}^{\langle x,y \rangle} = (P_{i,j}^{\langle x,y \rangle})_{i,j=1,2} = \begin{cases} \begin{pmatrix} \frac{\theta^2 u}{\theta^2 u + 1} & \frac{1}{\theta^2 u + 1} \\ \frac{u + \theta^2}{\theta^2 v} & \frac{u + \theta^2}{u + \theta^2} \end{pmatrix}, & \langle x,y \rangle \in \mathbb{Z}\text{-path}, \\ \begin{pmatrix} \frac{\theta^2 v + 1}{v + \theta^2} & \frac{\theta^2 v + 1}{\theta^2 v + 1} \\ \frac{v}{v + \theta^2} & \frac{v + \theta^2}{v + \theta^2} \end{pmatrix}, & \langle x,y \rangle \notin \mathbb{Z}\text{-path}, \end{cases}$$

where (u, v) is the solution of system (6) (mentioned in Lemma 2). Note that each matrix $\mathbb{P}^{\langle x,y \rangle}$ does not depend on $\langle x, y \rangle$ itself, but depends on the \mathbb{Z} -path to which it belongs.

Stationary distributions are easy to find:

$$\pi^{\langle x,y \rangle} = \begin{cases} \left(\frac{\theta^2 u^2 + u}{\theta^2 u^2 + 2u + \theta^2}, \frac{u + \theta^2}{\theta^2 u^2 + 2u + \theta^2} \right), & \langle x,y \rangle \in \mathbb{Z}\text{-path}, \\ \left(\frac{\theta^2 v^2 + v}{\theta^2 v^2 + 2v + \theta^2}, \frac{v + \theta^2}{\theta^2 v^2 + 2v + \theta^2} \right), & \langle x,y \rangle \notin \mathbb{Z}\text{-path}. \end{cases}$$

The following statement is known as the ergodic theorem for positive stochastic matrices (see [18]).

Theorem 4. Let \mathbb{P} be a positive stochastic matrix and π be the unique probability vector with $\pi\mathbb{P} = \pi$ (i.e. π is a stationary distribution). Then

$$\lim_{n \rightarrow \infty} x\mathbb{P}^n = \pi$$

for all initial vectors x .

In the case where the Gibbs measure (and the corresponding Markov chains) are not unique, we have different stationary states for different measures. These states depend on the temperature and the fixed measure.

Recall that a DNA molecule is a configuration $\sigma \in \{-1, 1\}^{\mathbb{Z}}$ on a \mathbb{Z} -path. According to the definition of our model, only neighboring DNAs can interact. Interaction occurs through an edge $l = \langle x, y \rangle \notin \mathbb{Z}$ -path connecting two DNA molecules when the configuration at the ends of this edge satisfies $\sigma(x) = \sigma(y)$. Neighboring DNAs do not interact if $\sigma(x) \neq \sigma(y)$.

The following theorem can be proved similarly to Theorem 4 in [9].

Theorem 5. *In the stationary state of the DNA set we have the following statements:*

1. *Two neighboring DNAs do not interact with probability (here and below, index i corresponds to measure $\mu_i^{(k)}$, $i = 1, 2, 3$)*

$$\mathbb{P}_{i,k} = \frac{2v_i^{(k)}}{\theta^2 \left(v_i^{(k)}\right)^2 + 2v_i^{(k)} + \theta^2},$$

where $(u_i^{(k)}, v_i^{(k)})$ are defined in Lemma 2 and, therefore, interact with probability $1 - \mathbb{P}_{i,k}$.

2. *Two neighboring base pairs (on the vertices of an edge $l = \langle x, y \rangle \in \mathbb{Z}$ -path) in a DNA molecule have distinct values (i.e., $\sigma(x) \neq \sigma(y)$) with the probability*

$$\mathbb{Q}_{i,k} = \frac{2u_i^{(k)}}{\theta^2 \left(u_i^{(k)}\right)^2 + 2u_i^{(k)} + \theta^2},$$

and they consequently have the same value with the probability $1 - \mathbb{Q}_{i,k}$.

Remark 5. Since each DNA molecule has a countable set of neighboring DNA molecules, at the same temperature it can interact with several of its neighbors. In the case where DNA does not interact with its neighbors, it is isolated. We can consider the interacting DNA molecules as a branched DNA molecule. In the case of coexistence of more than one Gibbs measure, the branches of the DNA molecule can consist of different phases and different stationary states.

We are interested in the stationary distributions of $\pi^{\langle x, y \rangle, i, k}$ for $k = 2, 3, 4, 5$ (which correspond to the Markov chain generated by the Gibbs measure μ_i) in the cases when the temperature $T \rightarrow 0$ and $T \rightarrow +\infty$. To calculate the limit, note that $u_i^{(k)}$ and $v_i^{(k)}$, $i = 1, 2, 3$, vary with $T = 1/\beta$.

Proposition 1. *Regardless of the edge $\langle x, y \rangle$ for $k = 2, 3, 4, 5$, we have the following limit relations*

$$\lim_{T \rightarrow 0} \pi^{\langle x, y \rangle, 1, k} = \left(\frac{1}{2}, \frac{1}{2}\right), \quad \lim_{T \rightarrow 0} \pi^{\langle x, y \rangle, 2, k} = (0, 1), \quad \lim_{T \rightarrow 0} \pi^{\langle x, y \rangle, 3, k} = (1, 0)$$

in case of low temperatures and

$$\lim_{T \rightarrow +\infty} \pi^{\langle x, y \rangle, 1, k} = \lim_{T \rightarrow T_c} \pi^{\langle x, y \rangle, i, k} = \left(\frac{1}{2}, \frac{1}{2}\right), \quad i = 1, 2, 3$$

in case of high temperatures.

Proof. The proof is obtained from the explicit formulas for $k = 2, 3, 4, 5$ for $u_i^{(k)}$ and $v_i^{(k)}$, $i = 1, 2, 3$, respectively, by direct calculations.

Remark 6. Using this proposition, we obtain the structure of DNA at $k = 2, 3, 4, 5$ for low and high temperatures.

In the case of $T \rightarrow 0$, the DNA set has the following stationary states (configurations).

For a measure of $\mu_1^{(k)}$, the base pairs $-1 = A + T$ and $1 = C + G$ at each point of the DNA molecule are found with equal probability $1/2$ for states -1 and 1.

For measure $\mu_2^{(k)}$ all DNAs are rigid and interact, and $\sigma(x) = 1$ for all $x \in \mathbb{Z}$ -paths.

For measure $\mu_3^{(k)}$, all DNAs are rigid and interact, and $\sigma(x) = -1$ for all $x \in \mathbb{Z}$ -paths.

In the case $T \rightarrow +\infty$, the sequence of states -1 and 1 in the DNA molecule on the \mathbb{Z} -path is free, the states are independent and identically distributed. There is a state -1 with probability $1/2$ and a state 1 with probability $1/2$.

4. Conditions (not) extremes of measures $\mu_1^{(k)}, \mu_2^{(k)}, \mu_3^{(k)}$

It is known that the set of all limit Gibbs measures (corresponding to a given Hamiltonian) forms a non-empty convex compact subset in the set of all probability measures. In this connection, the description of all extreme points of this convex set, i.e. extreme Gibbs measures, is of particular interest.

To check the (non)extremality of the measure, we use the methods from [32,33]. For this, we consider Markov chains with states $\{-1, 1\}$ and the matrix P_μ of probability transitions $P_{\sigma(x)\sigma(y)}$ defined by the given translation-invariant Gibbs measure μ , i.e. $P_{\sigma(x)\sigma(y)}$ is the probability of a shift from the state $\sigma(x)$ to the state $\sigma(y)$.

A sufficient condition for the Gibbs measure corresponding to the matrix P_μ to be non-extreme is that $k\lambda_2^2 > 1$, where λ_2 is the second largest eigenvalue of the matrix P_μ (the Kesten-Stigum condition).

To check this condition, we need to know the explicit form of the solution of the system (6). Exact solutions are currently known to us only for $k \leq 5$.

It is clear that for $k \geq 2$, the system of equations (6) for $\theta \leq \theta_{cr} = \sqrt{\frac{k+1}{k-1}}$ has a unique solution $(u_1^{(k)}, u_1^{(k)}) = (1, 1)$ and for $\theta > \theta_{cr} = \sqrt{\frac{k+1}{k-1}}$ has three solutions $(u_1^{(k)}, u_1^{(k)}) = (1, 1), (u_2^{(k)}, u_2^{(k)}), (u_3^{(k)}, u_3^{(k)})$.

Let us find the conditions for non-extremality of the measures corresponding to these solutions. Since $u = v$ for any $\langle x, y \rangle \in L$. Then we obtain

$$\mathbb{P}_k^{\langle x, y \rangle} = \mathbb{P}_k = \begin{pmatrix} \frac{\theta^2 u^{(k)}}{\theta^2 u^{(k)} + 1} & \frac{1}{\theta^2 u^{(k)} + 1} \\ \frac{u^{(k)}}{u^{(k)} + \theta^2} & \frac{\theta^2}{u^{(k)} + \theta^2} \end{pmatrix}. \quad (15)$$

It is clear that eigenvalues of this matrix

$$s_1^{(k)} = 1, s_2^{(k)} = \frac{u^{(k)}(\theta^4 - 1)}{(\theta^2 u^{(k)} + 1)(\theta^2 + u^{(k)})}.$$

First, we check the condition of non-extremity of the measure $\mu_1^{(k)}$ corresponding to the solution $(u_1^{(k)}, u_1^{(k)}) = (1, 1)$.

Now let us check the condition of non-extreme measures: $k \cdot (s_2^{(k)})^2 > 1$. For the solution under consideration, this inequality will take the form:

$$k \cdot \left(\frac{\theta^2 - 1}{\theta^2 + 1} \right)^2 > 1. \quad (16)$$

By solving inequality (16), one comes to the following theorem.

Theorem 6. *Let $k \geq 2$. Then for the DNA-Ising model of the molecule the measure $\mu_1^{(k)}$ at*

$$\theta \in \left(0; \sqrt{\frac{\sqrt{k}-1}{\sqrt{k}+1}} \right) \cup \left(\sqrt{\frac{\sqrt{k}+1}{\sqrt{k}-1}}; +\infty \right)$$

is not extreme.

We check the condition of non-extremity of the measures $\mu_2^{(k)}, \mu_3^{(k)}$ for $k = 2$, corresponding to the solutions $(u_2^{(2)}, u_2^{(2)}), (u_3^{(2)}, u_3^{(2)})$. Now let us check the condition of non-extreme measure: $2 \cdot (s_2^{(2)})^2 > 1$. For solutions $(u_2^{(2)}, u_2^{(2)})$ and $(u_3^{(2)}, u_3^{(2)})$ this inequality will take the form:

$$2 \cdot \left(\frac{u_{2,3}^{(2)}(\theta^4 - 1)}{(\theta^2 u_{2,3}^{(2)} + 1)(\theta^2 + u_{2,3}^{(2)})} \right)^2 > 1. \quad (17)$$

In (17), substituting our expressions $u_{2,3}^{(2)}$ and reducing them, we obtain

$$2 \cdot \left(\frac{1}{\theta^2 - 1} \right)^2 > 1. \quad (18)$$

Since $\theta > \sqrt{3}$, inequality (18) does not have a solution. Thus, for $k = 2$, the non-extreme condition does not exist for the solution $(u_2^{(2)}, u_2^{(2)}), (u_3^{(2)}, u_3^{(2)})$. This means that the measures corresponding to these solutions might be extreme. We will check this in further studies.

We check the condition of non-extremity of the measures $\mu_2^{(k)}, \mu_3^{(k)}$ for $k = 3$, corresponding to the solutions $(u_2^{(3)}, u_2^{(3)}), (u_3^{(3)}, u_3^{(3)})$. Let us check the condition of non-extreme measure: $3 \cdot (s_2^{(3)})^2 > 1$. For solutions $(u_2^{(3)}, u_2^{(3)})$ and $(u_3^{(3)}, u_3^{(3)})$, this inequality will take the form:

$$3 \cdot \left(\frac{u_{2,3}^{(3)}(\theta^4 - 1)}{(\theta^2 u_{2,3}^{(3)} + 1)(\theta^2 + u_{2,3}^{(3)})} \right)^2 > 1. \quad (19)$$

In (19), substituting our expressions $u_{2,3}^{(3)}$ and reducing them, we obtain

$$3 \cdot \left(\frac{1}{\theta^4 - 1} \right)^2 > 1. \quad (20)$$

Since $\theta > \sqrt{2}$, inequality (20) does not have a solution. Thus, for $k = 3$, the non-extreme condition does not exist for the solution $(u_2^{(3)}, u_2^{(3)}), (u_3^{(3)}, u_3^{(3)})$. This means that the measures corresponding to these solutions might be extreme. We will check this in further studies.

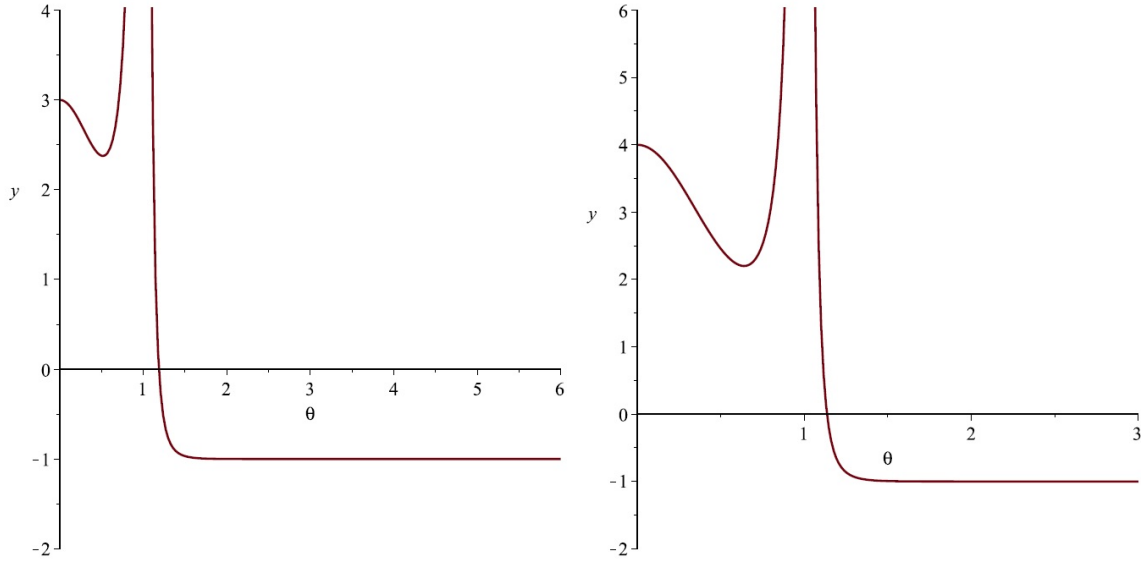


FIG. 1. Plots of the functions $4 \cdot (s_2^{(4)})^2 - 1$ (left) and $5 \cdot (s_2^{(5)})^2 - 1$ (right)

We check the condition of non-extremity of the measures $\mu_2^{(k)}, \mu_3^{(k)}$ for $k = 4$, corresponding to the solutions $(u_2^{(4)}, u_2^{(4)}), (u_3^{(4)}, u_3^{(4)})$, i.e. we check the condition: $4 \cdot (s_2^{(4)})^2 > 1$. For solutions $(u_2^{(4)}, u_2^{(4)})$ and $(u_3^{(4)}, u_3^{(4)})$ this inequality will take the form:

$$4 \cdot \left(\frac{u_{2,3}^{(4)}(\theta^4 - 1)}{(\theta^2 u_{2,3}^{(4)} + 1)(\theta^2 + u_{2,3}^{(4)})} \right)^2 > 1. \quad (21)$$

Finding an analytical solution to inequality (21) is difficult. Using the Maple program, one can see that the last inequality is not satisfied for any $\theta > \sqrt{\frac{5}{3}}$ (see Fig. 1). Thus, for $k = 4$, the non-extreme condition does not exist for the solution $(u_2^{(4)}, u_2^{(4)}), (u_3^{(4)}, u_3^{(4)})$. This means that the measures corresponding to these solutions might be extreme. We will check this in further studies.

We check the condition of non-extremity of the measures $\mu_2^{(k)}, \mu_3^{(k)}$ for $k = 5$, corresponding to the solutions $(u_2^{(5)}, u_2^{(5)}), (u_3^{(5)}, u_3^{(5)})$. Now let us check the condition of non-extreme measure: $5 \cdot (s_2^{(5)})^2 > 1$. For solutions $(u_2^{(5)}, u_2^{(5)})$ and $(u_3^{(5)}, u_3^{(5)})$ this inequality will take the form:

$$5 \cdot \left(\frac{u_{2,3}^{(5)}(\theta^4 - 1)}{(\theta^2 u_{2,3}^{(5)} + 1)(\theta^2 + u_{2,3}^{(5)})} \right)^2 > 1. \quad (22)$$

Using the Maple program, one can see that the last inequality is satisfied for any $\theta > \sqrt{\frac{3}{2}}$ (see Fig. 1). Thus, for $k = 5$, the non-extreme condition does not exist for the solution $(u_2^{(5)}, u_2^{(5)}), (u_3^{(5)}, u_3^{(5)})$. This means that the measures corresponding to these solutions might be extreme. We will check this in further studies.

5. Conditions of extremity of measures $\mu_1^{(k)}, \mu_2^{(k)}, \mu_3^{(k)}$

Methods from [33] are known for studying the extremum. Let us carry out the necessary definitions from [33]. If we remove an arbitrary edge $\langle x^0, x^1 \rangle = l \in L$ from the Cayley tree Γ^k , then it is separated into two components $\Gamma_{x^0}^k$ and $\Gamma_{x^1}^k$, each of which is called a semi-infinite tree or a semi-Cayley tree.

Consider a finite complete subtree \mathfrak{S} that contains all initial points of the half-tree $\Gamma_{x^0}^k$. The boundary $\partial\mathfrak{S}$ of the subtree \mathfrak{S} consists of the nearest neighbors of its vertices that lie in $\Gamma_{x^0}^k \setminus \mathfrak{S}$. We identify the subtree \mathfrak{S} with the set of its vertices. By $E(A)$ we denote the set of all edges of A and ∂A .

In [33], two key quantities were introduced: κ and γ , which play an important role in studying the extremity of the TI of Gibbs measures. These quantities are properties of the set of Gibbs measures $\{\mu_{\mathfrak{S}}^{\tau}\}$, where the boundary condition τ is fixed and \mathfrak{S} is an arbitrary, initial, complete, final subtree of $\Gamma_{x^0}^k$. Given an initial subtree $\Gamma_{x^0}^k$ and a vertex $x \in \mathfrak{S}$, we write \mathfrak{S}_x for the (maximal) subtree of \mathfrak{S} with initial point at x . When x is not the initial point of \mathfrak{S} , we denote by

$\{\mu_{\mathfrak{S}}^s\}$ the Gibbs measure in which the "ancestor" of x has spin s and the configuration on the lower bound of \mathfrak{S}_x (i.e. on $\partial\mathfrak{S}\setminus\{\text{"ancestor" of } x\}$) is given by Γ .

For two measures on Ω , let μ_1 and μ_2 , let us denote the distance in the norm

$$\|\mu_1 - \mu_2\|_x = \frac{1}{2} \sum_{i \in \{-1,1\}} |\mu_1(\sigma(x) = i) - \mu_2(\sigma(x) = i)|.$$

Let $\eta^{x,s}$ be a configuration η with spin at x set at s .

Following [33], we define

$$\begin{aligned} \kappa &\equiv \kappa(\mu) = \sup_{x \in \Gamma^k} \max_{x,s,s'} \|\mu_{\mathfrak{S}_x}^s - \mu_{\mathfrak{S}_x}^{s'}\|_x, \\ \gamma &\equiv \gamma(\mu) = \sup_{A \subset \Gamma^k} \max \|\mu_A^{\eta^{y,s}} - \mu_A^{\eta^{y,s'}}\|_x, \end{aligned}$$

where the maximum is taken over all boundary conditions η , all $y \in \partial A$, all neighbors $x \in A$ of vertex y and all spins $s, s' \in \{-1, 1\}$.

First, we find the condition for the extremity of the measure μ_0 .

Note that κ has a particularly simple formula

$$\kappa = \frac{1}{2} \max \sum_{l \in \{-1,1\}} |P_{il} - P_{jl}|.$$

Then for κ we get

$$\kappa^{(k)} = \frac{u^{(k)} |\theta^4 - 1|}{(\theta^2 u^{(k)} + 1)(\theta^2 + u^{(k)})}.$$

Now, similar to the work ([33], p. 15), we will look for an estimate for γ , in the following form:

$$\gamma = \max\{\|\mu_A^{\eta^{y,1}} - \mu_A^{\eta^{y,-1}}\|_x\},$$

where

$$\|\mu_A^{\eta^{y,1}} - \mu_A^{\eta^{y,-1}}\|_x = \frac{1}{2} \sum_{s \in \{-1,1\}} |\mu_A^{\eta^{y,1}}(\sigma(x) = s) - \mu_A^{\eta^{y,0}}(\sigma(x) = s)|.$$

Then for γ , we also have

$$\gamma^{(k)} = \frac{u^{(k)} |\theta^4 - 1|}{(\theta^2 u^{(k)} + 1)(\theta^2 + u^{(k)})}.$$

First, we check the condition of extremity of the measure $\mu_1^{(k)}$ corresponding to the solution $(u_1^{(k)}, u_1^{(k)}) = (1, 1)$.

Now let's check the condition of extreme measures: $k\kappa^{(k)}\gamma^{(k)} < 1$, i.e.

$$k \cdot \left(\frac{u^{(k)} |\theta^4 - 1|}{(\theta^2 u^{(k)} + 1)(\theta^2 + u^{(k)})} \right)^2 < 1.$$

Remark 7. Note that $\kappa^{(k)}\gamma^{(k)} = (s_2^{(k)})^2$.

For the solution under consideration, this inequality will take the form:

$$k \cdot \left(\frac{\theta^2 - 1}{\theta^2 + 1} \right)^2 < 1. \quad (23)$$

By solving inequality (23), one comes to the following theorem.

Theorem 7. Let $k \geq 2$. Then for the DNA-Ising molecule model the measure μ_1 at

$$\theta \in \left(\sqrt{\frac{\sqrt{k} - 1}{\sqrt{k} + 1}}; \sqrt{\frac{\sqrt{k} + 1}{\sqrt{k} - 1}} \right)$$

is extreme.

Remark 8. Note that, in comparison with the work [9], in the present work we also study extremality problems for these measures.

Now let us check the condition of extremity of the measures $\mu_2^{(k)}, \mu_3^{(k)}$ for $k = 2$, corresponding to the solutions $(u_2^{(2)}, u_2^{(2)}), (u_3^{(2)}, u_3^{(2)})$. Now let us check the condition of the extreme measure: $2\kappa^{(2)}\gamma^{(2)} < 1$. For solutions $(u_2^{(2)}, u_2^{(2)})$ and $(u_3^{(2)}, u_3^{(2)})$ this inequality will take the form:

$$2 \cdot \left(\frac{u_{2,3}^{(2)}(\theta^4 - 1)}{(\theta^2 u_{2,3}^{(2)} + 1)(\theta^2 + u_{2,3}^{(2)})} \right)^2 < 1. \quad (24)$$

In (24), substituting our expressions $u_{2,3}^{(2)}$ and reducing them, we get

$$2 \cdot \left(\frac{1}{\theta^2 - 1} \right)^2 < 1. \quad (25)$$

For $\theta > \sqrt{3}$ the above inequality is satisfied. It follows that in the case $k = 2$ the condition of extremity of the measures $\mu_2^{(k)}$ and $\mu_3^{(k)}$ is satisfied, where they exist.

Now let us check the condition of extremity of the measures $\mu_2^{(k)}, \mu_3^{(k)}$ for $k = 3$, corresponding to the solutions $(u_2^{(3)}, u_2^{(3)}), (u_3^{(3)}, u_3^{(3)})$.

Now let us check the condition of the extreme measure: $3\kappa^{(3)}\gamma^{(3)} < 1$. For solutions $(u_2^{(3)}, u_2^{(3)})$ and $(u_3^{(3)}, u_3^{(3)})$ this inequality will take the form:

$$3 \cdot \left(\frac{u_{2,3}^{(3)}(\theta^4 - 1)}{(\theta^2 u_{2,3}^{(3)} + 1)(\theta^2 + u_{2,3}^{(3)})} \right)^2 < 1. \quad (26)$$

In (26), substituting our expressions $u_{2,3}^{(3)}$ and reducing them, we get

$$3 \cdot \left(\frac{1}{\theta^4 - 1} \right)^2 < 1. \quad (27)$$

For $\theta > \sqrt{2}$ the above inequality is satisfied. It follows that in the case $k = 3$, the condition of extremity of the measures $\mu_2^{(k)}$ and $\mu_3^{(k)}$ is satisfied, where they exist.

We check the condition of extremity of the measures $\mu_2^{(k)}, \mu_3^{(k)}$ for $k = 4$, corresponding to the solutions $(u_2^{(4)}, u_2^{(4)}), (u_3^{(4)}, u_3^{(4)})$. Now let us check the condition of the extreme measure: $4\kappa^{(4)}\gamma^{(4)} < 1$. For solutions $(u_2^{(4)}, u_2^{(4)})$ and $(u_3^{(4)}, u_3^{(4)})$ this inequality will take the form:

$$4 \cdot \left(\frac{u_{2,3}^{(4)}(\theta^4 - 1)}{(\theta^2 u_{2,3}^{(4)} + 1)(\theta^2 + u_{2,3}^{(4)})} \right)^2 < 1. \quad (28)$$

This inequality is valid for all values of $\theta > 1.187$ (see Fig. 1). Consequently, in the case $k = 4$ the condition of extremity of the measures $\mu_2^{(k)}$ and $\mu_3^{(k)}$ is satisfied for any values of $\theta > \sqrt{\frac{5}{3}}$, i.e. in the domain of existence of these measures.

Now let us check the condition of extremity of the measures $\mu_2^{(k)}, \mu_3^{(k)}$ for $k = 5$, corresponding to the solutions $(u_2^{(5)}, u_2^{(5)}), (u_3^{(5)}, u_3^{(5)})$. We check the condition of the extreme measure: $5\kappa^{(5)}\gamma^{(5)} < 1$. For solutions $(u_2^{(5)}, u_2^{(5)})$ and $(u_3^{(5)}, u_3^{(5)})$ this inequality will take the form:

$$5 \cdot \left(\frac{u_{2,3}^{(5)}(\theta^4 - 1)}{(\theta^2 u_{2,3}^{(5)} + 1)(\theta^2 + u_{2,3}^{(5)})} \right)^2 < 1. \quad (29)$$

This inequality is valid for all values of $\theta > 1.136$ (see Fig. 1). Consequently, in the case $k = 5$ the condition of extremity of the measures $\mu_2^{(k)}$ and $\mu_3^{(k)}$ is satisfied for any values of $\theta > \sqrt{\frac{3}{2}}$, i.e. in the domain of existence of these measures. Thus, we have proven the following theorem.

Theorem 8. Let $k \in \{2, 3, 4, 5\}$. Then for the DNA-Ising molecule model with $\theta > \theta_{cr} = \sqrt{\frac{k+1}{k-1}}$ the measures $\mu_2^{(k)}$ and $\mu_3^{(k)}$ are extreme.

From this theorem, using the methods of work [3], it is easy to prove the following theorem.

Theorem 9. Let $k \in \{2, 3, 4, 5\}$. Then for the DNA-Ising molecule model with $\theta > \theta_{cr} = \sqrt{\frac{k+1}{k-1}}$ there exists a continuum of Gibbs measures that are not translation-invariant.

6. Conclusion

In this study, we have investigated the thermodynamic properties of the DNA-like system using the Ising model applied to a nano-scale system. The results presented in this paper have direct implications for biophysics, particularly in DNA studies. The Ising-like representation allows us to model the stability of DNA under thermal fluctuations, which is crucial for applications in molecular biology, nanotechnology, and genetic sequencing. Specifically, the phase diagrams obtained (Fig. 1) demonstrate how external parameters influence DNA stability, offering insights into experimental DNA denaturation curves.

Future work could extend this study by incorporating sequence heterogeneity and external factors such as ionic strength and molecular crowding, which are known to influence DNA stability. Furthermore, experimental validation of these theoretical predictions would help bridge the gap between computational models and real biological systems.

In summary, our study contributes to the theoretical understanding of DNA stability and denaturation by utilizing an adapted Ising model approach. This work not only refines theoretical predictions but also offers a foundation for future experimental and computational studies in DNA biophysics.

References

- [1] Rozikov U.A., Rahmatullaev M.M. Description of weakly periodic Gibbs measures of the Ising model on the Cayley tree. *Theoretical and Mathematical Physics*, 2008, **156**(2), P. 1218–1227.
- [2] Rozikov U.A. *Gibbs Measures on Cayley Trees*. World Scientific. Singapore, 2013.
- [3] Blekher P.M., Ganikhodjaev N. N. On pure phases of the Ising model on the Bethe lattice. *Probability Theory and Its Applications*, 1990, **35**(2), P. 920–930.
- [4] Akin H., Rozikov U.A., Temur S. A new set of limiting Gibbs measures for the Ising model on a Cayley tree. *J.Stat.Phys.*, 2011, **142**, P. 314–321.
- [5] Gandolfo D., Rozikov U.A., Ruiz J. Rahmatullaev M.M. On free energies of the Ising model on the Cayley tree. *J.Stat.Phys.*, 2013, **150**, P. 1201–1217.
- [6] Gandolfo D., Haydarov F.H., Rozikov U.A., Ruiz J. New phase transitions of the Ising model on Cayley trees. *J.Stat.Phys.*, 2013, **153**, P. 400–411.
- [7] Rozikov U.A. Tree-hierarchy of DNA and distribution of Holliday junctions. *J.Math.Biol.*, 2017, **75**, P. 1715–1733.
- [8] Rozikov U.A. Holliday junctions for the Potts model of DNA. *Algebra, Complex Analysis*. Springer, Switzerland 2018, P. 151–165.
- [9] Rozikov U.A. Thermodynamics of interacting systems of DNA molecules. *Theoretical and Mathematical Physics*, 2021, **206**(2), P. 174–183.
- [10] Khatamov N.M. Holliday junctions in the Blume-Capel model of DNA. *Theoretical and Mathematical Physics*, 2021, **206**(3), P. 383–390.
- [11] Khatamov N.M. Holliday junctions in the HC Blume-Capel model in "one case" on DNA. *Nanosystems: physics, chemistry, mathematics*, 2021, **12**(5), P. 563–568.
- [12] Khatamov N.M., Malikov N.N. Holliday junctions in a set of DNA molecules for new translation-invariant Gibbs measures of the Potts model. *Theoretical and Mathematical Physics*, 2024, **218**(2), P. 346–356.
- [13] Rozikov U.A. Thermodynamics of DNA-RNA renaturation. *Inter.Jour.G geom.Methods Mod.Phys.*, 2021, **18**(6), P. 2150096 (14 pages).
- [14] Rozikov U.A. *Gibbs measures in biology and physics: The Potts model*. World Sci. Publ. Singapore, 2022.
- [15] Alberts B., Johnson A., Lewis J., Raff M., Roberts K., Walter P. *Molecular biology of the cell*. 4-th edn. Garland Science, New York, 2002.
- [16] Swigon D. The mathematics of DNA structure, mechanics, and dynamics. *Mathematics of DNA Structure, Function and Interactions*, 2009, **150**, P. 293–320.
- [17] Thompson C. *Mathematical Statistical Mechanics*, Princeton Univ. Press, Princeton, 1972.
- [18] Georgii H.-O. *Gibbs measures and phase transitions*. de Gruyter studies in Math; Berlin, 1988.
- [19] Khatamov N.M. Extremality of the Gibbs measures for the HC-Blume-Capel model on the Cayley tree. *Mathematical notes*, 2022, **111**(5), P. 768–781.
- [20] Khatamov N.M., Khakimov R.M. Translation-invariant Gibbs measures for the Blume-Capel model on a Cayley tree. *Journal of Mathematical Physics, Analysis, Geometry*, 2019, **15**(2), P. 239–255.
- [21] Khatamov N.M. Periodic Gibbs measures and their extremes for the HC-Blume-Capel model in the case of a "wand" on the Cayley tree. *Lobachevskii Journal of Mathematics*, 2019, **43**(9), P. 2515–2524.
- [22] Khatamov N.M. Translation-invariant extreme Gibbs measures for the Blume-Capel model with a wand on a Cayley tree. *Ukrainian Mathematical Journal*, 2020, **72**(4), P. 540–556.
- [23] Khatamov N.M. Periodic Gibbs measures and their extremality for the HC-Blume-Capel model in the case of a "wand" with a chemical potential on the Cayley tree. *Mathematical notes*, 2024, **115**(1), P. 89–101.
- [24] Mossel E. Reconstruction on trees: beating the second eigenvalue. *Ann. Appl. Probab.*, 2001, **11**(1), P. 285–300.
- [25] Mossel E., Peres Y. Information flow on trees. *Ann. Appl. Probab.*, 2003, **13**(3), P. 817–844.
- [26] Mossel E. Survey: information flow on trees. *Graphs. Morphisms and statistical physics. Ser. Discrete Math. Theoret.Comput. Sci.*, 2004, **63**, P. 155–170.
- [27] Rozikov U.A. Ishankulov F.T. Description of periodic p-harmonic functions on Cayley trees. *Nonlinear Differ. Equ. Appl.*, 2010, **17**, P. 153–160.
- [28] Bogachev L.V. and Rozikov U.A. On the uniqueness of Gibbs measure in the Potts model on a Cayley tree with external field. *J. Stat. Mech. Theory Exp.*, 2019, **7**, 073205. 77 pp.
- [29] Külske C., Rozikov U.A. and Khakimov R.M. Description of all translation-invariant splitting Gibbs measures for the Potts model on a Cayley tree. *J. Stat. Phys.*, 2014, **156**, P. 189–200.
- [30] Külske C., Rozikov U.A. Fuzzy transformations and extremality of Gibbs measures for the Potts model on a Cayley tree. *Random Structures Algorithms*, 2017, **50**, P. 636–678.
- [31] Haydarov F.H., Rozikov U.A. Gradient Gibbs measures of a SOS model on Cayley trees: 4-periodic boundary laws. *Reports on Mathematical Physics*, 2022, **90**(1), P. 81–101.
- [32] Kesten H., Stigum B.P. Additional limit theorem for indecomposable multi-dimensional Galton-Watson processes. *Annals of Mathematical Statistics*, 1966, **37**, P. 1463–1481.
- [33] Martinelli F., Sinclair A., Weitz D. Fast mixing for independent sets, coloring and other models on trees. *Random Structures and Algorithms*, 2007, **31**, P. 134–172.

Information about the authors:

Nosirjon M. Khatamov – Namangan state university, Boburshox street, 161, 160107, Namangan, Uzbekistan; V.I. Romanovskiy Institute of Mathematics, Uzbekistan Academy of Sciences, 4B, St. University, 100174, Tashkent, Uzbekistan; ORCID 0000-0002-2902-7982; nxatamov@mail.ru

Nematulla N. Malikov – Namangan state university, Boburshox street, 161, 160107, Namangan, Uzbekistan; ORCID 0009-0009-1710-1004; malikovnematulla24@gmail.com

Conflict of interest: the authors declare no conflict of interest.

Pinned gradient measures of SOS model associated with H_A -boundary laws on Cayley trees

Farhod H. Haydarov^{1,2,a}, Risolat A. Ilyasova^{2,3,b}, Khudoyor S. Mamayusupov^{2,c}

¹V. I. Romanovskiy Institute of Mathematics, Uzbekistan Academy of Sciences, Tashkent, Uzbekistan

²New Uzbekistan University, Tashkent, Uzbekistan

³National University of Uzbekistan, Tashkent, Uzbekistan

^af.khaydarov@newuu.uz, ^br.ilyasova@newuu.uz, ^ck.mamayusupov@newuu.uz

Corresponding author: F. H. Haydarov, f.khaydarov@newuu.uz

ABSTRACT This paper investigates pinned gradient measures for SOS (Solid-On-Solid) models associated with H_A -boundary laws of period two, a class that encompasses all 2-height periodic gradient Gibbs measures corresponding to a spatially homogeneous boundary law. While previous research has predominantly focused on a spatially homogeneous boundary law and corresponding GGMs on Cayley trees, this study extends the analysis by providing a comprehensive characterization of such measures. Specifically, it demonstrates the existence of pinned gradient measures on a set of G -admissible configurations and precisely quantifies their number under certain temperature conditions.

KEYWORDS SOS model, gradient configuration, G -admissible configuration, spin values, Cayley tree, gradient measure, gradient Gibbs measure, two periodic boundary law

ACKNOWLEDGEMENTS We sincerely thank the referee for their valuable and insightful comments, which have helped improve this work.

FOR CITATION Haydarov F.H., Ilyasova R.A., Mamayusupov K.S. Pinned gradient measures of SOS model associated with H_A -boundary laws on Cayley trees. *Nanosystems: Phys. Chem. Math.*, 2025, **16** (2), 154–163.

1. Introduction

Gradient Gibbs measures (GGMs) on trees, particularly on the Cayley tree, are an important class of models in statistical mechanics used to study interfaces and phase transitions. These measures arise in systems where the spin variables, i.e. “heights” are defined on the vertices of a tree and exhibit a gradient interaction between neighboring sites, meaning the energy of the system depends on the difference between spins at adjacent vertices. The main interest in GGMs on trees lies in their ability to capture complex behaviors such as long-range correlations, coexistence of multiple phases, and non-trivial periodic solutions, even in low-dimensional settings.

The Cayley tree, an infinite, connected, acyclic graph where each vertex has a fixed number of neighbors (called the order of the tree), serves as a natural setting for studying such measures. Unlike lattice systems, the tree structure introduces unique challenges due to the absence of loops, resulting in boundary effects that play a dominant role in the behavior of the system (e.g., [1–5]).

For GGMs on trees, the construction is typically based on boundary laws as solutions of recursive equations that describe the influence of the outer boundary on the system. This recursive structure facilitates the exploration of non-translation-invariant solutions, including periodic or quasi-periodic Gibbs measures. Notably, the work of Zachary [6] laid the foundation for describing Gibbs measures on trees using these boundary conditions. Models with denumerable (non-compact) set of spin values which potentials are invariant under a joint height-shift of all values of the spin-variables are notable in statistical mechanics, under the names interface models or gradient models. For lattice spin systems, a theory demonstrates the existence and uniqueness of gradient Gibbs measures with a fixed tilt, assuming uniform strictly convex potentials in dimensions $d = 2$ investigated by Funaki and Spohn [7]. (See however Remark 4.4 of [8] on existence for non-convex potentials.) This extends to random models [9, 10] in dimensions $d \geq 3$, while for $d = 2$ such random gradient states cannot exist ([11]) since they experience local destabilization due to the impact of quenched randomness. In [12], the establishment of gradient Gibbs measures on trees through boundary laws is provided. Also, in the paper, authors generalize the theory of Zachary [6, 13] for a non-normalizable boundary law (i.e. Zachary’s theory can not be applied).

In the context of the SOS model, a classic example of an interface model, GGMs on the Cayley tree have been shown to exhibit rich behavior, including multiple periodic solutions and phase transitions depending on the parameters of the model. Such systems allow for the study of gradient Gibbs measures that are both translation-invariant and those that break translation symmetry, leading to periodic configurations (e.g. [14–20]).

In this paper, we build upon the research presented in the preceding papers by investigating the existence of 2-height periodic pinned gradient measures for the SOS model restricted to a set of G -admissible configurations on the Cayley tree of order $k \geq 2$. The notion of H_A -periodicity is typically defined (see [4]) for boundary conditions. If pinned gradient measures (GGMs) exist for such boundary conditions, they are referred to as H_A -periodic pinned gradient measures (GGMs). We define H_A -boundary laws by formula (3.14). Note that if there exists spatially translation invariant GGMs corresponding to a spatially homogeneous boundary law (i.e. $\{l_{xy}\} = \{l\}$), then it is possible to call these GGMs corresponding to H_A -boundary laws. In this case, we set $l^{(1)} = l^{(2)} := l$ for the family of vectors $\{l_{xy}\}_{\langle x,y \rangle \in \vec{L}} = \{l^{(1)}, l^{(2)}\}$.

The results in Theorem 1 show that all three H_A -boundary laws of period two define a spatially homogeneous boundary law resulting in three GGMs (see [17, 21, 22]). On the other hand, the results in Theorem 2 indicate that for specific ranges of the interaction parameter θ , there are exactly three 2-height periodic pinned gradient measures on a G_2 -admissible configuration space: one of them is associated with a trivial boundary law and the other two are derived from spatially inhomogeneous (H_A) boundary laws. This reveals the presence of symmetry breaking in the model, where distinct periodic solutions emerge depending on the parameter θ .

2. Preliminaries

We would like to emphasize that the information below is based on the references [12, 18, 21–23]. Let us denote the Cayley tree of order k by $\Gamma^k = (V, L)$, where V and L is the set of vertices and the set of edges, respectively. An unoriented edge between two vertices $x, y \in V$ is denoted by $b = \{x, y\}$. For an oriented edge going from x to y , we write $\langle x, y \rangle$ and \vec{L} is the set of all such edges. $d(x, y)$ denotes the number of edges along the unique smallest path from x to y . Let \mathcal{N} be the collection of a finite subsets of V . The outer boundary set of $\Lambda \in \mathcal{N}$ is defined as

$$\partial\Lambda := \{x \notin \Lambda : d(x, y) = 1 \text{ for some } y \in \Lambda\}.$$

Let $\Omega := \mathbb{Z}^V = \{(\omega_x)_{x \in V} | \omega_x \in \mathbb{Z}\}$ denote the set of (integer-valued) height-configurations endowed with the product σ -algebra $\mathcal{F} = \mathcal{P}(\mathbb{Z})^V$ generated by the spin variables $\pi_x : \mathbb{Z}^V \rightarrow \mathbb{Z}$ is defined by $\pi_x(\omega) = \omega_x$ the projection onto the coordinate $x \in V$.

Let $\Lambda \subset V$ and $\pi_\Lambda : \Omega \rightarrow \mathbb{Z}^\Lambda$ be the projection onto the coordinates in Λ . We can write

$$\mathcal{F}_\Lambda = \sigma(\{\pi_y | y \in \Lambda\}) = \mathcal{P}(\mathbb{Z})^\Lambda$$

for the σ -algebra generated by the height-variables in the vertices $x \in \Lambda$.

Let ω_x be the state of the configuration ω at the vertex $x \in V$ and $b = \langle v, w \rangle \in \vec{L}$. The equation $\nabla\omega_b = \omega_w - \omega_v$ denotes the height difference of b . We define the gradient field of ω as

$$\nabla\omega := \{\nabla\omega_b | b \in \vec{L}\}.$$

The set of spin values $\eta_{\langle x,y \rangle} = \pi_y - \pi_x$ is called gradient spin variables for each $\langle x, y \rangle \in \vec{L}$. The state space of the gradient configurations is defined by $\Omega^\nabla = \mathbb{Z}^V / \mathbb{Z} = \mathbb{Z}^{\vec{L}}$. We will consider the standard σ -algebra on $\mathbb{Z}^{\vec{L}}$ which is defined as follows

$$\mathcal{F}^\nabla = \sigma(\{\eta_b | b \in \vec{L}\}) = \mathcal{P}(\mathbb{Z})^{\vec{L}}.$$

For each $b = \{x, y\} \in L$, a symmetric nearest-neighbor gradient interaction potential $U_b : \mathbb{Z} \rightarrow \mathbb{R}$ is given by $U_b(m) = U_b(-m)$ and the family of functions, i.e. transfer operators are defined by $Q_b(m) = \exp(-\beta U_b(m))$ for all $m \in \mathbb{Z}$. Here β is interpreted as the inverse of a temperature. The following finite quantity is called [22] a Hamiltonian in the finite volume $\Lambda \in \mathcal{N}$ is as follows

$$H_\Lambda^U(\omega) = \sum_{b \cap \Lambda \neq \emptyset} U_b(\nabla\omega_b), \quad \Lambda \in \mathcal{N}.$$

In the SOS model on a Cayley tree, U_b is an unbounded symmetric nearest-neighbor gradient interaction potential defined by

$$U_b(\omega_x, \omega_y) = J_b |\omega_x - \omega_y|,$$

where $J_b \in \mathbb{R}$ is a coupling constant, which determines the energy cost of height differences.

In the article, it is assumed that $J_b = J > 0$, indicating the spatial homogeneity of the coupling constant. Furthermore, the system's energy increases as the height difference between adjacent sites increases. Thus, we can conclude that the parameter $\theta := e^{-J\beta}$ lies within the interval $0 < \theta < 1$.

The family of probability kernels [22] for the given Hamiltonian H_Λ^U , i.e., $(\gamma_\Lambda)_{\Lambda \in \mathcal{N}}$ from $(\Omega, \mathcal{F}_{\Lambda^c})$ to (Ω, \mathcal{F}) is given by

$$\gamma_\Lambda(A|\tilde{\omega}) = Z_\Lambda^{-1}(\tilde{\omega}) \int_A \exp\left(-\sum_{b \subset \Lambda} U_b(\nabla\omega_b) - \sum_{\substack{i \in \Lambda, j \in \Lambda^c \\ i \sim j}} U_{\{i,j\}}(\omega_i - \tilde{\omega}_j)\right) d\omega_\Lambda \quad (2.1)$$

for all $A \in \mathcal{F}$, where $Z_\Lambda(\tilde{\omega})$ denotes a normalization constant and $d\omega_\Lambda$ is the counting measure on $\Omega_\Lambda = \mathbb{Z}^\Lambda$.

A transfer operator $Q_b = Q$ induces *local Gibbsian specification*

$$\gamma = \{\gamma_\Lambda : \mathcal{F} \times \Omega \rightarrow [0, 1]\}_{\Lambda \in \mathcal{N}}$$

by the assignment which represent (2.1) in the form

$$\gamma_\Lambda(\sigma_\Lambda = \tilde{\omega}_\Lambda | \omega) = \frac{1}{Z_\Lambda(\omega_{\partial\Lambda})} \left(\prod_{\{x,y\} \subset \Lambda} Q(\tilde{\omega}_x - \tilde{\omega}_y) \right) \prod_{\substack{x \in \Lambda, y \in \Lambda^c \\ x \sim y}} Q(\tilde{\omega}_x - \omega_y)$$

for every $\Lambda \in \mathcal{N}$, $\tilde{\omega} \in \Omega_\Lambda$ and $\omega \in \Omega$. Here, the partition function Z_Λ gives for every $\omega \in \Omega$ the normalisation constant $Z_\Lambda(\omega) = Z_\Lambda(\omega_{\partial\Lambda})$ turning $\gamma_\Lambda(\cdot | \omega)$ into a probability measure on the height configuration space (Ω, \mathcal{F}) , ω_Λ and Ω_Λ denote the restrictions on $\Lambda \in V$.

The kernels γ_Λ can be projected to the *gradient Gibbs specification*

$$\gamma^\nabla = \{\gamma_\Lambda^\nabla : \mathcal{F}^\nabla \times \Omega^\nabla \rightarrow [0, 1]\}_{\Lambda \in \mathcal{N}}.$$

The *outer gradient σ -algebra* [22] on Ω^∇ is defined by

$$\mathcal{T}_\Lambda^\nabla := \sigma((\eta_b)_{b \subset \Lambda^c}, [\eta]_{\partial\Lambda}) \subset \mathcal{F}^\nabla.$$

The kernels [21] are

$$\gamma_\Lambda^\nabla(\eta_\Lambda = \zeta_\Lambda | \zeta) := \gamma_\Lambda(\sigma_\Lambda = \omega_\Lambda | \omega)$$

for any $\omega \in \Omega$ such that $(\nabla\omega)_{\Lambda^c} = \zeta_{\Lambda^c}$ and $[\nabla\omega]_{\partial\Lambda} = [\zeta]_{\partial\Lambda}$.

Then a collection $\Sigma := (V, \mathcal{N}, \Omega^\nabla, \{\mathcal{T}_\Lambda^\nabla\}_{\Lambda \in \mathcal{N}})$ can be considered as a *lattice system*. Let $\gamma = \{\gamma_\Lambda\}_{\Lambda \in \mathcal{N}}$ be a local specification on lattice systems. Then a probability measure $\mu \in P(\mathcal{F})$ is called a *Gibbs measure with specification* γ if $\mu = \mu\gamma_\Lambda$ for each $\Lambda \in \mathcal{N}$. This definition of Gibbs measures originates from Dobrushin and Lanford and Ruelle (see [24–26]), and the last equations are called the *DLR-equations*. A Gibbs measure with the specification $\gamma^\nabla = \{\gamma_\Lambda^\nabla(\cdot | \zeta) | \zeta \in \Omega^\nabla, \Lambda \in \mathcal{N}\}$ is called a *gradient Gibbs measure* on the lattice system Σ .

3. Pinned gradient measures corresponding to two periodic boundary laws

It is known that the problem of expressing periodic Gibbs measures corresponding to various Hamiltonians typically reduces to solving systems of algebraic equations. Due to the lack of general formulas for solving such systems, many difficulties arise. Initially, we analyze the solutions of the following system of equations:

$$\begin{cases} x = \left(\frac{ay + b}{cy + a + b - c} \right)^k \\ y = \left(\frac{ax + b}{cx + a + b - c} \right)^k \end{cases}, \tag{3.1}$$

which is a generalization of systems of equations encountered in many papers [14, 15, 17, 27]. As an example for the case $b \neq c$, one can apply the result of the following proposition to the system of equations (4.3) analyzed in [27]. Applications of our proposition for the case $b = c$ will be explored later in Theorems 1 and 2.

Proposition 1. *Let $a, b, c > 0$ be real numbers satisfying the condition $a + b - c > 0$. The number of positive solutions (x, y) to the system (3.1) is determined by the value of $k \in \mathbb{N}$ and the relationship between a and c :*

- (1) *If $a = c$ or $k = 1$, then the system has exactly one solution which is $(x, y) = (1, 1)$.*
- (2) *If $a > c$ and $k > \frac{a+b}{a-c}$, then the system has exactly three distinct solutions which satisfy $x = y$.*
- (3) *If $a < c$ and $k > \frac{a+b}{c-a}$, then the system also has exactly three distinct solutions one solution satisfies $x = y$ and the other two satisfy the condition $x \neq y$.*

Proof. Let's start with the following notation for simplicity

$$f(x) := \left(\frac{ax + b}{cx + a + b - c} \right)^k. \tag{3.2}$$

The case $a = c$ is indeed quite trivial, as in this scenario, the function simplifies to $f(x) = 1$ for all positive x . Consequently, there is only one pair of solutions, which is $(x, y) = (1, 1)$.

For the case $a \neq c$, the function $f(x)$ exhibits specific properties depending on the relationship between a and c . The derivative of $f(x)$ is given by

$$f'(x) = \frac{k(a+b)(a-c)f(x)}{(ax+b)(cx+a+b-c)}.$$

The function $f(x)$ is bounded, strictly increasing when $a > c$, and strictly decreasing when $a < c$. For $x > 0$, it holds that $f(0) = \left(\frac{b}{a+b-c}\right)^k > 0$, and as $x \rightarrow \infty$ we find that $\lim_{x \rightarrow \infty} f(x) = \left(\frac{a}{c}\right)^k$.

Now assume that $a < c$. In this case, we conclude that there exists a unique solution, given by $x = y = 1$ on the assumption that $x = y$.

Let $x \neq y$. Now we find the conditions for the existence of solutions with $x \neq y$ in the system (3.1). To do this, we will study the equation

$$f(f(x)) = x. \quad (3.3)$$

Since the function $f(x)$ is invertible for $x > 0$, we can rewrite the equation as $f(x) = f^{-1}(x) := g(x)$, where

$$g(x) = f^{-1}(x) = \frac{(a+b-c)\sqrt[k]{x} - b}{-c\sqrt[k]{x} + a}. \quad (3.4)$$

From $f(x) > 0$, it follows that $g(x) > 0$. Therefore, the domain of the function $g(x)$ is (x_1, x_2) , where

$$\begin{cases} x_1 = \left(\frac{a}{c}\right)^k < x < \left(\frac{b}{a+b-c}\right)^k = x_2, & \text{if } a < c \\ x_1 = \left(\frac{b}{a+b-c}\right)^k < x < \left(\frac{a}{c}\right)^k = x_2, & \text{if } a > c \end{cases}. \quad (3.5)$$

Now let us consider the case $a < c$. Note that by solving the equation $h(x) = 0$ for the function $h(x) = \ln \frac{f(x)}{g(x)} = \ln f(x) - \ln g(x)$, we obtain the same solution set as for equation (3.3). Clearly, $x = 1$ is a solution to this equation, i.e., $h(1) = 0$. Using the derivatives

$$f'(x) = \frac{k(a+b)(a-c)f(x)}{(ax+b)(cx+a+b-c)}$$

and

$$g'(x) = \frac{(a+b)(a-c)g(x)}{k\sqrt[k]{x^{k-1}} [(a+b-c)\sqrt[k]{x} - b] (-c\sqrt[k]{x} + a)},$$

we have

$$h'(x) = \frac{f'(x)}{f(x)} - \frac{g'(x)}{g(x)} = \frac{(a+b)(a-c)}{k} \cdot \left(\frac{k^2}{(ax+b)(cx+a+b-c)} \right) - \frac{(a+b)(a-c)}{k} \cdot \frac{1}{\sqrt[k]{x^{k-1}} [(a+b-c)\sqrt[k]{x} - b] (-c\sqrt[k]{x} + a)}.$$

Denoting $\sqrt[k]{x} = t$, we rewrite the derivative $h'(x)$ as

$$v(t) = \frac{(a+b)(c-a)p(t)}{kt^{k-1}(at^k + b)(ct^k + a + b - c)[(a+b-c)t - b](-ct + a)},$$

where

$$p(t) = act^{2k} + k^2c(a+b-c)t^{k+1} - (k^2-1)(a^2 + ab + bc - ac)t^k + k^2abt^{k-1} + b^2 + ab - bc. \quad (3.6)$$

Let $k = 1$. Then the function $h'(x)$ gets always positive ($a < c$) or negative ($a > c$) value for any $x \in (x_1, x_2)$. Therefore, the only way for the function $h(x)$ to cross the x-axis is at the point $x = 1$.

Let $k \geq 2$. Then by Descartes' rule [28] of signs, the polynomial (3.6) has at most two positive roots. It is easy to verify that

$$\lim_{x \rightarrow x_1} h(x) = -\infty, \quad h(1) = 0, \quad \lim_{x \rightarrow x_2} h(x) = +\infty. \quad (3.7)$$

Hence, the equation $h(x) = 0$ has at least one solution x_0 for $x < 1$ and at least one solution x'_0 for $x > 1$ if $h'(1) < 0$. From this condition,

$$h'(1) = \frac{(a+b)(a-c)}{k} \cdot \left(\frac{k^2}{(a+b)^2} - \frac{1}{(a-c)^2} \right) < 0, \quad (3.8)$$

we find that $k > \frac{a+b}{c-a}$ since $\frac{a+b}{c-a} > 0$. Moreover,

$$\lim_{x \rightarrow x_1} h'(x) = +\infty, \quad \lim_{x \rightarrow x_2} h'(x) = +\infty \quad (3.9)$$

for all $k > \frac{a+b}{c-a}$. From the condition $h'(1) < 0$, it follows that the function $h(x)$ has exactly two critical points ξ_1 and ξ_2 such that $x_1 < \xi_1 < 1$ and $1 < \xi_2 < x_2$ (see Figure 1).

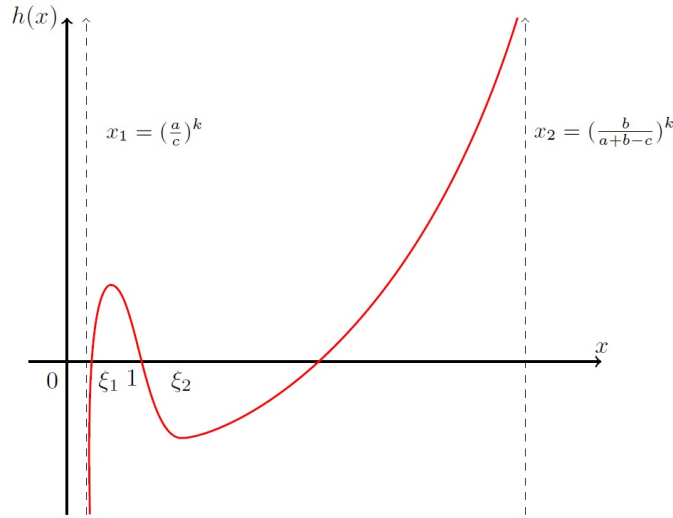


FIG. 1. The graph illustrates the number of possible solutions to the equation (3.3) for $a < c$ and $k > \frac{a+b}{c-a}$

This indicates that $h(x)$ is increasing on the intervals $x_1 < x < \xi_1$ and $\xi_2 < x < x_2$ and decreasing on the interval $\xi_1 < x < \xi_2$. Therefore, the equation $h(x) = 0$ has exactly two solutions except for 1, denoted as $x_0 < 1 < x'_0$.

Finally, since the function $f(x)$ is strictly decreasing for $a < c$, from the second equation of the system (3.1), we have $f(x_0) := y_0 > f(1) = 1 > f(x'_0) := y'_0$. We conclude that $x_0 \neq y_0$ ($x'_0 \neq y'_0$) for the pairs of solutions (x_0, y_0) and (x'_0, y'_0) corresponding to x_0 and x'_0 respectively. Thus, the system of equations (3.1) has exactly three distinct solutions under the condition $k > \frac{a+b}{c-a}$.

The case $a > c$ is analogous to the case $a < c$, so we will provide a brief proof. In this case the function f is a strictly increasing function for $x > 0$. Assume that $y < x$ and (x, y) is a solution to (3.1). This would imply $f(x) < f(y)$ but due to the fact that f is strictly increasing, we would have $x < y$ which contradicts our assumption. The case $x < y$ proceeds analogously and consequently there can not be a solution $x \neq y$ if $a > c$.

Therefore, it suffices to consider the case of $x = y$ as the solutions to the system (3.1).

After denoting $\sqrt[k]{x} := z$, the system of equations (3.1) becomes the following equation

$$z = \frac{az^k + b}{cz^k + a + b - c}. \tag{3.10}$$

Alternatively, using the function (3.4), the equation (3.10) can be rewritten in the following form

$$z^k = g(z^k) = \frac{(a+b-c)z - b}{-cz + a}. \tag{3.11}$$

In this case, for the values $\sqrt[k]{x_1} := z_1$ and $\sqrt[k]{x_2} := z_2$ in the domain (z_1, z_2) of the function $g(z^k)$ the equations in (3.7) take the form

$$\lim_{z \rightarrow z_1} h(z) = +\infty, \quad h(1) = 0, \quad \lim_{z \rightarrow z_2} h(z) = -\infty.$$

The inequality corresponding to (3.8) becomes

$$h'(1) = \frac{(a+b)(a-c)}{k} \cdot \left(\frac{k^2}{(a+b)^2} - \frac{1}{(a-c)^2} \right) > 0, \tag{3.12}$$

and the derivative condition in (3.9) transforms to

$$\lim_{z \rightarrow z_1} h'(z) = -\infty, \quad \lim_{z \rightarrow z_2} h'(z) = -\infty,$$

for $k > \frac{a+b}{a-c}$. Under this condition, the system (3.1) admits exactly two solutions, apart from the trivial case $z = y = 1$ (see Figure 2).

□

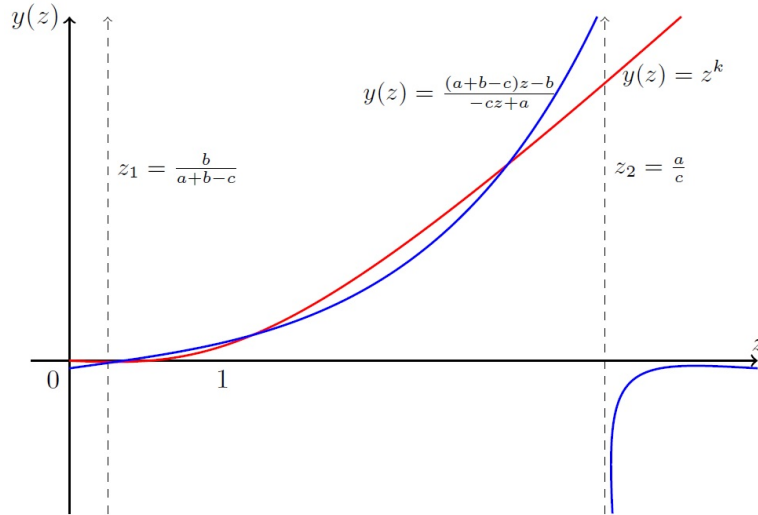


FIG. 2. The graph depicts the number of possible solutions to the equation (3.11) in the case $a > c$ and $k > \frac{a+b}{c-a}$

Definition 1. [22] A family of vectors $\{l_{xy}\}_{\langle x,y \rangle \in \vec{L}}$, where $l_{xy} \in (0, \infty)^{\mathbb{Z}}$, is called a boundary law for the transfer operators $\{Q_b\}_{b \in L}$ if for each $\langle x, y \rangle \in \vec{L}$, there exists a constant $c_{xy} > 0$ such that the consistency equation

$$l_{xy}(\omega_x) = c_{xy} \prod_{z \in \partial x \setminus \{y\}} \sum_{\psi_z \in \mathbb{Z}} Q_{zx}(\omega_x - \psi_z) l_{zx}(\psi_z) \quad (3.13)$$

holds for every $\omega_x \in \mathbb{Z}$. A boundary law is called q -periodic if $l_{xy}(\omega_x + q) = l_{xy}(\omega_x)$ for every oriented edge $\langle x, y \rangle \in \vec{L}$ and each $\omega_x \in \mathbb{Z}$.

Gradient measures and gradient Gibbs measures are constructed using q -periodic boundary laws on the space of gradient configurations (see Chapters 3 and 4 in [22]). Theorem 3.1 establishes that for a vertex $\Lambda \in \mathcal{N}$ and class label $s \in \mathbb{Z}_q$, any q -periodic boundary law $\{l_{xy}\}_{\langle x,y \rangle \in \vec{L}}$ for $\{Q_b\}_{b \in L}$ defines a consistent family of probability measures (pinned gradient measures) on Ω^∇ . Chapter 4 discusses a spatially homogeneous boundary law, with the gradient Gibbs measure given by equation (4.3).

Let G_k be the free product of $k+1$ cyclic groups of order two, with generators a_1, a_2, \dots, a_{k+1} . It is known that there is a one-to-one correspondence between the set of vertices V of the Cayley tree Γ^k and the group G_k (see Proposition 1.1 in [4]).

Any element $x \in G_k$ has the following form

$$x = a_{i_1} a_{i_2} \dots a_{i_n}, \quad \text{where } 1 \leq i_m \leq k+1, \quad m = 1, \dots, n.$$

The number n is called the length of the word and the number of letters $a_i, i = 1, \dots, k+1$, that enter the non contractible representation of the word x is denoted by $\omega_x(a_i)$. Let $N_k = \{1, \dots, k+1\}$, and define the set

$$H_A = \left\{ x \in G_k \mid \sum_{i \in A} \omega_x(a_i) \text{ is even} \right\}.$$

By Proposition 1.2 in [4], for any $\emptyset \neq A \subseteq N_k$, the set $H_A \subset G_k$ is a normal subgroup of index two.

Now, we define a spatially inhomogeneous boundary law associated with H_A (a H_A -boundary law), i.e., $\{l_{xy}\}_{\langle x,y \rangle \in \vec{L}} = \{l^{(1)}, l^{(2)}\}$ assuming $A = N_k$ as follows

$$l_{xy} = \begin{cases} l^{(1)}, & \text{if } x \in H_A \text{ and } y \in G_k \setminus H_A \\ l^{(2)}, & \text{if } y \in H_A \text{ and } x \in G_k \setminus H_A \end{cases}. \quad (3.14)$$

It is essential to observe that when $l^{(1)} = l^{(2)}$, the boundary conditions are spatially homogeneous [17, 21, 22]. Conversely, when $l^{(1)} \neq l^{(2)}$, the boundary conditions become spatially inhomogeneous, a phenomenon that is further investigated in this paper.

Now we define the vectors $z = (\dots z_{-2}, z_{-1}, 1, z_1, z_2, \dots)$ and $t = (\dots t_{-2}, t_{-1}, 1, t_1, t_2, \dots)$ for simplicity under the assumption $l_{xy}(0) \neq 0$ in the following way

$$\frac{l_{xy}(i)}{l_{xy}(0)} = \begin{cases} z_i, & \text{if } x \in H_A \text{ and } y \in G_k \setminus H_A \\ t_i, & \text{if } y \in H_A \text{ and } x \in G_k \setminus H_A \end{cases},$$

where $i \in \mathbb{Z}$.

Let G be a given graph. We specify the set of G -admissible configurations as follows.

Definition 2. [14] A configuration ω is called a G -admissible configuration on the Cayley tree if $\{\omega_x, \omega_y\}$ is the edge of the graph G for any pair of nearest neighbors x, y in V .

Let Ω_G denote the set of G -admissible configurations, Ω_G^∇ indicate the set of G -admissible gradient configuration space and $L(G)$ be the set of edges of a graph G . We let $A \equiv A^G = (a_{ij})_{i,j \in \mathbb{Z}}$ denote the adjacency matrix of the graph G , i.e.,

$$a_{ij} = a_{ij}^G = \begin{cases} 1 & \text{if } \{i, j\} \in L(G) \\ 0 & \text{if } \{i, j\} \notin L(G) \end{cases}.$$

Applying the matrix A to the system of boundary law equations (3.13) for the SOS model, restricted to the set of G -admissible configurations, results in

$$\begin{cases} z_i = \left(\frac{a_{i0}\theta^{|i|} + \sum_{j \in \mathbb{Z}_0} a_{ij}\theta^{|i-j|}t_j}{a_{00} + \sum_{j \in \mathbb{Z}_0} a_{0j}\theta^{|j|}t_j} \right)^k \\ t_i = \left(\frac{a_{i0}\theta^{|i|} + \sum_{j \in \mathbb{Z}_0} a_{ij}\theta^{|i-j|}z_j}{a_{0,0} + \sum_{j \in \mathbb{Z}_0} a_{0j}\theta^{|j|}z_j} \right)^k \end{cases}, \quad (3.15)$$

where $i \in \mathbb{Z}_0 := \mathbb{Z} \setminus \{0\}$.

It should be noted that for any graph with the vertex set \mathbb{Z} , the system of equations (3.15) simplifies to the form (3.1). It is easily demonstrable that by altering the graph, one can derive parameter values b and c such that $b \neq c$. Specifically, the scenario where $b = c$ is examined for two selected graphs throughout the paper.

Let G_1 be the complete graph with vertex set \mathbb{Z} , where each vertex has a loop, i.e., $a_{ij} = 1$ for all $i, j \in \mathbb{Z}$. Using the transfer operator defined in the preliminaries and the parameter $\theta = e^{-J\beta}$ (with $0 < \theta < 1$), the system of equations (3.15) for our model becomes

$$\begin{cases} z_i = \left(\frac{\theta^{|i|} + \sum_{j \in \mathbb{Z}_0} \theta^{|i-j|}t_j}{1 + \sum_{j \in \mathbb{Z}_0} \theta^{|j|}t_j} \right)^k \\ t_i = \left(\frac{\theta^{|i|} + \sum_{j \in \mathbb{Z}_0} \theta^{|i-j|}z_j}{1 + \sum_{j \in \mathbb{Z}_0} \theta^{|j|}z_j} \right)^k \end{cases}. \quad (3.16)$$

We study the 2-periodic solutions of (3.16), assuming $u_i = \sqrt[k]{z_i}$ and $v_i = \sqrt[k]{t_i}$. In the 2-periodic case, the sequences are given by

$$\begin{aligned} l^{(1)} &\sim (\dots, u_1, 1, u_1, 1, u_1, \dots), \\ l^{(2)} &\sim (\dots, v_1, 1, v_1, 1, v_1, \dots). \end{aligned}$$

By denoting $u_1 := x$ and $v_1 := y$ we obtain the following system of equations

$$\begin{cases} x = \frac{(\theta^2 + 1)y^k + 2\theta}{2\theta y^k + \theta^2 + 1} \\ y = \frac{(\theta^2 + 1)x^k + 2\theta}{2\theta x^k + \theta^2 + 1} \end{cases}. \quad (3.17)$$

Theorem 1. Let $\theta_{cr} = \frac{\sqrt{k} - 1}{\sqrt{k} + 1}$ with $k \geq 2$. Then 2-height periodic boundary law of the type (3.14) determines 2-height periodic spatially homogeneous boundary law. Consequently, for the SOS model on Cayley tree of order k with the parameter $\theta \in (0, \theta_{cr})$ there exist precisely three 2-height periodic GGMs on $\Omega_{G_1}^\nabla$.

Proof. We apply Proposition 1 with parameters $a = \theta^2 + 1$, $b = 2\theta$, and $c = 2\theta$. It's clear that we are in the regime where $a > c$ and consequently we obtain three different GGMs corresponding to the spatially homogeneous boundary law, i.e. $l^{(1)} = l^{(2)}$.

To determine the conditions for the existence of three gradient Gibbs measures corresponding to the subgroup H_A , we solve the following inequality as stated in part (2) of Proposition 1

$$k > \frac{(\theta + 1)^2}{(\theta - 1)^2}.$$

Through straightforward calculations, we establish the interval $0 < \theta < \theta_{cr}$ within which the system of equations (3.17) possesses exactly three solutions. Here, θ_{cr} is defined as $\theta_{cr} = \frac{\sqrt{k} - 1}{\sqrt{k} + 1}$ for $k \geq 2$. \square

Now we consider the graph G_2 containing \mathbb{Z} as the vertices, i.e. one-dimensional lattice graph where additionally each vertex is connected to itself, considered in [14] (see Figure 3) with its adjacency matrix

$$a_{ij} = \begin{cases} 1, & \text{if } i = j \text{ or } |i - j| = 1, \quad i, j \in \mathbb{Z} \\ 0, & \text{otherwise} \end{cases}.$$

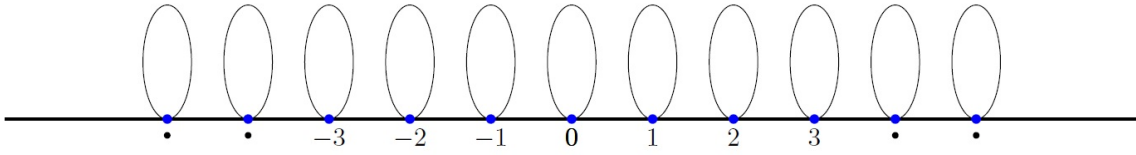


FIG. 3. The graph G_2 with the set \mathbb{Z} of vertices

Then the system of equations (3.15) on the space Ω_{G_2} for the 2-periodic case becomes

$$\begin{cases} x = \left(\frac{y + 2\theta}{2\theta y + 1} \right)^k \\ y = \left(\frac{x + 2\theta}{2\theta x + 1} \right)^k \end{cases}. \tag{3.18}$$

Theorem 2. Let $\theta_{cr}^- = \frac{k - 1}{2k + 2}$ for $k \geq 2$ and $\theta_{cr}^+ = \frac{k + 1}{2k - 2}$ for $k \geq 4$. Then for the SOS model restricted to a set of G_2 -admissible configurations on the Cayley tree of order k the following assertions hold

- The boundary law (3.14) associated with H_A coincides with the spatially homogenous boundary law for $\theta \in (0, \theta_{cr}^-)$ which provides exactly three 2-height periodic GGMs on $\Omega_{G_2}^\nabla$.
- The boundary law (3.14) associated with H_A becomes spatially inhomogeneous for $\theta \in (\theta_{cr}^+, 1)$ resulting in three 2-height periodic pinned gradient measures on $\Omega_{G_2}^\nabla$.

Proof. For the graph G_2 in Figure 3 we derive the parameters $a = 1$, $b = 2\theta$, and $c = 2\theta$ to apply Proposition 1 once more.

Case 1. Let $0 < \theta < \frac{1}{2}$. Then, it is evident that $a > c$, leading to three distinct GGMs corresponding to the spatially homogeneous boundary law, i.e., $l^{(1)} = l^{(2)}$. In this case, we use the inequality $k > \frac{a + b}{a - c}$ stated in part (2) of Proposition 1 in the form

$$k > \frac{2\theta + 1}{1 - 2\theta}.$$

By solving last inequality, we obtain $0 < \theta < \theta_{cr}^-$, where $\theta_{cr}^- = \frac{k - 1}{2k + 2}$.

Case 2. Let $\frac{1}{2} < \theta < 1$. Then, it is evident that $a < c$, resulting in spatially inhomogeneous, i.e., $l^{(1)} \neq l^{(2)}$, boundary laws which always defines gradient measures by the equation (3.4) in [22]. In this case, the inequality $k > \frac{a + b}{c - a}$ stated in part (3) of Proposition 1 becomes

$$k > \frac{2\theta + 1}{2\theta - 1}.$$

Thus, it follows that the system of equations (3.18) has exactly three solutions, provided that $\theta_{cr}^+ < \theta < 1$, where $\theta_{cr}^+ = \frac{k + 1}{2k - 2}$. It is important to note that this condition on θ is valid when the order of the Cayley tree is strictly greater than 3. \square

Remark 1. Are the two pinned gradient measures identified in Theorem 2 classified as gradient Gibbs measures (GGMs)? This question remains open.

4. Conclusion

Our main goal is to quantify the number of pinned gradient measures for the SOS model on the Cayley tree of order $k \geq 2$ by analyzing boundary law equations (3.13) under certain temperature conditions. This work distinguishes itself from previous studies, which have focused on spatially homogeneous q -periodic boundary laws and their corresponding GGMs (see [14–19, 22]). The paper is organized as follows: we first prove Proposition 1, then use it to solve an infinite system of equations (3.13), i.e., to find 2-periodic boundary laws. In Theorem 1, we demonstrate the existence of three GGMs on the Cayley tree of order $k \geq 2$ for certain values of θ using different methods (see [17, 21, 22]). We also determine the critical temperature condition, i.e., $\theta \in (\theta_{cr}^+, 1)$, where spatially inhomogeneous boundary laws of period two defines pinned gradient measures for the SOS model restricted to the G_2 -admissible configuration space.

References

- [1] Friedli S., Velenik Y. Statistical mechanics of lattice systems. A concrete mathematical introduction. Cambridge University Press, Cambridge, 2018.
- [2] Georgii H.O. Gibbs Measures and Phase Transitions, Second edition. de Gruyter Studies in Mathematics, 9. Walter de Gruyter, Berlin, 2011.
- [3] Mukhamedov F. Extremality of Disordered Phase of λ -Model on Cayley Trees. *Algorithms*, 2022, **15**(1), 18 pages.
- [4] Rozikov U.A. Gibbs measures on Cayley trees, World Scientific Publishing Co. Pte. Ltd., Hackensack, NJ, pp. xviii+385, 2013.
- [5] Souissi A., Hamdi T., Mukhamedov F., Andolsi A. On the structure of quantum Markov chains on Cayley trees associated with open quantum random walks, *Axioms*, 2023, **12**(9), 864 pages.
- [6] Zachary S. Bounded, attractive and repulsive Markov specifications on trees and on the one-dimensional lattice. *Stochastic Process. Appl.*, 1985, **20**(2), P. 247–256.
- [7] Funaki T., Spohn H. Motion by mean curvature from the Ginzburg-Landau $\nabla\varphi$ interface model. *Comm. Math. Phys.*, 1997, 185.
- [8] Funaki T. Stochastic interface models. Lectures on Probability Theory and Statistics, Lecture Notes in Math., Springer-Verlag, Berlin, 2015, P. 103–274.
- [9] Cotar C., Külske C., Existence of Random Gradient States. *Ann. Appl. Probab.*, 2012, **22**(4), P. 1650–1692.
- [10] Cotar C., Külske C., Uniqueness of gradient Gibbs measures with disorder. *Probab. Theory Relat. Fields*, 2015, **162**, P. 587–635.
- [11] Van Enter A.C., Külske C. Non-existence of random gradient Gibbs measures in continuous interface models in $d = 2$. *Ann. Appl. Probab.*, 2008, **18**, P. 109–119.
- [12] Henning F., Külske C. Existence of gradient Gibbs measures on regular trees which are not translation invariant. *Ann. Appl. Probab.*, 2023, **33**(4), P. 3010–3038.
- [13] Zachary S. Countable state space Markov random fields and Markov chains on trees. *Ann. Probab.*, 1983, **11**(4), P. 894–903.
- [14] Ganikhodjaev N.N., Khatamov N.M., Rozikov U.A. Gradient Gibbs measures of an SOS model with alternating magnetism on Cayley trees. *Reports on Mathematical Physics*, 2023, **92**(3), P. 309–322.
- [15] Haydarov F.H., Ilyasova R.A., Gradient Gibbs measures with periodic boundary laws of a generalised SOS model on a Cayley tree. *J. Stat. Mech. Theory Exp.*, 2023, vol. 123101, 12 pages.
- [16] Henning F. Gibbs measures and gradient Gibbs measures on regular trees. PhD Thesis, Ruhr University, 2021, 109 pp.
- [17] Haydarov F.H., Rozikov U.A. Gradient Gibbs measures of an SOS model on Cayley trees: 4-periodic boundary laws. *Reports on Mathematical Physics*, 2022, **90**(1), P. 81–101.
- [18] Henning F., Külske C., Le Ny A., and Rozikov U.A. Gradient Gibbs measures for the SOS model with countable values on a Cayley tree. *Electron. J. Probab.*, 2019, **24**(104), 23 pages.
- [19] Ilyasova R.A. Height-periodic gradient Gibbs measures for generalised SOS model on Cayley tree. *Uzbek Mathematical Journal*, 2024, **68**(2), P. 92–99.
- [20] Rozikov U.A. Mirror Symmetry of Height-Periodic Gradient Gibbs Measures of an SOS Model on Cayley Trees. *J. Stat. Phys.*, 2022, **188**, 26 pages.
- [21] Henning F., Külske C. Height-offset variables and pinning at infinity for gradient Gibbs measures on trees.
- [22] Külske C., Schriever P. Gradient Gibbs measures and fuzzy transformations on trees. *Markov Process. Relat. Fields*, 2017, **23**(4), P. 553–590.
- [23] Henning F., Külske C. Coexistence of localized Gibbs measures and delocalized gradient Gibbs measures on trees. *Ann. Appl. Probab.*, 2021, **31**(5), P. 2284–2310.
- [24] Dobrushin R.L. Description of a random field by means of conditional probabilities and the conditions governing its regularity. *Theory Prob. and its Appl.*, 1968, **13**, P. 197–224.
- [25] Lanford O.E., Ruelle D. Observables at infinity and states with short range correlations in statistical mechanics. *Comm. Math. Physics*, 1968, **13**, P. 194–215.
- [26] Ruelle D. Superstable interactions in statistical mechanics. *Comm. Math. Physics*, 1970, **18**, P. 127–159.
- [27] Khakimov R.M., Haydarov F.H. Translation-invariant and periodic Gibbs measures for the Potts model on the Cayley tree. *Theoretical and mathematical physics*, 2016, **289**, P. 286–295.
- [28] Prasolov V.V. *Polynomials*. Springer, Berlin. 2004.
- [29] Sheffield S. Random surfaces, Large deviations principles and gradient Gibbs measure classifications. PhD Thesis, Stanford University, 2003, 205 pages.

Information about the authors:

Farhod H. Haydarov – Institute of Mathematics, 9, University str., Tashkent, 100174, Uzbekistan; New Uzbekistan University, 54, Mustaqillik Ave., Tashkent, 100007, Uzbekistan; ORCID 0000-0001-9388-122X; haydarov_imc@mail.ru, f.khaydarov@newuu.uz

Risolat A. Ilyasova – New Uzbekistan University, 54, Mustaqillik Ave., Tashkent, 100007, Uzbekistan; National University of Uzbekistan, University str., 4 Olmazor district, Tashkent, 100174, Uzbekistan; ORCID 0009-0003-2145-2196; r.ilyasova@newuu.uz, ilyasova.risolat@mail.ru

Khudoyor S. Mamayusupov – New Uzbekistan University, 54, Mustaqillik Ave., Tashkent, 100007, Uzbekistan; ORCID 0000-0001-8511-4856; k.mamayusupov@newuu.uz

Conflict of interest: the authors declare no conflict of interest.

Translation-invariant p -adic quasi Gibbs measures for the Potts model with an external field on the Cayley tree

Muzaffar M. Rakhmatullaev^{1,2,a}, Nurkhon D. Samijonova^{3,b}¹V. I. Romanovskiy Institute of Mathematics, Uzbekistan Academy of Sciences, Tashkent, Uzbekistan²New Uzbekistan University, Tashkent, Uzbekistan³Namangan State University, Namangan, Uzbekistan^amrahmatullaev@rambler.ru, ^bnurxonsamijonova@gmail.comCorresponding author: M. M. Rahmatullaev, mrahmatullaev@rambler.ru

ABSTRACT The study is focused on investigation of p -adic Gibbs measures for the q -state Potts model with an external field and determination of the conditions for the existence of a phase transition. In this work, we derive a functional equation that satisfies the compatibility condition for p -adic quasi-Gibbs measures on a Cayley tree of order $k \geq 2$. Furthermore, we prove that if $|q|_p = 1$ there exists a unique p -adic Gibbs measure for this model. Additionally, for the Potts model on a binary tree, we identify three p -adic quasi-Gibbs measures under specific circumstances: one bounded and two unbounded, which implies a phase transition.

KEYWORDS p -adic numbers, the Potts model with external field, p -adic quasi Gibbs measure, translation-invariant, Cayley tree

ACKNOWLEDGEMENTS The authors thank Akbarkhuja M. Tukhtabaev for valuable advice and an anonymous referee for helpful suggestions that improved the paper.

FOR CITATION Rahmatullaev M.M., Samijonova N.D. Translation-invariant p -adic quasi Gibbs measures for the Potts model with an external field on the Cayley tree. *Nanosystems: Phys. Chem. Math.*, 2025, **16** (2), 164–175.

1. Introduction

A comprehensive understanding of the interactions between individual atoms and molecules within nanosystems, along with their statistical mechanical modeling, is crucial for the development in nanotechnology [1]. To formulate the thermodynamics of small systems, one has to start evaluating thermodynamics from the first principles reviewing the concepts, laws, definitions, and formulations, and to draw a set of guidelines for their applications to small systems [2–5]. Such questions as property relations and phase transitions in small (nano) systems are subjects to be investigated and formulated provided the formulation of working equations of thermodynamics and statistical mechanics of small systems. It is worth mentioning that the molecular self-assembly (bottom-up technology) that was originally proposed by Feynman [6] has its roots in phase transitions.

p -adic probabilities, a novel concept in theoretical physics, have spontaneously appeared in physical models based on p -adic numbers, similar to the p -adic string, first proposed by I. Volovich [7]. In [8], a theory of stochastic processes was developed for values in p -adic and more general non-Archimedean fields. These processes have probability distributions with non-Archimedean values. A non-Archimedean analog of the Kolmogorov theorem was established, enabling the construction of a wide range of stochastic processes using finite-dimensional probability distributions. This foundation has opened the door for investigating and developing certain problems in statistical mechanics within the framework of p -adic probability theory.

The Potts model is a statistical mechanics model that generalizes the Ising model to allow for more than two components [9]. It has been extensively studied in recent years due to its rich mathematical structure and its applications to various physical systems [10, 11]. The studies in [12–16] for the Ising, in [17–19] for the Potts have contributed to our understanding of these models. Note that papers [20–23] are focused on translation-invariant p -adic Gibbs measures. In [24–29], different aspects or specific cases of non-periodic, constructive p -adic quasi-Gibbs measures for the Ising and Potts models are explored.

In this paper, we investigate translation-invariant p -adic quasi Gibbs measures for the Potts model with an external field. The theory immediately shows the effect of an external force. For example, in [30], translation-invariant p -adic Gibbs measures were investigated in the Ising model with an external field, and a phase transition was identified for $p \equiv 1 \pmod{4}$. In [31], weakly periodic Gibbs measures were investigated for the same model, and the existence of a phase transition was shown for any odd prime number. Moreover, in [22], it was proved: if $|q|_p = 1$, then there is no translation-invariant p -adic Gibbs measure for the Potts model corresponding to \mathbf{h}_x on the set $\mathcal{E}_p \setminus \{1\}$. However, we

prove that, if $|q|_p = 1$, then there is a unique p -adic Gibbs measure for the Potts model with an external field. Therefore, we apply those ideas to a more complicated situation.

The purpose of this research is to examine p -adic Gibbs measures for the q -state Potts model with an external field and to provide sufficient conditions for a phase transition. In contrast to a real case, such measures for the model are not explained in a p -adic setting. In this work, we have derived a functional equation satisfying the compatible condition for p -adic quasi-Gibbs measures on a Cayley tree of order k for the given model. Moreover, we have proved the existence of a unique p -adic Gibbs measure for this model. Additionally, for the Potts model on a binary tree, we have determined under the some specific cases three p -adic quasi Gibbs measures which one of them is bounded, and others are unbounded and derived a new conditions for the existence of a phase transition.

1.1. p -adic numbers

Let \mathbb{Q} be a field of rational numbers. For a fixed prime number p , every rational number $x \neq 0$ can be represented in the form $x = p^r \frac{n}{m}$ where, $r, n \in \mathbb{Z}$, m is a positive integer, and (n, p) and (m, p) , where number r is called a p -order of x and it is denoted by $ord_p(x) = r$. The p -adic norm of x is given by

$$|x|_p = \begin{cases} p^{-r}, & x \neq 0, \\ 0, & x = 0. \end{cases}$$

The norm of $|\cdot|_p$ is non-Archimedean, i.e., it satisfies the strong triangle inequality:

$$|x + y|_p \leq \max\{|x|_p, |y|_p\}, \quad \forall x, y \in \mathbb{Q}.$$

We note that the following essential properties are relevant to the non-Archimedeanity of the norm:

- i) if $|x|_p \neq |y|_p$, then $|x \pm y|_p = \max\{|x|_p, |y|_p\}$;
- ii) if $|x|_p = |y|_p$, then $|x - y|_p \leq |x|_p$.

The completion of \mathbb{Q} with respect to the p -adic norm defines the p -adic field \mathbb{Q}_p . Any p -adic number $x \neq 0$ can be uniquely represented in the canonical form $x = p^{\gamma(x)}(x_0 + x_1p + x_2p^2 + \dots)$, where $\gamma(x) \in \mathbb{Z}$ and the integers x_j satisfy: $x_0 > 0$, $0 \leq x_j \leq p - 1$. In this case $|x|_p = p^{-\gamma(x)}$.

An integer $b \in \mathbb{Z}$ is called *quadratic residue modulo p* if the congruent equation $x^2 \equiv b \pmod{p}$ has a solution $x \in \mathbb{Z}$. Let p be odd prime and a be an integer not divisible by p . The *Legendre symbol* (see [32]) is defined by

$$\left(\frac{b}{p}\right) = \begin{cases} 1, & \text{if } b \text{ is quadratic residue of } p, \\ -1, & \text{if } b \text{ is quadratic nonresidue of } p. \end{cases} \tag{1}$$

Let $a \in \mathbb{Q}_p$, $a \neq 0$, $a = p^{\gamma(a)}(a_0 + a_1p + a_2p^2 + \dots)$, $0 \leq a_j \leq p - 1, j \in \mathbb{N}$, $a_0 > 0$.

Lemma 1. [33] *The equation $x^2 = a$ has a solution in $x \in \mathbb{Q}_p$ iff the followings hold:*

- i) $\gamma(a)$ is even;
- ii) a_0 is a quadratic residue modulo p if $p \neq 2$; the equality $a_1 = a_2 = 0$ hold if $p = 2$.

Lemma 2.(Hensel’s lemma [34]) *Let $f(x) = c_0 + c_1x + \dots + c_nx^n$ be a polynomial whose coefficients are p -adic integers. Let $f'(x) = c_1 + 2c_2x + \dots + nc_nx^{n-1}$ be the derivative of $f(x)$. Let x^* be a p -adic integer such that $f(x^*) \equiv 0 \pmod{p}$ and $f'(x^*) \not\equiv 0 \pmod{p}$. Then there exists a unique p -adic integer root x_* such that*

$$f(x_*) = 0 \text{ and } x_* \equiv x^* \pmod{p}.$$

In [35], the authors introduced new symbols, "O" and "o", which simplify certain calculations. Essentially, these symbols help us to write down the calculations in our work more concisely. To understand their meanings, one can note: for a given p -adic number x , $O[x]$ refers to a p -adic number whose norm satisfies $|x|_p = |O[x]|_p$. On the other hand, $o[x]$ refers to a p -adic number such that $|o[x]|_p < |x|_p$. For example, if $x = 1 + p + p^3$, we write $O[1] = x$, $o[1] = x - 1$ or $o[p^2] = x - 1 - p$.

For any $a \in \mathbb{Q}_p$ and $r > 0$, we denote

$$B(a, r) = \{x \in \mathbb{Q}_p : |x - a|_p < r\},$$

and the set

$$\mathbb{Z}_p = \{x \in \mathbb{Q}_p : |x|_p \leq 1\}, \quad \mathbb{Z}_p^* = \mathbb{Z}_p \setminus p\mathbb{Z}_p.$$

\mathbb{Z}_p is called the set of p -adic integers, \mathbb{Z}_p^* is called the set of p -adic units. Note that the p -adic exponential is defined by the series

$$\exp_p(x) = \sum_{n=0}^{\infty} \frac{x^n}{n!},$$

which converges for $x \in B(0, \frac{1}{2})$ if $p = 2$ and $x \in B(0, 1)$ if $p \neq 2$. For simplicity of notation, we write $\exp(x)$ instead of $\exp_p(x)$.

Put

$$\mathcal{E}_p = \left\{ x \in \mathbb{Q}_p : |x - 1|_p < p^{-1/(p-1)} \right\}.$$

A more thorough explanation of p -adic calculus and p -adic mathematical physics is provided in [36, 37].

Let (X, \mathcal{B}) be a measurable space, where \mathcal{B} is an algebra of subsets X . A function $\mu : \mathcal{B} \rightarrow \mathbb{Q}_p$ is said to be a p -adic measure if for any $A_1, A_2, \dots, A_n \in \mathcal{B}$ such that $A_i \cap A_j = \emptyset, i \neq j$, the following holds:

$$\mu \left(\bigcup_{j=1}^n A_j \right) = \sum_{j=1}^n \mu(A_j).$$

If $\mu(X) = 1$, then a p -adic measure is called *probability*. One of the important conditions is boundedness, namely, a p -adic measure μ is called *bounded* if $\sup\{|\mu(A)|_p : A \in \mathcal{B}\} < \infty$. For more detail information about p -adic measures we refer to [36, 38].

1.2. Cayley Tree

Let $\Gamma_+^k = (V, L)$ be a semi-infinite Cayley tree [39] of order $k \geq 1$ with the root $x^0 \in V$. Here V is the set of vertices and L is the set of edges. The vertices x and y are referred to as *nearest neighbors* when there is an edge l connecting them and this is shown by the notation $l = \langle x, y \rangle$. Note that each vertex of Γ_+^k has exactly $k + 1$ nearest neighbors, except for the root x^0 , which has k nearest neighbors. A collection of the pairs $\langle x, x_1 \rangle, \dots, \langle x_{d-1}, y \rangle$ is called a *path* from the point x to the point y . The distance $d(x, y)$ on the Cayley tree is the length (number of edges) of the shortest path from x to y .

Let us set

$$W_n = \{x \in V : d(x, x^0) = n\}, \quad V_n = \bigcup_{m=0}^n W_m,$$

$$L_n = \{\langle x, y \rangle \in L : x, y \in V_n\}.$$

We introduce a coordinate structure in Γ_+^k : every vertex x (except for x^0) of Γ_+^k has coordinates (i_1, \dots, i_n) , here $i_m \in \{1, \dots, k\}, 1 \leq m \leq n$ and for the vertex x^0 we put (0) . Namely, the symbol (0) constitutes level 0, and the sites (i_1, \dots, i_n) form level n (i.e. $d(x^0, x) = n$) of the lattice. Let us define on Γ_+^k binary operation $\circ : \Gamma_+^k \times \Gamma_+^k \rightarrow \Gamma_+^k$ as follows: for any two elements $x = (i_1, \dots, i_n)$ and $y = (j_1, \dots, j_m)$ put

$$x \circ y = (i_1, \dots, i_n) \circ (j_1, \dots, j_m) = (i_1, \dots, i_n, j_1, \dots, j_m) \tag{2}$$

and

$$x \circ x^0 = x^0 \circ x = (i_1, \dots, i_n) \circ (0) = (i_1, \dots, i_n). \tag{3}$$

By means of the defined operation Γ_+^k becomes a noncommutative semigroup with a unit. Let us denote this group (G^k, \circ) . Using this semigroup structure one defines translations $\tau_g : G^k \rightarrow G^k, g \in G_k$ by

$$\tau_g(x) = g \circ x.$$

It is clear that $\tau_{(0)} = id$.

Let $G \subset G^k$ be a sub-semigroup of G^k and $h : G^k \rightarrow Y$ be a Y -valued function defined on G^k . We say that h is G -periodic if $h(\tau_g(x)) = h(x)$ for all $g \in G$ and $x \in G^k$. We say that any G^k -periodic function is *translation-invariant*.

Now, for each $m \geq 2$ we put

$$G_m = \{x \in G^k : d(x, x^0) \equiv 0 \pmod{m}\}. \tag{4}$$

It is easy to verify that G^k is a sub-semigroup of G_m .

2. p -adic quasi Gibbs measure for the Potts model

Let \mathbb{Q}_p be the field of p -adic numbers and $\Phi = \{1, 2, \dots, q\}$ be a finite set. A configuration σ on V is defined as $x \in V \mapsto \sigma(x) \in \Phi$. The set of all configurations coincides with the set $\Omega = \Phi^V$. For given configurations $\sigma \in \Omega_{V_{n-1}}$ and $\omega \in \Omega_{W_n}$, we define their concatenation by

$$(\sigma \vee \omega)(x) = \begin{cases} \sigma_{n-1}(x), & \text{if } x \in V_{n-1}, \\ \omega(x), & \text{if } x \in W_n. \end{cases}$$

It is clear that $\sigma \vee \omega \in \Omega_{V_n}$.

We consider p -adic q -state Potts model on a Cayley tree with an external field.

The (formal) Hamiltonian of p -adic Potts model is

$$H(\sigma) = J \sum_{\langle x, y \rangle \in L} \delta_{\sigma(x)\sigma(y)} + \alpha \sum_{x \in V} \delta_{q\sigma(x)}, \quad (5)$$

where $J, \alpha \in B(0, p^{-1/(p-1)})$ are constant, $\langle x, y \rangle$ stands for nearest neighbor vertices and δ_{ij} is the Kronecker symbol, i.e.,

$$\delta_{ij} = \begin{cases} 0, & \text{if } i \neq j, \\ 1, & \text{if } i = j. \end{cases}$$

Assume that $h : V \rightarrow \mathbb{Q}_p^{|\Phi|}$ is a mapping, i.e. $h_x = (h_{1,x}, h_{2,x}, \dots, h_{q,x})$, where $h_{i,x} \in \mathbb{Q}_p$ ($i \in \Phi$) and $x \in V$. Given $n \in \mathbb{N}$, we consider a p -adic probability measure $\mu_{h,\sigma}^{(n)}$ on Ω_{V_n} defined by

$$\mu_h^{(n)}(\sigma) = \frac{1}{Z_n^{(h)}} \exp\{H_n(\sigma)\} \prod_{x \in W_n} h_{\sigma(x),x}, \quad (6)$$

Here, $\sigma \in \Omega_{V_n}$, and $Z_n^{(h)}$ is the corresponding normalizing factor or a partition function given by

$$Z_n^{(h)} = \sum_{\sigma \in \Omega_{V_n}} \exp\{H_n(\sigma)\} \prod_{x \in W_n} h_{\sigma(x),x}. \quad (7)$$

We say that p -adic probability distributions (6) are compatible if for all $n \geq 1$ and $\sigma_{n-1} \in \Phi^{V_{n-1}}$:

$$\sum_{\omega \in \Omega_{W_n}} \mu_h^{(n)}(\sigma_{n-1} \vee \omega) = \mu_h^{(n-1)}(\sigma_{n-1}) \quad (8)$$

We notice that a non-Archimedean analogue of the Kolmogorov extension theorem was proved in [40, 41]. According to this theorem, there exists a unique p -adic quasi measure μ_h on $\Omega = \Phi^V$ such that for all $n \geq 1$ and $\sigma \in \Phi^{V_n}$,

$$\mu(\sigma \in \Omega : \sigma|_{V_n} \equiv \sigma_n) = \mu_h^{(n)}(\sigma_n)$$

Such measure is called a p -adic quasi Gibbs measure corresponding to the Hamiltonian (5) and vector-valued function $\mathbf{h}_x, x \in V$. By $QG(H)$ we denote the set of all p -adic quasi Gibbs measure associated with function $\mathbf{h} = \{\mathbf{h}_x, x \in V\}$. If all coordinates of \mathbf{h}_x belong to the set \mathcal{E}_p then it is called p -adic Gibbs measure. If there are at least two distinct p -adic quasi Gibbs measure $\mu, \nu \in QG(H)$ such that μ is bounded and ν is unbounded, then we say that a *phase transition* occurs.

The following statement describe conditions \mathbf{h}_x providing compatibility of $\mu_h^{(n)}(\sigma)$.

Theorem 1. The measures $\mu_h^{(n)}(\sigma), n = 1, 2, \dots$ (6) associated with the Potts model (5) satisfy the compatibility condition (8) if and only if for any $n \in \mathbb{N}$ the equation that follows holds:

$$\hat{\mathbf{h}}_x = \prod_{y \in S(x)} F(\hat{\mathbf{h}}_y, \theta, \eta), \quad (9)$$

here $\theta = \exp\{J\}$, $\eta = \exp\{\alpha\}$ and below a vector $\hat{\mathbf{h}}_x = (\hat{h}_{1,x}, \hat{h}_{2,x}, \dots, \hat{h}_{q-1,x}) \in \mathbb{Q}_p^{q-1}$ is defined by a vector $\mathbf{h}_x = (h_{1,x}, h_{2,x}, \dots, h_{q,x}) \in \mathbb{Q}_p^q$ as follows

$$\hat{h}_{i,x} = \frac{h_{i,x}}{h_{q,x}}, \quad i = 1, 2, \dots, q-1$$

and mapping

$F : \mathbb{Q}_p^{q-1} \rightarrow \mathbb{Q}_p^{q-1}$ is defined by $F(x; \theta, \eta) = (F_1(x; \theta, \eta), \dots, F_{q-1}(x; \theta, \eta))$ with

$$F_i(x; \theta, \eta) = \frac{(\theta - 1)x_i + \sum_{j=1}^{q-1} x_j + \eta}{\sum_{j=1}^{q-1} x_j + \theta\eta}, \quad x = \{x_i\} \in \mathbb{Q}_p^{q-1}, \quad i = 1, 2, \dots, q-1.$$

Proof Necessity. Assume that (8) holds. We must demonstrate (9). Substituting (6) into (8), we have

$$\begin{aligned} & \sum_{\omega \in \Phi^{W_n}} \frac{1}{Z_n^{(h)}} \exp \left\{ H_{n-1}(\sigma) + \left(\sum_{x \in W_{n-1}} \sum_{y \in S(x)} (J\delta_{\sigma_{n-1}(x)\omega_n(y)} + \alpha\delta_{q\omega_n(y)}) \right) \right\} \prod_{x \in W_n} h_{\sigma(x),x} \\ &= \frac{1}{Z_{n-1}^{(h)}} \exp\{H_{n-1}(\sigma)\} \prod_{x \in W_{n-1}} h_{\sigma(x),x}. \end{aligned}$$

By eliminating the expressions on the left side of the equality outside the sign of the sum that do not depend on the sum, we obtain the following equality:

$$\begin{aligned} \frac{Z_{n-1}}{Z_n} \sum_{\omega \in \Phi^{W_n}} \exp \left(\sum_{x \in W_{n-1}} \sum_{y \in S(x)} (J\delta_{\sigma_{n-1}(x)\omega_n(y)} + \alpha\delta_{q\omega_n(y)}) \right) \prod_{x \in W_n} h_{\omega_n(x),x} \\ = \prod_{x \in W_{n-1}} h_{\sigma_{n-1}(x),x}. \end{aligned}$$

It yields that

$$\frac{Z_{n-1}}{Z_n} \sum_{\omega \in \Phi^{W_n}} \prod_{x \in W_{n-1}} \prod_{y \in S(x)} \exp(J\delta_{\sigma_{n-1}(x)\omega_n(y)} + \alpha\delta_{q\omega_n(y)}) h_{\omega_n(y),y} = \prod_{x \in W_{n-1}} h_{\sigma_{n-1}(x),x}. \quad (10)$$

Fix $x \in W_{n-1}$ and consider two configurations $\sigma_{n-1} = \bar{\sigma}_{n-1}$ and $\sigma_{n-1} = \tilde{\sigma}_{n-1}$ on W_{n-1} which coincide on $W_{n-1} \setminus \{x\}$, and the equality (10) for $\bar{\sigma}_{n-1}$ is divided by (10) for $\tilde{\sigma}_{n-1}$. Then we obtain

$$\prod_{y \in S(x)} \frac{\sum_{j \in \Phi} \exp(J\delta_{ij} + \alpha\delta_{qj}) h_{j,y}}{\sum_{j \in \Phi} \exp(J\delta_{qj} + \alpha\delta_{qj}) h_{j,y}} = \frac{h_{i,x}}{h_{q,x}}.$$

It follows that

$$\prod_{y \in S(x)} \frac{\sum_{j=1}^{q-1} \hat{h}_{j,y} + (\theta - 1)\hat{h}_{i,y} + \eta}{\sum_{j=1}^{q-1} \hat{h}_{j,y} + \theta\eta} = \hat{h}_{i,x},$$

where $\hat{h}_{i,x} = \frac{h_{i,x}}{h_{q,x}}$ which implies (9).

Sufficiency. Suppose that (9) holds. It yields

$$\prod_{y \in S(x)} \frac{\sum_{j \in \Phi} \exp(J\delta_{ij} + \alpha\delta_{qj}) h_{j,y}}{\sum_{j \in \Phi} \exp(J\delta_{qj} + \alpha\delta_{qj}) h_{j,y}} = \frac{h_{i,x}}{h_{q,x}},$$

then for some function $a(x) \in \mathbb{Q}_p$, $x \in V$, we have

$$\prod_{y \in S(x)} \sum_{j \in \Phi} \exp(J\delta_{ij} + \alpha\delta_{qj}) h_{j,y} = a(x) \exp(h_{i,x}), \quad i \in \Phi. \quad (11)$$

We rewrite (6) as

$$\sum_{\omega \in \Omega_{W_n}} \mu_h^{(n)}(\sigma_{n-1} \vee \omega) = \frac{1}{Z_n} \exp\{H(\sigma_{n-1})\} \prod_{x \in W_{n-1}} \prod_{y \in S(x)} \sum_{j \in \Phi} \exp(J\delta_{\sigma_{n-1}(x)j} + \alpha\delta_{qj}) h_{j,y}. \quad (12)$$

Substituting (11) into (12) and denoting $A_{n-1} = \prod_{x \in W_{n-1}} a(x)$, we obtain

$$\sum_{\omega \in \Omega_{W_n}} \mu_h^{(n)}(\sigma_{n-1} \vee \omega) = \frac{A_{n-1}}{Z_n} \exp\{H(\sigma_{n-1})\} \prod_{x \in W_{n-1}} h_{\sigma_{n-1}(x),x}. \quad (13)$$

Since $\mu^{(n)}$ is a probability measure, we have

$$\sum_{\sigma \in \Omega_{V(n-1)}} \sum_{\omega \in \Omega_{W_n}} \mu_h^{(n)}(\sigma_{n-1} \vee \omega) = 1.$$

(13) yields

$$\sum_{\omega \in \Omega_{W_n}} \mu_h^{(n)}(\sigma_{n-1} \vee \omega) = \frac{A_{n-1}}{Z_n} \mu_h^{(n-1)}(\sigma_{n-1}) Z_{n-1} \quad (14)$$

or

$$1 = \sum_{\sigma \in \Omega_{V(n-1)}} \sum_{\omega \in \Omega_{W_n}} \mu_h^{(n)}(\sigma_{n-1} \vee \omega) = \frac{A_{n-1}}{Z_n} Z_{n-1} \sum_{\sigma \in \Omega_{V(n-1)}} \mu_h^{(n-1)}(\sigma_{n-1}) = \frac{A_{n-1}}{Z_n} Z_{n-1}.$$

It follows that

$$Z_n = A_{n-1} Z_{n-1}. \quad (15)$$

Substituting (15) into (14), we have

$$\sum_{\omega \in \Omega_{W_n}} \mu_h^{(n)}(\sigma_{n-1} \vee \omega) = \mu_h^{(n-1)}(\sigma_{n-1}).$$

Theorem was proven.

Remark 1. If $\eta = 1$, then Theorem 1 coincides with Theorem 3.1 in [39].

3. Translation-invariant p -adic quasi Gibbs measure for the Potts model with external field

We try to find the translation-invariant solutions of the system of equations (9). It requires to solve the following system of equations

$$\widehat{h}_i = \left(\frac{(\theta - 1)\widehat{h}_i + \sum_{j=1}^{q-1} \widehat{h}_j + \eta}{\sum_{j=1}^{q-1} \widehat{h}_j + \theta\eta} \right)^k, \quad i = 1, 2, \dots, q - 1. \quad (16)$$

We assume that $\widehat{h} := \widehat{h}_1 = \widehat{h}_2 = \dots = \widehat{h}_{q-1}$. Then equation (16) reduces to the following one

$$\widehat{h} = \left(\frac{(\theta + q - 2)\widehat{h} + \eta}{(q - 1)\widehat{h} + \theta\eta} \right)^k. \quad (17)$$

Lemma 3. For equation (17), the following statements hold:

- 1) Equation (17) has no solution on $p\mathbb{Z}_p$;
- 2) If $q \notin \mathcal{E}_p$ then the solutions of (17) belong to \mathbb{Z}_p^* .

Proof At first, we show that equation (17) has no solution on $p\mathbb{Z}_p$. Assume that $\widehat{h} \in p\mathbb{Z}_p$, i.e. $|\widehat{h}|_p < 1$. Since $\eta, \theta \in \mathcal{E}_p$ and $q \in \mathbb{Z}_p$, we obtain

$$|\widehat{h}|_p = \left| \left(\frac{(\theta + q - 2)\widehat{h} + \eta}{(q - 1)\widehat{h} + \theta\eta} \right)^k \right|_p = \left| \frac{\eta}{\theta\eta} \right|_p^k = 1.$$

However, it contradicts to our assumption. Therefore, equation (17) has no solution on $p\mathbb{Z}_p$.

Now, we proof the second part of the theorem. We assume that $q \notin \mathcal{E}_p, |\widehat{h}|_p > 1$. From (17), we have

$$\left| \left(\frac{(\theta + q - 2)\widehat{h} + \eta}{(q - 1)\widehat{h} + \theta\eta} \right)^k \right|_p = \left| \left(\frac{(\theta - 1 + q - 1)\widehat{h}}{(q - 1)\widehat{h}} \right)^k \right|_p = 1 \neq |\widehat{h}|_p.$$

However, it contradicts to our assumption. Thus, equation (17) has no solution on $p\mathbb{Z}_p$, if $q \notin \mathcal{E}_p$, (17) has no solution on $\mathbb{Q}_p \setminus \mathbb{Z}_p$. To conclude, if equation (17) has a solution, it must belong to \mathbb{Z}_p^* . Lemma was proven.

Lemma 4. Let $|q|_p = 1, p \geq 3$. Then there is a unique solution of (17) in the form of $h^* \in \mathcal{E}_p$.

Proof We rewrite (17) as

$$\widehat{h}((q - 1)\widehat{h} + \theta\eta)^k - ((\theta + q - 2)\widehat{h} + \eta)^k = 0$$

Set the notation

$$F(\widehat{h}, \theta, \eta, q) = \widehat{h}((q - 1)\widehat{h} + \theta\eta)^k - ((\theta + q - 2)\widehat{h} + \eta)^k.$$

It can be seen that $F(\widehat{h}, \theta, \eta, q)$ is a polynomial with p -adic integer coefficients. For $h \equiv 1 \pmod{p}$, we verify that $F(\widehat{h}, \theta, \eta, q)$ satisfies the conditions of Lemma 2. Then we obtain that

$$\begin{aligned} F(1, \theta, \eta, q) &\equiv ((q - 1 + 1 + o[1])^k - (q - 1 + o[1] + 1 + o[1])^k) \\ &\equiv ((q + o[1])^k - (q + o[1])^k) \equiv 0 \pmod{p} \end{aligned}$$

and

$$F'(h, \theta, \eta, q) = ((q - 1)\widehat{h} + \theta\eta)^k + k(q - 1)h((q - 1)\widehat{h} + \theta\eta)^{k-1} - k(\theta + q - 2)((\theta + q - 2)\widehat{h} + \eta)^{k-1}.$$

We consider $F'(1, \theta, \eta, q) \equiv 0 \pmod{p}$, i.e.,

$$F'(1, \theta, \eta, q) \equiv (q - 1 + 1 + o[1])^k + k(q - 1)(q - 1 + 1 + o[1])^{k-1} - k(1 + o[1] + q - 2)(1 + o[1] + q - 2 + 1 + o[1])^{k-1} \equiv (q + o[1])^k \not\equiv 0 \pmod{p}.$$

Thus, the polynomial fulfills the requirements of Lemma 2. It implies that there is a unique integer root h^* such that

$$F(h^*, \theta, \eta, q) = 0, \quad h^* \equiv 1 \pmod{p}.$$

It yields $h^* \in \mathcal{E}_p$.

Remark 2. In [22] authors studied all translation-invariant p -adic Gibbs measures for the Potts model without external fields. It was shown that if $|q|_p = 1, \eta = 1$ then the system of equations (16) on $\mathcal{E}_p \setminus \{1\}$ does not have any solution. However, we proved that if $|q|_p = 1, \eta \neq 1$ then the system of equations (16) has a unique solution on $\mathcal{E}_p \setminus \{1\}$.

Remark 3. Further calculations are needed in order to study equation (17) for the case $q \in \mathcal{E}_p$. Hence, this problem will be studied in our upcoming work.

From Lemma 3, if $q \notin \mathcal{E}_p$, the solutions of equation (17) belonging to \mathbb{Z}_p^* . We obtain the following congruence from (17) after slight modification:

$$\widehat{h}((q-1)\widehat{h} + \theta\eta)^k - ((\theta + q - 2)\widehat{h} + \eta)^k \equiv 0 \pmod{p}. \tag{18}$$

Theorem 2. For congruence (18), the following statements hold:

i) If $|q|_p < 1$ then (18) has a solution with $\widehat{h} \equiv 1 \pmod{p}$;

ii) If $q \in \mathbb{Z}_p^* \setminus \mathcal{E}_p$ then (18) has the solutions with $\widehat{h}^{(1)} \equiv 1 \pmod{p}$ and $h^{(2)} \equiv -(q-1)^{-1} \pmod{p}$, here $(q-1)^{-1}$ is inverse of $q-1$ modulo p .

Proof Let $|q|_p < 1$. Then it can be seen that

$$\widehat{h}((q-1)\widehat{h} + \theta\eta)^k - ((\theta + q - 2)\widehat{h} + \eta)^k \equiv (-1)^k (\widehat{h} - 1)^{k+1} \pmod{p}.$$

It follows that the solution of the congruence (17) is $\widehat{h}_1 \equiv 1 \pmod{p}$.

Let $|q|_p = 1$ and $q \notin \mathcal{E}_p$. Then we get

$$\widehat{h}((q-1)\widehat{h} + \theta\eta)^k - ((\theta + q - 2)\widehat{h} + \eta)^k \equiv (\widehat{h} - 1)((q-1)\widehat{h} + 1)^k \pmod{p}.$$

From this, we have two solutions $\widehat{h}_1 \equiv 1 \pmod{p}$ and $\widehat{h}_2 \equiv -(q-1)^{-1} \pmod{p}$ which implies (17).

Remark 5. We note that it is essential to find the first coefficient of the canonical form of the solution of (17). It gives a possibility to check the boundedness of the Gibbs measure.

If $q \in \mathbb{Z}^*$ then according to Lemma 4, equation (17) has a unique solution in \mathcal{E}_p . Now, we show that there is a solution of (16) such that $h \notin \mathcal{E}_p$. It is difficult to solve this problem in general case. We concentrate on the simplest case $k = 2$. In this case, we have

$$\widehat{h} = \left(\frac{(\theta + q - 2)\widehat{h} + \eta}{(q-1)\widehat{h} + \theta\eta} \right)^2. \tag{19}$$

Let us consider the following depressed cubic equation

$$x^3 + ax = b.$$

In [42], the criteria for solvability of the depressed cubic equation over \mathbb{Z}_p^* are given.

Let $D = -4(a|_p)^3 - 27(b|_p)^2 \neq 0, D = \frac{D^*}{|D|_p}, D^* \in \mathbb{Z}_p^*, D^* = d_0 + d_1p + \dots, D_0 = -4a_0^3 - 27b_0^2$ and $u_1 = 0, u_2 = -a_0, u_3 = b_0$ and $u_{n+3} = b_0u_n - a_0u_{n+1}$.

Theorem 3. [42] Let $p > 3$ be a prime number and \mathcal{N} be the cardinality of the set of solution to $x^3 + ax - b = 0$ in \mathbb{Z}_p . Then the following statements hold:

$$\mathcal{N} = \begin{cases} 3, & |a|_p^3 < |b|_p^2 \leq 1, \quad 3 \mid \log_p |b|_p, \quad p \equiv 1 \pmod{3}, \quad b_0^{\frac{p-1}{3}} \equiv 1 \pmod{p}; \\ 3, & |a|_p^3 = |b|_p^2 \leq 1, \quad D = 0; \\ 3, & |a|_p^3 = |b|_p^2 \leq 1, \quad 0 < |D|_p < 1, \quad 2 \mid \log_p |D|_p, \quad d_0^{\frac{p-1}{2}} \equiv 1 \pmod{p}; \\ 3, & |a|_p^3 = |b|_p^2 \leq 1, \quad |D|_p = 1 \text{ and } u_{p-2} \equiv 0 \pmod{p}; \\ 3, & |b|_p^2 < |a|_p^3 \leq 1, \quad 2 \mid \log_p |a|_p, \quad (-a_0)^{\frac{p-1}{2}} \equiv 1 \pmod{p}; \\ 1, & |a|_p^3 < |b|_p^2 \leq 1 \quad 3 \nmid \log_p |b|_p, \quad p \equiv 2 \pmod{3}; \\ 1, & |a|_p^3 = |b|_p^2 \leq 1, \quad 0 < |D|_p < 1, \quad 2 \mid \log_p |D|_p, \quad d_0^{\frac{p-1}{2}} \not\equiv 1 \pmod{p}; \\ 1, & |a|_p^3 = |b|_p^2 \leq 1, \quad 0 < |D|_p < 1, \quad 2 \nmid \log_p |D|_p; \\ 1, & |a|_p^3 = |b|_p^2 \leq 1, \quad D_0 u_{p-2}^2 \not\equiv 0 \pmod{p}, \quad D_0 u_{p-2}^2 \not\equiv 9a_0^2 \pmod{p}; \\ 1, & |b|_p^2 < |a|_p^3 \leq 1, \quad 2 \mid \log_p |a|_p, \quad (-a_0)^{\frac{p-1}{2}} \not\equiv 1 \pmod{p}; \\ 1, & |b|_p^2 < |a|_p^3 \leq 1, \quad 2 \nmid \log_p |a|_p; \\ 1, & |b|_p^2 < |a|_p^3, \quad |b|_p \leq |a|_p, \quad |a|_p > 1; \\ 0, & \text{otherwise,} \end{cases}$$

where $a \mid b$ means a divides b .

Lemma 5. Let $p > 3, q \in \mathbb{Z}_p^* \setminus \mathcal{E}_p, \mathcal{N}$ be the cardinality of the set of the solutions of (19). Then we have

$$\mathcal{N} = \begin{cases} 3, & \text{if } (1-q)^{\frac{p-1}{2}} \equiv 1 \pmod{p}; \\ 1, & \text{otherwise.} \end{cases}$$

Proof We rewrite equation (17) as follows

$$\widehat{h}^3 + \frac{2\theta\eta(q-1) - (\theta+q-2)^2}{(q-1)^2} \widehat{h}^2 + \frac{(\theta^2\eta^2 - 2\eta(\theta+q-2))}{(q-1)^2} \widehat{h} - \frac{\eta^2}{(q-1)^2} = 0. \tag{20}$$

We denote

$$z := \widehat{h} - \frac{2\theta\eta(q-1) - (\theta+q-2)^2}{3(q-1)^2}. \tag{21}$$

From (20) and (21), we obtain

$$z^3 + az - b = 0, \tag{22}$$

where

$$\begin{aligned} a &= -\frac{1}{3} \frac{(2\theta\eta(q-1) - (\theta+q-2)^2)^2}{(q-1)^4} + \frac{\theta^2\eta^2 - 2\eta(\theta+q-2)}{(q-1)^2}, \\ b &= \frac{1}{3} \frac{(\theta^2\eta^2 - 2\eta(\theta+q-2))(2\theta\eta(q-1) - (\theta+q-2)^2)}{(q-1)^4} + \frac{\eta^2}{(q-1)^2} - \\ &\quad \frac{2}{27} \frac{(2\theta\eta(q-1) - (\theta+q-2)^2)^3}{(q-1)^6}. \end{aligned} \tag{23}$$

It should be noted that due to Lemma 4, equation (17) has a unique solution $\widehat{h}^* \equiv 1 \pmod{p}$ and this statement also holds for (19). Therefore, we check the conditions of Theorem 3 for $\mathcal{N} = 3$. Since $q \notin \mathcal{E}_p, |q|_p = 1$, we obtain that $|a|_p = |b|_p = 1$.

One can see that

$$\begin{aligned} D &= -4(a \mid a|_p)^3 - 27(b \mid b|_p)^2 = \\ &= \frac{1}{(q-1)^8} m^2(s+1)^3(m+q)^2 (-4m^3qs^2 + m^4s - 6m^3qs + 4m^3s^2 + m^2q^2s - \\ &12m^2qs^2 + m^4 - 2m^3q + 8m^3s + m^2q^2 - 4m^2qs + 12m^2s^2 + 20mq^2s - 12mqs^2 - 4m^2q + 4m^2s + \\ &8mq^2 - 44mqs + 12ms^2 - 8q^2s - 4qs^2 + 4m^2 - 8mq + 24ms + 4q^2 + 8qs + 4s^2 + 4q^2 - 4q^3), \end{aligned}$$

where $m = \theta - 1, s = \eta - 1$.

It can be checked that $|D|_p < 1$. According to Theorem 3, if $2 \mid \log_p |D|_p, d_0^{\frac{p-1}{2}} \equiv 1 \pmod{p}$, then equation (22) has

three solutions. We show that $\text{ord}_p D$ is even, $\sqrt{d_0} \in \mathbb{Q}_p$.

At first, we check that $\sqrt{d_0} \in \mathbb{Q}_p$. For the sake of simplicity, we denote

$$D_1 = -4m^3qs^2 + m^4s - 6m^3qs + 4m^3s^2 + m^2q^2s - 12m^2qs^2 + m^4 - 2m^3q + 8m^3s + m^2q^2 - 4m^2qs + 12m^2s^2 + 20mq^2s - 12mq^2s^2 - 4m^2q + 4m^2s + 8mq^2 - 44mqs + 12ms^2 - 8q^2s - 4qs^2 + 4m^2 - 8mq + 24ms + 8qs + 4s^2 + 4q^2 - 4q^3, \\ q = q_0 + o[1], q_0 \in \overline{2, p-1}, m = p^\beta(m_0 + o[1]).$$

Using $|m|_p < 1, |s|_p < 1, |q|_p = 1$ and $q \notin \mathcal{E}_p$, we obtain

$$\begin{aligned} q - 1 &= q_0 - 1 + o[1]; \\ s + 1 &= 1 + o[1]; \\ m + q &= q_0 + o[1]; \\ D_1 &= 4q_0^2(1 - q_0) + o[1]. \end{aligned} \tag{24}$$

It yields that $d_0 \equiv \frac{4q_0^4(1 - q_0)m_0^2}{(q_0 - 1)^8} \pmod{p}$.

We deduce that if the Legendre symbol of $1 - q_0$ is equal to 1, then $\sqrt{d_0} \in \mathbb{Q}_p$.

Now, we define $|D|_p$ Using (24), we have

$$\begin{aligned} |q - 1|_p &= 1; \\ |s + 1|_p &= 1; \\ |m + q|_p &= 1; \\ |D_1|_p &= 1. \end{aligned}$$

It follows that $|D|_p = (|m|_p)^2$. So, $\text{ord}_p D$ is even. The proof is completed.

In [43], the cubic equation (22) is examined for the case $p = 3$. If $|a|_3 > |b|_3, 2 \mid \log_3 |a|_3, \frac{a}{|a|_3} \equiv 2 \pmod{3}$, then equation (22) has three solutions over \mathbb{Q}_3 . Using this criteria, we get the following lemma.

Lemma 6. Let $p = 3, |q|_3 = 1$, then equation (19) has a unique solution.

Proof We note that, due to Lemma 4, equation (19) has a unique solution on \mathcal{E}_3 . For this case, let us find the remaining solutions of (19).

Case I. $q \equiv 2 \pmod{3}$.

From (23), we get $|a|_3 = 3, |b|_3 = 27$. This does not satisfy the conditions of the above criteria.

Case II. $q \equiv 1 \pmod{3}$

Let $|2\theta\eta(q - 1) - (\theta + q - 2)|_3 = 3^\alpha, |q - 1|_3 = 3^m$. Then $|a|_3 = 3^{4m-2\alpha+1}, |b|_3 = 3^{6m-3\alpha+3}$. This also does not meet the required conditions. Therefore, we conclude that equation (19) has a unique solution.

Lemma 7. Let $p \geq 3, |q|_p < 1$, then equation (19) has no solution.

Proof We assume that $|q|_p < 1$. According to Lemma 3 and Theorem 3, the solutions of equation (19) belong to \mathbb{Z}_p^* with $\hat{h} \equiv 1 \pmod{p}$. Due to (21), we obtain that

$$\frac{2\theta\eta(q - 1) - (\theta + q - 2)^2}{3(q - 1)^2} = -1 + o[1], z \equiv 2 \pmod{p}.$$

It follows that $|z|_p = 1$.

Using (23) and $|q|_p < 1$, we have $|a|_p < 1, |b|_p < 1$. We rewrite equation (22) as follows

$$z^3 = b - az.$$

It can be seen that

$$|b - az|_p < 1 \neq |z^3|_p.$$

It follows that equation(19) has no solution given the conditions in the lemma. Lemma was proved.

Using Lemmas 5,6, and 7, we come to the following result:

Theorem 4. The following statements are true for p -adic Potts model with external field on the Cayley tree of order two.

- 1) if $|q|_p = 1, p = 3$ or $|q|_p = 1, p > 3, (1 - q)^{\frac{p-1}{2}} \not\equiv 1 \pmod{p}$ then there is one translation-invariant p -adic quasi Gibbs measure;

- 2) if $p > 3, |q|_p = 1, q \notin \mathcal{E}_p, (1 - q)^{\frac{p-1}{2}} \equiv 1 \pmod{p}$, then there are three translation-invariant p -adic quasi Gibbs measures;
- 3) if $p \geq 3, |q|_p < 1$, then there is not any translation-invariant p -adic quasi Gibbs measure.

Corollary 1. Let \mathcal{N}_{TP} be number of p -adic quasi Gibbs measures for the Potts model with an external field on the Cayley tree of order two. Then we obtain

$$\mathcal{N}_{TP} = \begin{cases} 0, & \text{if } p = q = 3; \\ 1, & \text{if } q = 3, p > 3, p \equiv 5 \pmod{8} \text{ or } p \equiv 7 \pmod{8}; \\ 3, & \text{if } q = 3, p > 3, p \equiv 1 \pmod{8} \text{ or } p \equiv 3 \pmod{8}. \end{cases}$$

Proof 1) Let $p = q = 3$. This case satisfies the third condition in Theorem 4, therefore, there is no translation-invariant p -adic quasi Gibbs measure, that is, $\mathcal{N}_{TP} = 0$.

2) If $q = 3, p > 3$, then $1 - q = -2$. In [44], the following results are obtained

$$\left(\frac{-2}{p}\right) = \begin{cases} 1, & \text{if } p \equiv 1 \pmod{8} \text{ or } p \equiv 3 \pmod{8}; \\ -1, & \text{if } p \equiv 5 \pmod{8} \text{ or } p \equiv 7 \pmod{8}. \end{cases}$$

These conditions satisfy the first and the second conditions in Theorem 4. Keeping in mind these results, we obtain the assertions of the corollary.

4. Boundedness of the translation-invariant p -adic quasi Gibbs measures and phase transitions

Lemma 8. Let $\mu_{\mathbf{h}}$ be an associated p -adic quasi Gibbs measure, and let \mathbf{h} be a solution of (9). Then, the following equality is true for the appropriate partition function $Z_n^{(\mathbf{h})}$:

$$Z_n^{(\mathbf{h})} = A_{\mathbf{h},n-1} Z_{n-1}^{(\mathbf{h})}, \tag{25}$$

where $A_{\mathbf{h},n} = \prod_{x \in W_n} a_{\mathbf{h}}(x), \prod_{y \in S(x)} \sum_{j=1}^q \exp\{J\delta_{i,j} + \alpha\delta_{qj}\} h_{j,y} = a_{\mathbf{h}}(x) h_{i,x}$,

$$a_{\mathbf{h}}(x) \in \mathbb{Q}_p, \quad i = 1, 2, \dots, q.$$

Proof Assume that \mathbf{h} is a solution of (9), then equation (10) hold. We rewrite (10) for ordinary $i \in \Phi$ as follows

$$Z_n = Z_{n-1} \prod_{x \in W_{n-1}} \frac{\prod_{y \in S(x)} \sum_{j=1}^q \exp(J\delta_{i,j} + \alpha\delta_{qj}) h_{j,y}}{h_{i,x}}. \tag{26}$$

We present subsequent notations

$$A_{\mathbf{h},n} = \prod_{x \in W_n} a_{\mathbf{h}}(x) \text{ and } a_{\mathbf{h}}(x) = \frac{\prod_{y \in S(x)} \sum_{j=1}^q \exp\{J\delta_{i,j} + \alpha\delta_{qj}\} h_{j,y}}{h_{i,x}}.$$

Then equation (26) is reduced to (25).

Using Lemma 8, we come to the following statement.

Lemma 9. Let $k = 2, \mathbf{h}$ be a translation-invariant solution of (9), then for the corresponding partition function $Z_n^{(\mathbf{h})}$ the following equality is appropriate:

$$Z_n^{(\mathbf{h})} = ((q - 1)h + \eta\theta)^{3 \cdot 2^{n-1}} (h(q - 1) + \eta). \tag{27}$$

Proof It is easy to check that $\mathbf{h} = (h, h, \dots, h, 1)$ is a translation-invariant solution of (9), where h is a fixed point of (19). Since $\theta = \exp\{J\}$ and $\eta = \exp\{\alpha\}$, using (7) we obtain $Z_1^{(\mathbf{h})} = ((q - 1)h + \theta\eta)^2 ((q - 1)h + \eta)$. Then by Lemma 8, we come to the following equality:

$$a_{\mathbf{h}}(x) = \frac{((\theta + q - 2)h_{1,y} + \eta)^2}{h_{1,x}} = \frac{(\theta + q - 2)h + \eta)^2}{h} = ((q - 1)h + \theta\eta)^2.$$

From Lemma 8, we obtain

$$\begin{aligned} A_{\mathbf{h},n} &= ((q - 1)h + \eta\theta)^{3 \cdot 2^{n-1}}, \\ Z_n^{(\mathbf{h})} &= ((q - 1)h + \eta\theta)^{3 \cdot (2^n - 1)} ((q - 1)h + \eta\theta)^2 ((q - 1)h + \eta) = \\ &= ((q - 1)h + \eta\theta)^{3 \cdot 2^n - 1} (h(q - 1) + \eta). \end{aligned}$$

Lemma is proved.

Theorem 5. Let $p \geq 3, |q|_p = 1$. The following statements hold for p -adic Potts model with an external field on a Cayley tree of order two:

- 1) if $p = 3$ or $p > 3, (1 - q)^{\frac{p-1}{2}} \not\equiv 1 \pmod{p}$, then measure μ_{h^*} is bounded;
- 2) if $q \notin \mathcal{E}_p, p > 3, (1 - q)^{\frac{p-1}{2}} \equiv 1 \pmod{p}$, then measure μ_{h^*} is bounded, measures μ_{h_1}, μ_{h_2} are unbounded.

Proof Case 1. If $p = 3$ or $p > 3, (1 - q)^{\frac{p-1}{2}} \not\equiv 1 \pmod{p}$, then there exists measure μ_{h^*} . We note that $h^* \in \mathcal{E}_p$. From Lemma 9 and (6), we obtain

$$\lim_{n \rightarrow \infty} |\mu_{h^*}^{(n)}|_p = \lim_{n \rightarrow \infty} \left| \frac{1}{(q + o[1])^{3 \cdot 2^n} \exp\{H_n(\sigma)\}} \prod_{x \in W_n} h_{\sigma(x),x} \right|_p = 1.$$

Case 2. If $p > 3, (1 - q)^{\frac{p-1}{2}} \equiv 1 \pmod{p}$, there exist translation-invariant measures $\mu_{h^*}, \mu_{h_1}, \mu_{h_2}$. According to Lemma 4 and Theorem 3, $h^* = 1 \pmod{p}, h_{1,2} = -(q - 1)^{-1} \pmod{p}$. From Lemma 9 and (6), we obtain

$$\lim_{n \rightarrow \infty} |\mu_{h^*}^{(n)}|_p = \lim_{n \rightarrow \infty} \left| \frac{\prod_{x \in W_n} h_{\sigma(x),x}}{((q - 1)h^* + \eta\theta)^{3 \cdot 2^n - 1} (h^*(q - 1) + \eta)} \exp\{H_n(\sigma)\} \right|_p = 1.$$

$$\lim_{n \rightarrow \infty} |\mu_{h_{1,2}}^{(n)}|_p = \lim_{n \rightarrow \infty} \left| \frac{\prod_{x \in W_n} h_{\sigma(x),x}}{((q - 1)h_{1,2} + \eta\theta)^{3 \cdot 2^n - 1} (h_{1,2}(q - 1) + \eta)} \exp\{H_n(\sigma)\} \right|_p = \infty.$$

We have proved that the measure μ_{h^*} is bounded, μ_{h_1}, μ_{h_2} measures are unbounded as in the case 2.

Theorem 6. Let $p > 3, |q|_p = 1, q \notin \mathcal{E}_p$. Then there exists a phase transition for p -adic q -state Potts model with an external field on a Cayley tree of order two if $(1 - q)^{\frac{p-1}{2}} \equiv 1 \pmod{p}$.

Proof The proof is straightforward due to Theorem 5.

Corollary 2. Let $q = 3$. If $p > 3, p \equiv 1 \pmod{8}$ or $p \equiv 3 \pmod{8}$ then there is a phase transition for p -adic Potts model with an external field on the Cayley tree of order two.

Remark 6. a) In [23], the authors focused on the Potts model without an external field. The phase transition conditions determined in this study were consistent with the results of Corollary 2.

b) In [24], the existence a quasi-phase transition is defined for the $q + 1$ Potts model without an external field is proven if $|q|_p = 1$. However, we define a phase transition for this model if $|q|_p = 1, |q - 1|_p = 1$, and $(1 - q)^{\frac{p-1}{2}} \equiv 1 \pmod{p}$.

c) Note that we have considered translation-invariant p -adic quasi Gibbs measures for the Potts model with an external field only for the case $\mathbf{h} = \{h, h, \dots, h\}, \mathbf{h} \in \mathbb{Q}_p^{q-1}$. The remaining cases are left as an open problem.

5. Conclusion

It should be noted that so far, p -adic quasi-Gibbs measures have been obtained for the Potts model without an external field. Therefore, we have dedicated this work to the study of p -adic quasi-Gibbs measures for the Potts model with an external field. Analyzing functional equation which defines p -adic quasi Gibbs measure for the Potts model with the external field on a semi-infinite Cayley tree, we have derived three translation-invariant p -adic quasi Gibbs measures under some condition. We also obtained a system of functional equations that satisfy the consistency condition for p -adic quasi-Gibbs measures for the Potts model with an external field on the Cayley tree of order $k \geq 2$. This system corresponds to the functional equation in [39] when the external field is zero.

In [24], a quasi-phase transition was identified for the $q + 1$ state Potts model when $|q|_p = 1$. Moreover, we identified the phase transition for the q -state Potts model with an external field when $|q|_p = 1, |q - 1|_p = 1$, and $(1 - q)^{\frac{p-1}{2}} \equiv 1 \pmod{p}$.

In [28], [23], p -adic quasi-Gibbs measures were determined for the 3-state Potts model, and we extend these results to the general case $q \geq 3$ and q external field. In particular, if $q = 3$, our result coincides with the result in [23].

References

- [1] Esfarjani K., Ali Mansoori G., Statistical Mechanical Modeling and Its Application to Nanosystems, Handbook of Theoretical and computational Nanotechnology, 2004, pp. 45.
- [2] Hill L. Thermodynamics of Small Small Systems, Benjamin, New York, 1963, pp. 417.
- [3] Hill T.L. A different approach to nanothermodynamics, *Nano Lett.*, 2001, **1**(5).
- [4] Onsager L., Machlup S. *Phys. Verhandlungen*, 1952, **3**(84).
- [5] Prigogine I. *Introduction to Thermodynamics of Irreversible Processes*. Wiley, New York, 1967, pp. 147.
- [6] Feynman R.P. There's Plenty of Room at the Bottom. *Eng. Sci. Mag.*, 1960, **23**(5), P. 22–36.
- [7] Volovich I.V. p -Adic String. *Classical Quantum Gravity*, 1987, **4**, P. 83–87.
- [8] Derrida B., Seze De.L., Itzykson C. Fractal structure of zeros in hierarchical models, *J. Stat. Phys.*, 1983, **33**, P. 559–569.
- [9] Potts R.B. Some generalized order-disorder transformations. *Proc.Camb.Phil.Soc.*, 1952, **48**(1), P. 106–109.
- [10] Rozikov U.A. Gibbs measures in biology and physics: The Potts model. World. Sci. publ., Singapore 2023.
- [11] Wu F.Y. The Potts model, *Rev. Mod. Phys.*, 1982, **54**, P. 235.
- [12] Ganikhodjaev N.N., Rahmatullaev M.M. and Mohd Hirzie Bin Mohd Rodzhan, Weakly periodic Gibbs measures of the Ising model on the Cayley tree of order five and six. *Math. Phys. Anal. Geom.*, 2018, **21**(2).

- [13] Khatamov N.M. Holliday junctions in the HC Blume-Capel model in "one case" on DNA. *Nanosystems: Physics, Chemistry, Mathematics*, 2021, **12**(5), P. 563–568.
- [14] Rahmatullaev M.M., Egamov D.O. Translation-invariant Gibbs measures for the mixed spin-1/2 and spin-1 Ising model with an external field on a Cayley tree. *Nanosystems: Physics, Chemistry, Mathematics*, 2024, **15**(5), P. 576–585.
- [15] Rahmatullaev M.M. Ising model on trees: (k_0) – non translation-invariant Gibbs measures. *Journal of Physics Conference Series* 2019, **1**(819).
- [16] Rukiah bin Ali, Mukhamedov F. Chin Hee Pah Ising Model with Competing Interactions on Cayley Tree of Order 4: An Analytic Solution. *J. Phys.: Conf.Ser.*, 2013, **435**, P. 012–032.
- [17] Ganikhodjaev N.N., Mukhamedov F.M. and Rozikov U.A. Existence of a phase transition for the Potts p -adic model on the set Z . *Theor. Math. Phys.*, 2002, **130**, P. 425–431.
- [18] Ganikhodjaev N.N., Rozikov U.A. The Potts model with countable set of spin values on a Cayley tree. *Lett. Math. Phys.*, 2006, **75**, P. 99–109.
- [19] Rozikov U.A., Rahmatullaev M.M., Khakimov R.M. Periodic Gibbs measures for the Potts model in translation-invariant and periodic external fields on the Cayley tree. *Theor. Math. Phys.*, 2022, **210**(1), P. 135–153.
- [20] Khakimov O. On a generalized p -adic Gibbs measure for Ising model on trees. *p-Adic Numbers, Ultrametric Anal. Appl.*, 2014, **6**(3), P. 207–217.
- [21] Mukhamedov F., Rozikov U.A. On Gibbs measure of p -adic Potts model on the Cayley tree. *Indag. Math. N. S.*, 2004, **15**(1), P. 85–99.
- [22] Rozikov U.A., Khakimov O.N. Description of all translation-invariant p -adic Gibbs measures for the Potts model on the Cayley tree. *Markov Proces.Rel.Fields*, 2015, **21**, P. 177–204.
- [23] Tukhtabaev A.M. On G_2 -Periodic Quasi Gibbs Measures of p -Adic Potts Model on a Cayley Tree. *p-Adic Numbers, Ultrametric Anal. Appl.*, 2021, **13**(4), P. 291–307.
- [24] Mukhamedov F. On dynamical systems and phase transitions for $q + 1$ state p -adic Potts model on Cayley tree. *Math.Phys.Anal.Geom.*, 2013, **26**, P. 49–87.
- [25] Rahmatullaev M.M., Abdukaxorova Z.T. H_A -weakly periodic p -adic generalized Gibbs measures for Ising model on a Cayley tree. *Lobachevskii Journal of Mathematics*, 2024, **1**(24), P. 504–517.
- [26] Rahmatullaev M.M., Khakimov O.N., Tukhtaboev A.M. A p -adic generalised Gibbs measure for the Ising model on a Cayley tree. *Theor. Math.Phys.*, 2019, **1**(201), P. 1521–1530.
- [27] Rahmatullaev M.M., Tukhtabaev A.M. Non periodic p -adic generalised Gibbs measure for the Ising model. *p-Adic Numbers Ultrametric Anal. Appl.*, 2019, **11**, P. 319–327.
- [28] Rahmatullaev M., Tukhtabaev A., Samijonova N. Weakly periodic p -adic quasi Gibbs measures for the Potts model on a Cayley tree. *Lett. Math. Phys.*, 2024, **114**(6).
- [29] Rahmatullaev M., Abdukaxorova Z. H_A -weakly periodic p -adic generalized Gibbs measures for the p -Adic Ising model on the Cayley tree of order two. *p-Adic Numbers, Ultrametric Anal. Appl.*, 2024, **3**(16), P. 233–263.
- [30] Mukhamedov F., Rahmatullaev M., Tukhtabaev A., Mamadjonov R. On p -adic Ising model with external field on a Cayley tree: Periodic Gibbs measures. *Theor. Math. Phys.*, 2023, **216**(2), P. 383–400.
- [31] Rahmatullaev M.M., Abdukaxorova Z.T., "On H_A -weakly periodic p -adic generalized Gibbs measures for the p -adic Ising model with an external field on the Cayley tree of order two". *Rep. Math. Phys.*, 2025, **95**(1), P. 93–106.
- [32] Rosen K.H. *Elementary Number Theory and Its Applications*, 1986, pp. 452. Addison-Westley, Canada.
- [33] Vladimirov V.S., Volovich I.V. and Zelenov E.I. *p-Adic analysis and Mathematical physics*. World Scientific, Singapoure 1994.
- [34] Koblitz N. *p-Adic Numbers, p-Adic Analysis, and Zeta-Functions*, Springer, Berlin 2004, pp. 166.
- [35] Mukhamedov F., Khakimov O. On equation $x^k = a$ over Q_p and its applications. *Izvestiya Math.*, 2020, **84**(2), P. 348–360.
- [36] Khrennikov A.Yu., Nilson M. *p-Adic Deterministic and Random Dynamical Systems*, Kluwer. Dordrecht 2004, pp. 270.
- [37] Volovich I.V. Number theory as the ultimate physical theory. *p-Adic Numbers Ultrametric Anal.App.*, 2010, **2**(1), P. 77–87.
- [38] Khrennikov A.Yu. p -adic valued probability measures. *Indag.Mathem.N.S.*, 1996, **7**, P. 311–330.
- [39] Mukhamedov F. On p -adic quasi Gibbs measures for $q + 1$ -state Potts model on the Cayley tree. *p-Adic Numbers Ultrametric Anal.Appl.*, 2010, **2**(3), P. 241–251.
- [40] Ganikhodjaev N.N., Mukhamedov F.M., Rozikov U.A. Phase transitions of the Ising model on \mathbb{Z} in the p -adic number field. *Uzbek. Math. Jour.*, 1998, **4**, P. 23–29.
- [41] Khrennikov A.Yu., Ludkovsky S. Stochastic process on non-Archimedean space with values in non-Archimedean fields. *Markov Proces. Related Fields* 2003, **9**(1), P. 131–162.
- [42] Mukhamedov F., Omirov B., Saburov M. On cubic equations over p -adic fields. *Inter. J. Number Theory.*, 2014, **10**, P. 1171–1190.
- [43] Ahmad M.A.Kh., Saburov M. The number of solution of cubic equation over \mathbb{Q}_3 . *Sains Malaysiana* 2015, **44**(5), P. 765–769.
- [44] Tukhtabaev A.M., Bunazarov X.K. Some problems related to the square root in the field \mathbb{Q}_p . *B.I.M.*, 2021, **3**(4), P. 1–5.
- [45] Ludkovsky S.V. Non-Archimedean valued quasi-invariant descending at infinity measures. *Int. J. Math. Math. Sci.*, 2005, **23**.

Submitted 19 November 2024; revised 5 March 2025; accepted 6 March 2025

Information about the authors:

Muzaffar M. Rakhmatullaev – V.I. Romanovskiy Institute of Mathematics, Uzbekistan Academy of Sciences, University str. 9, 100174, Tashkent, Uzbekistan; New Uzbekistan University, 100000, Tashkent, Uzbekistan; ORCID 0000-0003-2987-7714; mrahmatullaev@rambler.ru

Nurkhon D. Samijonova – Namangan State University, 161, Boburshox str, 160107, Namangan, Uzbekistan; ORCID 0009-0004-0060-2180; nurxonsamijonova@gmail.com

Conflict of interest: the authors declare no conflict of interest.

Quantum coupling between radio modes in a single-atom maser with two resonators

Eugeniy N. Popov^{1,a}, Alexander I. Trifanov^{1,b}, Maria A. Moskalenko^{1,c}, Vladimir A. Reshetov^{2,d}

¹ITMO University, Saint Petersburg, Russia

²Togliatti State University, Tolyatti, Russia

^aenp-tion@yandex.ru, ^balextrifanov@gmail.com, ^cmoskalenko.mary@gmail.com, ^dvareshetov@tltso.ru

Corresponding author: Eugeniy N. Popov, enp-tion@yandex.ru

ABSTRACT In this work, we investigate the effect of quantum coupling between radio fields in a single-atom maser with two spatially separated resonators. Each atom in a beam, depending on its state, can emit one photon into the first resonator and absorb another from the second, thereby entangling the quantum states of two independent modes. Resulting from entanglement, we obtain a coherence between states of two-mode field with the same total number of photons in the both modes. To study the arising coupling, an analytical solution of the stationary master equation is found under conditions of a trapped field state and the dependence of the von Neumann entanglement entropy on the quality factor of the resonators. Numerical analysis reveals that the best conditions for the appearance of quantum coupling are the low quality factor of the first resonator and the high quality factor of the second one.

KEYWORDS single-atom maser, quantum coupling, trapped field state

ACKNOWLEDGEMENTS The work was supported by the Ministry of Science and Education of the Russian Federation (Passport No. 2019-0903).

FOR CITATION Popov E.N., Trifanov A.I., Moskalenko M.A., Reshetov V.A. Quantum coupling between radio modes in a single-atom maser with two resonators. *Nanosystems: Phys. Chem. Math.*, 2025, **65** (2), 176–182.

1. Introduction

A single-atom maser is widely accepted as one of the most efficient tools for observing the quantum effects of the atom-field interaction [1, 2]. An example of its application is the verification of the Jaynes-Cummings model [3]. Multiple publications containing a lot of experimental and theoretical work have also been published [4–14]. The most important research on the development of a single-atom masers was carried out by G. Walter at the end of the previous century. Thereby, the quantum properties of a single-atom masers with one resonator has already been described [15, 16]. Despite its success, the technical implementation of such a quantum single-atom maser circuit has proven to be a rather difficult and complex task. Therefore, further research continued only after the appearance of alternative schemes of controlled interaction between selected mode and atom. More recent research, most notably, includes the observation and prediction of new effects using a nanomaser on an ultra-fast driving LC circuit [17–20] as well as experiments on the study of interaction effects between single atoms and a series of coupled resonators [21–23]. Furthermore, active development is underway in the theory of single-atom masers [24]. However, in fact, we have not found any work on the formation of quantum connection between several independent modes using a common pumping system in a single-atom maser. Therefore, in this work, we build the initial theoretical foundation for this phenomenon with the ultimate goal of obtaining new physical results in subsequent studies.

Our article describes the initial theory of a single-atom masers that contains two resonators located in the path of the atomic beam, as shown in Fig. 1. With the use of focused pumping light, beam atoms are excited into a mixed populational state of lower and upper levels. Then the prepared atoms fly through a pair of resonators. The atomic beam is considered to be quite sparse, so that only one atom can possibly be located inside a pair of resonators at the same moment of time. During the propagation through each resonator, the atom periodically moves from one level to another, either emitting a photon into the mode or absorbing it. After the atom leaves the second resonator, the quantum state of the atom is destroyed due to the interaction with the environment. The atomic field wave function experiences collapse: the two-mode field will turn into a statistical ensemble of those states that correspond to the atom that was flew out at the lower or upper level. The process repeats for each atom in the beam.

Based on the described physical model, we propose a theoretical description for the formation of quantum coupling between the modes of spatially separated resonators. This coupling is explained by the preservation of the quantum state of the atom during its flight between the first and second resonators. During the interaction, the information about the field of the first resonator is recorded into a superposition of quantum states and then transferred to the second resonator by the atom. The information transfer process looks like this: an atom absorbs a photon from the first resonator and emits it

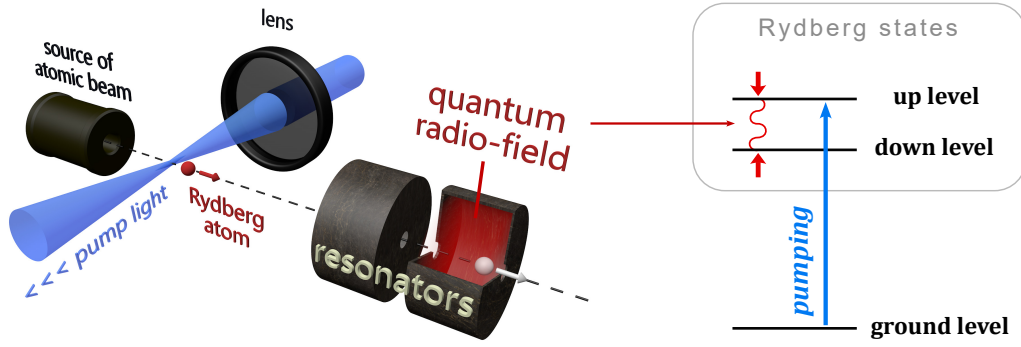


FIG. 1. The scheme of a single-atom maser with double resonator. Red and white spheres are atoms emitted from the source of the atomic beam. There is a scheme of atomic levels on right.

into the second, or vice versa; as a result, coherence is formed between field states with the same total number of photons in both modes. Strictly speaking, our task is to find an analytical form of the stationary state field modes under atomic pumping. The analysis of coupling between two cavities containing bosons is important in many theoretical and applied problems, so this observation may be useful in other studies [25–28].

2. Evolution of two-mode field

To model a single-atom maser with two resonators, we use the density matrix ρ_F , which describes the state of two coupled field modes. Each mode belongs to its own resonator. The first resonator, an atom flies through which, will be denoted as a , and the second as b :

$$\rho_F(t) = \sum_{m,n,\mu,\nu} \mathcal{F}_{m,n|\mu,\nu} |m, n\rangle \langle \mu, \nu|, \quad m, n, \mu, \nu \in \mathbb{N}_0; \quad (1)$$

$$|m, n\rangle = |m\rangle_a \otimes |n\rangle_b, \quad \langle \mu, \nu| = \langle \mu|_a \otimes \langle \nu|_b. \quad (2)$$

Here $|k\rangle_\alpha$ is the Fock-state of the resonator mode α with occupation number k , and $\mathcal{F}_{m,n|\mu,\nu}$ are elements of a field density matrix.

In our case, the beam atoms inside the resonator can be in two orthogonal energy states: lower $|d\rangle$ with energy E_d , and upper $|u\rangle$ with energy E_u . These two states collectively constitute a two-dimensional subspace \mathbb{C}_2 , within which all atomic transformations are described by the algebra of the following operators:

$$\sigma_z = |u\rangle\langle u| - |d\rangle\langle d|, \quad \sigma_+ = |u\rangle\langle d|, \quad \sigma_- = |d\rangle\langle u|. \quad (3)$$

When an atom in the beam propagates through one of the resonators with index $\alpha \in a, b$, then in accordance with the Jaynes-Cummings model, the evolution of such an atomic field system is described using the von Neumann equations in the rotating wave approximation [29]:

$$\frac{d\rho_{AF}}{dt} = i[V_\alpha, \rho_{AF}], \quad (4)$$

$$V_\alpha = \left(\frac{\omega_\alpha}{2} - \frac{E_u - E_d}{2\hbar} \right) \cdot \sigma_z + g_\alpha (\alpha^\dagger \sigma_- + \alpha \sigma_+), \quad (5)$$

where V_α is the interaction operator; density matrix ρ_{AF} is represented in the basis of atomic-field's states; α^\dagger and α are the operators of photon creation and annihilation inside the cavity mode α ; ω_α is the frequency of the mode of the resonator α ; real coefficient g_α characterizes the coupling between the mode and the passing atom.

The solution of equation (3) can be written using the operator exponent, since the interaction operators V_α corresponding to different moments of time commute:

$$\rho_{AF}(t') = e^{-iV_\alpha(t'-t)} \rho_{AF}(t) e^{iV_\alpha(t'-t)}. \quad (6)$$

Thus, evolution of the atom-field density matrix when an atom passes through a pair of resonators can be written as

$$\rho'_{AF} = U \rho_{AF}^{(0)} U^\dagger, \quad U = e^{-iV_b T_b} \cdot e^{-iV_a T_a}. \quad (7)$$

where $\rho_{AF}^{(0)}$ is the atom-field density matrix at the moment the atom enter the resonator α ; ρ'_{AF} is the density matrix at the moment the atom leaves the resonator b ; T_α is the time of propagation of an atom through the resonator α . Before the interaction begins, the atom of beam and the field are independent, so we can write:

$$\rho_{AF}^{(0)} = \rho_A \otimes \rho_F(0), \quad (8)$$

where ρ_A is the mixed state of the atom after pumping, and $\rho_F(0)$ is the state of the field before the start of interaction with the atom.

For simplicity, we will assume that the frequency of the atomic transition coincides with the frequencies of the modes of both resonators: $\hbar\omega_\alpha = \hbar\omega_b = E_u - E_d$. Then the evolution operator U in equation (6) can be represented in the following form:

$$U = \sum_{f,i} U_{fi} |f\rangle\langle i|, \quad f, i \in d, u; \quad (9)$$

$$U_{dd} = C_a \otimes C_b - S_a \otimes S'_b, \quad U_{uu} = C'_a \otimes C'_b - S'_a \otimes S_b, \quad (10)$$

$$U_{du} = -i(S'_a \otimes C_b + C'_a \otimes S'_b), \quad U_{ud} = -i(S_a \otimes C'_b + C_a \otimes S_b). \quad (11)$$

The second term in equations (9) corresponds to the re-emission of a photon from one resonator to another through the passing atom. Operators C_α , C'_α , S_α , and S'_α act in the subspace of mode states resonator α . Using the notation $\theta_k^\alpha = g_\alpha T_\alpha \sqrt{k}$, one can present their explicit forms:

$$C_\alpha |k\rangle_\alpha = \cos \theta_k^\alpha |k\rangle_\alpha, \quad S_\alpha |k\rangle_\alpha = \sin \theta_{k+1}^\alpha |k-1\rangle_\alpha, \quad (12)$$

$$C'_\alpha |k\rangle_\alpha = \cos \theta_{k+1}^\alpha |k\rangle_\alpha, \quad S'_\alpha |k\rangle_\alpha = \sin \theta_{k+1}^\alpha |k+1\rangle_\alpha. \quad (13)$$

We consider the case when the time of propagation of an atom through the resonators is short enough to neglect the relaxation processes for both the atom and the field. The relaxation and its effects will be taken into account later in the master equation, which describes the dynamics of the field over a long time interval, during which much more than one atom passes through the resonators.

3. Master equation

The dynamics of the micromaser field over a long time interval is described by the master equation [2, 9, 17]. We modify it for the case of a two-mode resonator, leaving the structure of the equation unchanged. That is, the first term on the right-hand side describes the transformation of the field due to interaction with the atoms of the beam, and the second term describes the decay of field modes:

$$\frac{d\rho_F}{dt} = \mathcal{I} (\langle U (\rho_F \otimes \rho_A) U^\dagger \rangle_{at} - \rho_F) - \sum_{\alpha=a,b} \frac{\gamma_\alpha}{2} (\alpha^\dagger \alpha \rho_F - 2\alpha \rho_F \alpha^\dagger + \rho_F \alpha^\dagger \alpha), \quad (14)$$

$$\rho_A = \xi_d |d\rangle\langle d| + \xi_u |u\rangle\langle u|. \quad (15)$$

The quantity \mathcal{I} characterizes the intensity of the atomic beam, and the constants γ_α are equal to the inverse lifetimes of a photon inside the resonator α . Averaging over atomic states in the first term occurs due to collapse of the atomic wave function after it leaves the second resonator. Thus, coupling with the field is destroyed.

It can be shown that in the master equation (14) there are no terms inducing the excitation of phase coherence between field states with different total numbers of photons in both modes. Physically, this can be explained by the fact that the emission or absorption of one photon while preserving the field phase occurs only with a change of atomic energy. In essence, coherence can arise only for a pair of atomic-field states in which the atom populates different levels, and corresponding terms in the master equation (14) are neglected during the trace over atomic variables. As a result, the field of a single-cavity single-atom maser in a stationary state is always an incoherent mixture of the Fock field states with a certain number of photons.

In the case of two resonators, the field is not a mix of the Fock states, since an atom can absorb a photon from the first resonator and emit it into the second, or vice versa. The atom enters and leaves the pair of resonators in the same state. Consequently, such a photon exchange process will induce the coherence between field states with the same total number of photons in the system. Formally, this will lead to non-zero off-diagonal elements of the density matrix $\mathcal{F}_{m,k-m|\mu,k-\mu}$, where k is the total number of photons in a pair of resonators.

The above reasoning allows us to split the field density matrix into non-zero blocks that describe excited field modes with a certain total number of photons k :

$$\rho_F = \rho_0 \oplus \rho_1 \oplus \rho_2 \oplus \dots, \quad (16)$$

$$\rho_k = \sum_{m,\mu=0}^k \mathcal{F}_{m,k-m|\mu,k-\mu} |m, k-m\rangle \langle \mu, k-\mu|. \quad (17)$$

In new notation, master equation (14) takes the form of a linear dynamic system for matrices ρ_k :

$$\frac{1}{\mathcal{I}} \frac{d\rho_k}{dt} = \mathcal{L}^\uparrow \rho_{k-1} + \mathcal{L}^o \rho_k + \mathcal{L}^\downarrow \rho_{k+1}, \quad \gamma_\alpha = \frac{\Gamma_\alpha}{\mathcal{I}}, \quad (18)$$

$$\mathcal{L}^\uparrow \rho_k = \xi_u U_{du} \rho_k U_{ud}^\dagger, \quad (19)$$

$$\mathcal{L}^o \rho_k = \xi_u U_{uu} \rho_k U_{uu}^\dagger + \xi_d U_{dd} \rho_k U_{dd}^\dagger - \rho_k - \sum_{\alpha=a,b} \frac{\gamma_\alpha}{2} [\alpha^\dagger \alpha, \rho_k], \quad (20)$$

$$\mathcal{L}^\downarrow \rho_k = \xi_d U_{ud} \rho_k U_{du}^\dagger + \sum_{\alpha=a,b} \gamma_\alpha \alpha \rho_k \alpha^\dagger, \quad (21)$$

where for any k linear maps \mathcal{L}^\uparrow act from the Hermitian matrix space ρ_k to the Hermitian matrix space ρ_{k+1} ; \mathcal{L}^o acts inside the Hermitian matrix space ρ_k ; \mathcal{L}^\downarrow acts from the Hermitian matrix space ρ_k to the Hermitian matrix space ρ_{k-1} .

We are interested in the case of stationary dynamics, in which the process of photons leaving the cavity is completely compensated by atomic pumping. However, the search for a stationary solution of equation (18) through the recurrence relation leads to the increasing number of unknown variables due to rank of matrices ρ_k . This problem can be solved for trapped states.

At a certain moment in time, while atoms propagate through the resonator, the number of photons reaches a maximum value and stops increasing. This effect occurs due to the integer value of the Rabi oscillations. That is, the atom has time to emit a photon into the mode and immediately absorb it while propagating through the resonator. In the case of two micromaser resonators, the condition for appearance of such trapped states must be written for each resonator α separately; it is expressed through solution (6):

$$g_\alpha T_\alpha \sqrt{N_\alpha + 1} = \pi k_\alpha, \quad k_\alpha \in \mathcal{N}, \quad (22)$$

where N_α is the maximum number of photons in the resonator α , after which the atoms in the upper level stop emitting a photon into the mode; k_α is the number of integer Rabi oscillations.

If condition (22) is satisfied for both resonators, then the number of photons k in a pair of resonators does not exceed the maximum value $N_a + N_b$. The matrix ρ_k rank in the case of trapping is determined by the number of all states $|m, k - m\rangle$ in which the sum of photons is equal to k and the occupation number of each mode does not exceed the maximum value N_α :

$$\text{rank}[\rho_k] = \min(N_\alpha, k) + 1 - k. \quad (23)$$

The number of non-zero matrices ρ_k becomes finite and equal to $N = N_a + N_b + 1$, and the first and last matrices have rank 1. The constraint of the sequence ρ_k allows us to solve the stationary master equation through the recurrence relation:

$$\frac{d\rho_k}{dt} = \mathcal{L}^\uparrow \rho_{k-1} + \mathcal{L}^o \rho_k + \mathcal{L}^\downarrow \rho_{k+1} = 0, \quad (24)$$

$$\rho_k = r_k + \mathcal{A}_k \rho_{k-1}, \quad \rho_0 = r_0, \quad (25)$$

$$\mathcal{A}_k = -(\mathcal{L}^o + \mathcal{L}^\downarrow \mathcal{A}_{k+1})^{-1} \mathcal{L}^\uparrow, \quad \mathcal{A}_N = 0, \quad (26)$$

$$r_k = -(\mathcal{L}^\uparrow + \mathcal{L}^\downarrow \mathcal{A}_{k+1})^{-1} \mathcal{L}^\downarrow r_{k+1}, \quad r_N = \rho_N, \quad (27)$$

where $\rho_N = \mathcal{F}_{N_a, N_b | N_a, N_b}$ is firstly equal to unity and then calculated using renormalization ρ_F .

In the next chapter, solution (25) of the stationary governing equation (24) is used to observe the entanglement between modes for different single-atom maser parameters.

4. Entanglement of resonator modes

By varying the parameters $\gamma_a, \gamma_b, \xi_u, N_a, k_a, N_b, k_b$, it is possible to distinguish four stationary regimes of a single-atom maser, which allow one to observe its main qualitative properties:

- (1) Both resonators are high-Q, and the beam consists of atoms at the upper level only;
- (2) Both resonators are high-Q, and the beam consists of atoms at the upper and lower levels;
- (3) The first resonator is high-Q, the second is low-Q, and the beam consists mainly of atoms at the upper level;
- (4) The first resonator is low-Q, the second is high-Q, and the beam consists mainly of atoms at the upper level.

Let us assume that each mode can be excited only up to the one-photon state $N_a = N_b = 1$. In this case, the density matrix contains three elements: $\rho_0[1 \times 1]$, $\rho_1[2 \times 2]$ and $\rho_2[1 \times 1]$. Besides, let $k_a = k_b = 1$, that is, the atom has time to emit and absorb a photon in each mode only once. Explicit form of the density matrices are follow:

$$\rho_0 = \left(\mathcal{F}_{00|00} \right), \quad \rho_1 = \begin{pmatrix} \mathcal{F}_{01|01} & \mathcal{F}_{01|10} \\ \mathcal{F}_{10|01} & \mathcal{F}_{10|10} \end{pmatrix}, \quad \rho_2 = \left(\mathcal{F}_{11|11} \right). \quad (28)$$

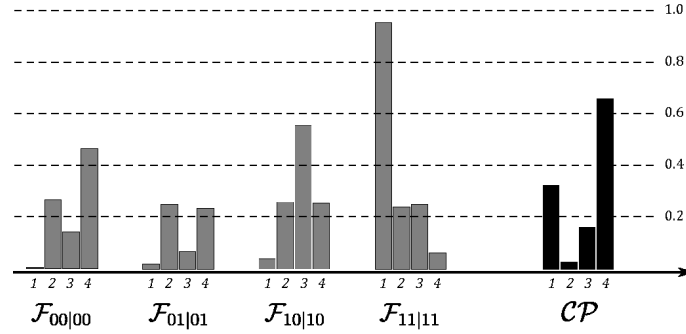


FIG. 2. Population diagram of the field density matrix. The gray bars show the value of the diagonal elements $\mathcal{F}_{m,n|\mu\nu}$, the numbers under the bars indicate the regime from the list. The black bars show the coherence parameters. The parameters for which a stationary solution was evaluated are given in the table above the graph.

TABLE 1. The parameters of four regimes for which a stationary solution (25) was evaluated

regime	ξ_d	ξ_u	γ_a	γ_b
(1)	0	1	10^{-3}	10^{-3}
(2)	0.5	0.5	10^{-3}	10^{-3}
(3)	0.2	0.8	10^{-3}	1
(4)	0.2	0.8	1	10^{-3}

Figure 2 shows the results from which we can make a conclusion about the conditions for the emergence of a coherence between the states $|0, 1\rangle$ and $|1, 0\rangle$ in the matrix ρ_1 . No other cases are generated in the system, since the rank of the matrices ρ_0 and ρ_2 is equal to one. To estimate the coherence, we consider the product \mathcal{CP} :

$$\mathcal{C} = \frac{|\lambda_2 - \lambda_1|}{\lambda_2 + \lambda_1}, \quad (29)$$

where λ_1 and λ_2 are the eigenvalues of the matrix ρ_1 .

$$\mathcal{P} = 1 - \frac{|\mathcal{F}_{0,1|0,1} - \mathcal{F}_{1,0|1,0}|}{\mathcal{F}_{0,1|0,1} + \mathcal{F}_{1,0|1,0}}. \quad (30)$$

The parameter \mathcal{C} tends toward unity if ρ_2 can be represented as the pure state density matrix, while the parameter \mathcal{P} characterizes the degree of mutual excitation of both modes of a maser and tends to zero if only single of the states $|0, 1\rangle$ and $|1, 0\rangle$ is populated.

Let us focus to main results. Firstly, in the second regime, the coherence is approximately zero (black bars in the Fig. 2), despite the high quality of the resonators. We explain this effect by the fact that coherence is formed by atoms at the lower level and atoms at the upper level with the opposite phases. If all states of the field are populated equally, as in this regime, then the total contribution to coherence turns out to be practically empty. If the beam consists of atoms only at the upper level, as in the first regime, then coherence between the states $|0, 1\rangle$ and $|1, 0\rangle$ arises, but these states are practically unpopulated compared to the state $|1, 1\rangle$. Secondly, in the fourth regime, the coherence is significant increased (black bars), and the levels $|0, 1\rangle$ and $|1, 0\rangle$ are populated equally (gray bars). It is worth noting that the condition for the coherence occurrence is the low quality factor of the first resonator into which the atom flies, while the lifetime of photons in the second resonator should be long. We explain this by the fact that the atoms at the upper level compensate for the decay process of the field in the first resonator, emit photons into it, and enter the second resonator already in a state of superposition of two levels.

In addition to observing coherence within a subspace of states with the same number of photons, we looked for conditions under which two field modes approach to the maximum entanglement. To estimate this one, we used the entanglement entropy [29] and denoted it by \mathcal{S} . Micromaser generates a mix of the field quantum states, therefore we should calculate entropy for each one and then sum it using the probabilities. Moreover, since the density matrix is a direct sum (16), the entropy can be calculated for each of the terms ρ_k independently.

$$\mathcal{S} = \sum_{k=0}^{N_a+N_b} \left(\sum_{j=1}^{\text{rank}[\rho_k]} p_{k,j} \mathcal{S}_{k,j} \right), \quad \mathcal{S}_{k,j} = - \sum_{q=1}^{\text{rank}[\rho_k]} \lambda_{k,j,q} \ln \lambda_{k,j,q}, \quad (31)$$

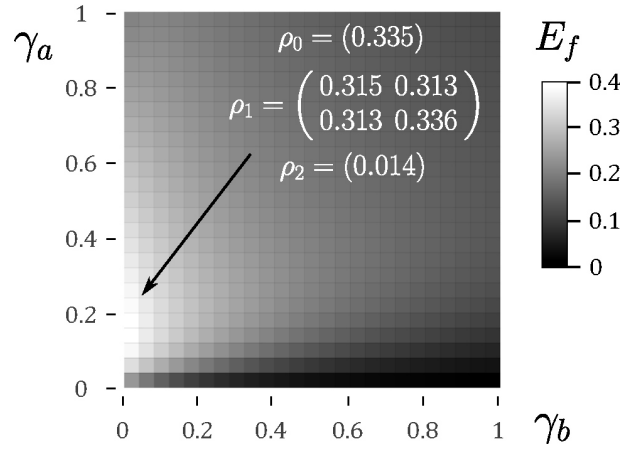


FIG. 3. The dependence of the parameter \mathcal{S} defined by equation (30) of the maser's double-mode field on the quality factor of the resonators. The calculation was made with the following values: $\xi_u = 1$, $\xi_d = 0$, $k_a = k_b = 3$, $N_a = N_b = 1$. The figure contains the density matrix when the maximum entanglement $\mathcal{S} \approx 0.4$ is reached.

where $\mathcal{S}_{k,j}$ is the bipartite von Neumann entropy for j -th quantum state $|\Psi_{k,j}\rangle$ in the mix described by the density matrix ρ_k , symbol $\lambda_{k,j,q}$ denotes the q -th eigenvalue of the matrix $\rho_{k,j}^{\text{Tr}}$.

$$\rho_k = \sum_{j=1}^{\text{rank}[\rho_k]} p_{k,j} \rho_{k,j}, \quad \rho_{k,j} = |\Psi_{k,j}\rangle \langle \Psi_{k,j}|, \quad (32)$$

$$\rho_{k,j}^{\text{Tr}} = \sum_m \langle m|_a \rho_{k,j} |m\rangle_a. \quad (33)$$

Figure 3 shows a graph of the entanglement entropy dependence on the relaxation constants of the resonators. When plotting the graph (as in the study of coherence), the case of trapped states with $N_a = N_b = 1$ is considered, the beam atoms are at the upper level, and the number of Rabi oscillations is set to new: $k_a = k_b = 3$. With these parameters, entanglement appears especially clearly.

Note that entanglement occurs when the quality factor of the first resonator is much less than the quality factor of the second resonator. The peak of entanglement at a certain value of the field relaxation rate in the first resonator γ_a seems to be curious, as it might show that there is a certain balance between the pumping and relaxation processes, in which the modes interact with the beam atoms as a single quantum system.

5. Conclusion

In this work, we have proposed the fundamental theory of a single-atom maser with two resonators, the field of which is pumped by a sparse atomic beam. In the case of trapped field states, a simple form of recurrence relation for the stationary solution of the master equation of the single-atom maser is obtained. The properties of the stationary solution indicate the existence of coherence between the states of a pair of modes with the same total number of photons. This effect was absent in a single-cavity single-atom maser, in which the stationary field is represented as an incoherent mixture of the Fock field states. The predicted coherence in our case leads to the possibility of generating entangled states, which was demonstrated by evaluating the entanglement entropy. In this work, we consider only one special case of trapped states of a pair of resonators, which is the simplest for qualitative research of the properties of the proposed quantum system. Other trapped states may exhibit quantum properties that were not discovered in this work, which opens the prospect for further research.

References

- [1] Scully M.O., Zubairy M.S. *Quantum Optics*. 13-th chapter: Theory of the micromaser, Cambridge: Cambridge University Press, 1997, P. 383–401.
- [2] Walter H. One-atom maser and other experiments on cavity quantum electrodynamics. *Physics–Uspekhi*, 1996, **39** (7), P. 727–743.
- [3] Jaynes E.T., Cummings F.W. Some New Features of Photon Statistics in a Fully Quantized Parametric Amplification Process. *Proceedings of the IEEE*, 1963, **51** (1), P. 89–109.
- [4] Filipowicz P., Javanainen J., Meystre P. Theory of a microscopic maser. *Phys. Rev. A*, 1986, **34**, P. 3077–3087.
- [5] Reshetov V.A., Yevseyev I.V. On the polarization properties of the micromaser pumped by the atoms with degenerate levels. *Las. Phys. Lett.*, 2004, **1**, P. 124–133.
- [6] Raimond J.M., Brune M., Haroche S. Manipulating quantum entanglement with atoms and photons in a cavity. *Rev. Mod. Phys.*, 2001, **73**, P. 565–582.
- [7] Huver S.D., Wildfeuer C.F., Dowling J.P. Entangled Fock states for robust quantum optical metrology, imaging, and sensing. *Phys. Rev. A*, 2008, **78**, 063828/1-5.
- [8] Walther H., Varcoe B.T.H., Englert B., Becker T. Cavity quantum electrodynamics. *Reports on Progress in Physics*, 2006, **69**, P. 1325–1382.

- [9] Reshetov V.A., Popov E.N., Yevseyev I.V. One-atom maser pumped by the atoms at mixed states. *Las. Phys. Lett.*, 2010, **7**, P. 218–224.
- [10] Popov E.N., Reshetov V.A. Controllable Source of Single Photons Based on a Micromaser with an Atomic Beam without Inversion. *JETP Letters*, 2020, **111**, P. 727–733.
- [11] Jin L., Pfender M., Aslam N., Neumann P., Yang S., Wrachtrup J., Liu R.-B. Proposal for a room-temperature diamond maser. *Nature Communications*, 2015, **6**, 8251.
- [12] Varcoe B.T.H., Brattke S., Weidinger M., Walther H. Preparing pure photon number states of the radiation field. *Nature*, 2000, **403**, P. 743–746.
- [13] Miroshnichenko G.P. Single photon sources and detectors based on micro- and nano-optical structures. *Nanosystems: Physics, Chemistry, Mathematics*, 2011, **2** (1), P. 47–63.
- [14] Weidinger M., Varcoe B.T.H., Heerlein R., Walther H. Trapping States in the Micromaser. *Phys. Rev. Lett.*, 1999, **82**, P. 3795–3798.
- [15] Lugiato L.A., Scully M.O., Walter H. Connection between microscopic and macroscopic maser theory. *Phys. Rev. A*, 1987, **36**, P. 740–743.
- [16] Meschede D., Walther H., Müller G. One-Atom Maser. *Phys. Rev. Lett.*, 1985, **54**, P. 551–554.
- [17] Yu D., Kwek L.C., Amico L., Dumke R. Theoretical description of a micromaser in the ultrastrong-coupling regime. *Phys. Rev. A*, 2017, **95** (5), 53811/1–10.
- [18] Sokolova A.A., Fedorov G.P., Il'ichev E.V., Astafiev O.V. Single-atom maser with an engineered circuit for population inversion. *Phys. Rev. A*, 2021, **103** (1), 013718/1–9.
- [19] Sokolova A.A., Kalacheva D.A., Fedorov G.P., Astafiev O.V. Overcoming photon blockade in a circuit-QED single-atom maser with engineered metastability and strong coupling. *Phys. Rev. A*, 2021, **107** (3), L031701/1–6.
- [20] Jin L., Pfender M., Aslam N., Neumann P., Yang S., Wrachtrup J., Liu R. Proposal for a room-temperature diamond maser. *Nature Communications*, 2015, **6** (1), 8251/1–8.
- [21] Will E., Masters L., Rauschenbeutel A., Scheucher M., Volz J. Coupling a Single Trapped Atom to a Whispering-Gallery-Mode Microresonator. *Phys. Rev. Lett.*, 2021, **126** (23), 233602/1–5.
- [22] Garziano L., Ridolfo A., Miranowicz A., Falci G., Savasta S., Nori F. Atoms in separated resonators can jointly absorb a single photon. *Scientific Reports*, 2020, **10** (1), 21660.
- [23] Rosenblit M., Horak P., Fleming E., Japha Y., Folman R. Design of microcavity resonators for single-atom detection. *J. of Nanophotonics*, 2007, **1** (1), 011670.
- [24] Benoist T., Bruneau L., Pellegrini C. Quantum trajectory of the one atom maser. ArXiv:2403.20094 [math-ph], 2024.
- [25] Vatutin A.D., Miroshnichenko G.P., Trifanov A.I. Hidden polarization in open quantum systems. *Nanosystems: Phys. Chem. Math.*, 2023, **14** (2), P. 626–632.
- [26] Muminov Z.I., Aktamova V.U. The point spectrum of the three-particle Schrödinger operator for a system comprising two identical bosons and one fermion on Z . *Nanosystems: Phys. Chem. Math.*, 2024, **15** (4), P. 438–447.
- [27] Goncharov F.M., Pervushin B.E., Nasedkin B.A., Goncharov R.K., Yashin D.A., Gellert M.E., Sulimov D.V., Morozova P.A., Filipov I.M., Adam I.A., Chistiakov V.V., Samsonov E.O., Egorov V.I. Increase of signal to reference ratio for phase compensation in continuous-variable quantum key distribution systems. *Nanosystems: Phys. Chem. Math.*, 2023, **14** (1), P. 59–68.
- [28] Melikhova A.S., Popov A.I., Blinova I.V., Popov I.Y. Mathematical model of weakly coupled spherical resonator chains under the influence of external magnetic field. *Nanosystems: Phys. Chem. Math.*, 2024, **15** (2), P. 155–159.
- [29] Nielsen M.A., Chuang I.L. *Quantum Computation and Quantum Information*. 10th Anniversary Edition, Cambridge: Cambridge University Press, 2010, P. 510–519.

Submitted 5 July 2024; revised 29 March 2025; accepted 6 April 2025

Information about the authors:

Eugeniy N. Popov – Laboratory of Quantum Processes and Measurements, Center of Mathematics, ITMO University, Kroverkskiy, 49, St. Petersburg, 197101, Russia; ORCID 0000-0003-0223-097X; enp-tion@yandex.ru

Alexander I. Trifanov – Center of Mathematics, ITMO University, Kroverkskiy, 49, St. Petersburg, 197101, Russia; ORCID 0000-0002-5109-2086; alextrifanov@gmail.com

Maria A. Moskalenko – Center of Mathematics, ITMO University, Kroverkskiy, 49, St. Petersburg, 197101, Russia; moskalenko.mary@gmail.com

Vladimir A. Reshetov – Togliatti State University, Belorusskaya str., 14, Togliatti, 445667, Russia; ORCID: 0009-0000-6418-6121; vareshetov@tlt.su.ru

Conflict of interest: the authors declare no conflict of interest.

Simulation of a quasi-ballistic quantum-barrier field-effect transistor based on GaAs quantum wire

Dmitry V. Pozdnyakov^{1,a}, Andrei V. Borzdov^{1,b}, Vladimir M. Borzdov^{1,c}

¹Belarusian State University, Minsk, Belarus

^apozdneyakovdv@bsu.by, ^bborzdovav@bsu.by, ^cborzdov@bsu.by

Corresponding author: D. V. Pozdnyakov, pozdneyakovdv@bsu.by

PACS 73.21.Hb; 73.63.Nm; 85.30.De; 85.35.Be

ABSTRACT A new constructive solution of field-effect transistor (FET) with a Schottky barrier in a conducting channel has been identified. The FET is a quasi-ballistic quantum-barrier transistor based on a cylindrical undoped GaAs quantum wire in Al₂O₃ matrix surrounded by a cylindrical metallic gate. A technique for determining the optimal variation of the semiconductor quantum wire diameter along its axis has been developed. The optimal dependence of the nanowire diameter on the spatial coordinate along its axis has been determined providing the possibility of both the elimination of quantum barrier for electrons by the positive gate voltage and the minimization of transistor channel electrical resistance in contrast to a typical FET with a Schottky barrier in its conducting channel. The current-voltage characteristics of the transistor based on GaAs quantum wire with an optimal cross-section have been calculated within the framework of a developed combined physico-mathematical model describing the electron transport in the transistor channel. This model takes into account the nonparabolicity of the semiconductor band structure, the quantum-dimensional effects, and such secondary quantum effects as the collisional broadening and displacement of electron energy levels.

KEYWORDS field-effect transistor, semiconductor quantum wire, quasi-ballistic electron transport.

FOR CITATION Pozdnyakov D.V., Borzdov A.V., Borzdov V.M. Simulation of a quasi-ballistic quantum-barrier field-effect transistor based on GaAs quantum wire. *Nanosystems: Phys. Chem. Math.*, 2025, **16** (2), 183–191.

1. Introduction

The basic element of digital integrated electronics, which performs the role of a normally open switch, is still a silicon metal-insulator-semiconductor field-effect transistor (MIS FET) with an induced channel [1]. Fulfillment of three basic requirements for such kind of switching elements for further increasing the degree of integration of the micro- and nanoelectronics component base, in particular, reducing geometric dimensions, increasing switching speed, and reducing dissipated power, forces the developers of this kind of device structures to reduce the values of operating voltages on the gate and drain of the transistor [2,3], to select alternative materials for its conductive channel [4–9], to use other principles for controlling its switching [10, 11], and also to search new design and topological solutions [3–19]. At least most of the above requirements can be satisfied by a ballistic nanotransistor with a cylindrical gate, which has the following features [3, 8, 16–20]: 1) the cylindrical conducting channel contains a one-dimensional electron gas under the electric quantum limit conditions; 2) the conductive channel is formed of a very high-tech material with a very high electron mobility; 3) the material of the insulating matrix of the transistor is technologically compatible with the materials of its conductive channel and electrodes; 4) as in a tunnel FET, the height and width of the potential barrier for charge carriers is directly controlled by the gate voltage; 5) in the open state of the transistor its electrical conductivity achieves the maximum possible quantum-mechanical value $g\pi^{-1}\hbar^{-1}e^2$ [21], where g is the degree of electron gas degeneracy, \hbar is the reduced Planck constant, e is the absolute value of the electron charge.

In due time in scientific papers [22, 23] and monograph [24], a design and topological solution satisfying the above mentioned conditions was proposed in the form of a normally open transistor switch based on Al_XGa_{1-X}As with a variable fraction of aluminum in the semiconductor lengthwise the conductive channel of the transistor with optimal geometry. As it was shown in [23, 24], the proposed solution practically achieves the maximum possible theoretical values for such key parameters of the transistor as the subthreshold swing, the channel conductivity and the ratio of electric currents in the open and closed states. The geometry of the transistor considered in [22–24] meets the current production capabilities in the electronics industry. At the same time the necessity of smooth variation of the stoichiometry of Al_XGa_{1-X}As lengthwise the transistor conductive channel, taking into account the possibilities of both molecular beam epitaxy and other methods of forming semiconductor structures with specified physical and chemical properties, limits the range of possible structural and topological solutions for such device structures. In particular, this is why the vertical transistor was considered in [22–24]. But it is possible to control the electron potential energy profile in the conductive channel

of a quantum-barrier transistor not only by changing the stoichiometry of the ternary semiconductor quantum wire, but also by varying its diameter along the wire axis, which determines the local position of the electron subband levels in the semiconductor relative to the bottom of its conduction band [22–24]. And such a method of profiling the effective potential energy of electrons in the conductive channels of quantum-barrier transistors, firstly, removes the limitation on the production of the transistors only in the vertical design and, secondly, expands the range of semiconductors that could be used as base materials for the conducting channels of such kind of device structures.

Thus, in view of the above, the purpose of this work is to optimize a number of topological parameters of a quasi-ballistic FET with a cylindrical metallic gate and one-dimensional electron gas in the conducting channel based on a cylindrical undoped GaAs quantum wire with a variable cross-section lengthwise the conductive channel of the transistor, as well as to calculate its current-voltage characteristics (CVC).

2. Theory

As a starting point, let's consider the design of a vertical ballistic quantum-barrier FET proposed in refs. [22–24]. Its schematic view is shown in Fig. 1.

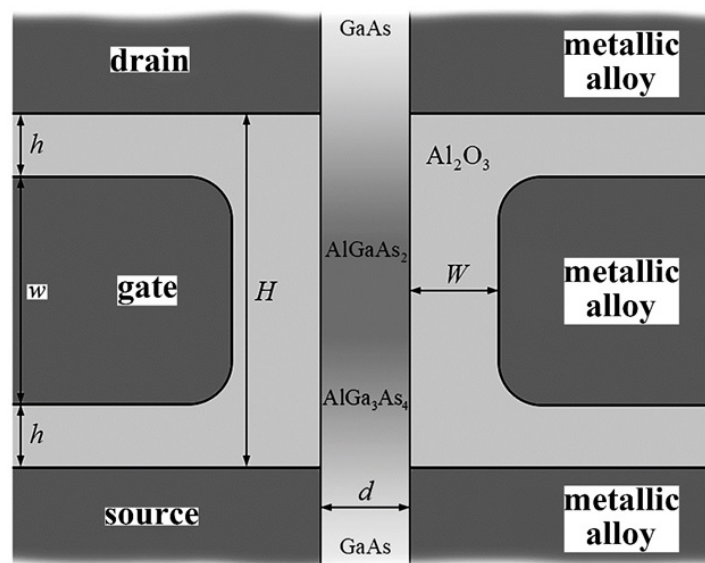


FIG. 1. Cross-section of the transistor by a plane passing through its longitudinal axis of symmetry ($W = 3$ nm, radius of rounding of the gate corner regions is 1 nm) [23, 24]

But in contrast to [23, 24], in which the selection of parameters $d = 10$ nm, $H = 30$ nm, $w = 24$ nm and $h = 3$ nm of a transistor with optimal geometry was justified, a transistor with varying diameter should not have such a short conductive channel. The point is that according to [25], the varying cross section of the semiconductor quantum wire causes the de Broglie waves of electrons to be reflected from regions with varying geometry. To minimize this effect, the changing cross-section region should be as extended as possible. However, in this case instead of the ballistic regime of electron transport in the transistor channel, a quasi-ballistic or even diffusive (diffuse) regime takes place [26, 27] with a sharp drop in the values of channel conductivity and saturation current. In a GaAs quantum wire with a diameter of 10 nm and temperature of 300 K, the average free path lengths for electrons being scattered by polar optical and acoustic phonons are minimal for near-zero kinetic energy of electrons and their energies slightly higher than the polar optical phonon energy (35.5 meV), and according to calculations are respectively about 36 and 28 nm in the regime of current saturation considering the Pauli prohibition principle, the nonparabolicity of semiconductor band structure and the secondary quantum effects. According to [26, 27], if the length of the conducting channel of the transistor is 30 nm or less then almost all electrons transfer through the channel in the ballistic regime. Taking into account all aforementioned, the compromise length of the transistor channel should be of such a minimum possible value, which for the majority of particles from the electron ensemble, on the one hand, corresponds to the transport regime not worse than quasi-ballistic, and on the other hand, as much as possible ensures the accuracy of the Wentzel-Kramers-Brillouin approximation [28] in the quasi-classical description of the one-dimensional longitudinal motion of electrons as much as possible in large regions of the conductive channel of the transistor [29], when one can neglect the reflection of the de Broglie waves from regions with spatially varying potential energy. According to the theory developed in [25], it is enough to increase the length H of the conductive channel of the transistor based on GaAs quantum wire by a factor of 3 to minimize the coherent reflection of most electrons from the classically accessible regions for them in the channel. So it is reasonable to choose

the values of the geometrical parameters of the transistor as follows: $H = 100$ nm, $w = 30$ nm, $h = 35$ nm, $d = d(z)$ ($d_0 = d(0) = d(H) = 10$ nm).

To determine the optimal dependence of the GaAs quantum wire diameter on the z coordinate along its axis ($z = 0$ corresponds to the beginning of the conductive channel of the transistor at the source boundary, $z = H$ corresponds to its end at the drain boundary), it is first necessary to find the distribution of the electric potential $\varphi(r, z)$ in the transistor structure at the defined values of the voltage at the drain ($V_D = 0$) and at the gate V_G (the voltage at the source is assumed to be always equal to zero). It is necessary to calculate the dependence of $\varphi(r, z)$ under such conditions for the following reasons: first, at zero potential at the source and drain, the minimum possible voltage applied to the gate should completely eliminate the potential barrier in the conductive channel of the transistor with the formation of flat subbands and almost unity probability of coherent transfer of electrons through the source-drain region over the entire range of their energy; second, at zero potential at the gate and nominal voltage at the drain, the electric current in the conductive channel of the transistor should be vanishingly small for both transfer of the particles over the barrier and their tunneling through it. These two contradicting requirements can be resolved for some single value of the reference gate voltage V_{G0} . In [22], it was proposed to choose a typical value of V_{G0} equal to 0.5 V for transistors with one-dimensional conducting channels [3, 19, 20]. However, in contrast to [22], according to [23, 24], higher values of electrophysical parameters and electrical characteristics of the nanotransistor can be obtained at a lower value of the reference gate voltage ($V_{G0} = 0.4$ V) due to the consideration of a device with optimal geometrical parameters. Taking it into account, it is reasonable to choose the reference gate voltage equal to 0.4 V.

In the case under consideration, the spatial distribution of the electric potential in the conductive channel of the transistor structure shown in figure 1 can be obtained by numerical solution of the Poisson equation in cylindrical coordinates. In this case, for significant reduction of the computational complexity of $\varphi(r, z)$ calculation, as in [22–24], a number of standard approximations can be applied. First, taking into account a small difference between the values of relative dielectric permittivity of Al_2O_3 [30] and GaAs [31], one can neglect a small jump in the value of the normal component of the electric field strength at the boundary of $\text{Al}_2\text{O}_3/\text{GaAs}$, which only slightly affects the potential energy of electrons in the electric field through the local displacement of their energy levels in the semiconductor quantum wire. Second, the electric charge of electrons in the conductive channel of the transistor can be neglected. In the closed state of the transistor, neglecting the mobile charge is obviously quite justified. In the open state of the transistor, the maximum possible electric current flowing in its conducting channel, according to the estimates made for the considered geometry of the structure and the position of the Fermi level ($E_F = 0.2$ eV [22–24]) relative to the bottom of the GaAs conduction band in the source and drain regions of the transistor, creates an additional rise in the potential barrier between the source and the gate in the maximum by about 30 mV [22–24]. This results in a shift of no more than 60 mV in the transistor CVC by V_G ($V_G \rightarrow V_G + 0.06$ V). Whereas the above approximation frees from the necessity of iterative self-consistent solution of two-dimensional Schrödinger and Poisson equations for each of the calculated points of the transistor CVC. The result of the accepted approximations is the possibility of reduction of the Poisson equation to the Laplace equation in the form of

$$\frac{\partial^2 \phi}{\partial r^2} + \frac{1}{r} \frac{\partial \phi}{\partial r} + \frac{\partial^2 \phi}{\partial z^2} = 0 \quad (1)$$

with corresponding Dirichlet boundary conditions at the Al_2O_3 /“metallic alloy” boundaries, Neumann boundary conditions at the boundary of the modeling domain in Al_2O_3 and at the symmetry axis of the conductive channel of the transistor taking into account that $\varphi \sim r^2$ at $r \rightarrow 0$ for any values of z .

After solving the Laplace equation, the electron effective potential energy $u_\varphi(z)$ in an electric field can be estimated by means of standard methods of quantum mechanics, namely in the framework of perturbation theory [20, 32, 33]:

$$u_\varphi(z) = -\frac{8e}{d^2(z)J_1^2(\beta_{10})} \int_0^{d(z)/2} \phi(r, z) J_0^2\left(\frac{2\beta_{10}r}{d(z)}\right) r dr. \quad (2)$$

In equality (2), J_n is the Bessel function of the first kind of n -th order, $\beta_{10} = 2.404825558$ [32]. Here, as in other studies [20, 22–24, 27, 32–34], the approximation of the $\text{Al}_2\text{O}_3/\text{GaAs}$ boundary being impermeable for electrons (infinitely high potential barrier) and the approximation of the electric quantum limit are considered. In the latter one, the excited quantum states in Γ valley and quantum states in L and X valleys of the semiconductor quantum wire are not taken into account that in due time was justified in [22–24]. Under the conditions of the electric quantum limit almost all electrons are in the ground quantum state of Γ valley of GaAs. The transverse component of their energy E_0 can be calculated by the formula [20, 22–24, 31, 34–36].

$$E_0(z) = \frac{1}{2\alpha} \left(\sqrt{1 + \frac{8\alpha\beta_{10}^2 \hbar^2}{m^* d^2(z)}} - 1 \right), \quad (3)$$

where m^* is the effective mass of electron in the GaAs conduction band, α is its nonparabolicity parameter.

Calculation of the optimal dependence $d = d(z)$ under the flat subband condition for the ground quantum state in Γ valley of GaAs at $\varphi_D = \varphi_S = 0$ and $\varphi_G = V_G = V_{G0}$ is carried out by solving the equation [22–24].

$$U(z) = u_\phi(z) + \Delta E_0(d(z)) = u_\phi(z) + (E_0(d(z)) - E_0(d(0))) = 0. \quad (4)$$

The numerical solution of equation (4) allows the profile $d(z)$ to be recovered, at which, for a given dependence $u_\varphi(z)$, the flat subband transfer regime is provided for electrons in the ground quantum state of GaAs over the entire length of the transistor channel ($U(z) \equiv 0$). Fig. 2 shows the result of such a numerical calculation for $V_{G0} = 0.4$ V.

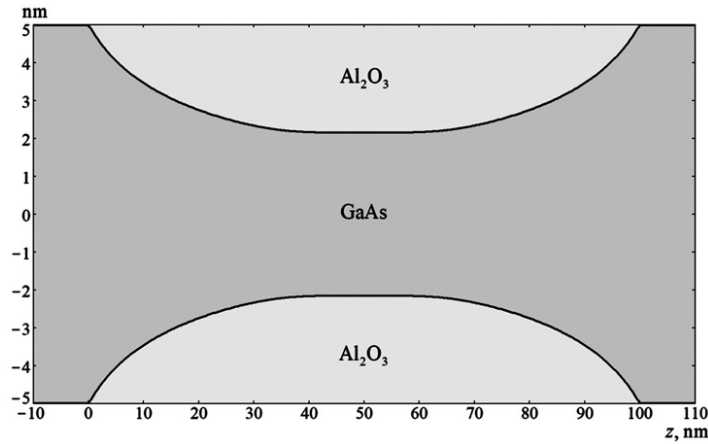


FIG. 2. Optimal dependence of GaAs quantum wire diameter along the transistor channel from the source to the drain

Fig. 3 shows a number of dependences characterizing the electron potential energy profiles lengthwise the transistor channel. In particular, it follows from this figure that, despite the significant voltage applied to the drain, the region of the conductive channel of the transistor near the source is still in the regime of the flat subband due to the screening of the drain field by the gate. At such a shape of the bottom of the semiconductor conduction band in the transistor the electron transfer from the source to the drain is ensured with practically unit probability even at $E \rightarrow E_0(0)$.

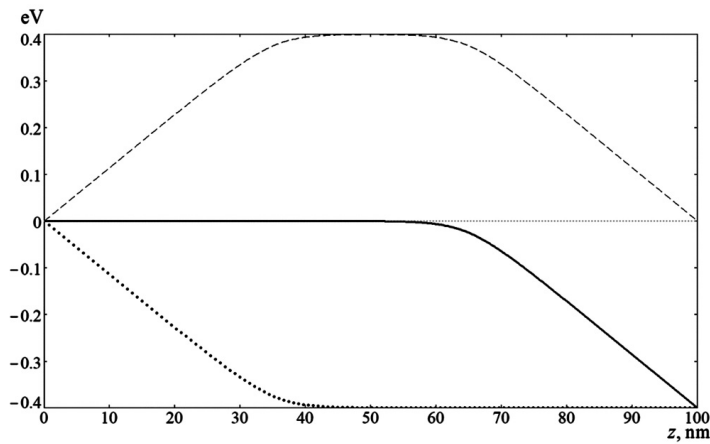


FIG. 3. Variation of electron potential energy profiles along the conductive channel of the transistor from source to drain: dashed curve – potential barrier ΔE_0 in the absence of electric fields ($V_D = V_G = 0$); dotted curve – the potential energy of electrons in the electric field u_φ at $V_D = V_G = V_{G0} = 0.4$ V; solid curve – total potential energy of electrons U at $V_D = V_G = V_{G0} = 0.4$ V

For the considered topology of the transistor structure the calculation of the absolute value of the electric current I_e flowing in the conducting channel can be carried out within the Landauer-Buttiker formalism [14, 21, 22] using the approximation [23, 24].

$$I_e = \frac{e}{\pi\hbar} \int_0^\infty (f_{\text{FD}}(E, E_F - E_0(0)) t_{\text{sc}}^{\text{S}}(E) - f_{\text{FD}}(E, E_F - E_0(0) - eV_D) t_{\text{sc}}^{\text{D}}(E)) t_{\text{ch}}(E) dE, \quad (5)$$

where E is the level of electron kinetic energy in the source, t_{ch} is the probability of coherent transfer of electron through the region between the transistor electrodes, $t_{\text{sc}}^{\text{S/D}}$ is the probability of the electron transfer without scattering through classically accessible regions in the conducting channel from the source (S) or drain (D) side.

To find the value of t_{ch} at a defined value of E , in general, the Schrödinger equation should be numerically solved with appropriate boundary conditions. However, its solution, taking into account the effects of nonparabolicity of the semiconductor band structure, is an extremely difficult problem from the computational point of view [36]. But, taking

into account a number of rigorous generalizations obtained in [36] for the boundary conditions imposed on the wave function when nonparabolicity effects are taken into consideration, it is possible to calculate the dependence $t_{ch}(E)$ in another way, in particular, by means of the transfer-matrix method [34, 37, 38]. For this purpose the entire region from the source ($z = 0$) to the drain ($z = H$) of the transistor is divided into a large number of Q ($q = 0, 1, \dots, Q$) intervals ($z_q - \Delta z/2, z_q + \Delta z/2$) of equal width $\Delta z = H/Q$, in each of which the dependence $U(z)$ is replaced by the constant values of $U_q = U(z_q)$ ($\forall f : f_q = f(z_q)$). That is, the dependence of the potential energy of electrons U in the transistor channel on the coordinate z is replaced by its piecewise stepwise approximation U_q . In such a case, applying the transfer-matrix method, the dependence $t_{ch}(E)$ can be rigorously calculated from U_q [36] with much higher accuracy than through the finite-difference approximation of the one-dimensional Schrödinger equation on the same spatial grid $\{z_q\}$ [22–24, 34, 37, 38]:

$$t_{ch}(E) = 1 - \left| \frac{B(E)}{A(E)} \right|^2, \quad (6)$$

$$\begin{pmatrix} A(E) \\ B(E) \end{pmatrix} = \left(\prod_{q=0}^{Q-1} \mathbf{M}_q(E) \right) \begin{pmatrix} 1 \\ 0 \end{pmatrix}, \quad (7)$$

$$\mathbf{M}_q = \frac{1}{2} \begin{pmatrix} \left(1 + \frac{m_q^* k_{q+1}}{m_{q+1}^* k_q} \right) \exp(-ik_q \Delta z) & \left(1 - \frac{m_q^* k_{q+1}}{m_{q+1}^* k_q} \right) \exp(-ik_q \Delta z) \\ \left(1 - \frac{m_q^* k_{q+1}}{m_{q+1}^* k_q} \right) \exp(ik_q \Delta z) & \left(1 + \frac{m_q^* k_{q+1}}{m_{q+1}^* k_q} \right) \exp(ik_q \Delta z) \end{pmatrix}, \quad (8)$$

$$m_q^* = m^* \left(\frac{(E - U_q)^2}{\Gamma_0^2 + (E - U_q)^2} \right)^{1/2} \left(\frac{(E - U_q)^2 (\gamma_q + 2\alpha(E - U_q))}{(\Gamma_0 + (\Gamma_0^2 + (E - U_q)^2)^{1/2})^2} + \frac{\Gamma_0 (2\gamma_q + 3\alpha(E - U_q))}{\Gamma_0 + (\Gamma_0^2 + (E - U_q)^2)^{1/2}} \right), \quad (9)$$

$$\gamma_q = 1 + 2\alpha E_0 (d_q) = \sqrt{1 + \frac{8\alpha\beta_{10}^2 \hbar^2}{m^* d_q^2}}, \quad (10)$$

$$k_q = \hbar^{-1} \left(\frac{2m^* |E - U_q| (E - U_q) (\gamma_q + \alpha(E - U_q))}{\Gamma_0 + (\Gamma_0^2 + (E - U_q)^2)^{1/2}} \right)^{1/2}. \quad (11)$$

In the presented equations, $\Gamma_0 = 10$ meV is a parameter characterizing the average value for the collisional broadening and displacement of the energy levels in the conductive channel of the transistor at temperature $T = 300$ K, which is calculated within the framework of the theory developed in manuscripts [23, 39–42], when considering the scattering of electrons by polar optical and acoustic phonons.

The dependence of $t_{sc}(E)$ can be estimated by Monte Carlo simulation of electron transport in classically accessible regions ($\forall z_q : U_q < E$) [37] applying rather simple algorithm. After casting the value of energy E for an electron injected into the transistor channel according to the Fermi-Dirac distribution function in the source or drain, it is supposed that the particle has overcome the classically accessible regions between the source and drain if during the time of simulation of its motion and scattering, taking into account the occupancy of the final quantum states according to the Pauli prohibition principle, it has achieved the boundary of the potential barrier in the tunneling regime or the boundary of the opposite electrode of the transistor in the case of over-barrier transport. Otherwise, if the electron has left the modeling region, returning back to the injection region, it is considered as reflected particle. To obtain a smooth and stable dependence $t_{sc}(E)$ with respect to the number of simulated particle trajectories, at least approximately 10 million simulation histories should be accumulated.

3. Calculation of the transistor CVCs and discussion of the obtained results

Figs. 4,5 show the results of calculation of the electric current in the conductive channel of the transistor at $T = 300$ K and different values of the voltages on its gate and drain. During the Monte Carlo simulation of charge carriers scattering processes, such electron scatterers as confined polar optical and acoustic phonons were considered according to [39, 41].

The dependencies of electric current in the transistor on the voltage on its drain at specific gate voltages, as illustrated in Fig. 4, are very typical and similar to those observed for conventional MIS-transistors. The current dependencies on the gate voltage at different values of the drain voltage, as presented in Fig. 5, also exhibit a highly characteristic form, corresponding to the pass-through CVCs of conventional MIS-transistors up to the voltage V_{G0} , at which the potential barrier for charge carriers is completely eliminated. But under the condition that $0.5V > V_G > V_{G0} = 0.4$ V, in contrast to the ballistic quantum-barrier transistor which has a plateau on the dependence of $I_e(V_G)$ in this region with negative differential conductivity close to zero, that takes place in case of neglecting the electron scattering processes [22], or positive differential conductivity close to zero, that takes place in case of taking into account these processes [24], the CVCs of the considered quasi-ballistic transistor has no such a valley at $0.4V < V_G < 0.5$ V.

As follows from the simulation results, the maximum saturation current, which is equal to $3.89 \mu\text{A}$ at $T = 300$ K and $V_D = V_G = V_{G0} = 0.4$, is 56.0 percent of the maximum possible current in the considered transistor (calculated by

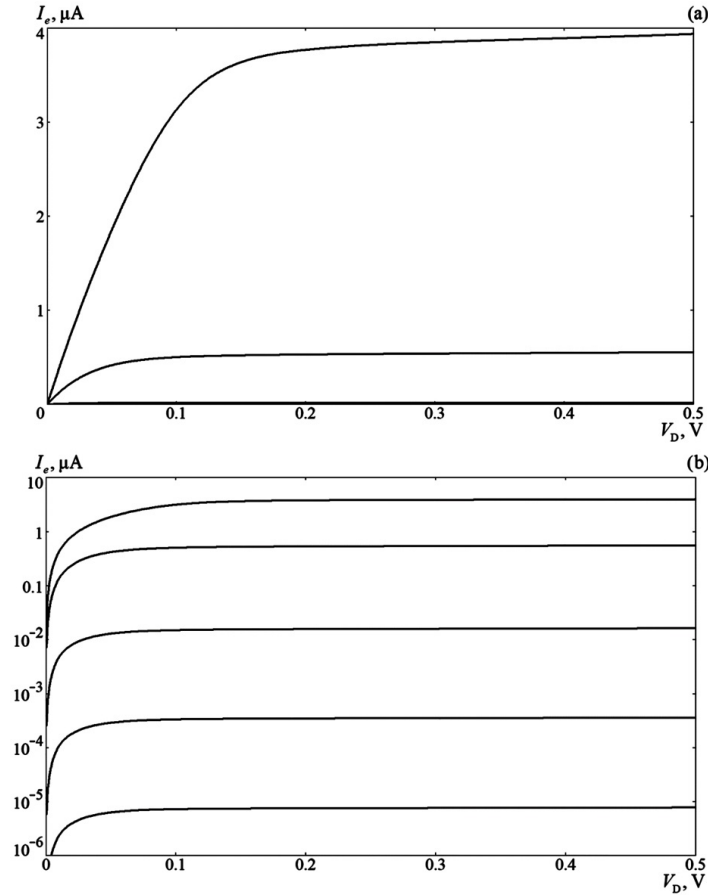


FIG. 4. Output CVC of the FET based on GaAs quantum wire in linear (a) and logarithmic (b) scales: curves in series from top to bottom – $V_G = 0.4, 0.3, 0.2, 0.1$ and 0 V

formula (5) at $V_D \rightarrow \infty$ under the condition that $t_{ch}(E)t_{sc}(E) \equiv 1$ [22–24]). The maximum channel conductance of the transistor at $V_G = V_{G0} = 0.4$ V, $V_D = 0$ and $T = 300$ K achieves 55.5 percent of the maximum possible quantum mechanical value of $e^2/(\pi\hbar)$. The ratio of the electric current in the open transistor I_{on} ($V_G = V_{G0}$) to the current in the closed transistor I_{off} ($V_G = 0$) is $5 \cdot 10^5$ at $T = 300$ K and $V_D = 0.2$ – 0.4 V. At $V_G = 0$ and $V_D = 0.2$ – 0.4 V the subthreshold swing takes a value of 101 percent relative to the minimum possible theoretical value of $\ln(10)k_B T/e$ which is equal to 59.53 mV/dec at a temperature equal to 300 K (k_B is the Boltzmann constant).

When the gate voltage is equal to 0.4 V and more, the transistor conducting channel is completely open due to the complete elimination of the potential barrier for electrons at $V_G \geq 0.4$ V (see Fig. 3,5). Moreover, despite the increase in the fraction of coherently reflected electrons from the region $[0, H]$ of the conducting channel of the quasi-ballistic transistor, there is no typical plateau on CVC of the ballistic transistor at $V_G > V_{G0}$ [22]. The obtained behavior of the pass-through CVC at $V_G > V_{G0}$ is explained by the decrease in the reverse flux of incoherently reflected electrons in the region $[0, H]$, significantly exceeding the increase in the reverse flux of charge carriers coherently reflected from this region. This fact indicates that the conductive channel length of the transistor equal to 100 nm is not optimal and can be reduced with increasing channel conductivity and saturation current along with increasing the subthreshold swing to values not worse than 105% relative to the minimum possible theoretical value [22–24]. In particular, basing on the results of the present study and the results from [22–24], it can be concluded that the optimum value of h_0 satisfies the inequality chain like $3 < h_0 < 30$ nm. Obviously, the optimum will be achieved when the backward flux of electrons incoherently reflected by phonons is equal to the backward flux of particles coherently reflected from the surface of the quantum wire which tapers sharply along its axis [25]. Unfortunately, within the approach considered in the present study, it is not possible to find the optimal value of h_0 in terms of the maximum channel conductance or maximum saturation current. To obtain a relevant optimal value of h_0 , it is necessary to use much more rigorous and computationally very complex methods for calculating the electric current in one-dimensional conducting channels with complex topology and decaying electron quantum states because of decoherence processes [43–45]. Here, we can only assume that $h_0 \sim 10$ nm ($H_0 \sim 50$ nm).

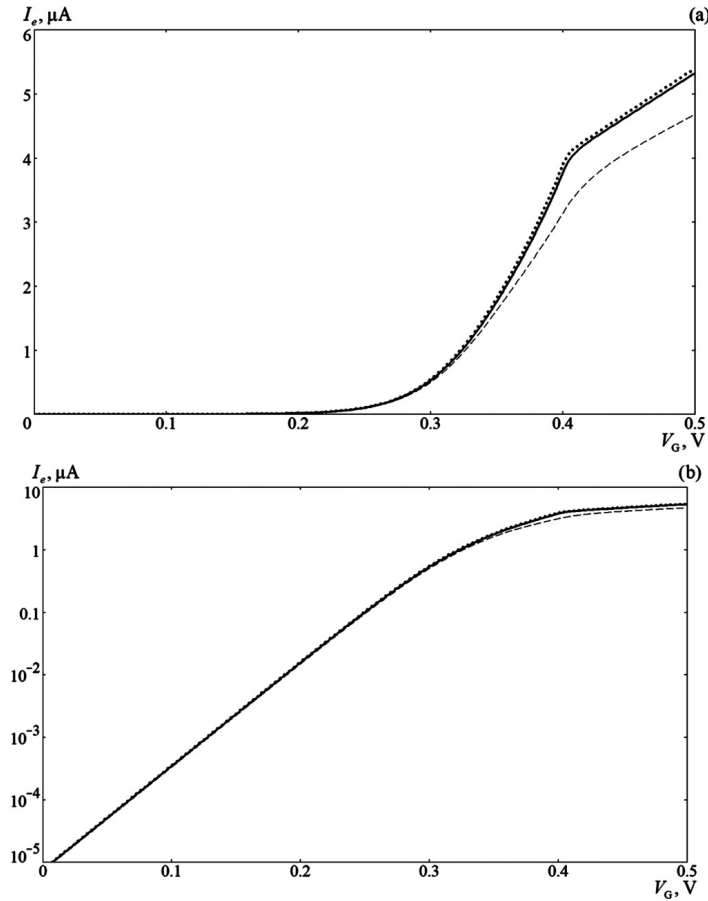


FIG. 5. Pass-through CVC of the FET based on GaAs quantum wire in linear (a) and logarithmic (b) scales: dashed curve – $V_D = 0.1$ V, solid curve – $V_D = 0.2$ V, dotted curve – $V_D = 0.4$ V

4. Conclusions

Thus, within the framework of the present study, a topological solution for a new construction of FET with a Schottky barrier in its conductive channel in the form of a quasi-ballistic quantum-barrier transistor based on a cylindrical undoped GaAs-in- Al_2O_3 quantum wire with an optimally varying cross-section lengthwise the conducting channel has been found. The CVCs of such a transistor have been calculated within the framework of the developed combined physico-mathematical model describing electron transport in its conducting channel taking into account the semiconductor band structure nonparabolicity, quantum-dimensional effects and such secondary quantum effects as the collisional broadening and displacement of the electron energy levels.

The proposed solution, among other things, opens the prospect of development and production of quantum-barrier FETs based on semiconductor quantum wires with varying rectangular cross-section lengthwise the conducting channel along one or both transverse directions. In the limit, it could be a semiconductor quantum layer with optimally varying thickness lengthwise the two-dimensional conducting channel of the transistor separated from two planar metal gates by some oxide or nitride insulator. As an example, it could be such a heterostructure as “metal/ SiO_2 / $\text{Si}[111]/\text{SiO}_2$ /metal”. Orientation of the semiconductor along the [111] direction perpendicular to the heterojunctions is necessary to ensure the same position of the lowest energy subbands in all six valleys of silicon relative to the bottom of its conduction band. When changing the Si quantum layer thickness from 4.8 nm (15 atomic layers) through 1.6 nm (5 atomic layers) to 4.8 nm (15 atomic layers), a profile of the potential barrier for electrons is formed close to the optimal profile obtained in the present study.

References

- [1] Weste N.H.E., Money Harris D. *CMOS VLSI Design: A circuits and systems perspective*. Addison-Wesley, Boston, 2010, 659 p.
- [2] Cheng H., Yang Z., Zhang C., Xie C., Liu T., Wang J., Zhang Z. A new approach to modeling ultrashort channel ballistic nanowire GAA MOSFETs. *Nanomaterials*, 2022, **12**(19), P. 3401-1–13.
- [3] Cheng H., Liu T., Zhang C., Liu Z., Yang Z., Nakazato K., Zhang Z. Nanowire gate-all-around MOSFETs modeling: ballistic transport incorporating the source-to-drain tunneling. *Jpn. J. Appl. Phys.*, 2020, **59**(7), P. 074002-1–20.
- [4] Burke A.M., Carrad D.J., Gluschke J.G., Storm K., Fahlvik Svensson S., Linke H., Samuelson L., Micolich A.P. InAs nanowire transistors with multiple, independent wrap-gate segments. *Nano Lett.*, 2015, **15**(5), P. 2836–2843.

- [5] Ullah A.R., Meyer F., Glusckhe J.G., Naureen S., Caroff P., Krogstrup P., Nygard J., Micolich A.P. p-GaAs nanowire metal–semiconductor field-effect transistors with near-thermal limit gating. *Nano Lett.*, 2018, **18**(9), P. 5673–5680.
- [6] Peng L.-M. High-performance carbon nanotube thin-film transistor technology. *ACS Nano*, 2023, **17**(22), P. 22156–22166.
- [7] Benjelloun M., Zaidan Z., Soltani A., Gogneau N., Morris D., Harmand J.-Ch. Design, simulation and optimization of an enhanced vertical GaN nanowire transistor on silicon substrate for power electronic applications. *IEEE Access*, 2023, **11**, P. 40249–40257.
- [8] Xu L., Xu L., Li Q., Fang Sh., Li Y., Guo Y., Wang A., Quhe R., Yee Sin A., Lu J. Sub-5 nm gate-all-around InP nanowire transistors toward high-performance devices. *ACS Appl. Electron. Mat.*, 2024, **6**(1), P. 426–434.
- [9] Fuad M.H., Nayan Md.F., Raihan Md.A., Yeassin R., Mahmud R.R. Performance analysis of graphene field effect transistor at nanoscale regime. *e-Prime – Adv. Electr. Eng., Electron. Energy*, 2024, **9**, P. 100679-1–7.
- [10] Rezgui H., Mukherjee Chhandak, Wang Y., Deng M., Kumar A., Müller J., Larriue G., Maneux C. Nanoscale thermal transport in vertical gate-all-around junction-less nanowire transistors-part II: multiphysics simulation. *IEEE Trans. Electron Devices*, 2023, **70**(12), P. 6505–6511.
- [11] Nazir G., Rehman A., Park S.-J. Energy-efficient tunneling field-effect transistors for low-power device applications: challenges and opportunities. *ACS Appl. Mater. Interfaces*, 2020, **12**(42), P. 47127–47163.
- [12] Mah S.K., Ker P.J., Ahmad I., Zainul Abidin N.F., Ali Gamel M.M. A feasible alternative to FDSOI and FinFET: optimization of W/La₂O₃/Si planar PMOS with 14 nm gate-length. *Materials*, 2021, **14**(19), P. 5721-1–15.
- [13] Zahoor F., Hanif M., Isyaku Bature U., Bodapati S., Chattopadhyay A., Azmadi Hussin F., Abbas H., Merchant F., Bashir F. Carbon nanotube field effect transistors: an overview of device structure, modeling, fabrication and applications. *Phys. Scr.*, 2023, **98**(8), P. 082003-1–34.
- [14] Cerdeira A., Estrada M., de Souza M., Pavanello M.A. Analytical model for the drain and gate currents in silicon nanowire and nanosheet MOS transistors valid between 300 and 500 K. *Int. J. Numer. Model.*, 2024, **37**(2), P. 3219-1–12.
- [15] Hashmi F., Nizamuddin M., Farshori M.A., Amin S.U., Khan Z.I. Graphene nanoribbon FET technology-based OTA for optimizing fast and energy-efficient electronics for IoT application: Next-generation circuit design. *Micro & Nano Lett.*, 2024, **19**(6), P. e70002-1–15.
- [16] Gupta S., Nandi A. Effect of air spacer in underlap GAA nanowire: an analogue/RF perspective. *IET Circ. Dev. Syst.*, 2019, **13**(8), P. 1196–1202.
- [17] Leonard F., Alec Talin A. Electrical contacts to one- and two-dimensional nanomaterials. *Nature Nanotech.*, 2011, **6**(12), P. 773–783.
- [18] Appenzeller J., Knoch J., Bjork M.T., Riel H., Schmid H., Riess W. Toward nanowire electronics. *IEEE Trans. Electron Devices*, 2008, **55**(11), P. 2827–2845.
- [19] Memisevic E., Svensson J., Hellenbrand M., Lind E., Wernersson L.-E. Vertical InAs/GaAsSb/GaSb tunneling field-effect transistor on Si with S = 48 mV/decade and Ion = 10 μA/μm for Ioff = 1 nA/μm at VDS = 0.3 V. *IEEE Int. Electron Devices Meeting (IEDM, San Francisco)*, 2016, 19.1.1–4.
- [20] Carrillo Nunez H. *Combining the modified local density approach with variational calculus: a flexible tandem for studying electron transport in nano-devices*. PhD thesis, Antwerp, 2012, 127 pp.
- [21] Datta S. *Electronic transport in mesoscopic systems*. Cambridge University Press, Cambridge, 1995, 377 pp.
- [22] Pozdnyakov D.V., Borzdov A.V., Borzdov V.M. Simulation of a vertical ballistic quantum-barrier field-effect transistor based on an undoped Al_xGa_{1-x}As quantum nanowire. *Rus. Microelectronics*, 2023, **52**(6), P. 483–492.
- [23] Pozdnyakov D.V., Borzdov A.V., Borzdov V.M. Calculation of electrophysical characteristics of semiconductor quantum wire device structures with one-dimensional electron gas. *Rus. Microelectronics*, 2023, 52(Suppl.1), P. S20–29.
- [24] Pozdnyakov D.V., Borzdov V.M. *Modeling of electrophysical properties of device structures with one-dimensional electron gas*. BSU, Minsk, 2025, 191 p. (in Russian).
- [25] Pozdnyakov D.V., Borzdov A.V., Borzdov V.M. Peculiarities of electron transport through the contact regions between semiconductor quantum wires with different cross sections. *Nanobiotechnology Reports*, 2024, 19(Suppl.1), P. S117–S123.
- [26] Neverov V.N., Titov A.N. *Physics of low-dimensional systems*. UrSU, Ekaterinburg, 2008, 240 p. (in Russian).
- [27] Radantsev V.F. *Electronic properties of semiconductor nanostructures*. UrSU, Ekaterinburg, 2008, 420 p. (in Russian).
- [28] Davydov A.S. *Quantum mechanics*. Pergamon Press, Oxford, 1976, 636 p.
- [29] Landau L.D., Lifshitz E.M. *Quantum mechanics. Non-relativistic theory*. Pergamon Press, Oxford, 1991, 677 p.
- [30] Shamala K.S., Murthy L.C.S., Narasimha R.K. Studies on optical and dielectric properties of Al₂O₃ thin films prepared by electron beam evaporation and spray pyrolysis method. *Mat. Sci. Eng. B*, 2004, **106**(3), P. 269–274.
- [31] Levinshtein M., Rumyantsev S., Shur M. *Handbook series on semiconductor parameters, Vol. 2: Ternary and quaternary III-V compounds*. World Scientific Publishing Co. Pte. Ltd., Singapore, 1999, 205 p.
- [32] Baltenkov A.S., Msezane A.Z. Electronic quantum confinement in cylindrical potential well. *Eur. Phys. J. D*, 2016, **70**(4), 81-1–9.
- [33] Gulyamov G., Gulyamov A.G., Davlatov A.B., Shahobiddinov B.B. Electron energy in rectangular and cylindrical quantum wires. *Journal of Nano- and Electronic Physics*, 2020, **12**(4), 04023-1–5.
- [34] Harrison P., Valavanis A. *Quantum wells, wires and dots. Theoretical and computational physics of semiconductor nanostructures*. Wiley, Chichester – Hoboken, 2016, 598 p.
- [35] Pozdnyakov D. Influence of surface roughness scattering on electron low-field mobility in thin undoped GaAs-in-Al₂O₃ nanowires with rectangular cross-section. *Phys. Status Solidi (b)*, 2010, **247**(1), P. 134–139.
- [36] Lopez-Villanueva J.A., Melchor I., Cartujo P., Carceller J.E. Modified Schrodinger equation including nonparabolicity for the study of a two-dimensional electron gas. *Phys. Rev. B*, 1993, **48**(3), P. 1626–1631.
- [37] Borzdov V.M., Komarov F.F. *Simulation of electrophysical properties of solid-state layered structures of integrated electronics*. BSU, Minsk, 1999, 236 p. (in Russian).
- [38] Yamamoto H. Resonant tunneling condition and transmission coefficient in a symmetrical one-dimensional rectangular double-barrier system. *Appl. Phys. A*, 1987, **42**, P. 245–248.
- [39] Borzdov A.V., Pozdnyakov D.V., Galenchik V.O., Borzdov V.M., Komarov F.F. Self-consistent calculations of phonon scattering rates in the GaAs transistor structure with one-dimensional electron gas. *Phys. Status Solidi (b)*, 2005, **242**(15), P. R134–R136.
- [40] Pozdnyakov D.V., Galenchik V.O., Borzdov A.V. Electron scattering in thin GaAs quantum wires. *Phys. Low-Dim. Struct.*, 2006, **2**, P. 87–90.
- [41] Borzdov A.V., Pozdnyakov D.V. Scattering of electrons in the GaAs/AlAs transistor structure. *Phys. Solid State*, 2007, **49**(5), P. 963–967.
- [42] Pozdnyakov D., Galenchik V., Borzdov A., Borzdov V., Komarov F. Influence of scattering processes on electron quantum states in nanowires. *Nanoscale Res. Lett.*, 2007, **2**(4), P. 213–218.
- [43] Abramov I.I. Problems and principles of physics and simulation of micro- and nanoelectronics device structures. IV. Quantum-mechanical formalisms. *Nano- and Microsystem Technology*, 2007, **9**(2), P. 24–32. (in Russian).
- [44] Thijssen J. *Computational physics*. Cambridge University Press, Cambridge, 2012, 620 p.
- [45] Gubernatis J.E., Kawashima N., Werner P. *Quantum Monte Carlo methods: Algorithms for lattice models*. Cambridge University Press, Cambridge, 2016, 512 p.

Submitted 16 January 2025; revised 15 April 2025; accepted 16 April 2025

Information about the authors:

Dmitry V. Pozdnyakov – Belarusian State University, Minsk, Nezavisimosti Av.4, 220030 Belarus; ORCID 0009-0005-2333-9829; pozdnyakovdv@bsu.by

Andrei V. Borzdov – Belarusian State University, Minsk, Nezavisimosti Av.4, 220030 Belarus; borzdovav@bsu.by

Vladimir M. Borzdov – Belarusian State University, Minsk, Nezavisimosti Av.4, 220030 Belarus; borzdov@bsu.by

Conflict of interest: the authors declare no conflict of interest.

Alcohol dehydrogenase: molecular dynamics study of conformational and orientational behaviour of the enzyme in complex with nad during sorption on the surface of electrode materials using graphite as an example

Ivan A. Baigunov^{1,a}, Kholmurzo T. Kholmurodov^{1,2,3,4,b}, Pavel P. Gladyshev^{1,c}

¹Dubna State University, Department of Chemistry, New Technologies and Materials, Dubna, Russia

²Frank Laboratory of Neutron Physics, Joint Institute for Nuclear Research, Dubna, Russia

³Lomonosov Moscow State University, Department of Fundamental Nuclear Interactions, Moscow, Russia

⁴S. U. Umarov Physical-Technical Institute (PhTI), Dushanbe, Republic of Tajikistan

^avanek1997fev@yandex.ru, ^bkholmurzo@gmail.com, ^cpglad@yandex.ru

Corresponding author: Ivan A. Baigunov, vanek1997fev@yandex.ru

PACS 02.70.Ns, 36.20.-r

ABSTRACT In this work, computer molecular dynamics (MD) studies of the orientation and structural conformations of the alcohol dehydrogenase enzyme (hereinafter ADH) in complex with nicotine adenine dinucleotide (hereinafter NAD) during sorption on the surface of electrode materials using graphite as an example were carried out.

KEYWORDS alcohol dehydrogenase, molecular dynamics

ACKNOWLEDGEMENTS ...

FOR CITATION Baigunov I.A., Kholmurodov Kh.T., Gladyshev P.P. Alcohol dehydrogenase: molecular dynamics study of conformational and orientational behaviour of the enzyme in complex with nad during sorption on the surface of electrode materials using graphite as an example. *Nanosystems: Phys. Chem. Math.*, 2025, **16** (2), 192–198.

1. Introduction

The current study is devoted to the structural aspect of the ADH (alcohol dehydrogenase) enzyme and its co-enzyme NAD (Nicotinamide-Adenine-Dinucleotide) [1–5]. As shown by X-ray crystallography, the ADH enzyme undergoes global conformational changes, including rotation of the catalytic domain relative to the coenzyme binding domain and rearrangement of the active center to obtain a catalytically active enzyme. The conformational change requires a complete coenzyme and depends on various chemical or mutational substitutions that can increase the catalytic activity due to changes in the isomerization kinetics and the rate of dissociation of coenzymes [2–6]. As for the structural aspect of the enzyme, using experimental observations and mathematical modeling of the protein, the orientation of ADH on various sorbents and conductive matrices were studied depending on the pH of the solution. As is known, deactivation of the enzyme caused by unsuitable conditions (temperature, pH), thereby introducing a change in the activity of the ADH enzyme. The implementation of various options includes, for example, the immobilization of a two-substrate enzyme on the surface of electrode materials [7–15]. However, it should be noted that the experimental study of the above issues is difficult. Therefore, in recent years, computational and simulation analysis methods have been widely used for these purposes [16–23]. Molecular dynamics (MD) modeling is currently widely used with many software packages designed for MD modeling (the DL_POLY, which contains and programmed all the potentials necessary for construction; the AMBER software package for simulating protein structures, Table 1).

Molecular dynamics simulation involves a series of steps, shown in Fig. 1.

In this work, we used computer molecular dynamics (MD) modeling to study the structural and conformational changes of the ADH enzyme with its cofactor NAD occurring in an aqueous solution interacting with the surface of the electrode material. Graphite serves as the surface and the MD analysis data allow studying the changes in the ADH + NAD structural conformations on atomic-molecular level in detail.

TABLE 1. Potentials used in the AMBER software package

Potential	Purpose
$U(R) = \sum_{\text{bonds}} K_r (r - r_{eq})^2$	Harmonic potential for two atoms
$U(R) = \sum_{\text{angles}} K_\theta (\theta - \theta_{eq})^2$	Harmonic potential for angular bond of three atoms
$U(R) = \sum_{\text{dihedrals}} \frac{V_n}{2} (1 - \cos [n\varphi - \gamma])$	Harmonic potential for four atoms
$U(R) = \sum_i \sum_j \left[\left(\frac{A_{ij}}{R_{ij}^{12}} - \frac{B_{ij}}{R_{ij}^6} \right) + \frac{q_i q_j}{R_{ij}} \right]$	Lennard-Jones potential (van der Waals interactions) and electrostatic interaction

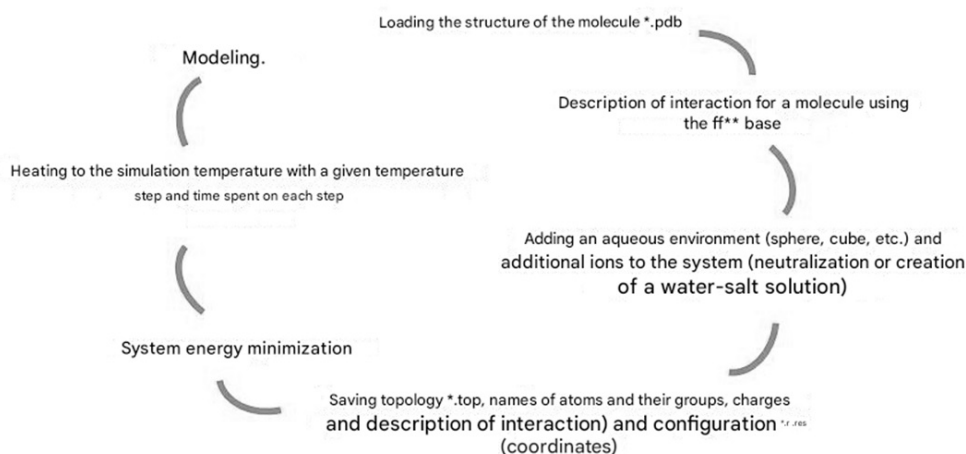


FIG. 1. Main stages of the numerical experiment

2. Experimental part

In this section, we present the descriptions of the main parameters and algorithms used in the computational molecular dynamics (MD) simulations. In this study, we used both CPU and GPU-based computing environments to perform the MD simulations using the AMBER package. We used multiple computing environments such as a 16-core cluster, Geforce GPU (GPU = (GTX 1080 Ti)) to implement the MD simulations in Amber 18 (pmemd; MD/AMBER) with GPU acceleration (pmemd.cuda). We refer to the Amber 2018 program code and reference manual [3, 16–18]. The calculations were carried out on the servers of the Heterogeneous Platform “HybriLIT” of the Multifunctional Information and Computing Complex (MIC), MLIT (M.G. Meshcheryakov Laboratory of Information Technologies), JINR (Joint Institute for Nuclear Research). The heterogeneous platform consists of the supercomputer “Govorun” and the educational and test site “HybriLIT” at JINR, Dubna, and on the local server of the Frank Laboratory of Neutron Physics (LNP) of JINR. We have implemented the main production MD simulations (CPU / GPU) (common also with many other simulation types) for PDB ID: 3COS crystal structure of human alcohol dehydrogenase class II (ADH) [19]. In this work, MD simulations were performed with the Amber 18 code (CPU/GPU environment). The MD simulations on the molecular system ADH + NAD + water + carbon surface (Fig. 2) were performed in three steps: energy minimization, NVT and NPT relaxation procedures. As for NVT: The canonical ensemble, where the system is kept from changes in moles (N), volume (V), and temperature (T). This set-up is also known as constant-temperature molecular dynamics, and requires a thermostat. The NPT: The isothermal-isobaric ensemble, where the system is kept from changes in moles (N), pressure (P), and temperature (T). Both a thermostat and barostat are needed. Due to the Amber 18 code’s capabilities we used the Langevin Dynamics (NVT and NPT) to attempt to mimic solvent viscosity by introducing things that occasionally cause friction and perturb the system. When used to control temperature, a small damping constant, γ , should be used. In the Berendsen Thermostat: the system is weakly coupled to a heat bath at a set temperature. The thermostat doesn’t

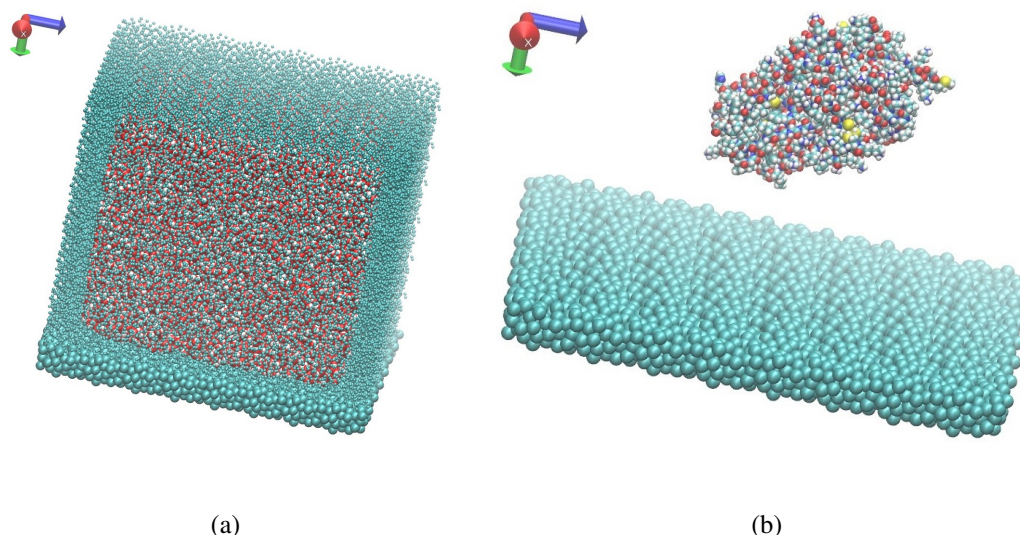


FIG. 2. General molecular design of the system ADH + NAD + water + graphite surface

mirror the canonical ensemble for small systems, but large systems are roughly ok. It uses a leap-frog algorithm to rescale velocities of particles, controlling temperature.

The MD simulations in Amber18 with CPU/GPU acceleration (pmemd/pmemd.cuda) were performed for three main setup phases that contain the main MD production:

- 1) Minimization of the system to reduce bad contacts;
- 2) Slowly heat the system to the target temperature;
- 3) Equilibration of the system at the target temperature.

In the first step, we minimized the system by applying constraints to the backbone atoms and to some atoms. The minimization was performed using sander instead of pmemd to ensure and evaluate the behavior of the energies during the minimization step. We then ran constant-volume heating simulations on the minimized structures to slowly heat the system from 10 to 303 K over some initial 2.0 ns steps of the simulation with a target temperature of 303 K. We retain the constraints on the backbone atoms, but with a weaker force constant than that used during the minimization. These simulations were performed using pmemd, pmemd.MPI, sander, or sander.MPI instead of using the GPU-accelerated code with pmemd.cuda. At the equilibration step, we equilibrate the system (ADH + NAD + surface + water) at a target temperature of 303 K.

3. Results and discussion

In Fig. 3(a–d), we present the obtained images of the ADH + NAD adsorption process on the graphitic carbon surface during long-term 100 ns dynamic changes from (a) the initially relaxed state to (b–c) intermediate states and (d) the final equilibrium state. The ADH + NAD enzyme underwent multimillion-second conformational and rotational changes before adsorption on this graphitic carbon (C-surface) to be finally trapped and relaxed on the surface. The dynamics of the ADH + NAD adsorption behavior on the graphitic carbon surface was monitored using MD/AMBER calculations and Visual Molecular Dynamics (VMD) software. Fig. 3(a–d) presents the results of MD calculation with (ntb=1) periodic boundaries of constant volume when minimizing and initially heating/equilibrating the whole system, ADH + NAD + aqueous solvent + graphite surface, and with (ntb=2) periodic boundaries of constant pressure when used for the production run after we heated and equilibrated at constant volume.

It is worth noting that finding the relaxed equilibrium of the ADH + NAD + water + surface system is a slow process, so far for each set of MD simulations we have performed 100 ns of calculations using the extremely fast module “pmemd.cuda”. One of the non-trivial events in the conformational structural dynamics of the whole ADH + NAD + water/graphite system and tracking of individual amino acid residues should be the behavior of the catalytic loops of the enzyme. Fig. 4(a–b) shows the dynamic patterns of the ADH + NAD/C-surface and the adsorption processes accompanied by gradual changes in the orientation of the two catalytic loops of the ADH + NAD molecule relative to the graphite surface. An important observation is that these two catalytic loops are located close inside the ADH + NAD molecule, upon reaching the adsorbing graphite surface we can see the separation of these loops from each other. The key summary of the whole process, as shown in Fig. 3(a–d), should be the separation from each other and hence the opening of the important catalytic loops of ADH + NAD due to the influence of the adsorbing C-surface of these two enzyme loops.

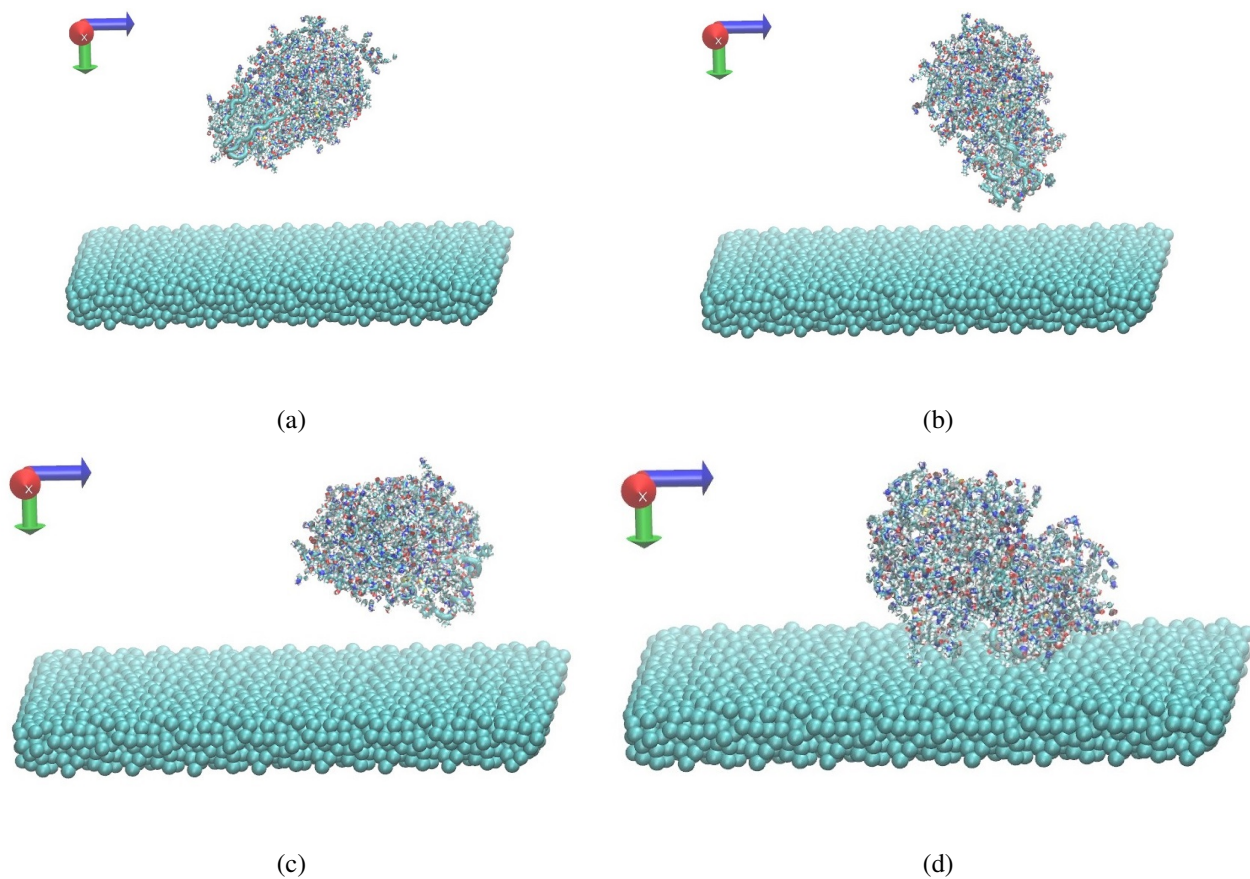


FIG. 3. Adsorption of ADH + NAD on graphite (C-surface) during 100 ns of dynamic and conformational changes

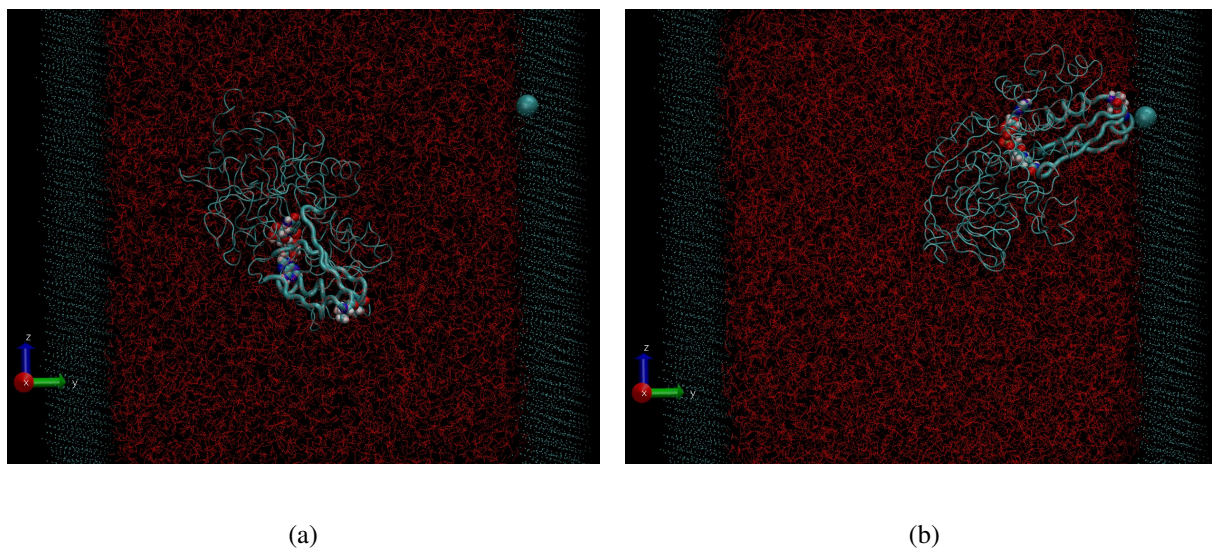


FIG. 4. The ADH + NAD orientation together with the position of the catalytic loops of ADH + NAD on the graphite surface of carbon

Next, Fig. 5 shows the arrangement of the two above-mentioned catalytic loops of the ADH + NAD molecule relative to the graphite surface. Here, the two terminal amino acid residues THR290 and ILE317 with the separations between these two terminal amino acids is shown.

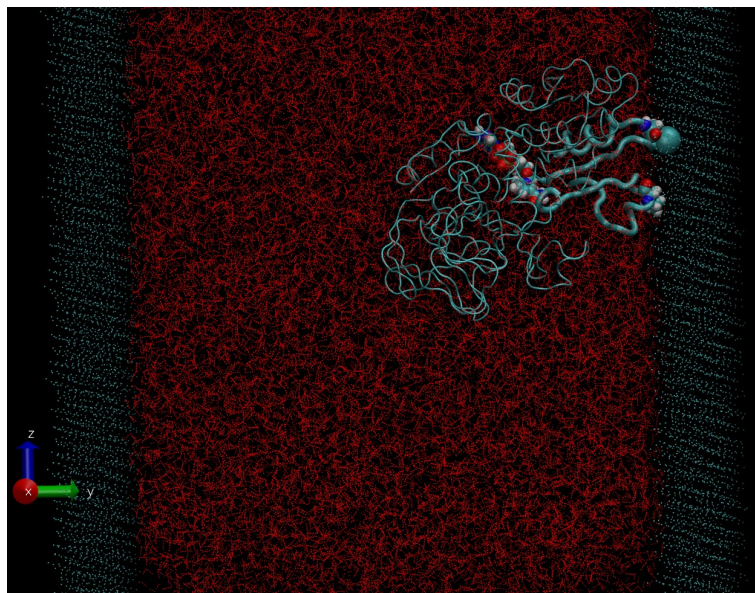


FIG. 5. Position of the catalytic loops of ADH + NAD on the graphite surface of carbon (a). Dynamics of the distance between the catalytic loops of ADH + NAD depending on time (b)

The MD results presented in Fig. 5 for the arrangement of the catalytic loops during the adsorption of the ADH + NAD molecule on the graphitic carbon surface in the final (100 ns) state of time clearly to confirm the important observation mentioned above that the two catalytic loops separate from each other upon reaching the adsorbing graphite surface, whereas they were initially located close to each other inside the ADH + NAD molecule. The above observation and the presented data on the dynamics of the ADH + NAD catalytic loops on the graphitic carbon surface correlate with the dynamic changes and rotations of the NAD coenzyme inside the ADH molecule. Using the data in Figs. 4–5, we observe the conformational changes of NAD upon ADH adsorption on the surface and the open gap between the catalytic loops. In Fig. 6, we have presented the positions of the atoms at the NAD chain, as well as the atoms in the central region of NAD. Fig. 6 shows the structure of the NAD molecule which correlate with the dynamical changes shown in Figs. 4–5 above.

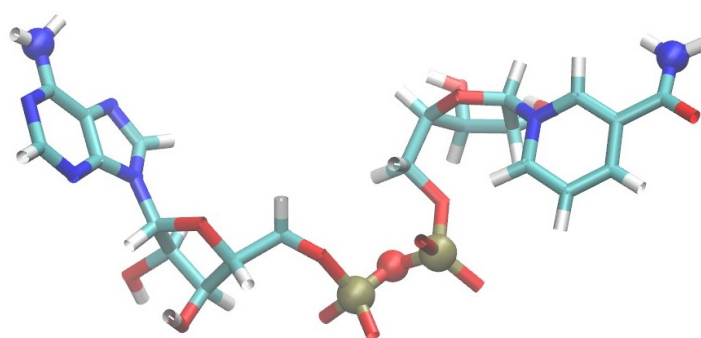


FIG. 6. The NAD structure with entered points correlates with dynamical changes in the ADH

It is worth noting that the current observations correlate with some experimental works related to the immobilization and adsorption of ADH enzyme on the carbon surface, the location of the enzyme and its fixation on the carbon platforms. It is seen that the dynamic changes of γ over time completely correlate with the dynamics of the change in the distance between the catalytic loops of ADH + NAD on the graphite surface. The comparison of the results in Figs. 4–5 are the key features of the entire process of ADH + NAD/C-surface adsorption, which is accompanied by a nontrivial structural transformation of the NAD coenzyme, correlating with the behavior of the catalytic loops of the ADH enzyme. The above observation and the presented data on the dynamics of the ADH + NAD catalytic loops on the graphite surface

correlate with the dynamic changes and rotations of the NAD coenzyme inside the ADH molecule. Moreover, the results also indicate that in order to maintain the environment in which the ADH enzyme exhibits good activity and to provide conditions for future technological applications, physiological conditions and ambient temperature can be satisfactorily applied to the enzymatic system including the dehydrogenase enzyme. At the same time, the choice of carbon surfaces and platforms is motivated by good control of the enzyme arrangement on the surface at a very low enzyme consumption. The kinetic rates obtained for the ADH enzyme attached to the carbon surface indicate a decrease in activity after the immobilization and fixation process, a significant loss of enzymatic activity observed after immobilization, although the affinity between the enzymes and their substrates and coenzymes is preserved.

4. Conclusion

In summary, the structural conformations of the alcohol dehydrogenase (ADH) enzyme with its cofactor nicotinamide adenine dinucleotide (NAD) were studied on a graphite surface (C-surface) using the MD (molecular dynamics) simulation method. The ADH + NAD enzyme was simulated in an aqueous environment, the molecules of which are constantly in thermal motion and collide with the protein globule, thereby providing chaotic linear and rotational motion, as well as conformational movements. Subsequently, the numerical MD experiment implemented in the current study using the AMBER-18 package (implementation of the fast module "pmemd.cuda") provides useful statistics regarding the most interesting aspects of the structural study of ADH related to the conformational changes of ADH, including the rotation of the catalytic domain, the coenzyme binding domain, the rearrangement of the active site, etc. The above analysis is important for understanding the atomic/molecular details of the catalytically active enzyme, so far the long dynamic simulation of 100 ns allows tracking the conformational and rotational changes of the ADH + NAD system in aqueous medium.

References

- [1] Wagenknecht P.S., Penney J.M., Hembre R.T. Transition-metal-catalyzed regeneration of nicotinamide coenzymes with hydrogen. *Organometallics*, 2003, **22** (6), P. 1180–1182.
- [2] Nakamura K., Yamanaka R. Light mediated cofactor recycling system in biocatalytic asymmetric reduction of ketone. *Chemical Communications*, 2002, **16**, P. 1782–1783.
- [3] Bilan D.S., Belousov V.V. Genetically encoded probes for NAD⁺/NADH monitoring. *Free Radical Biology and Medicine*, 2016, **100**, P. 32–42.
- [4] Presečki A.V., Vasić-Rački D. Modelling of the alcohol dehydrogenase production in baker's yeast. *Process biochemistry*, 2005, **40** (8), P. 2781–2791.
- [5] Tušek A., Šalić A., Kurtanjek Ž., Zelić B. Modeling and kinetic parameter estimation of alcohol dehydrogenase-catalyzed hexanol oxidation in a microreactor. *Engineering in Life Sciences*, 2012, **12** (1), P. 49–56.
- [6] Orlich B., Berger H., Lade M., Schomäcker R. Stability and activity of alcohol dehydrogenases in W/O-microemulsions: Enantioselective reduction including cofactor regeneration. *Biotechnology and Bioengineering*, 2000, **70** (6), P. 638–646.
- [7] Höhn S., Zheng K., Romeis S., Brehl M., Peukert W., de Ligny D., Boccaccini A.R. Effects of medium pH and preconditioning treatment on protein adsorption on 45S5 bioactive glass surfaces. *Advanced Materials Interfaces*, 2020, **7** (15), 2000420.
- [8] Benavidez T.E., Torrente D., Marucho M., Garcia C.D. Adsorption and catalytic activity of glucose oxidase accumulated on OTCE upon the application of external potential. *J. of colloid and interface science*, 2014, **435**, P. 164–170.
- [9] Wang F., Zhang Y.Q. Bioconjugation of silk fibroin nanoparticles with enzyme and peptide and their characterization. *Advances in protein chemistry and structural biology*, 2015, **98**, P. 263–291.
- [10] Welborn V.V. Structural dynamics and computational design of synthetic enzymes. *Chem. Catalysis*, 2022, **2** (1), P. 19–28.
- [11] Norde W., Lyklema J. Why proteins prefer interfaces. *J. of Biomaterials Science, Polymer Edition*, 1991, **2** (3), P. 183–202.
- [12] Andrade J.D. (Ed.). *Surface and interfacial aspects of biomedical polymers*, 1985, Plenum Press, New York, 1985, **1**, P. 249–292.
- [13] Gladyshev P.P., Shapovalov Yu.A., Kvasova V.P. *Reconstructed oxidoreductase systems*, Science, Alma-ata, KazSSR, 1987, 187 p.
- [14] Gladyshev P.P., Gorjaev M.I., Shpil'berg I.G., Iu A.S. Sorption immobilization of NAD-dependent enzyme systems. I. Influence of electrostatic interactions on the orientation of alcohol dehydrogenase on the sorbent surface. *Molekuliarnaia Biologiya*, 1982, **16** (5), P. 938–942. (in Russian).
- [15] Gladyshev P.P., Gorjaev M.I., Shpil'berg I.G. Sorption immobilization of NAD-dependent enzyme systems. II. Influence of hydrophobic interactions on the orientation of alcohol dehydrogenase on the sorbent surface. *Molekuliarnaia Biologiya*, 1982, **16** (5), P. 943–947. (in Russian).
- [16] Foresman J., Frish E. *Exploring chemistry*, Gaussian Inc., Pittsburg, USA, 1996, **21**, P. 93–123
- [17] Leach A.R. Molecular modelling: principles and applications. *Pearson education*, Harlow, 2001, 727 p.
- [18] Case D.A., Cheatham III T.E., Darden T., Gohlke H., Luo R., Merz Jr. K.M., Woods R.J. The Amber biomolecular simulation programs. *J. of Computational Chemistry*, 2005, **26** (16), P. 1668–1688.
- [19] Case D.A., Aktulga H.M., Belfon K., Cerutti D.S., Cisneros G.A., Cruzeiro V.W.D., Merz Jr. K.M. AmberTools. *J. of Chemical Information and Modeling*, 2023, **63** (20), P. 6183–6191.
- [20] Lee T.S., Cerutti D.S., Mermelstein D., Lin C., LeGrand S., Giese T.J., York D.M. GPU-accelerated molecular dynamics and free energy methods in Amber18: performance enhancements and new features. *J. of Chemical Information and Modeling*, 2018, **58** (10), P. 2043–2050.
- [21] Cruzeiro V.W.D., Amaral M.S., Roitberg A.E. Redox potential replica exchange molecular dynamics at constant pH in AMBER: Implementation and validation. *The J. of Chemical Physics*, 2018, **149** (7).
- [22] Kholmurov K.T. *Models in bioscience and materials research: Molecular dynamics and related techniques*, Nova Science Publishers Ltd., New York, 2013, 208 p.
- [23] Kholmurov K.T. *Computational materials and biological sciences*, Nova Science Publishers Ltd., New York, 2015, 188 p.

Information about the authors:

Ivan A. Baigunov – Dubna State University, Department of Chemistry, New Technologies and Materials, Universitetskaya, 19, Dubna, Moscow Region, 141980, Russia; ORCID 0009-0000-8380-6218; vanek1997fev@yandex.ru

Kholmirzo T. Kholmurodov – Dubna State University, Department of Chemistry, New Technologies and Materials, Universitetskaya, 19, Dubna, Moscow Region, 141980, Russia; Frank Laboratory of Neutron Physics, Joint Institute for Nuclear Research, Joliot-Curie, 6, Dubna, Moscow Region, 141980, Russia; Lomonosov Moscow State University, Department of Fundamental Nuclear Interactions, Faculty of Physics, Leninskiye Gory, GSP-1, Moscow, 119991, Russia; S.U. Umarov Physical-Technical Institute (PhTI), Aini ave., 299/1, Dushanbe, 734063, Republic of Tajikistan; ORCID 0000-0002-9415-8276; kholmirzo@gmail.com

Pavel P. Gladyshev – Dubna State University, Department of Chemistry, New Technologies and Materials, Universitetskaya, 19, Dubna, Moscow Region, 141980, Russia; ORCID 0000-0002-7449-4475; pglad@yandex.ru

Conflict of interest: the authors declare no conflict of interest.

Thermal and magnetic properties and density of state of in 3D SnTe (001) surface state under combined exchange and strain effects

Khaled Abdulhaq, Mohammad K. Elsaid, Diana Dahliah

Physics department, An-Najah National University, Nablus, Palestine

Corresponding author: Mohammad K. Elsaid, mkelsaid@najah.edu; Diana Dahliah, diana.dahliah@najah.edu

ABSTRACT This paper presents a comprehensive investigation of the essential properties of topological insulator materials like electronic, thermal, and magnetic quantities. We considered crystalline topological insulators tin telluride (SnTe), deposited on a magnetic substrate material. The anisotropic mass Hamiltonian is considered to obtain eigenenergy spectra expression in the presence of exchange proximity and strain effects. We showed that the strain has an important effect in shifting the position of the valley or Dirac points in the reciprocal space; an important result that leads to significant role in using the topological material as an electronic component in the new hot research area called valley electronics. We displayed the dependences of the computed density of states, heat capacity, and the magnetic susceptibility of the crystalline topological material, SnTe, on the Hamiltonian physical parameters.

KEYWORDS topology, SnTe, thermal properties, magnetic properties

FOR CITATION Abdulhaq K., Elsaid M.K., Dahliah D. Thermal and magnetic properties and density of state of in 3D SnTe (001) surface state under combined exchange and strain effects. *Nanosystems: Phys. Chem. Math.*, 2025, **16** (2), 199–208.

1. Introduction

Many aspects of condensed matter physics are related to classifying phases of matter [1, 2]. Over the past decades, the study of the quantum Hall effect has led to a different classification model, based on the notion of topological order. Recently, a new class of materials has been emerged which is called a topological insulator (TI) [3–5]. Topological insulators are electronic materials that have a bulk band gap like an ordinary insulator, but have protected conducting states on their edge or surface. Topological insulators come in various forms, including 2D topological insulators and 3D topological insulators, as well as topological superconductors, which have been investigated thoroughly qualitatively and quantitatively [6–8]. 3D topological insulators form a class of materials that exhibit interesting electronic properties, particularly in their surface states. These materials are insulators in the bulk, meaning that their interior does not conduct electricity. However, they have conductive surface states that are topologically protected [9]. The electronic properties of topological insulators are governed by their band structure, which is a representation of the allowed energy levels for electrons within the material. In a topological insulator, there is a band inversion between the valence and conduction bands, leading to the formation of surface states with a Dirac cone-like dispersion.

In topological crystalline insulators, the internal topology of the material preserving surface states are mirror symmetry, reflection symmetry, and rotational symmetry [10–13]. Additionally, there may be more than one symmetry types, some crystals have a group of symmetries depending on the crystal structure. It is important to note that these symmetries are dependent on the specific crystal lattice structure. In this paper, we are interested in SnTe crystal which is a topological crystalline insulator. The nontrivial topology in these crystals relies on the presence of reflection symmetry of the Rock-salt crystal structure with respect to the (110) mirror plane, and is mathematically characterized by an integer topological invariant the mirror Chern number [11]. Many researches were conducted to control the phase in Topological Crystalline Insulators TCIs via external factors such as temperature, symmetry breaking, strain, Rashba spin–orbit coupling, coupling to a ferromagnet, and charged impurities [10, 12, 14].

SnTe exhibits a naturally inverted band ordering, where the valence band originates from the cation Sn atoms, and the conduction band arises from Te atoms. This inversion, in contrast to a conventional ionic insulator, leads to the emergence of TCI phase in SnTe. SnTe is predicted to possess topological surface states on a set of crystal surfaces. Topological surface states on the (001) plane have been detected experimentally in angle-resolved photoemission spectroscopy (ARPES) investigations conducted on SnTe. Moreover, the spin texture observed in spin-resolved ARPES experiments offers a direct spectroscopic assessment of the mirror Chern number [11, 15].

On 2013, Yung Jui Wang, et al. conducted a first-principles calculations of the surface states in the CTI SnTe [5]. Timothy H. Hsieh et al. also showed that SnTe has metallic surface states with an even number of Dirac cones on high-symmetry crystal surfaces such as (001), (110) and (111) [10, 16].

By 2020, Researchers Pham, Binh, Viet, Dung, Hoi studied Rashba spin-orbit coupling (RSOC) effects on Dirac fermions in SnTe [17]. RSOC alters dispersion, group velocity and effective mass of the surface state electrons [17]. Hsieh et al. investigate the influence of breaking the mirror symmetry via external elastic strain or in-plane magnetic field [16]. On 2021, Ngo, Hieu, Lanh, Anh, and Hoi explored exchange field effects on the effective mass and the group velocity in SnTe/ferromagnet heterostructures [14].

SnTe has the potential, due to its unique electronics and thermoelectric properties, to make significant contributions to emerging technologies such as topological quantum computing and low power spintronics devices. Motivated by the noble material properties of SnTe, our aims to examine theoretically the properties of 3D CTI [18]. We will consider the Hamiltonian of surface state electrons under strain and exchange effects, and calculate energy levels via matrix diagonalization. The density of states will be computed using Green's functions. In addition, dynamic properties, group velocity and effective mass, will be investigated. The dynamic properties of the heterostructure of the topological SnTe/ferromagnetic device have not been thoroughly investigated theoretically for spintronic devices. In this paper, we explore these properties to assess the potential of SnTe.

The paper is organized as follows: In Section 2, we present theory. Section 3 shows results. Conclusion is presented in Section 4.

2. Theory and modeling

The surface states of the SnTe (001) TCI and related alloys around the x_1 point can be described by the following effective Hamiltonian [8, 11, 18, 19]:

$$\hat{H}_1(k) = v_1 k_x \sigma_y - v_2 k_y \sigma_x + n \tau_x + \delta \sigma_y \tau_y + M \sigma_z. \quad (1)$$

Here, the first two terms represent the Dirac model, resulting in energy linearly dependent on k , similar to photons. The third and fourth terms are to insure that the Hamiltonian of the (001) surface of SnTe must remain invariant under reflection along the x -axis, reflection along the y -axis, time-reversal symmetry. The last term signifies a mass term, arising from external factors like a ferromagnetic layer or an electric field. The values of the constants in this Hamiltonian are as follows: the Fermi velocity along x -axis given by $v_1 = 1.3 \text{ eV}\cdot\text{\AA}$ and that along the y -axis equals to $v_2 = 2.4 \text{ eV}\cdot\text{\AA}$. The two parameters $n = 0.07 \text{ eV}$ and $\delta = 0.026 \text{ eV}$ represent intervalley scattering at the lattice scale to reproduce the experimental observations [10, 18]. σ and τ are the Pauli matrices in spin and sublattice space.

The Hamiltonian in equation (1) can be diagonalized to find the energy levels:

$$E = \mu \sqrt{v_1^2 k_x^2 + v_2^2 k_y^2 + n^2 + \delta^2 + M^2} + 2v \sqrt{(n^2 + \delta^2)v_1^2 k_x^2 + n^2(v_2^2 k_y^2 + M^2)}, \quad (2)$$

where $\mu = \pm 1$, $v = \mp 1$.

The strain in the 2D materials induces a pseudo-magnetic field, which can be represented in the Hamiltonian as a vector potential. This vector potential shifts the Dirac cones, allowing strain to control the position of the Dirac cones. Here, the same effect is seen, but due to the existence of multi-valley massless Dirac fermions at low energy, which appear as four Dirac points in the surface state (001). Each two of them have the same Hamiltonian because they are projected to the same surface momenta in the Brillouin zone. Therefore, two vector potentials should be included, and from the rotational symmetry between the Dirac points, knowing that the vector potentials are linearly proportional to strain field u_{ij} , then general formula of vector potentials [20, 21]:

$$\mathbf{A}_1 = (\alpha_1 U_{xx} + \alpha_2 U_{yy}, \alpha_3 U_{xy}), \quad (3)$$

$$\mathbf{A}_2 = (\alpha_3 U_{xy}, \alpha_1 U_{yy} + \alpha_2 U_{xx}). \quad (4)$$

Here α_1 , α_2 and α_3 denote three independent constants. Knowing that the shear strain u_{xy} is very small with respect to U_{xx} and U_{yy} , U_{xy} can be ignored. The total vector potential can be written as:

$$\mathbf{A} = (\alpha_1 U_{xx} + \alpha_2 U_{yy}, \alpha_1 U_{yy} + \alpha_2 U_{xx}). \quad (5)$$

Then the shift in the momenta can be written as follows:

$$k_x \rightarrow k_x + \alpha_1 U_{xx} + \alpha_2 U_{yy}, \quad (6)$$

$$k_y \rightarrow k_y + \alpha_1 U_{yy} + \alpha_2 U_{xx}. \quad (7)$$

Under the influence of strain, the momentum will be shifted as expressed in Eqs. (6) and (7). Then, the energy dispersion relation of the SnTe (001) surface state under the influence of strain becomes:

$$E = \mu \sqrt{v_1^2 (k_x + \alpha_1 U_{xx} + \alpha_2 U_{yy})^2 + v_2^2 (k_y + \alpha_1 U_{yy} + \alpha_2 U_{xx})^2 + n^2 + \delta^2 + M^2} + 2vh(k), \quad (8)$$

where,

$$h(k) = \sqrt{(n^2 + \delta^2) v_1^2 (k_x + \alpha_1 U_{xx} + \alpha_2 U_{yy})^2 + n^2 \left(v_2^2 (k_y + \alpha_1 U_{yy} + \alpha_2 U_{xx})^2 + M^2 \right)}. \quad (9)$$

The obtained energy in Eq. (8) will be used to calculate the band structure. Following this, the dynamic properties will be investigated, and the density of states using Green's functions will be computed. Thermal and magnetic properties will then be studied.

The partition function ($Z = \sum_n e^{-\beta E_n}$) is a fundamental and crucial quantity in statistical mechanics used to calculate thermal and magnetic properties.

The average energy is the average of all possible state at certain temperature which is defined as $\langle E \rangle = -\frac{\partial \ln(Z)}{\partial \beta}$. The average energy can be used to evaluate the magnetization, one of the most important magnetic properties, which indicates the response of the material's electrons' spin to an external magnetic field. It is defined as: $\langle \mathbf{M} \rangle = -\frac{\partial \langle E \rangle}{\partial B}$. Then, the magnetic susceptibility which classes the materials to diamagnetic ($\chi < 0$) and paramagnetic ($\chi > 0$), is defined as: $\chi = \frac{\partial \langle \mathbf{M} \rangle}{\partial B}$. It's also important to study the thermal properties to assess its thermal applications, such as whether the material acts as a thermal insulator or conductor, and whether it exhibits magnetocaloric properties. Magnetocaloric materials can be used for heating or cooling by applying a magnetic field.

Entropy is a measure of the disorder or randomness in a system, which can be used to check the magnetocaloric effect: $\langle S \rangle = \frac{\partial}{\partial T} \left(\frac{1}{\beta} \ln(Z) \right)$.

Dynamic properties such as group velocity $\mathbf{v}_g = \frac{1}{\hbar} \nabla_{\mathbf{k}} E(k)$ and effective mass $m^* = \frac{\hbar^2}{\nabla_{\mathbf{k}}^2 E(k)}$ are essential properties for assessing the electronic applications of a material because the material's mobility depends on them.

Density of state which is the number of states per unit energy can give a lot of information about the band structure, Density of state mathematically is the delta function and it can be written in term of Green's function. Starting from the relationship between energy and wavefunction which is described by the Schrödinger equation $H\psi_n = E_n\psi_n$. The density of states can be expressed as the Dirac delta function of the energy: $D(E) = \sum_n \delta(E - E_n)$. The Green function

is given by the following formula: $G = \frac{1}{E + i\varepsilon - H}$, where H is the Hamiltonian, E is the energy, and ε is very small real number.

Let us multiply the Green function by $|\psi_n\rangle$ from the right, and $\langle \psi_l |$ from the left and sum over all values of n and l . This results in:

$$\sum_{n,l} \langle \psi_l | \psi_n \rangle \frac{1}{E + i\varepsilon - E_n} = \sum_{n,l} \delta_{n,l} \frac{1}{E + i\varepsilon - E_n} = \sum_n \frac{1}{E + i\varepsilon - E_n}.$$

It is obvious that only the diagonal elements of the G matrix have non-zero values. To obtain the density of states from the Green function, let's take the imaginary part of the Green function, as follows:

$$\sum_n G_n = \sum_n \frac{1}{E - E_n + i\varepsilon} \frac{E - E_n - i\varepsilon}{E - E_n - i\varepsilon} = \sum_n \frac{E - E_n - i\varepsilon}{(E - E_n)^2 + \varepsilon^2}, \quad (10)$$

$$\sum_n \text{Im}(G_n) = \sum_n -\frac{\varepsilon}{(E - E_n)^2 + \varepsilon^2}. \quad (11)$$

The Dirac delta function can be written in terms of the Lorentzian function, and the result is as follows:

$$\text{DOS}(E) = \sum_n \delta(E - E_n) = \lim_{\varepsilon \rightarrow 0} -\frac{1}{\pi} \sum_n \frac{\varepsilon}{(E - E_n)^2 + \varepsilon^2} = -\frac{1}{\pi} \lim_{\varepsilon \rightarrow 0} \sum_n \text{Im}(G_n). \quad (12)$$

3. Results and discussions

In this section, we will study in detail the effects of strain on the main properties of the electrons. It is obvious from the strained Hamiltonian that the strain effect shifts the Dirac cone. Therefore, the strain effect can be utilized to control the properties of the SnTe (001) surface state.

In Fig. 1(a, and b), we used the strained dispersion relation to display the variation of the electron velocity as function of the strain. Fig. 1 represents the x -component of the group velocity of Dirac fermions at the Dirac point of momentum ($k_x = \sqrt{n^2 + \delta^2}/v_1$, $k_y = 0$), both in the first and second conduction states. In Fig. 1(a), the x -component of the group velocity is plotted as a function of U_{xx} . It is obvious that the x -component of group velocity changes with variations in U_{xx} . In the first conduction state, when U_{xx} is negative (tensile strain), the x -component of group velocity is negative and close to zero. However, with very small positive values of U_{xx} (compress strain), v_x remains negative and then it changes significantly and reach its minimum value as U_{xx} approaching $\sqrt{n^2 + \delta^2}/v_1$. Then, as U_{xx} increases v_x converges to small positive value which means that the electron wave is propagating along the positive x -direction. The observed behavior can be attributed to the role of strain as an effective vector potential within a specific range of applied strain or stress. In this regime, strain modifies the electronic band structure, leading to an increase in energy around the Dirac cone

as a function of momentum. Consequently, the group velocity, which is defined as the gradient of energy with respect to crystal momentum, aligns with the direction of the crystal momentum itself. This results in a conventional electron-like behavior, where charge carriers exhibit positive effective mass characteristics.

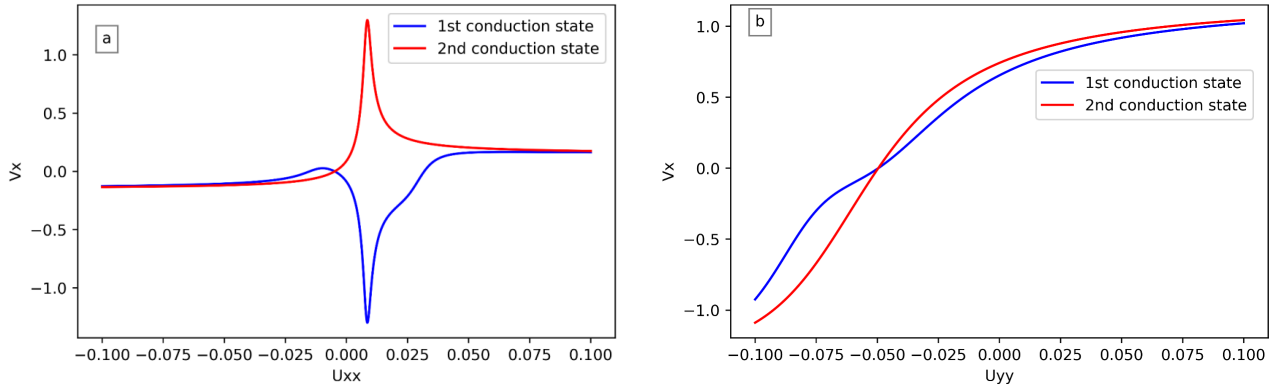


FIG. 1. x -component group velocity of Dirac fermions on SnTe (001) surface state with momentum $(\sqrt{n^2 + \delta^2}/v_1, 0)$ as a function of strain: (a) $U_{yy} = -0.04$; (b) $U_{xx} = 0.04$

However, if the applied strain or tensile deformation induces a shift in the Dirac point such that the crystal momentum is oriented opposite to the group velocity, the charge carriers within this regime will exhibit hole-like behavior. This phenomenon arises due to the band structure modification, where the energy-momentum dispersion relation is altered, effectively inverting the sign of the charge carrier velocity. In such cases, electrons in these regions behave similarly to holes, meaning they move as if they possess a positive charge within the material's electronic structure.

In the second conduction state when U_{xx} is negative/positive (tensile/compress strain), the x -component of group velocity converges to the same value as of the first conduction state. The only difference that around $U_{xx} = \sqrt{n^2 + \delta^2}/v_1$. The group velocity changes drastically to reach its positive maximum.

Fig 1(b) represents the x -component of group velocity of Dirac fermions that have $(\sqrt{n^2 + \delta^2}/v_1, 0)$ momentum in the SnTe (001) surface state in the first and second conduction states as a function with U_{yy} , when U_{yy} is negative, both fermions in the first and second conduction states have a negative group velocity, and the value of the x -component of the group velocity of fermions in the first conduction state is greater than the x -component of the group velocity in the second conduction state. Near $U_{yy} = -0.05$ (i.e when $U_{yy} = -\sqrt{n^2 + \delta^2}/v_1$) the group velocities in the first and second conduction states reach zero.

U_{yy} continues to increase, the x -component of the group velocity in both the first and second conduction states flips to positive values. At this critical value of U_{yy} , the wave propagation is switching from negative x -direction to positive one. Furthermore, the velocity becomes greater in the second conduction state. and as U_{yy} gets larger and larger the velocity in both bands converges to v_1 .

Due to the importance of saddle points, the group velocity in the y -direction of the Dirac fermions at the saddle point is studied as a function of strain. Fig. 2 demonstrates the y -component of the group velocity as a function of strain tensor components. At the saddle points, there are no Dirac points in the y -direction, but the strain components affect the group velocity at the saddle point. If the strain is included as a vector potential, it shifts the Dirac points, affecting the entire band structure (breaking inversion symmetry). As a result, the energy, as a function of crystal momentum, changes. Within a certain range of strain, the energy increases as a function of crystal momentum, leading to a positive group velocity. Conversely, within another range of energy, the group velocity decreases as a function of crystal momentum, resulting in a negative group velocity. Notice, if $U_{yy} < -0.123$, the y -component of the group velocity of the Dirac fermions in both the first and second conduction states is negative (the energy decrease as a function of crystal momentum), and the fermions in the second conduction state have a greater group velocity. At $U_{yy} = 0.0123$, the group velocity of fermions in both states vanishes. If $U_{yy} > 0.0123$ the y -component of the group velocity of fermions in both states becomes positive (the energy increases as a function of crystal momentum).

Figure 2(b) represents the y -component of the group velocity of the Dirac fermions, at the saddle point in the first and second conduction states, as a function of U_{yy} . The y -component of the group velocity in both conduction states is positive, fermions in the second conduction state have greater y -component group velocity when $U_{yy} < -0.047$. For $-0.047 < U_{yy} < 0.029$, fermions in the first conduction state have a greater y -component group velocity, while for $U_{yy} > 0.029$, fermions in the second conduction state have a greater y -component group velocity

As has been mentioned earlier, the strain effect shifts the Dirac cone, which can be used to tune the properties of the surface state Dirac fermions in SnTe (001). One of the most important parameters for understanding the behavior of fermions is effective mass. Effective mass (which is the mass of electrons in the crystal) is the dynamical quantity which

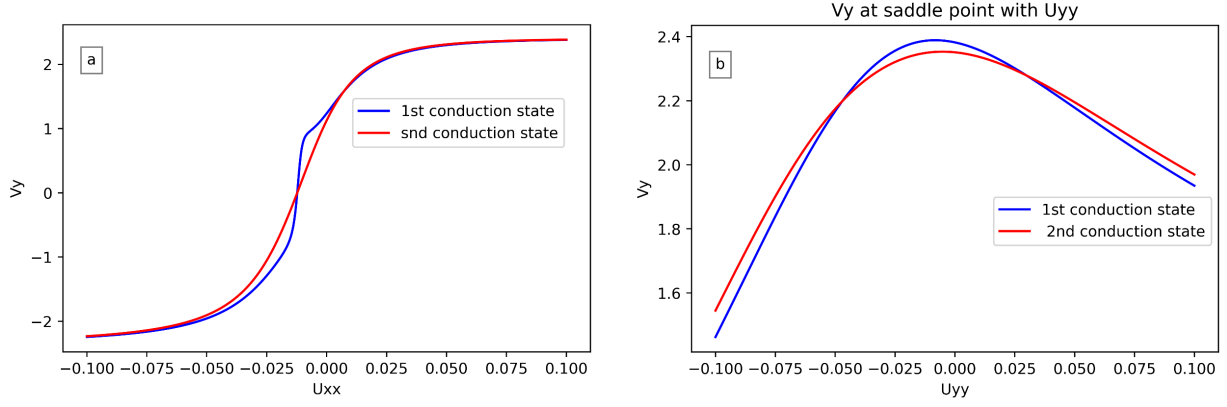


FIG. 2. y -component group velocity of Dirac fermions on SnTe (001) surface state that have $(0, n/v_2)$ momentum as a function of strain: (a) $U_{yy} = -0.04$; (b) $U_{xx} = 0.04$

is equal the reciprocal of the second derivative of the energy with respect to the crystal momentum. Fig. 3 represents the reciprocal of the effective mass in the x -direction for electrons in the conduction band as a function of strain tensor components at the Dirac point. The sign of the effective mass is determined by the curvature of the energy spectrum. In the first conduction state, the electrons are highly massive and behave like electrons due to the positive sign of the effective mass for $U_{xx} < -0.015$. However, when the energy is concave down the sign of the effective mass is negative as the first conduction band in Fig. 3(a), and the electrons behave like holes (they move in opposite direction to field lines in an electric field). In the range of $-0.015 < U_{xx} < 0.031$, the sign of the effective mass is negative, due to the downward concavity in the band curve in this region. So electrons behave like holes. Within this range of strain, the effective mass reaches two minimum values: one at $U_{xx} = 0.0063$ which is the absolute minimum and the other one at $U_{xx} = 0.011$. When $U_{xx} > 0.031$ the sign of the effective mass becomes positive again, and electrons behave like electrons, exhibiting high mass.

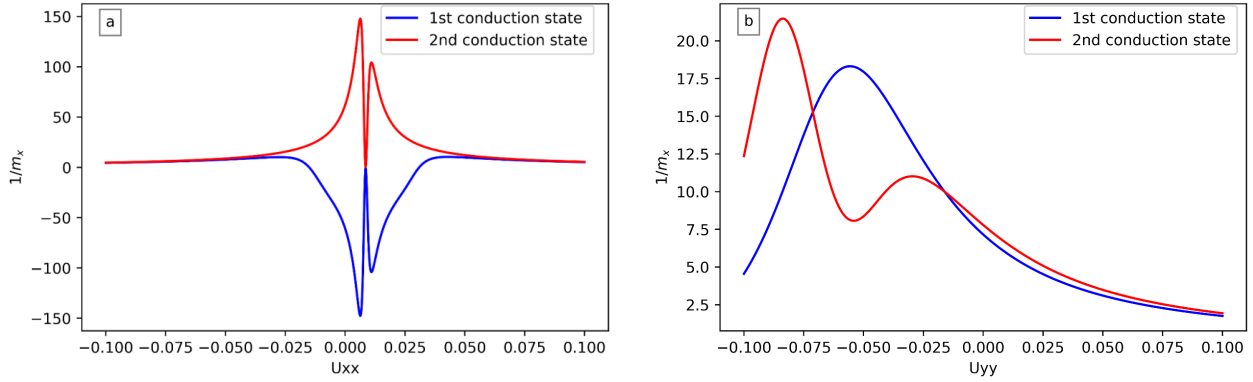


FIG. 3. Reciprocal effective mass in x -direction of the Dirac fermions on SnTe (001) surface state that have $(\frac{\sqrt{n^2 + \delta^2}}{v_1}, 0)$ momentum as a function of strain: (a) $U_{yy} = -0.04$, (b) $U_{xx} = 0.04$

In the second conduction state, the sign of the effective mass of Dirac fermions is positive for the strain range of $-0.1 < U_{xx} < 0.1$, indicating that electrons behave normally. However, in the range $U_{xx} < -0.015$ and $U_{xx} > 0.011$, the electrons exhibit high effective mass. The effective mass reaches its minimum values in the range of $-0.015 < U_{xx} < 0.011$ with one minimum at $U_{xx} = 0.0063$ which is the absolute minimum and the other one is at $U_{xx} = 0.011$.

Figure 3(b) represents the reciprocal effective mass in x -direction of Dirac fermions with $(\frac{\sqrt{n^2 + \delta^2}}{v_1}, 0)$ momentum as a function of U_{yy} , at $U_{xx} = 0.04$ in the first and second conduction states, in both states the sign of effective mass is positive so the electrons behave normally in these states.

When $U_{yy} < -0.56$, the effective mass in y -direction in the first conduction state decreases until it reaches its minimum value at $U_{yy} = -0.56$. when $U_{yy} > -0.56$ the effective mass increases.

In the second conduction state, the effective mass decreases when $U_{yy} < -0.084$, at this point the effective mass reaches an absolute minimum, for $-0.084 < U_{yy} < -0.054$, the effective mass increases. For $-0.054 < U_{yy} < -0.0295$,

the effective mass decreases again and reaches second minimum value at $U_{yy} = -0.0295$. When $U_{yy} > -0.0295$, the effective mass increases once more.

Figure 4(a and b) shows the effective mass in the y -direction at the saddle point as a function of the strain tensor components. The effective mass for both the first and second conduction states is positive, indicating that the energy states are concave up as a function of crystal momentum, and the electrons behave normally. In the first conduction state, the effective mass reaches an absolute minimum at $U_{xx} = -0.012$, and there is another minimum value of the effective mass at $U_{xx} = 0$. In the second conduction state, there is a minimum value at $U_{xx} = -0.011$. The effective mass can be negative only in the x -direction and for electrons in the first conduction state. This occurs because, in topological insulators, the first energy state bends only between the two Dirac points in the first conduction state.

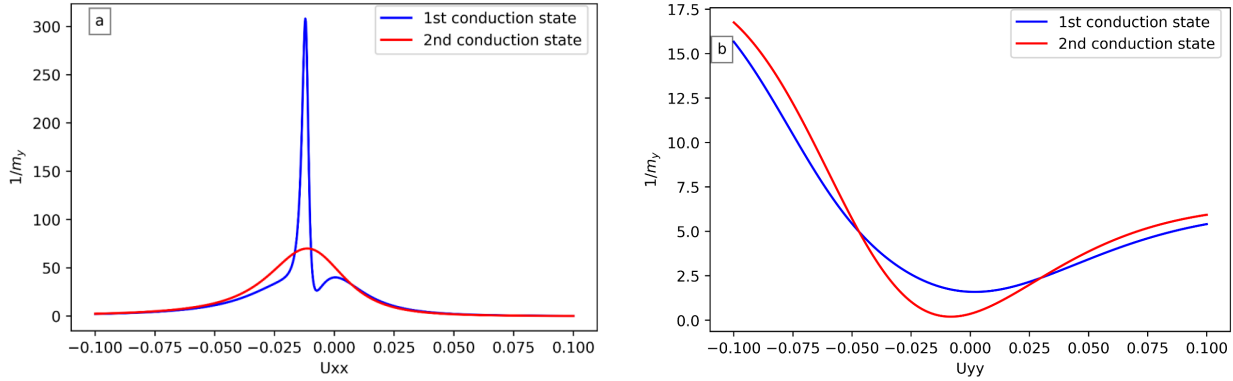


FIG. 4. Reciprocal effective mass in y -direction of the Dirac fermions on SnTe (001) surface state at the saddle point as a function of strain: (a) $U_{yy} = -0.04$; (b) $U_{xx} = 0.04$

Figure 4(b) represents the effective mass in y -direction as a function of U_{yy} at $U_{xx} = 0.04$, in both the first and second conduction states, the sign of the effective mass is positive, so the electrons behave like electrons.

In the first conduction state, the effective mass increases when $U_{yy} < 0.0019$, at $U_{yy} = 0.0019$ the effective mass reaches its maximum value. Then, when $U_{yy} > 0.0019$ the effective mass decreases.

In the second conduction state, the effective mass of Dirac fermions exhibits the same behavior, but it reaches its maximum value at $U_{yy} = -0.0083$. It's worth noting that the effective mass in the first conduction state is greater than that in the second conduction state when $-0.05 < U_{yy} < 0.028$, However, the effective mass in the second conduction state is greater when $U_{yy} < -0.05$ and $U_{yy} > 0.028$. In typical materials, the group velocity and the effective mass usually have the same sign. However, this can change in the presence of strong structural inversion asymmetry, which can arise due to spin-orbit interaction or strain, as in our case. By comparing our first four figures, we can identify regions where the signs of the effective mass and the group velocity differ.

4. Density of state of the Dirac fermions in 3D SnTe (001) surface state under combined exchange and strain effects

Density of state $D(E)$, which represents the number of states per unit energy, is a fundamental characteristics in solid state physics and condensed matter. It is used to study the electronic structure and the carrier concentration, which, in turn, determine the type of matter and its conductivity. Therefore, the density of state of the Dirac fermions in SnTe (001) surface state will be explored in this section.

Figure 5 displays the density of states $D(E)$ of the Dirac fermion surface states as a function of energy. Fig. 5(a) represents the pristine SnTe density of states, which is zero at zero energy and has a maximum value at $E = \pm\delta$, known as the Van Hove singularities. It is expected that the density of states has a maximum at $E = \pm\delta$ due to these being the energy values of the saddle points, and it has a local minimum at $E = \pm\sqrt{n^2 + \delta^2}$ located at $K = 0$.

Including the exchange effect ($M \neq 0$) which is a ferromagnetic substrate in our case, opens up an energy band gap E_g . Within this band gap, the density of states effectively approaches zero, as illustrated in Fig. 5(b). It's important to note that, as the exchange effect increases, the band gap widens, consequently expanding the energy range associated with zero density of states, the minimum point shift to the right. The density of state value at $E = \pm\delta$ increases when $-0.056 < M < 0.056$ and decreases when $M < -0.056$ and $M > 0.056$ as obvious in Fig. 6 which represent the density of state as a function of exchange effect when $E = \pm\delta$.

Figures 5(c and d) represents the density of states as a function of energy under the effect of x -direction uniaxial strain U_{xx} and y -direction uniaxial strain U_{yy} . The density of states at Van Hove singularities decreases with strain, indicating a decrease in the concavity of the bands in the y -direction. The Dirac points along the x -direction remain when the strain is small, but as the strain becomes sufficiently strong, the Dirac points are destroyed and an energy gap opens in

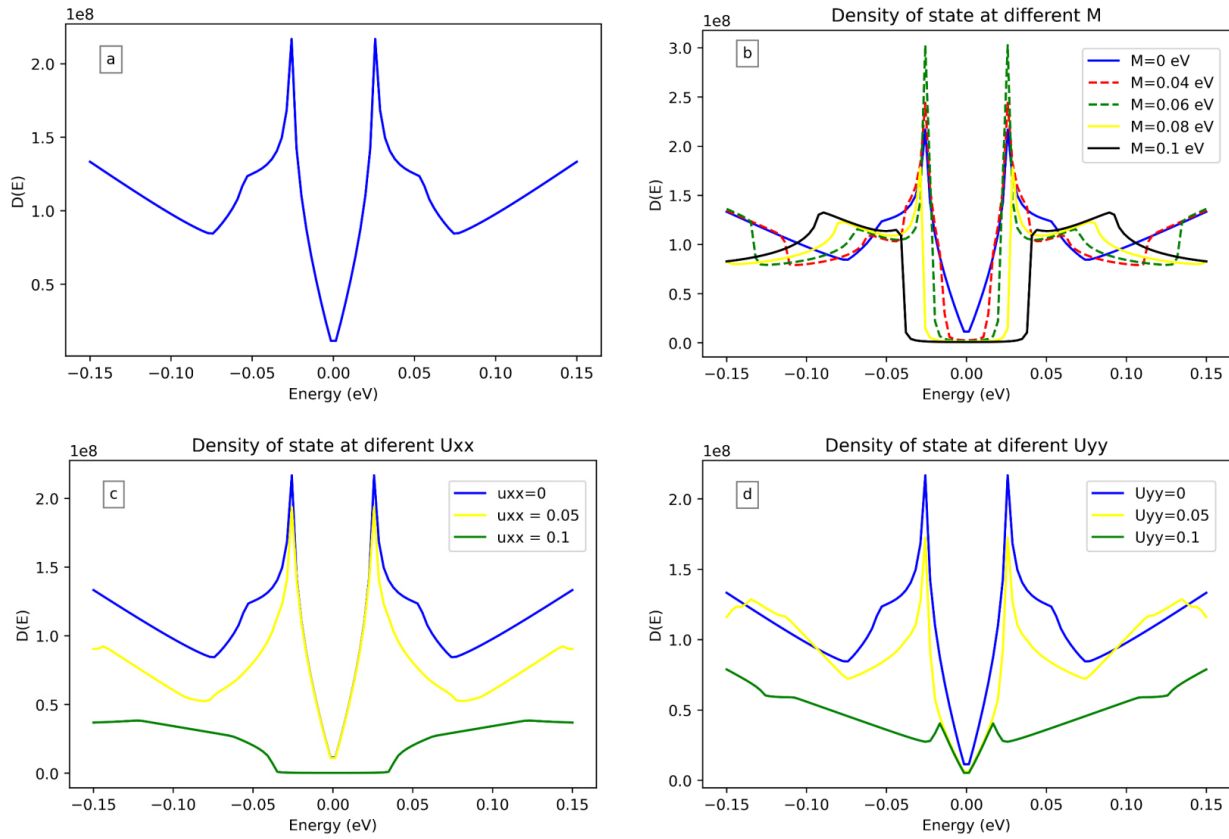


FIG. 5. Density of state of the Dirac fermions in SnTe (001) surface state as a function of energy: (a) Pristine SnTe; (b) at different values of M and zero strains; (c) at different values of uniaxial strain U_{xx} , $U_{yy} = 0$ and $M = 0$; (d) at different values of uniaxial strain U_{yy} , $U_{xx} = 0$ and $M = 0$

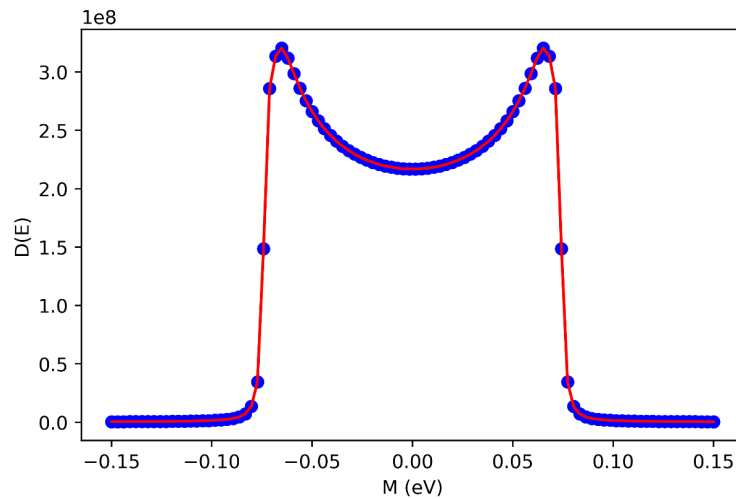


FIG. 6. Density of state of the Dirac fermions of SnTe (001) surface state as a function of exchange effect at $E = \pm\delta$

the x -direction. This effect becomes evident when $U_{xx} = 0.1$. Additionally, the minimum, located at $E = \pm\sqrt{n^2 + \delta^2}$ and $k = 0$, disappears when the strain becomes large enough.

5. Thermal properties of Dirac fermions of SnTe (001) surface state

Due to the importance of the thermal properties in thermal applications such as heating or cooling and thermal insulation, in this section, thermal properties such as heat capacity and entropy of the SnTe (001) surface state will be discussed.

The heat capacity represents the first derivative of the average energy with respect to temperature. Fig. 7 shows the heat capacity as a function of temperature, with Fig. 7(a) showing the heat capacity at different values of the exchange effect. When $M = 0$, the Schottky anomaly point which corresponds to the peak in the heat capacity curve occurs at 451.52 K. When M changes to 0.02 and $M = 0.04$, the Schottky anomaly point shifts to the right; when $M = 0.06$ and $M = 0.08$, it shifts to the left. Interestingly, when $M = 0.1$, the Schottky anomaly point shifts to the right again, as evident in Table 1. The heat capacity decreases as M increases (for $M = 0.02, 0.04, 0.06$, and 0.08). As the exchange effect increases, the heat capacity decreases. This occurs because the exchange effect opens an energy band gap, shifting the conduction states to higher energies. At low temperatures, the available thermal energy (given by $K_B T$) is small, making the higher-energy electronic states inaccessible.

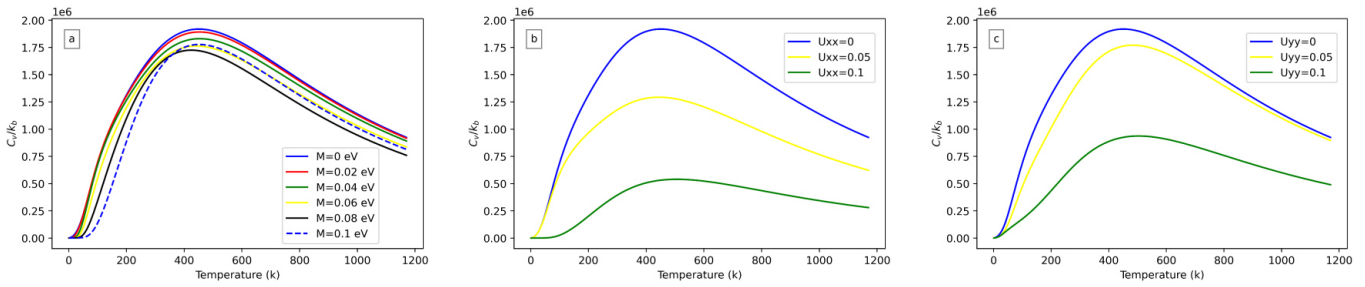


FIG. 7. Heat capacity of the Dirac fermions of SnTe(01) surface state as a function of temperature (a) at various values of exchange effect; (b) at different values of uniaxial strain in x -direction U_{xx} ; (c) at different values of uniaxial strain in y -direction U_{yy}

TABLE 1. Temperature of the Schottky anomaly point at different values of the exchange effect (M)

M	0	0.02	0.04	0.06	0.08	0.1
Temperature (K)	451.51	452.69	453.86	442.15	424.6	451.51

Figure 7(b and c) represents the heat capacity of the Dirac fermions at different values of uniaxial strain in x -direction and in y -direction. It is found that in both cases the heat capacity decreases when increasing the strain and the Schottky anomaly point shifts as indicated in Tables 2 and 3. This occurs because the strain increasing shifts the Dirac points to higher values of crystal momentum, leading to a decrease in the density of states, as shown in Fig. 5(b and c). Since the heat capacity is proportional to $D(E)$, its value is reduced by decreasing of $D(E)$.

TABLE 2. Temperature of the Schottky anomaly point at different values of uniaxial x -direction strain (U_{xx})

U_{xx}	0	0.05	0.1
Temperature (K)	451.51	444.49	506.51

TABLE 3. Temperature of the Schottky anomaly point at different values of uniaxial y -direction strain (U_{yy})

U_{yy}	0	0.05	0.1
Temperature (K)	451.51	484.28	504.17

Entropy is an important quantity in thermodynamics, predicting the direction of spontaneous processes, such as heat transfer, chemical reactions, and phase changes. In statistical mechanics, it provides a bridge between the macroscopic

properties and microscopic configurations of a system, because it can be defined as the number of microscopic configurations consistent with a given macroscopic state of a system. Here the entropy of the Dirac fermions in SnTe (001) surface state will be studied.

Figure 8 represents the entropy as a function of temperature at different values of the exchange effect (Fig. 8(a)) and uniaxial strain (Fig. 8(b,c)), all these effects have the same qualitative influence on the entropy of the system: they decrease the entropy of the Dirac fermions. This occurs due to a decrease in the disordering of the system. Note that the entropy decreases more significantly when the strain is applied in the x -direction as shown in Fig. 8(b), in contrast to the y -direction as in Fig. 8(c).

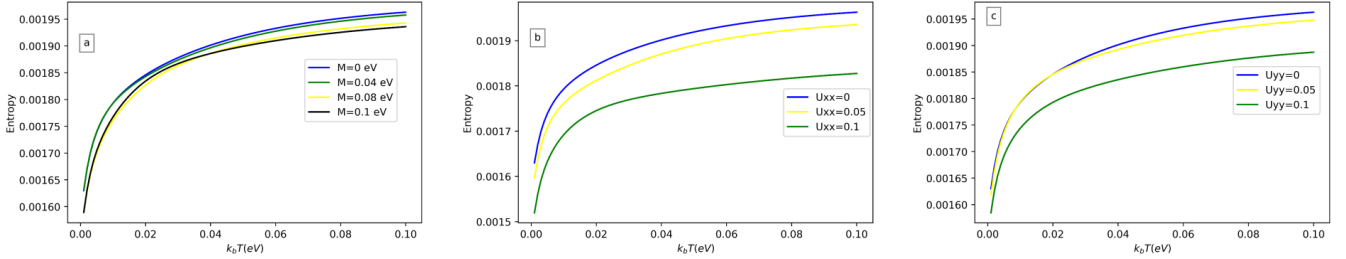


FIG. 8. Entropy of the Dirac fermions in SnTe (001) surface state as a function of temperature: (a) at different values of the exchange effect; (b) at different values of x -direction strain U_{xx} ; (c) at different values of y -direction strain U_{yy}

6. Magnetic properties of the Dirac fermions of 3D SnTe (001) surface state

Magnetic properties such as magnetization M and magnetic susceptibility X are important in applications such as magnetic devices, sensors, detectors, and data storage. Magnetic susceptibility, which classifies materials into paramagnetic ($X > 0$) and diamagnetic ($X < 0$) categories, will be calculated.

Figure 9 represents the magnetic susceptibility as a function of temperature at different exchange effects and various uniaxial strain values. SnTe is a paramagnetic material since its magnetic susceptibility is greater than zero. However, the magnetic susceptibility decreases with increasing exchange effect or uniaxial strain, yet it remains greater than zero. Thus, SnTe remains paramagnetic under the influence of both the exchange effect and uniaxial strains. In Dirac materials, the magnetic susceptibility is zero because two conduction bands are identical. It means that there are no single electrons. However, in topological insulators, these identical states split into two spin-dependent states, leading to the presence of single electrons, which results in a magnetic susceptibility greater than zero. As the exchange effect or strain tensor components increase, the density of states decreases, reducing the number of single electrons and consequently decreasing the magnetic susceptibility.

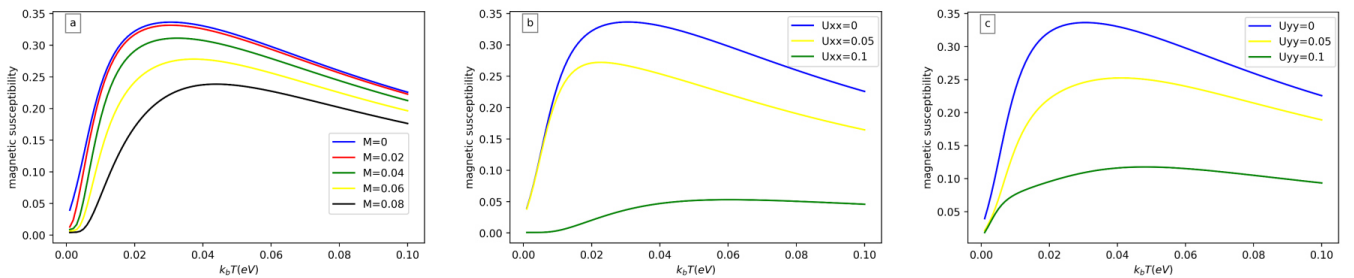


FIG. 9. Magnetic susceptibility of the Dirac fermions at SnTe (001) surface state as a function of temperature at (a) different value of exchange effect; (b) different values of uniaxial strain in x -direction U_{xx} ; (c) different values of uniaxial strain in y -direction U_{yy}

7. Conclusion

This study has provided a comprehensive theoretical investigation into the electronic, thermal, and magnetic properties of topological insulators. By analyzing crystalline topological insulator SnTe, we have gained valuable insights into the behavior of these materials under different conditions. Our analysis revealed significant alterations in electronic properties due to the effects of exchange and strain. The examination of the group velocity, the effective mass, and the density of states provided a detailed understanding of its electronic structure. Furthermore, our investigation into thermal

and magnetic properties shed light on its potential applications in diverse fields, ranging from electronics to magnetism. It's obvious that the strain effect and the exchange effect can be used to control the properties of SnTe.

References

- [1] Moore J.E. The birth of topological insulators. *Nature*, 2010, **464** (7286), P. 194–198.
- [2] Qi, Xiao-Liang, Shou-Cheng Zhang. Topological insulators and superconductors. *Reviews of Modern Physics*, 2011, **83** (4), P. 1057–1110.
- [3] Moore J. The next generation. *Nature Physics*, 2009, **5** (6), P. 378–380.
- [4] Zhang, Haijun, et al. Topological insulators in Bi_2Se_3 , Bi_2Te_3 and Sb_2Te_3 with a single Dirac cone on the surface. *Nature Physics*, 2009, **5** (6), P. 438–442.
- [5] Hasan, Zahid M., Moore J.E. Three-dimensional topological insulators. *Annu. Rev. Condens. Matter Phys.*, 2011, **2** (1), P. 55–78.
- [6] Batra, Navketan, Goutam Sheet. Physics with coffee and doughnuts: Understanding the physics behind topological insulators through Su-Schrieffer-Heeger model. *Resonance*, 2020, **25** (6), P. 765–786.
- [7] Boothroyd A.T. Topological electronic bands in crystalline solids. *Contemporary Physics*, 2022, **63** (4), P. 305–327.
- [8] Furchi, Marco, et al. Microcavity-integrated graphene photodetector. *Nano Letters*, 2012, **12** (6), P. 2773–2777.
- [9] Ma, Eric Yue, et al. Unexpected edge conduction in mercury telluride quantum wells under broken time-reversal symmetry. *Nature Communications*, 2015, **6** (1), 7252.
- [10] Xu, Su-Yang, et al. Observation of a topological crystalline insulator phase and topological phase transition in $\text{Pb}_{1-x}\text{Sn}_x\text{Te}$. *Nature Communications*, 2012, **3** (1), 1192.
- [11] Tanaka Y., et al. Experimental realization of a topological crystalline insulator in SnTe. *Nature Physics*, 2012, **8** (11), P. 800–803.
- [12] Dziawa P., et al. Topological crystalline insulator states in $\text{Pb}_{1-x}\text{Sn}_x\text{Se}$. *Nature Materials*, 2012, **11** (12), P. 1023–1027.
- [13] Hsieh, Timothy H., et al. Topological crystalline insulators in the SnTe material class. *Nature Communications*, 2012, **3** (1), 982.
- [14] Ngo B.V.Q., et al. Exchange field effects on the electronic properties of heterostructured ferromagnetic/topological crystalline insulator. *Physica E: Low-dimensional Systems and Nanostructures*, 2021, **126**, 114441.
- [15] Liu, Junwei, Wenhui Duan, Liang Fu. Two types of surface states in topological crystalline insulators. *Physical Review B – Condensed Matter and Materials Physics*, 2013, **88** (24), 241303.
- [16] Hsieh D., Xia Y., Wray L., Qian D., Pal A., Dil J. H., Osterwalder J., Meier F., Bihlmayer G., Hasan M.Z. Observation of unconventional quantum spin textures in topological insulators. *Science*, 2009, **323** (5916), P. 919–922.
- [17] Pham, Khang D., et al. Controlling anisotropic surface group velocity and effective mass in topological crystalline insulator SnTe by Rashba effect. *Physica E: Low-dimensional Systems and Nanostructures*, 2020, **120**, 114118.
- [18] Mitchell D.L., Wallis R.F. Theoretical energy-band parameters for the lead salts. *Physical Review*, 1966, **151** (2), 581.
- [19] Ando, Yoichi, Liang Fu. Topological crystalline insulators and topological superconductors: From concepts to materials. *Annu. Rev. Condens. Matter Phys.*, 2015, **6** (1), P. 361–381.
- [20] Tang, Evelyn, Liang Fu. Strain-induced partially flat band, helical snake states and interface superconductivity in topological crystalline insulators. *Nature Physics*, 2014, **10** (12), P. 964–969.
- [21] Tien, Tong S., Pham TC Van, Le P.T.T. The strain and electric field modulation of magnetic properties in topological crystalline insulator thin films. *Chemical Physics Letters*, 2020, **751**, 137512.

Submitted 23 January 2025; revised 29 March 2025; accepted 31 March 2025

Information about the authors:

Khaled Abdulhaq – Physics department, An-Najah National University, Nablus, Palestine; khaled.j.abdulhaq@gmail.com

Mohammad K. Elsaid – Physics department, An-Najah National University, Nablus, Palestine; ORCID 0000-0002-1392-3192; mkelsaid@najah.edu

Diana Dahliah – Physics department, An-Najah National University, Nablus, Palestine; ORCID 0000-0002-6919-3539; diana.dahliah@najah.edu

Conflict of interest: the authors declare no conflict of interest.

Understanding the electronic properties of carbon polyprismanes from the sp^3 tight-binding model

Vladimir A. Kurakin¹, Tatyana N. Kobernik²¹National Research Nuclear University MEPhI, Moscow, Russia²Energy Technology Center, Skolkovo Institute of Science and Technology, Moscow, RussiaCorresponding author: Vladimir A. Kurakin, fromkurakin@mail.ru

ABSTRACT Carbon polyprismanes are 1D nanostructures that should be classified as diamond-like phases because they (polyprismanes) also consist of the 4-coordinated carbon atoms. A carbon polyprismane contains polygonal atomic rings arranged in layers along the common symmetry axis, at uniform distances from each other. According to previous density functional theory based studies, carbon polyprismanes can exhibit metallic conductivity, which is very unusual for diamond-like phases. In this paper, we present the sp^3 tight-binding model based calculations of the band structures for carbon polyprismanes of different diameters and compare the obtained results with their analogs for a 2D square carbon lattice, which can be considered as the limiting case of a carbon polyprismane of infinite diameter. Our results confirm that the sp^3 tight-binding model describes the electronic properties of carbon polyprismanes well, since we obtain their band structures over a wide range of parameter values for the proposed model. We believe that such electronic transport characteristics are an intrinsic topological feature of polyprismanes and should also occur in non-carbon polyprismanes.

KEYWORDS band structure, tight-binding model, polyprismane, carbon nanostructures

FOR CITATION Kurakin V.A., Kobernik T.N. Understanding the electronic properties of carbon polyprismanes from the sp^3 tight-binding model. *Nanosystems: Phys. Chem. Math.*, 2025, **16** (2), 209–215.

1. Introduction

In recent years, carbon nanotubes (CNTs) have found increasingly diverse applications in nanotechnology, engineering, and industry. CNTs are actively used in the fabrication of various electronic components such as ionic diodes [1], electrodes [2], and field-effect transistors (FETs) [3–5]. Many of the modern advances in CNT-based electronics have evolved from devices employing a single CNT to implementations using aligned CNTs and even CNT thin films, as demonstrated in [6]. Aligned CNT-based field-effect transistors have already been scaled down to sizes below 10 nm, surpassing their silicon counterparts in terms of charge carrier mobility and the Fermi velocity [7]. Moreover, artificial synaptic thin-film transistors, fabricated on an ultrathin flexible substrate with semiconductor single-walled CNTs (SWCNTs) exhibiting high charge carrier mobility, have proved useful for the development of neuromorphic electronic skin [8]. In addition, CNTs have helped researchers fabricate highly conductive polymer composites for rapid-response electrical heaters [9] and even electroactive porous filters for water purification [10].

A notable feature of CNTs is that their carbon atoms are in an sp^2 -hybridized state and can form additional covalent bonds. Consequently, CNTs tend to be quite sensitive to environmental contaminants (free radicals). Carbon polyprismanes (CPPs), or $C_{[n,m]}$ prismanes – systems of regular atomic m -gons stacked in layers along a common symmetry axis at uniform inter-layer distances (n is the number of such m -gons; see Fig. 1) – do not suffer from this disadvantage because the atoms in such CPPs are in an sp^3 -hybridized state and cannot form any additional covalent bonds. CPPs also have much smaller cross-sectional areas compared to SWCNTs. These two factors make $C_{[n,m]}$ prismanes particularly attractive in certain high-tech applications requiring atomic-scale precision (e.g., in the fabrication of ultrathin nanoneedles for biological applications or tips for atomic force microscopy [11]).

However, CPPs are not without their drawbacks, one of which is low thermal stability. Thus far, only the simplest $C_{[n,m]}$ prismanes have been synthesized [12–14]. Nevertheless, we believe that even these CPPs can be very useful in nanoelectronics. It is well known that scaling down FET contact lengths is challenging as it can degrade device performance [15]. Some studies report significant deterioration of FETs at their contact lengths below 30 nm [16]. We believe that even the simplest $C_{[n,m]}$ prismanes could be promising candidates for nanomaterials to help solve these scaling issues.

In addition, computational modeling indicates that long ($n \geq 10$ or even $n \rightarrow \infty$) $C_{[n,4]}$, $C_{[n,5]}$, and $C_{[n,6]}$ prismanes are sufficiently stable [17, 18], and also predicts the feasibility of creating $C_{[3,4]}$ and $C_{[4,4]}$ prismanes [19]. Direct molecular-dynamics simulations confirm the high kinetic stability of short $C_{[2,6]}$ and $C_{[2,8]}$ prismanes [20]. Density functional theory (DFT) calculations have also been applied to study specific CPP-based electronic components, such as Schottky nanodiodes [21].

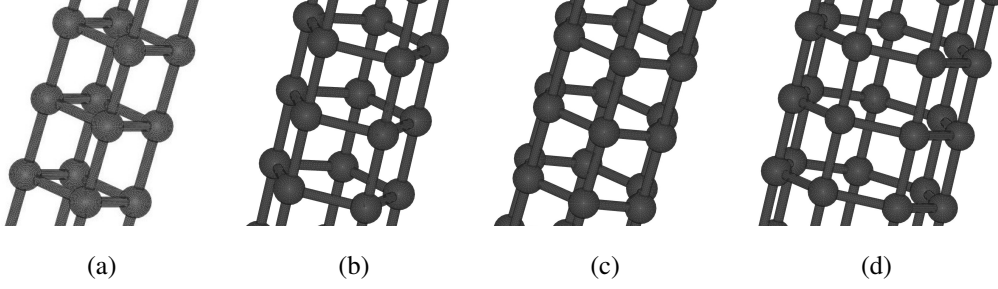


FIG. 1. Atomic structures of $C_{[n,4]}$ (a), $C_{[n,5]}$ (b), $C_{[n,6]}$ (c), and $C_{[n,7]}$ (d) prismanes

Many diamond-like phases are very robust and can withstand substantial mechanical loads, as demonstrated by atomistic modeling [22–24]. Some diamond-like phases have hardness values comparable to that of diamond [25]. Such distinctive physical properties open a broad range of commercial applications for diamond-like phases. Furthermore, like diamond, most diamond-like phases comprise fully sp^3 -bonded carbon atoms and often have sizable (> 3.0 eV) band gaps (diamond’s band gap is about 5.45 eV [26]), i.e., they display dielectric behavior [27]. Although $C_{[n,m]}$ prismanes are structural units of diamond-like phases, CPPs can exhibit metallic conductivity, which is highly unusual for sp^3 -hybridized carbon materials. This has been shown via DFT-based studies [28, 29]. Notably, analogous metallic properties also appear in silicon and germanium (classical semiconductors) polyprismanes [30–32], suggesting that the electrical transport characteristics of $C_{[n,m]}$ prismanes are driven by their topology rather than by carbon’s intrinsic nature.

The tight-binding model (TBM) is a relatively simple and intuitive approach to calculating the band structures of both carbon [33, 34] and non-carbon [35–37] materials. In this paper, we understand the metallic conductivity of CPPs from the sp^3 tight-binding model (sp^3 -TBM).

2. Materials and methods

We applied the sp^3 -TBM to compute the band structures of sufficiently long $C_{[n,m]}$ prismanes ($n \rightarrow \infty$, $m = 4, 5, 6, 7$). The $2s$, $2p_x$, $2p_y$, and $2p_z$ orbitals of each carbon atom were used as the basis set for expressing this model. The Bloch functions used in our proposed model can be described as follows:

$$|\psi_\lambda(\mathbf{k}, \boldsymbol{\rho})\rangle = -\frac{1}{\sqrt{N_0}} \sum_{i=1}^{N_0} e^{-i(\mathbf{k} \cdot \mathbf{a}_i)} |\phi_\lambda(\boldsymbol{\rho} - \mathbf{a}_i - \boldsymbol{\tau}_\eta)\rangle,$$

where the index λ runs over the $2s$, $2p_x$, $2p_y$, and $2p_z$ atomic orbitals, l is the number of CPP unit cell, \mathbf{a}_l is the translation vector of the l -th unit cell along the $C_{[n,m]}$ prismane symmetry axis, $\boldsymbol{\tau}_\eta$ is the relative displacement of the η -th atom in the unit cell of this CPP, \mathbf{k} is the wave vector (directed along the CPP symmetry axis and lying in the 1st Brillouin zone), N_0 is the total number of CPP unit cells ($N_0 = n \rightarrow \infty$), $\boldsymbol{\rho}$ is the electron radius-vector. The general form of the $m \times m$ Hamiltonian sub-block for a long $C_{[n,m]}$ prismane in the basis set $|\phi_\lambda(\boldsymbol{\rho} - \mathbf{a}_i - \boldsymbol{\tau}_\eta)\rangle$ is detailed in Table 1, where it is assumed that the q -th atom is the nearest neighbor of the p -th atom, and the r -th atom is the nearest neighbor of the q -th atom but not of the p -th atom.

TABLE 1. General form of the $m \times m$ Hamiltonian sub-block

Atom index	p -th atom	q -th atom	r -th atom
p -th atom	E	$-e^{-i(\mathbf{k} \cdot \mathbf{d}_{p,q})} E_{p,q}$	0
q -th atom	$-e^{-i(\mathbf{k} \cdot \mathbf{d}_{q,p})} E_{q,p}$	E	$-e^{-i(\mathbf{k} \cdot \mathbf{d}_{q,r})} E_{q,r}$
r -th atom	0	$-e^{-i(\mathbf{k} \cdot \mathbf{d}_{r,q})} E_{r,q}$	E

In Table 1, the elements E , $E_{q,p}$, $E_{p,q}$, $E_{q,r}$, and $E_{r,q}$ are 4×4 matrices describing the interaction energies of the long $C_{[n,m]}$ prismane atoms with indices p , q , and r . The vector $\mathbf{d}_{i,j}$ represents the position of atom j of such a CPP relative to its atom i . The matrices $E_{q,p}$, $E_{p,q}$, $E_{q,r}$, and $E_{r,q}$ were calculated according to the Slater–Koster approach (see Table 2) [38]. We likewise computed the elements E , taking into account that each atom in the $C_{[n,m]}$ prismane ($n \rightarrow \infty$) unit cell interacts with its 2 images in the nearest neighboring unit cells of this CPP. The matrices E also included the energies of the s - and p -orbitals of carbon. Since we only considered the interactions of the nearest neighboring atoms of CPPs, $(p; r)$ and $(r; p)$ blocks in Table 1 are 0.

In Table 2, L , M , and N are the direction cosines of $\mathbf{d}_{i,j}$ with respect to x -, y -, and z -axes, respectively. Throughout this work, we assumed that all covalent bond-lengths in $C_{[n,m]}$ prismanes ($n \rightarrow \infty$) are equal ($\sim 1.50 - 1.60$ Å),

TABLE 2. Elements of the matrices $E_{q,p}$, $E_{p,q}$, $E_{q,r}$, and $E_{r,q}$

Atomic orbitals	$2s$	$2p_x$	$2p_y$	$2p_z$
$2s$	$t_{ss\sigma}$	$Lt_{sp\sigma}$	$Mt_{sp\sigma}$	$Nt_{sp\sigma}$
$2p_x$	$Lt_{sp\sigma}$	$L^2t_{pp\sigma} + (1 - L^2)t_{pp\pi}$	$LM(t_{pp\sigma} - t_{pp\pi})$	$LN(t_{pp\sigma} - t_{pp\pi})$
$2p_y$	$Mt_{sp\sigma}$	$LM(t_{pp\sigma} - t_{pp\pi})$	$M^2t_{pp\sigma} + (1 - M^2)t_{pp\pi}$	$NM(t_{pp\sigma} - t_{pp\pi})$
$2p_z$	$Nt_{sp\sigma}$	$LN(t_{pp\sigma} - t_{pp\pi})$	$NM(t_{pp\sigma} - t_{pp\pi})$	$N^2t_{pp\sigma} + (1 - N^2)t_{pp\pi}$

as previous studies indicate that in long CPPs the difference between intra-layer and inter-layer bond-lengths does not exceed 5 % [11]. Thus, our focus was on elucidating the electronic properties of long $C_{[n,m]}$ prismanes rather than on fine details of their geometry. In explaining the electrical transport characteristics of such CPPs, we adopted the simplest possible model.

All eigenvalue calculations of the Hamiltonians and the band structure plots were performed numerically using Python.

3. Results and discussion

In the first phase of our study, we adopted the following parameter values for the sp^3 -TBM: $E_{2s} = -7.30$, $E_{2p} = 0.00$, $t_{ss\sigma} = -4.30$, $t_{sp\sigma} = 4.98$, $t_{pp\sigma} = 6.38$, and $t_{pp\pi} = -2.66$ eV, as indicated in [39–41].

Before calculating the band structures of $C_{[n,m]}$ prismanes ($n \rightarrow \infty$, $m = 4, 5, 6, 7$) with these sp^3 -TBM parameter values, we tested them by computing the band structures of long zigzag $(\chi, 0)$ SWCNTs. For $\chi = 6, 7, 8, 9$ our results qualitatively confirmed the well-known rule: if χ is a multiple of 3, then long $(\chi, 0)$ SWCNTs are quasi-metallic [42]. Fig. 2 shows the band structures of long $(6, 0)$, $(7, 0)$, $(8, 0)$, and $(9, 0)$ SWCNTs under the chosen parameter values for the sp^3 -TBM. The corresponding band gaps of these SWCNTs are summarized in Table 3.

TABLE 3. Band gaps of long $(\chi, 0)$ SWCNTs

χ	6	7	8	9
Band gap, eV	0.08	1.14	1.11	0.08

We initially validated the above sp^3 -TBM parameter values on $(\chi, 0)$ SWCNTs because they are 1D systems (like CPPs). In addition, the electric transport characteristics of such SWCNTs are fairly well understood. However, each carbon atom in long SWCNTs has only three nearest neighbors. In long $C_{[n,m]}$ prismanes, each carbon atom is covalently bonded to its four nearest neighbors. Therefore, we additionally tested the same sp^3 -TBM parameter values by reproducing the electronic properties of diamond, which indeed demonstrated a distinct dielectric character under these conditions.

Using the above parameter values for the sp^3 -TBM, we then calculated the band structures of long $[n, 4]$, $[n, 5]$, $[n, 6]$, and $[n, 7]$ CPPs. Our results indicate that $C_{[n,m]}$ prismanes begin to exhibit metallic properties for $m \geq 5$, whereas $C_{[n,4]}$ prismanes display a pronounced dielectric character ($n \rightarrow \infty$). These findings for long $C_{[n,4]}$ and $C_{[n,m]}$ prismanes with $m \geq 7$ are in qualitative agreement with the DFT-based calculations in [29]. Fig. 3 shows the band structures of long $C_{[n,4]}$, $C_{[n,5]}$, $C_{[n,6]}$, and $C_{[n,7]}$ prismanes under the chosen parameter values for the sp^3 -TBM. The corresponding band gaps of these CPPs are provided in Table 4.

TABLE 4. Band gaps of $[n, m]$ CPPs at $n \rightarrow \infty$

m	4	5	6	7
Band gap, eV	5.48	0.00	0.00	0.00

The accuracy of both TBM- and DFT-based calculations depends on the choice of parameter values and other approximations [43–46]. Consequently, in the second phase of our work, we varied each of the sp^3 -TBM parameter values by ± 30 % of their respective initial values and evaluated the effect of these variations on the electronic properties of long $[n, 4]$, $[n, 5]$, $[n, 6]$, and $[n, 7]$ CPPs. The band gaps of $C_{[n,4]}$ and $C_{[n,m]}$ prismanes with $m \geq 7$ and $n \rightarrow \infty$ proved to be qualitatively stable under these changes. In contrast, the band gaps for long $[n, 5]$ and $[n, 6]$ CPPs ranged from 0.00 to 1.00 eV under the similar shifts of the parameter values for the sp^3 -TBM, indicating a quasi-metallic to semiconducting behavior of such CPPs, in agreement with [29]. The persistence of the qualitative results for the band gaps of long $C_{[n,4]}$

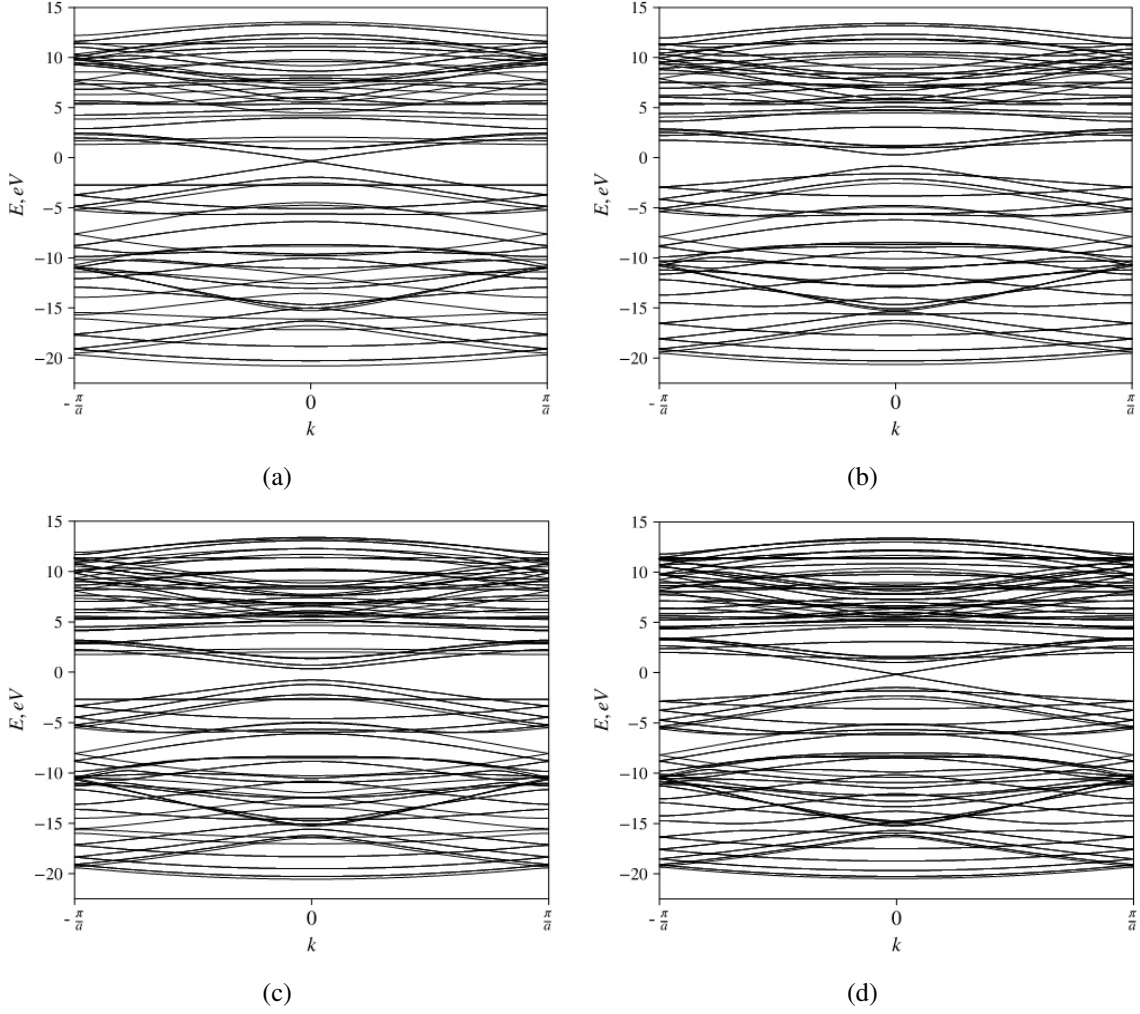


FIG. 2. Band structures of long (6, 0) (a), (7, 0) (b), (8, 0) (c), and (9, 0) (d) SWCNTs

and $C_{[n,m]}$ prismanes ($m \geq 7$) suggests that their electric transport characteristics are mainly due to the topology of these CPPs and are not very sensitive to specific sp^3 -TBM parameter values. Table 5 compiles the resulting intervals of the band gaps for long $[n, 4]$, $[n, 5]$, $[n, 6]$, and $[n, 7]$ CPPs under the above variations of sp^3 -TBM parameter values.

TABLE 5. Band gap intervals for long $[n, m]$ CPPs under a variation of the sp^3 -TBM parameter values (E_{2s} , E_{2p} , $t_{ss\sigma}$, $t_{sp\sigma}$, $t_{pp\sigma}$, $t_{pp\pi}$)

m	4	5	6	7
Band gap intervals, eV	2.12 – 10.18	0.00 – 0.93	0.00 – 0.80	0.00 – 0.00

It is well known that the band gap of a long $(\chi, 0)$ SWCNT decreases with increasing its diameter, and such a SWCNT itself herewith tends asymptotically towards graphene [42]. Similarly, a long $C_{[n,m]}$ prismane with very large diameter ($m \rightarrow \infty$) asymptotically approaches a hypothetical infinite 2D square carbon lattice (Fig. 4(a)). Although in a long $C_{[n,m]}$ prismane the intra-layer atomic distances differ slightly from their inter-layer analogs, this discrepancy diminishes for larger diameter of this CPP [11]. As the surface curvature of a long CPP approaches 0 and all its covalent bond-lengths become equal, the structure of such a $C_{[n,m]}$ prismane essentially becomes to a hypothetical infinite 2D square carbon lattice. Although this ideal lattice is likely to be unstable in practice, it is instructive to consider it as the limiting case of a long CPP with a very large diameter. Fig. 4(b) shows the band structure of a hypothetical infinite 2D square carbon lattice calculated with the above sp^3 -TBM parameter values. Varying these parameter values did not have a qualitative impact on the outcome: for $C_{[n,m]}$ prismanes in the limits $n \rightarrow \infty$ and $m \rightarrow \infty$, the band gap remains zero, indicating robust metallic conduction of the ideal carbon lattice.

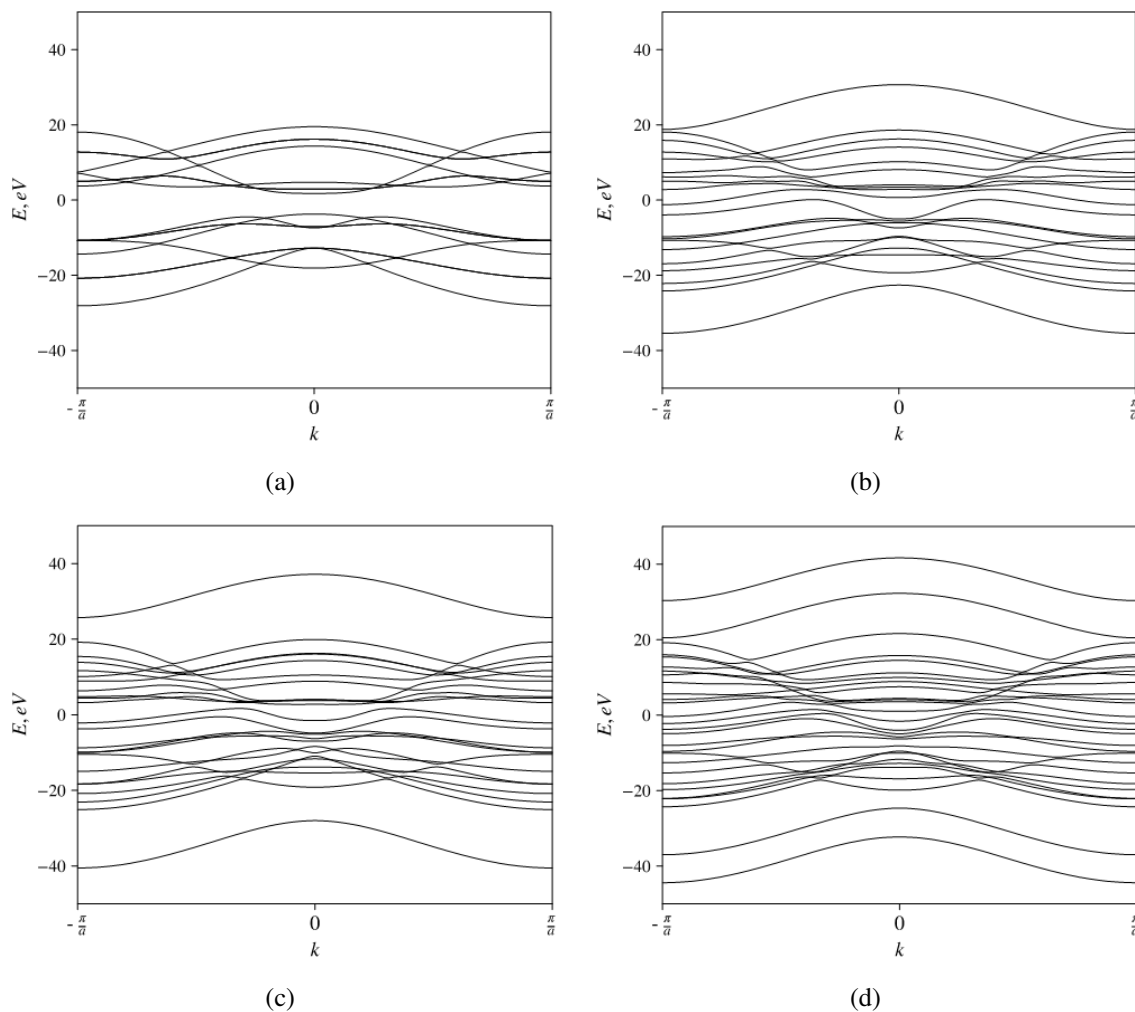


FIG. 3. Band structures of $[n, 4]$ (a), $[n, 5]$ (b), $[n, 6]$ (c), and $[n, 7]$ (d) CPPs at $n \rightarrow \infty$

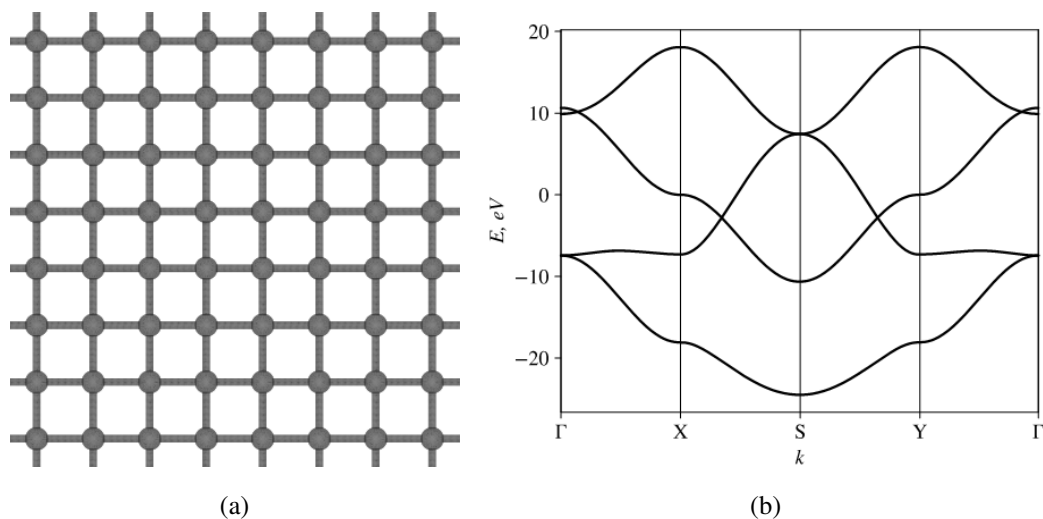


FIG. 4. A hypothetical infinite 2D square carbon lattice (a) and its band structure (b)

4. Conclusion

In this paper, we applied the sp^3 -TBM to study the electronic properties of long $C_{[n,4]}$, $C_{[n,5]}$, $C_{[n,6]}$, and $C_{[n,7]}$ prismanes. Our findings show that $C_{[n,4]}$ prismanes ($n \rightarrow \infty$) feature relatively wide ($\sim 2 - 10$ eV) band gaps and can be classified as semiconductors or dielectrics. Meanwhile, long $C_{[n,m]}$ prismanes with $m \geq 7$ (including $m \rightarrow \infty$) possess no band gap at all, thus acting as good electrical conductors. Large variations in the sp^3 -TBM parameter values do not have a qualitative effect on these results. We also found that long $[n, 5]$ and $[n, 6]$ CPPs can exhibit metallic, quasi-metallic, or semiconductor properties depending on the choice of these parameter values. Therefore, the electronic features of $C_{[n,4]}$ and $C_{[n,m]}$ prismanes at $m \geq 7$ and $n \rightarrow \infty$ are governed primarily by their topology rather than by the specific nature of carbon. We predict that similar behavior will occur in polyprismanes of other chemical elements (e.g., silicon and germanium). The demonstrated electronic transport properties of CPPs open fresh avenues for exploiting these carbon nanostructures as sub-nanometer wires and in other nanoelectronic device components.

References

- [1] Peng R., Pan Y., Liu B., Li Z., Pan P., Zhang S., Qin Z., Wheeler A., Tang X., Liu X. Understanding Carbon Nanotube-Based Ionic Diodes: Design and Mechanism. *Small*, 2021, **17** (31), 2100383.
- [2] Liang X., Li H., Dou J., Wang Q., He W., Wang C., Li D., Lin J.-M., Zhang Y. Stable and Biocompatible Carbon Nanotube Ink Mediated by Silk Protein for Printed Electronics. *Advanced Materials*, 2020, **32** (31), 2000165.
- [3] Cao Q. Carbon nanotube transistor technology for More-Moore scaling. *Nano Research*, 2021, **14** (9), 3051.
- [4] Shi H., Ding L., Zhong D., Han J., Liu L., Xu L., Sun P., Wang H., Zhou J., Fang L., Zhang Z., Peng L.-M. Radiofrequency transistors based on aligned carbon nanotube arrays. *Nature Electronics*, 2021, **4** (6), 405.
- [5] Lin Y., Liang S., Xu L., Liu L., Hu Q., Fan C., Liu Y., Han J., Zhang Z., Peng L.-M. Enhancement-Mode Field-Effect Transistors and High-Speed Integrated Circuits Based on Aligned Carbon Nanotube Films. *Advanced Functional Materials*, 2021, **32** (11), 2104539.
- [6] Franklin A.D., Hersam M.C., Wong P.H.-S. Carbon nanotube transistors: Making electronics from molecules. *Science*, 2020, **378** (6621), 726.
- [7] Lin Y., Cao Y., Ding S., Zhang P., Xu L., Liu C., Hu Q., Jin C., Peng L.-M., Zhang Z. Scaling aligned carbon nanotube transistors to a sub-10 nm node. *Nature Electronics*, 2023, **6**, 506.
- [8] Wan H., Cao Y., Lo L.-W., Zhao J., Sepulveda N., Wang C. Flexible Carbon Nanotube Synaptic Transistor for Neurological Electronic Skin Applications. *ACS Nano*, 2020, **14** (8), 10402.
- [9] Wang Z.-X., Du P.-Y., Li W.-J., Meng J.-H., Zhao L.-H., Jia S.-L., Jia L.-C. Highly rapid-response electrical heaters based on polymer-infiltrated carbon nanotube networks for battery thermal management at subzero temperatures. *Composites Science and Technology*, 2023, **231**, 109796.
- [10] Li Z., Shen C., Liu Y., Ma C., Li F., Yang B., Huang M., Wang Z., Dong L., Wolfgang S. Carbon Nanotube Filter Functionalized with Iron Oxide for Flow-through Electro-Fenton. *Applied Catalysis B: Environmental*, 2020, **260**, 118204.
- [11] Katin K.P., Shostachenko S.A., Avkhadiyeva A.I., Maslov M.M. Geometry, Energy, and Some Electronic Properties of Carbon Polyprismanes: Ab Initio and Tight-Binding Study. *Advances in Physical Chemistry*, 2015, **2015**, 506894.
- [12] Katz T.J., Acton N. Synthesis of prismane. *J. of the American Chemical Society*, 1973, **95** (8), 2738.
- [13] Eaton P.E., Cole T.W. The Cubane System. *J. of the American Chemical Society*, 1964, **86** (5), 962.
- [14] Eaton P.E., Or Y.S., Branca S.J. Pentaprismane. *J. of the American Chemical Society*, 1981, **103** (8), 2134.
- [15] Su S.-K., Chen E., Hung T.Y. T., Li M.-Z., Pitner G., Cheng C.-C., Wang H., Cai J., Wong H.-S.P., Radu I.P. Perspective on Low-dimensional Channel Materials for Extremely Scaled CMOS. *2022 IEEE Symposium on VLSI Technology and Circuits (VLSI Technology and Circuits)*. Honolulu, HI, USA, 12 – 17 June 2022, IEEE, 2022, P. 403.
- [16] Qiu C., Zhang Z., Xiao M., Yang Y., Zhong D., Peng L.-M. Scaling carbon nanotube complementary transistors to 5-nm gate lengths. *Science*, 2017, **355** (6322), 271.
- [17] Autreto P.A.S., Legoas S.B., Flores M.Z.S., Galvao D.S. Carbon nanotube with square cross-section: An ab initio investigation. *The Journal of Chemical Physics*, 2010, **133** (12), 124513.
- [18] Ohno K., Satoh H., Iwamoto T., Tokoyama H., Yamakado H. Exploration of Carbon Allotropes with Four-membered Ring Structures on Quantum Chemical Potential Energy Surfaces. *J. of Computational Chemistry*, 2018, **40** (1), 14.
- [19] Lewars E.G. *Modeling Marvels: Computational Anticipation of Novel Molecules*, Springer Science+Business Media, Luxembourg, 2008, P. 187–192.
- [20] Shostachenko S.A., Maslov M.M., Prudkovskiy V.S., Katin K.P. Thermal stability of hexaprismane $C_{12}H_{12}$ and octaprismane $C_{16}H_{16}$. *Physics of the Solid State*, 2015, **57** (5), 1023.
- [21] Sergeev D. One-dimensional Schottky nanodiode based on telescoping polyprismanes. *Advances in Nano Research*, 2021, **10** (4), 339.
- [22] Baimova J.A., Rysaeva L.K., Rudskoy A.I. Deformation behavior of diamond-like phases: Molecular dynamics simulation. *Diamond and Related Materials*, 2017, **81**, 154.
- [23] Rysaeva L.K., Lisovenko D.S., Gorodtsov V.A., Baimova J.A. Stability, elastic properties and deformation behavior of graphene-based diamond-like phases. *Computational Materials Science*, 2019, **172**, 109355.
- [24] Baimova J.A., Galiakhmetova L.K., Mulyukov R. R. Diamond-like structures under hydrostatic loading: Atomistic simulation. *Computational Materials Science*, 2021, **192**, 110301.
- [25] Lyakhov A.O., Oganov A.R. Evolutionary search for superhard materials: Methodology and applications to forms of carbon and TiO. *Physical Review B*, 2011, **84** (9), 092103.
- [26] Kohn E., Denisenko A. Concepts for diamond electronics. *Thin Solid Films*, 2007, **515** (10), 4333.
- [27] Belenkov E.A., Greshnyakov V.A. Diamond-like phases prepared from graphene layers. *Physics of the Solid State*, 2015, **57** (1), 205.
- [28] Novikov N.V., Maslov M.M., Katin K.P., Prudkovskiy V.S. Effect of DFT-functional on the energy and electronic characteristics of carbon compounds with the unconventional geometry of the framework. *Letters on Materials*, 2017, **7** (4), 433.
- [29] Maslov M.M., Grishakov K.S., Gimaldinova M.A., Katin K.P. Carbon vs silicon polyprismanes: a comparative study of metallic sp^3 -hybridized allotropes. *Fullerenes, Nanotubes and Carbon Nanostructures*, 2019, **28** (2), 97.
- [30] Gimaldinova M.A., Katin K.P., Salem M.A., Maslov M.M. Energy and electronic characteristics of silicon polyprismanes: Density functional theory study. *Letters on Materials*, 2018, **8** (4), 454.

- [31] Katin K.P., Grishakov K.S., Gimaldinova M.A., Maslov M.M. Silicon rebirth: Ab initio prediction of metallic sp^3 -hybridized silicon allotropes. *Computational Materials Science*, 2020, **174**, 109480.
- [32] Merinov V.B., Khrushkova A.A. Ab initio prediction of metallic nature of sp^3 -hybridized germanium structures. *Computational and Theoretical Chemistry*, 2024, **1231**, 114441.
- [33] Gaur A., Srivastava J. A tight-binding study of the electron transport through single-walled carbon nanotube-graphene hybrid nanostructures. *J. of Chemical Physics*, 2021, **155** (24), 244104.
- [34] Xin B., Zou K., Liu D., Li B., Dong H., Cheng Y., Liu H., Zou L.-J., Luo F., Lu F., Wang W.-H. Electronic structures and quantum capacitance of twisted bilayer graphene with defects based on three-band tight-binding model. *Physical Chemistry Chemical Physics*, 2024, **26** (12), 9687.
- [35] Mostafaei A., Semiromi E.H. A tight-binding model for the electronic structure of MXene monolayers. *Nanoscale*, 2022, **14**, 11760.
- [36] Peng Z., Guan Z., Wang H., Srolovitz D.J., Lei D. Modified tight-binding model for strain effects in monolayer transition metal dichalcogenides. *Physical Review B*, 2024, **109**, 245412.
- [37] Candioto G. Exploring the electronic potential of effective tight-binding Hamiltonians. *Materials Today Quantum*, 2024, **1**, 100001.
- [38] Slater J.C., Koster G.F. Simplified LCAO Method for the Periodic Potential Problem. *Physical Review*, 1954, **94** (6), P. 1498–1524.
- [39] Charlier J.-C., Lambin Ph., Ebbesen T.W. Electronic properties of carbon nanotubes with polygonized cross sections. *Physical Review B*, 1996, **54** (12), R8377–R8380.
- [40] Dag S., Senger R.T., Ciraci S. Theoretical study of crossed and parallel carbon nanotube junctions and three-dimensional grid structures. *Physical Review B*, 2004, **70** (20), 205407.
- [41] Wei-Yang Lo, George Y.-S. Wu, Kuei-Ching Wu. Tight-binding calculation with up to the 3rd nearest “neighbor” coupling for small-radius carbon nanotubes. *Physica E: Low-dimensional Systems and Nanostructures*, 2010, **43** (1), P. 482–486.
- [42] Kulbachinsky V.A. *Physics of nanosystems*. Phymathlit, Moscow, 2023, P. 513–515.
- [43] Schattauer C., Todorovic M., Ghosh K., Rinke P., Libisch F. Machine learning sparse tight-binding parameters for defects. *NPJ Computational Materials*, 2022, **8**, 116.
- [44] Nakhaee M., Ketabi S.A., Peeters F.M. Tight-Binding Studio: A technical software package to find the parameters of tight-binding Hamiltonian. *Computer Physics Communications*, 2020, **254**, 107379.
- [45] Zhang G., Musgrave C.B. Comparison of DFT Methods for Molecular Orbital Eigenvalue Calculations. *J. of Physical Chemistry A*, 2007, **111** (8), 1554.
- [46] Krylova K.A., Baimova Y.A., Dmitriev S.V., Mulyukov R.R. Calculation of the structure of carbon clusters based on fullerene-like C_{24} and C_{48} molecules. *Physics of the Solid State*, 2016, **58** (2), 394.

Submitted 10 March 2025; revised 5 April 2025; accepted 6 April 2025

Information about the authors:

Vladimir A. Kurakin – National Research Nuclear University MEPhI (Moscow Engineering Physics Institute), 31 Kashirskoe Hwy, Moscow 115409, Russian Federation; ORCID 0009-0001-1358-3685; fromkurakin@mail.ru

Tatyana N. Kobernik – Energy Technology Center, Skolkovo Institute of Science and Technology, Territory of Innovation Center “Skolkovo”, 30 (bld 1) Bolshoy Blvd, Moscow 121205, Russian Federation; ORCID 0009-0003-0223-9111; kobernik-t-n@yandex.ru

Conflict of interest: the authors declare no conflict of interest.

Application of carbon nanomaterials in semiconductor electronics

Rostyslav V. Shalayev, Victor N. Varyukhin

Galkin Donetsk Institute for Physics and Engineering, Donetsk, Russia

Corresponding author: Rostyslav V. Shalayev, sharos@donfti.ru

PACS 61.46.+w, 81.05.ue, 81.05.ug

ABSTRACT This review examines the development of modern semiconductor technologies using various carbon nanomaterials, as an element base, to replace classical semiconductors (silicon, germanium, etc.). Examples of specific electronic devices demonstrate the gradual displacement of classical semiconductors by carbon compounds, which are much more promising, with the potential to create all-carbon electronics.

KEYWORDS carbon electronics, semiconductor technology, carbon nanostructures, fullerenes, nanotubes, graphene

FOR CITATION Shalayev R.V., Varyukhin V.N. Application of carbon nanomaterials in semiconductor electronics. *Nanosystems: Phys. Chem. Math.*, 2025, **16** (2), 216–224.

1. Introduction

For a significant part of the 20th century, classical semiconductors (silicon and germanium) dominated in semiconductor technologies. But gradually, alternative materials for using in electronics were sought, and by the beginning of the 21st century, there was noticeable progress in this area, especially after the “nanostructure boom” that broke out at the turn of the century. Indeed, nanometer-scale objects, according to many experts, have been called the most in-demand over the past decades in various fields of science and technology, including electronics.

Nanoelectronics includes technologies that use electronic devices with structural working areas of nanometer sizes [1, 2]. These include emission devices, various types of nanoantennas, semiconductor lasers, field and bipolar transistors with characteristic element sizes of approximately 100 nm, nanoscale electromechanical systems, etc. When reducing the size of electronic devices, it is necessary to take into account qualitatively new effects associated with the discreteness of the electric charge and the quantum-wave nature of electrons. Therefore, single-electron devices with discrete tunneling, as well as quantum dots, are also an important component of nanoelectronics.

For decades, progress in electronics has been accompanied by a reduction in the size of individual elements and an increase in their number on a chip. In turn, this has increased energy consumption and the amount of heat generated (the problem of heat removal still remains one of the most difficult in electronics). Therefore, increasingly complex technological problems emerged with the transition to more miniature technological processes. The growing problems led to the emergence of questions: are there limits to such miniaturization, will the Moore effect of increasing the number of elements in microelectronic circuits be observed in the future? Despite the fact that commercial production of chips using the 2 nm process technology is expected in 2025, there is an assumption that developments in the field of electronics will no longer obey this law in the future and silicon, as a material will approach the physically insurmountable limit of miniaturization of about 10 Å.

It is known that carbon is one of the most amazing chemical elements, forming a wide variety of structures and allotropic forms and possessing a variety of properties (often radically opposite) [3, 4]. In addition to the well-known graphite and diamond, the researchers are focused on the recently discovered fullerenes, carbon nanotubes (CNT), and graphene, the discovery of which gave a new impetus to the creation of specialized electronics. In fact, carbon nanostructures, due to their size, are a kind of transition bridge between individual molecules and crystalline formations and, accordingly, a very promising material for the elemental base of modern nanoelectronics, allowing a significant increase in the density of transistors in integrated circuits.

Therefore, there is currently an active discussion in the scientific community about the possibility of practical application of various carbon nanostructures in microelectronics as working elements of field-effect transistors, memory cells, integrated circuits, as well as in the creation of quantum computers and, in general, in the design of various promising composite materials. It is nanoelectronics that is one of the most attractive areas of use of carbon nanostructures (graphene, graphane, nanotubes and other similar structures) [5, 6] due to their small size, the most diverse (often unique) electrical and optical properties, superior mechanical strength and chemical stability. Each of these nanostructures has its own individual properties and prospects for application in nanoelectronics.

As mentioned above, today the obvious exhaustibility of silicon as a base for a semiconductor platform is already a practically indisputable fact, and more exotic gallium arsenide and diamond, despite the great hopes that were placed on

them, have not become widely used materials in industrial electronics [7]. The nanostructured carbon materials (possessing many forms and modifications) are the potential alternative to classical semiconductors, namely as a fundamentally new component base for electronics, judging by the results of the latest research.

Some time ago researchers are already talking about completely “carbon” electronics [8, 9] in the near future, which, due to the combination of its unique properties, can become a replacement for “silicon” electronics. However, in our opinion, even at that time such a conclusion was somewhat premature.

Of course, today the contribution of carbon materials to the development of micro- and nanoelectronics is significant, especially, the contribution of carbon nanotubes, since they were obtained quite a long time ago, have been better studied [10] and many of their applications in electronics are already known. Developments related to fullerenes, and especially graphene, are still much fewer, but in general, graphene is a more promising material than CNTs. This is explained by the relative simplicity of the planar integrated circuits production, using planar graphene layers. No specific equipment is required for this, and it is enough to use already well-established nanolithography techniques for the mass production of new electronic devices.

In this article, we will consider only some areas of carbon nanostructured materials using in electronic engineering today, assess the prospects for the development of carbon electronics and applications in the widest areas of modern science and technology.

2. Electronics of fullerenes

Fullerenes, discovered in 1985, are an amazing class of carbon molecules with unique structural and electronic properties, are self-organizing structures, and are the third allotropic modification of carbon, in addition to the already known diamond and graphite structures. These are closed spherical carbon molecules consisting of pentagons and hexagons. Fullerenes containing from 28 to 100 carbon atoms have been discovered, but the most stable molecules are C_{60} and C_{70} . The best-known fullerene is C_{60} . It consists of 60 carbon atoms arranged in the form of a ball, similar to a football. Each carbon atom is connected to three neighboring carbon atoms, forming hexagons and pentagons.

Fullerenes have a wide range of properties which makes them the subject of considerable scientific interest and practical application. For example, studies have shown that fullerene is an organic semiconductor with a band gap of $\sim 1.5 - 2$ eV and exhibits strong acceptor properties with respect to most organic compounds. Fullerene can be used in artificial photosynthesis systems and organic solar cells based on high-molecular bulk heterojunctions, as a part of donor-acceptor complexes [11]. Field-effect transistors with a fairly high carrier mobility have already been created based on single-layer fullerene films. Due to the mobile π -electron system, the fullerene molecule is easily polarized and has nonlinear optical properties. Fullerenes also have interesting photochemical properties, including the ability to absorb and emit light. This makes them interesting for such areas of application as photovoltaic cells and optoelectronic devices. A solar cell is a device that converts solar radiation into electrical current, and fullerene plays an important role in increasing the overall efficiency of such a cell. Fullerenes short photoresponse time is the advantage of fullerene solar cells over traditional silicon. In addition, fullerenes are already used as components of molecular electromechanical transistors, single-electron transistors, Kondo effect elements, and much more.

In most organic materials, especially those used to create electronic devices, hole conductivity predominates over electron conductivity. One of the promising devices for organic electronics is an organic field-effect transistor (OFET) with a transport layer no more than ten nanometers thick, in which the flow of charge carriers is controlled by changing the charge density in an electric field.

Multilayer transistors have been created in which the semiconductor (fullerene C_{60}) and the light-controlled compound (spiropyran SpO_x) form separate layers (see Fig. 1) [12, 13]. A study of the current-voltage characteristics of the obtained transistors showed that the currents in the phototransistors are less than 1 nA in the absence of irradiation. The current between the source and drain increases by three orders of magnitude when irradiated with ultraviolet light (350 nm) in the transistor gap area, i.e. the ratio of the on-off currents is about 1000.

Also physical principles have been developed for creating a transistor analogue on a single fullerene molecule, which can work as a current amplifier in the nanoampere range [14]. Two gold point contacts on a silicon oxide substrate are the source and drain, respectively, between which a C_{60} molecule is located. The third electrode, which is a small piezoelectric crystal, is brought to the van der Waals distance opposite the C_{60} molecule (like a gate opposite the channel in a MOSFET transistor). The input signal is fed to the tip of the piezoelectric element, which deforms the C_{60} molecule located between the electrodes and modulates the conductivity of the intramolecular junction. The transparency of the molecular current flow channel depends on the degree of blurring of the metal wave functions in the region of the fullerene molecule. A simple model of this transistor effect is a tunnel barrier, the height of which is modulated independently of its width, i.e. the C_{60} molecule is used as a natural tunnel barrier. The supposed advantages of such an element are its small size and very short electron transit time in the tunnel mode, and, consequently, higher response speed of the active element.

The use of a fullerene molecule as a ready-made nano-sized object for creating nanoelectronic devices and devices based on new physical principles is very promising. For example, fullerene molecules can be used to create memory devices. It is proposed to place them on the surface of a substrate in a specially specified way using a scanning tunnel or

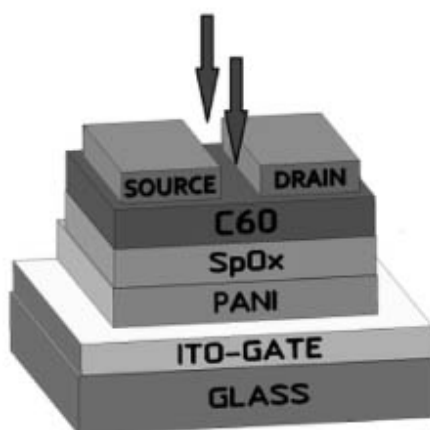


FIG. 1. Photocontrolled organic field-effect transistor [12]

atomic force microscope, and use this as a way to record information. To read information, the surface is scanned by the same probe. In this case, one bit of information is the presence or absence of a molecule with a diameter of 0.7 nm, which allows achieving record values of information recording density. Such experiments were conducted by Bell company.

Researchers from Cornell University have proposed a concept for non-volatile solid-state computer memory based on silicon dioxide and fullerene C_{60} . The memory cell in the proposed version is one C_{60} molecule (buckyball). The energy levels of such a molecule allow for charge tunneling, which enables data recording and deletion. The advantage of the new development is that buckyballs are relatively easily and evenly distributed in silicon, as they are not prone to aggregation and cluster formation.

The use of C_{60} molecules, according to the developers, makes it possible to increase the ratio of recording retention time to recording/erasing time by an order of magnitude compared to memory based on metal nanocrystals.

In the field of nanoelectronics, quantum dots are of the greatest interest in terms of possible applications. Such dots have a number of unique optical properties that allow them to be used, for example, to control fiber optic communications, or as processor elements in the optical supercomputer currently being designed. Fullerenes are ideal quantum dots in many respects, and, accordingly, have a chance to become the smallest microcircuit in a computer nanoprocessor.

3. Electronics of CNTs

The discovery of carbon nanotubes in 1991 [15] practically led to the emergence of a new field of solid-state physics, since CNTs (which combine the properties of both individual molecules and a solid) generally represent a unique intermediate state of matter.

It is known that carbon nanotubes can serve as excellent conductors in electronic integrated circuits, since they have good contact with metals widely used in modern microelectronics – platinum, gold, titanium, and are capable of conducting currents without noticeable heating, three to four orders of magnitude higher than conventional metal conductors. Carbon nanotubes can switch currents with a density of up to $10^8 - 10^9$ A/cm² (up to 10^{10} A/cm² for multi-walled CNTs) due to the low defect concentration. At the same time, a copper conductor is destroyed due to heat release already at current densities of $\sim 10^6$ A/cm².

The current demand for carbon nanotubes is driven by the growing desire to miniaturize semiconductor components [16]. Nanotubes, with their superior mechanical strength and chemical stability, small size and conductivity controlled by synthesis, are considered a desirable material for the production of working elements in microelectronics. Materials containing CNTs are already being used by companies producing semiconductor components due to their exceptional electrical characteristics, combining both metallic and semiconductor properties. Let us consider some realistic examples of the use of carbon nanotubes in electronics.

3.1. CNT transistors

The first field-effect transistors on carbon nanotubes were obtained at the end of the 20th century, and the technology of their production continues to improve [17–20]. It is possible to achieve a higher response speed of the transistor junction when using carbon nanotubes with semiconductor properties in transistors, and, accordingly, operation at higher frequencies, due to the higher electron mobility than in classical semiconductors. In addition, for CNT transistors there is no miniaturization limit of tens nanometers, typical for silicon semiconductor devices, i.e. today they already have dimensions an order of magnitude smaller than silicon ones.

The approximate structure of a CNT-based field-effect transistor is shown in Fig. 2. Carbon nanotubes with semiconductor properties (channel) are placed between two metal electrodes (source and drain) deposited on a silicon wafer, which is the gate of the device. If there is no voltage on the gate, the transistor channel (nanotube) is closed, since there is a barrier in the forbidden zone of the semiconductor nanotube. If voltage is applied to the gate, the electric field causes the channel band diagram to rearrange and conductivity to appear in it. Consequently, it is possible to control conductivity (open or close the transistor junction) by changing the voltage applied to the gate.

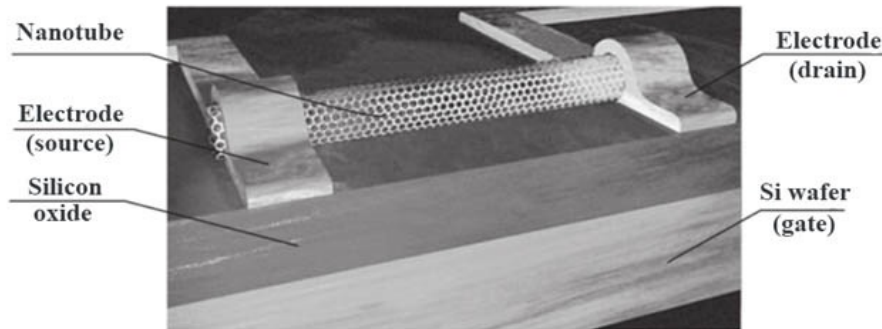


FIG. 2. Structure of a CNT field-effect transistor

There are also Y-shaped CNT transistors, first proposed by researchers at the University of California, San Diego and Clemson University (USA). Their construction is fundamentally different from the construction of the field-effect transistor discussed above, but it has electronic properties similar to those of traditional metal-oxide MOSFETs used to produce computer microprocessors, RAM, and other integrated circuits.

These transistors were obtained using a special technique of branching conventional carbon nanotubes during growth, with the addition of an iron-titanium catalyst, the particles of which stimulated the branching of the growing nanotube. The result was Y-shaped nanotubes with metal particles at the junction of the trunk and branches (see Fig. 3(a)). When such a structure is connected to a source of electric current, it becomes possible to control the electrons entering one of the branches by switching them through a metal nanoparticle at the junction (as in a conventional MOSFET transistor, see Fig. 3(b)). The metal particle of the catalyst either passes or does not pass current from one branch to another (drain – source), depending on the potential applied to the main trunk of the nanotube (gate).



FIG. 3. SEM image (a) and schematic diagram (b) of a transistor built on a Y-shaped carbon nanotube

3.2. CNT memory devices

The use of CNTs makes it possible to develop various versions of computer flash memory, with the possibility of a noticeable increase in capacity per unit area due to the small size of the nanotubes [21, 22]. Fig. 4 shows a memory cell on a CNT transistor with a cantilever. The cell is assembled on a field-effect transistor located on a silicon plate (1) with a source (2), drain (3), channel-tube (7) and a “floating” gate (4). An electric charge is supplied to the gate through an electrode (6) and a metal cantilever (5), which, by default, has no contact with the gate. But if a potential is supplied to the control electrode (8) during the recording process, electrostatic forces bend the cantilever, and it contacts the gate. As a result, an electric charge flows to it, which is equivalent to recording a logical unit. Even if the potential on the control electrode disappears, the charge on the insulated gate is retained for a long time, i.e. such memory is non-volatile. The power consumption of this type of memory during operation can be significantly lower than that of classic flash memory, since the cantilever switches under the influence of electrostatics with minimal heat dissipation.

Modification variants of such memory cells by selection of dielectric materials for gate insulation (silicon oxide, hafnium oxide, etc.) allow one to reduce the time of information reading/writing cycle to hundreds of nanoseconds, which in principle is not the final value for the productivity and speed of this memory type. And the high memory speed can contribute to the use of such cells not only as non-volatile flash memory, but also as high-speed RAM.

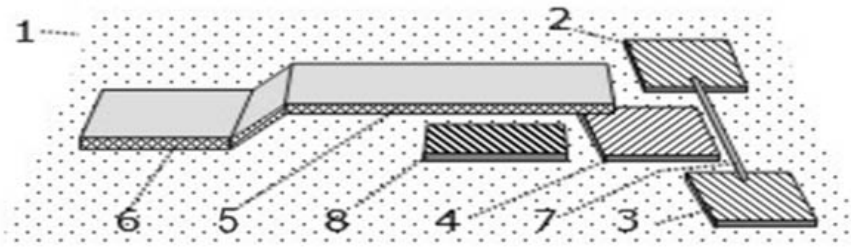


FIG. 4. Design of an elementary cell of flash memory on CNTs [1]: 1 – silicon wafer, 2 – source, 3 – drain, 4 – “floating” gate, 5 – metal cantilever, 6 – electrode, 7 – channel-tube, 8 – control electrode

3.3. CNT displays

Carbon nanotubes are used to produce various types of displays now: as a field emitter in field emission display (FED), a transparent electrode in organic light-emitting devices (OLED), a polarizer in liquid crystal displays (LCD). The use of CNTs in displays is primarily associated with FED technology, developed and introduced by LETI company in 1991. FED displays were supposed to use a matrix of “cold” cathodes. But the first FED displays turned out to be uncompetitive due to the high percentage of defects and the reduction in cost of competing display production technologies.

But this technology came back to life in the early 21st century, when FED displays were developed that proposed using CNT arrays as cathodes [23], which significantly reduced the cost of FED display production. Large-area field emission displays were manufactured using single-layer carbon nanotube emitters. Triode-type field emission display structures were also studied to achieve ultra-high brightness. In this form, carbon nanotube FED displays can compete equally with large-diagonal panels, and they will also compete with plasma panels in the future, which currently dominate the field of ultra-large screen diagonals.

Single-walled carbon nanotubes can also be used as electrodes in OLED displays based on organic light-emitting diodes and light-emitting transistors [17, 24] operating at low voltage, with low power dissipation and high luminosity in three primary colors. Such OLED displays can be extremely flexible and transparent due to the high strength of the nanotubes and the ultra-thin thickness of the electrode matrix, which will allow the creation of sheets of very thin electronic paper. In general, the main trend of the world market in recent years has been the growth in demand for touch screens. Therefore, the development of flexible electronics is one of the main technologies that will only gain momentum in the coming years [25]. It is necessary that the material used to create a flexible display have the ability to deform when pressure is applied. CNTs are such a promising material, suitable for the production of flexible electronics.

The development of a low-temperature method for producing carbon nanotubes, which would allow them to be applied to substrates made of various materials (for example, not to damage the glass substrate used in the final device) was one of the important tasks facing researchers working in this area. This problem has now been solved, particularly, in the works of employees of the Donetsk Institute for Physics and Engineering (DonIPE) [26, 27], which made it possible to obtain arrays of carbon and carbon-nitrogen nanotubes on glass substrates.

3.4. CNT integrated circuits

After the creation of the field-effect transistor on nanotubes, periodic reports appear on the development of electronic devices consisting of a relatively large number of transistors and other elements of circuitry implemented using CNTs. As an example, we can point to elements that perform logical functions, high-frequency pulse generators, electromagnetic wave detectors, and even microprocessors [28–30].

It is necessary to form hundreds and thousands of transistors in a crystal to achieve more complex functionality of integrated circuits. Back in 2013, Stanford University scientists created a simple processor of only 178 transistors (modern silicon processors contain billions of transistors) on carbon nanotubes [28]. Its performance was low, it operated at a frequency of 1 kHz and had extremely limited capabilities. But microelectronics on a silicon platform also went through this path, so this important result can be considered as the first milestone in the development of all-carbon electronics. Already in 2019, a fully functional 16-bit microprocessor with more than 14,000 CNT transistors on the RISC-V architecture was presented [29], which could execute the 32-bit set of commands.

To sum up, despite significant efforts in the field of applied research on carbon nanotubes, they have not yet led to any radical breakthrough in the development of modern nanoelectronics over the past few decades. The unique properties of CNTs as working elements of nanoelectronic devices have not yet been fully implemented, and their combination with existing silicon technologies raises many questions.

4. Electronics of graphene

The discovery of graphene and initial studies of its unique properties give hope that an alternative material that can become the basis for the creation of future universal electronic nanotechnologies has been found, and carbon nanotubes are only the first step in the development of carbon nanoelectronics. Over the past few years, graphene-based electronics have been the subject of hot discussions. It is assumed that graphene sheets of a sufficiently large area will allow the formation of electronic elements using long-known methods of modern microelectronics, such as thin-film technology, various types of nanolithography and carbon particle printing, which will make it possible to implement the density of electronic elements required today and in the future.

Graphene was discovered in 2004 by Russian-born scientists Konstantin Novoselov and Andre Geim [31]. Graphene is a layer of carbon atoms in a hexagonal two-dimensional lattice, and, in fact, it is a one atom thick carbon film with a strictly ordered crystalline structure. Its disadvantages include the absence of a forbidden zone in unmodified graphene, as well as the difficulty of obtaining large homogeneous sheets of such material. A great advantage of graphene is that it can work as a single base material for both nanoelectronics and nanooptics [32], and can be combined in different combinations with elements of optoelectronic circuits, which is very convenient.

It turned out that graphene has many interesting properties, including high stability, high thermal and electrical conductivity (including at room temperature). The mobility of electrons in graphene is 10 – 20 times higher than in classical silicon semiconductors, and, therefore, such a material is promising for creating electronic circuits suitable for operation at terahertz frequencies [33] (as well as the CNT devices discussed above). Conventional planar technologies tested in microelectronics for many decades are applicable to graphene and this is the advantage of graphene over carbon nanotubes. In addition, the control current of the electronic devices used graphene can be proportionally increased by changing the width of the conductive channel, due to the two-dimensional structure of the material. Let us consider practical examples of using graphene in modern electronics.

4.1. Graphene transistors

Today, the main applied electronic application of graphene is in the field of analog electronics, since the problem of forming its energy gap has not yet been finally solved. The main advantage of electronic devices designed on graphene basis is their high performance, due to the record value of charge carrier mobility in graphene. Therefore, graphene attracted much attention immediately after its discovery as a material for creating field-effect transistors [34, 35] and research in this direction continues [36]. The first experimental field-effect transistor on graphene was obtained in the same 2004, on a doped silicon substrate (gate), covered with a layer of silicon oxide (gate dielectric) hundreds of nanometers thick. The simplicity of the design had its drawbacks in the form of parasitic capacitance formed by the conductive silicon substrate, so the applicability of such a transistor in radio-frequency circuits is very problematic. But a start had been made and the prospects of the newly discovered material have been demonstrated in practice.

It is necessary to reduce both the thickness of the gate dielectric and the width of the graphene channel as much as possible to improve the electrical and frequency characteristics of field-effect transistors. The high permittivity group dielectrics is desirable to use instead of the silicon oxide used in the first trial transistor model. The design of a graphene field-effect transistor with a gate dielectric made of Al_2O_3 (the layer thickness is a few nanometers, which is a few orders of magnitude lower than the thickness of the previously used SiO_2) is shown in Fig. 5.

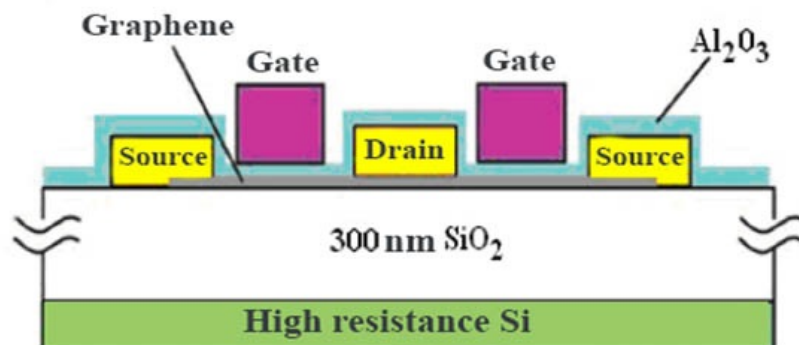


FIG. 5. Structure of a field-effect transistor on graphene [1]

As mentioned above, the lack of a closed state in graphene transistors is an obstacle to the use of such devices in digital circuits due to the inaccessibility of the forbidden zone in graphene. Under normal conditions, a graphene field-effect transistor does not close completely, therefore, devices using such circuitry are not energy efficient enough. However, there are modifications of graphene transistor designs where the current exponentially depends on the gate

voltage [35]. Such a device is distinguished by a low closed-state current, typical for conventional semiconductor field-effect transistors, and a high open-state current, typical for graphene. Analog electronics do not require a forbidden zone, so many analog radio-frequency devices are already built on graphene transistors. From year to year, the size of such devices is decreasing, and their operating frequency is increasing. Graphene transistors with a length of 600 nm and an operating frequency of up to 34 GHz, then 150 nm and a frequency of 26 GHz, 240 nm and 100 GHz, and so on, up to 400 GHz, have been consistently reported. Therefore, even experimental field-effect transistors on graphene are already comparable in frequency to the best semiconductor electronics of III-V group compounds, and have significantly outpaced their silicon counterparts.

4.2. Graphene memory devices

Similarly to CNT, graphene, with its unusual properties, is promising for building various types of memory [37–39], including high-performance non-volatile memory. Graphene is able to capture a significantly larger charge and, thus, is promising as a material for the field-effect transistor electrode in the cell for building memory.

The prototype of the new memory, proposed at Rice University (USA) under the supervision of Prof. James Tour, consists of silicon modules with a dozen atomic layers of graphene, no more than 5 nm thick (see Fig. 6). Accordingly, this affects the size of the memory cell, which is at least an order of magnitude smaller than the cells of modern NAND memory. This will allow a multiple increase in the capacity of memory modules without deteriorating its performance and reliability – tests confirm a large number of memory cell rewriting cycles. Graphene-based memory also is capable of operating in a wide range of temperatures, which makes it possible to function with poor heat dissipation or even the absence of cooling and ventilation. Perhaps, the most interesting property of graphene memory is its low sensitivity to the destructive effects of penetrating radiation, which allows such memory to be used in extreme conditions.

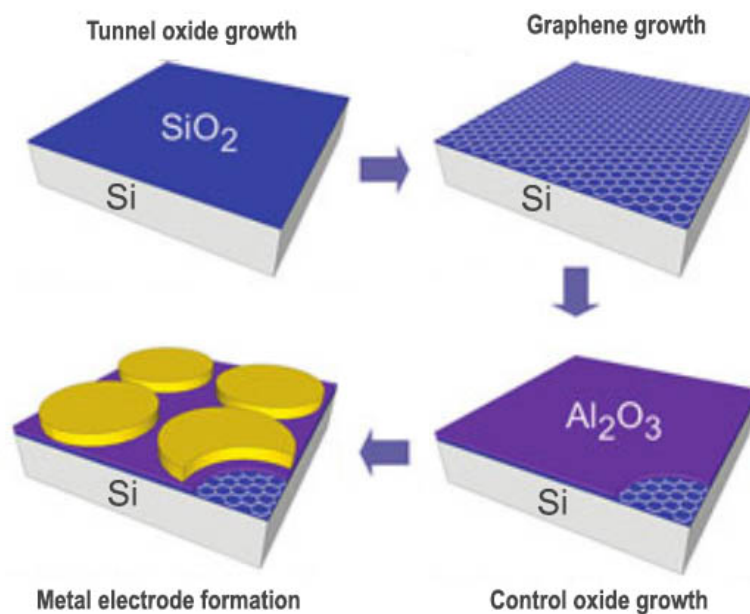


FIG. 6. Flash memory cell based on graphene layers [37]

One of the lacks of the proposed graphene memory is the access time, which is still several times longer than the characteristic response time of modern memory devices, but there is no doubt that further improvement of the proposed prototype will solve this problem. Moreover, Professor J. Tour's group continues to actively work towards improving industrial technologies for obtaining graphene memory [38].

4.3. Graphene integrated circuits

The first integrated circuit based on graphene was created back in 2011 by employees of the IBM Research division [40]. It was a prototype of a frequency mixer operating at frequencies up to 10 GHz and based on a graphene transistor. A broadband frequency mixer is one of the key components of high-frequency radio equipment, generating a signal at the output that is the sum or difference of the signals arriving at the inputs of the device.

The proposed circuit consisted of a graphene transistor with a characteristic size of 550 nm and two aluminum inductors several micrometers thick, located on a silicon carbide substrate (see Fig. 7). The problems of layout of the component elements were solved in the process of creating a single chip. They consisted in the fact that when placing

metal components (inductor coil) on top of the graphene transistor, they damaged the graphene sheet and disrupted the functionality of the circuit. Changing the sequence of the RF circuit manufacturing process (first forming passive metal components, and then graphene transistors) made it possible to eliminate the previously observed damage to the graphene layers in order to obtain the expectedly high device characteristics. The circuit operated in the temperature range from room temperature to 125 °C at a frequency of 10 GHz with stable characteristics.

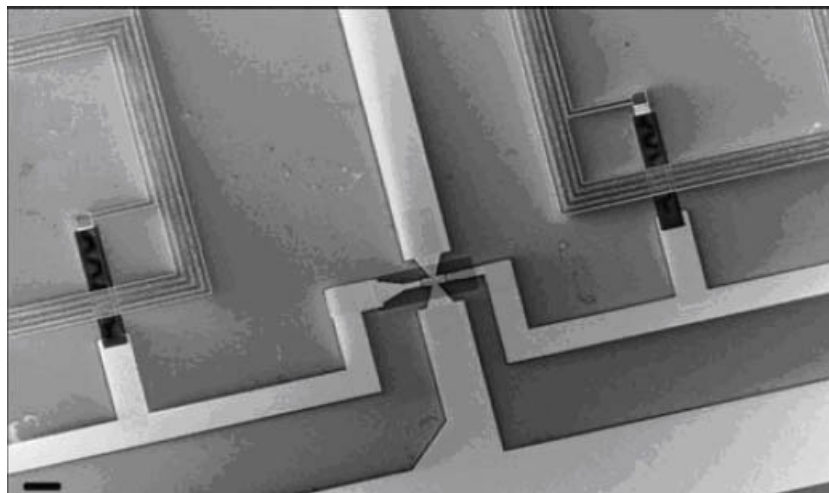


FIG. 7. SEM image of a graphene frequency mixer integrated circuit [1]

However, despite significant progress in the development of graphene field-effect transistors in recent years and the favorable prospects for their use [41], a number of unresolved problems that prevent the mass appearance of radio-frequency integrated circuits using graphene components still remain.

5. Conclusion

So, as we see, promising carbon compounds are partially replacing silicon and other classic semiconductors in the electronics industry. Most elements of modern micro- and nanoelectronics can already be implemented (at least as test devices) on the basis of graphene or carbon nanotubes. Such world industry leaders as IBM and Intel are the largest sponsors of research projects in the field of using nanostructured carbon in microelectronics.

IBM researchers have already achieved multiple increases in the speed of electronic circuits based on carbon nanotubes. Although this speed is still lower than that of modern silicon chips, there is confidence that new nanotechnological processes will eventually unlock the enormous potential of carbon-based electronics. But only if the problems associated with the influence of structural defects on the electronic properties of carbon nanomaterials will be solved in the future (since ideal graphene layers or ideal nanotubes still do not exist).

On the other hand, it is too early to abandon silicon absolutely. It is still unlikely that classical semiconductors will be completely replaced by carbon nanostructures in microchips within the next few decades. In the future, silicon still has many potential applications in nanoelectronics as nanowires, nanotubes, nanodots and other structures, which are the subject of research in many modern laboratories around the world. There are many prospects for the development of modern nanoelectronics and it is impossible to predict what will happen in this industry in 10 or 20 years.

References

- [1] Smirnov V.I. *Nanoelectronics, nanophotonics and microsystems engineering: a tutorial*. UISTU, Ulyanovsk, 2017, 280 p.
- [2] Kelsall R., Hemley I., Geoghegan M. *Scientific foundations of nanotechnology and new devices*. Intellect, Moscow, 2008, 800 p.
- [3] Georgakilas V., Perman J.A., Tuček J., Zbořil R. Broad family of carbon nanoallotropes: classification, chemistry, and applications of fullerenes, carbon dots, nanotubes, graphene, nanodiamonds, and combined superstructures. *Chemical reviews*, 2015, **115** (11), P. 4744–4822.
- [4] Podgorny D.A. *Carbon in all its diversity: a tutorial*. SUrSU, Chelyabinsk, 2014, 31 p.
- [5] Avouris P., Chen Z., Perebeinos V. Carbon-based electronics. *Nat. Nanotechnol.*, 2007, **2**, P. 605–615.
- [6] Nicholas R., Mainwood A., Eaves L. Introduction. Carbon-based electronics: Fundamentals and device applications. *Philosophical transactions A.*, 2007, **366**, P. 189–193.
- [7] Kang Y.H. *Semiconductor Technologies in the Era of Electronics*. Springer, Dordrecht, 2014, 149 p.
- [8] Gubin S.P. All-carbon nanoelectronics (project). *Radioelectronics. Nanosystems. Information technology*, 2011, **3** (1), P. 47–55.
- [9] Weiss P.S. A Conversation with Phaedon Avouris, nanoscience Leader of IBM. *ACS Nano*, 2010, **4** (12), P. 7041–7047.
- [10] Dyachkov P.N. *Carbon nanotubes. Structure, properties, applications*. Binom, Moscow, 2006, 293 p.
- [11] Kronholm D., Hummelen J.C. Fullerene-Based n-Type Semiconductors in Organic Electronics. *Material Matters.*, 2007, **2**, P. 16–19.
- [12] Tuktarov A.R., Salikhov R.B., Khuzin A.A., Popod'ko N.R., Safargalin I.N., Mullagaliev I.N., Dzhemileva U.M. Photocontrolled organic field effect transistors based on the fullerene C₆₀ and spiropyran hybrid molecule. *RSC Adv.*, 2019, **9**, P. 7505–7508.

- [13] Woebkenberg P.H., Bradley D.C., Kronholm D., Hummelen J.C., de Leeuw D.M., Coelle M., Anthopoulos T.D. High mobility n-channel organic field-effect transistors based on soluble C₆₀ and C₇₀ fullerene derivatives. *Synthetic Metals*, 2008, **158** (11), P. 468–472.
- [14] Park H., Park J., Lim A.K.L., Anderson E.H., Alivisatos A.P., McEuen P.L. Nanomechanical oscillations in a single-C₆₀ transistor. *Nature*, 2000, **407**, P. 57–60.
- [15] Iijima S. Helical Microtubules of Graphitic Carbon. *Nature*, 1991, **354** (5), P. 56–58.
- [16] Jagessar R.C. Carbon Nanotubes and its Application in Nanotechnology. *J. of Nanosciences Research & Reports*, 2021, **3** (4), P. 1–4.
- [17] Wang C., Zhang J., Ryu K., Badmaev A., Arco L. G. D., Zhou C. Wafer-Scale Fabrication of Separated Carbon Nanotube Thin-Film Transistors for Display Applications. *Nano Lett.*, 2009, **9** (12), P. 4285–4291.
- [18] Crippa P., Biagetti G., Turchetti C., Falaschetti L. et al. A high-gain CNTFET-based LNA developed using a compact design-oriented device model. *Electronics*, 2021, **10** (22), P. 2835–2914.
- [19] Zhang Z., Passlack M., Pitner G., Natani Sh. et al. Complementary carbon nanotube metal–oxide–semiconductor field-effect transistors with localized solid-state extension doping. *Nat. Electron.*, 2023, **6**, P. 999–1008.
- [20] Lee Y., Buchheim J., Hellenkamp B., Lynall D. et al. Carbon-nanotube field-effect transistors for resolving single-molecule aptamer–ligand binding kinetics. *Nat. Nanotechnol.*, 2024, **19**, P. 660–667.
- [21] Gilmer D.C., Rueckes T., Cleveland L. NRAM: A disrupting carbon-nanotube resistance-change memory. *Nanotechnology*, 2018, **29**, 134003.
- [22] Qu T.Yu., Sun Y., Chen M., Liu Z., Zhu Q.B. et al. A Flexible Carbon Nanotube Sen-Memory Device. *Advanced Materials*, 2020, **32** (9), 1907288.
- [23] Lee N.-S., Chung D., Han I., Kang J.H. et al. Application of carbon nanotubes to field emission displays. *Diamond and Related Materials*, 2001, **10**, P. 265–270.
- [24] McCarthy M.A., Liu B., Donoghue E.P., Kravchenko I., Kim D.Y., So F., Rinzler A.G. Low-Voltage, Low-Power, Organic Light-Emitting Transistors for Active Matrix Displays. *Science*, 2011, **332**, P. 570–573.
- [25] Cai L., Wang C. Carbon Nanotube Flexible and Stretchable Electronics. *Nanoscale research letters*, 2015, **10** (1), P. 1013–1021.
- [26] Shalaev R.V., Ulyanov A.N., Prudnikov A.M., Shin G.M., Yoo S.I., Varyukhin V.N. Noncatalytic synthesis of carbon-nitride nanocolumns by DC magnetron sputtering. *Phys.Status Solidi A.*, 2010, **207** (10), P. 2300-2302.
- [27] Liechtenstein I.Ya., Schemchenko E.I., Varyukhin V.N. Mechanism of formation of the internal structure in multi-walled carbon nanotubes produced by a DC-magnetron. *PHPT*, 2021, **31** (4), P. 42–47.
- [28] Shulaker M.M., Hills G., Patil N., Hai W., Chen H.Y., Wong H.S.P., Mitra S. Carbon nanotube computer. *Nature*, 2013, **501**, P. 526–530.
- [29] Hills G., Lau C., Wright A., Fuller S., Bishop M.D. et al. Modern microprocessor built from complementary carbon nanotube transistors. *Nature*, 2019, **572**, P. 595–602.
- [30] Si J., Zhang P., Zhao C., Lin D., Xu L., Xu H. et al. A carbon-nanotube-based tensor processing unit. *Nature Electronics*, 2024, **7**, P. 684–693.
- [31] Novoselov K.S., Geim A.K., Morozov S.V., Jiang D., Zhang Y., Dubonos S.V., Grigorieva I.V., Firsov A.A. Electric field effect in atomically thin carbon films. *Science*, 2004, **306**, P. 666-669.
- [32] Avouris P., Xia F. Graphene applications in electronics and photonics. *MRS Bulletin*, 2012, **37**, P. 1225–1234.
- [33] Golovanov O.A., Makeeva G.S., Varenitsa V.V. Conductivity of graphene in the terahertz and infrared frequency ranges. *Reliability and Quality of Complex Systems*, 2014, **4** (8), P. 26–33.
- [34] Meric I., Han M.Y., Young A.F. et al. Current saturation in zero-bandgap, top-gated graphene field-effect transistors. *Nature nanotechnology*, 2008, **3** (11), P. 654–659.
- [35] Svintsov D.A., Vyurkov V.V., Lukichev V.F., Orlikovsky A.A., Burenkov A., Ochsner R. Tunnel field-effect transistors based on graphene. *Semiconductors*, 2013, **47** (2), P. 244–250.
- [36] Hu B., Sun H., Tian J., Mo J., Xie W., Song Q.M., Zhang W., Dong H. Advances in flexible graphene field-effect transistors for biomolecule sensing. *Front. Bioeng. Biotechnol.*, 2023, **11**, 1218024.
- [37] Hong A., Song E.B., Yu H.S., Allen M.J., Kim J., Fowler J.D. et al. Graphene flash memory. *ACS nano*, 2011, **5** (10), P. 7812-7817.
- [38] Wang G., Lee J.-H., Yang Y., Ruan G., Kim N.D., Ji Y., Tour J.M. Three-Dimensional Networked Nanoporous Ta₂O_{5-x} Memory System for Ultrahigh Density Storage. *Nano Letters*, 2015, **15** (9), P. 6009–6014.
- [39] Zongjie S., Chun Z., Yanfei Q., Mitrovic I.Z., Li Y., Jiacheng W. et al. Memristive Non-Volatile Memory Based on Graphene Materials. *Micromachines*, 2020, **11** (4), 341.
- [40] Lin Yu-M., Valdes-Garcia A., Han S.-J., Farmer D. et al. Wafer-Scale Graphene Integrated Circuit. *Science*, 2011, **332**, P. 1294–1297.
- [41] Fadil D., Passi V., Wei W., Ben Salk S., Zhou D. et al. A Broadband Active Microwave Monolithically Integrated Circuit Balun in Graphene Technology. *Appl. Sci.*, 2020, **10**, 2183:8.

Submitted 21 March 2025; revised 5 April 2025; accepted 6 April 2025

Information about the authors:

Rostyslav V. Shalaye – Galkin Donetsk Institute for Physics and Engineering, R. Luxembourg str. 72, 283048, Donetsk, Russia; ORCID 0000-0003-1258-2434; sharos@donfti.ru

Victor N. Varyukhin – Galkin Donetsk Institute for Physics and Engineering, R. Luxembourg str. 72, 283048, Donetsk, Russia; ORCID 0000-0001-7717-8745; director@donfti.ru

Conflict of interest: the authors declare no conflict of interest.

Elastic and thermal properties of some ternary β -Ti based alloys

Sergey O. Kasparyan^{1,2,a}, Adil E. Ordabaev^{2,b}, Alexander V. Bakulin^{1,c}, Svetlana E. Kulkova^{1,d}

¹Institute of Strength Physics and Materials Science of the Siberian Branch of the Russian Academy of Sciences, Tomsk, Russia

²National Research Tomsk State University, Tomsk, Russia

^aks-fff-isopams@mail.ru, ^badil.ordabaev04@gmail.com, ^cbakulin@ispms.ru, ^dkulkova@ispms.ru

Corresponding author: Sergey O. Kasparyan, ks-fff-isopams@mail.ru

PACS 62.20.-x, 62.20.de, 72.15.Eb

ABSTRACT The elastic moduli and some thermal properties of four series of ternary β -Ti based alloys of the XY_3Ti_{11} composition, where X and Y are elements of IVB–VIB, IIIA and IVA groups, have been studied using the projector augmented wave method within the density functional theory. It has been shown that the calculated Young's moduli in these series of alloys are lower than those in commercially pure α -Ti titanium or in the Ti-6Al-4V alloy. With an increase in the concentration of s, p -elements and the number of electrons in the d -band of the X-metal, the Young's modulus tends to decrease. The variation of Debye temperature, acoustic Grüneisen parameter and thermal conductivity in titanium alloy series is discussed. It is shown that high thermal conductivity correlates with high Debye temperature, which in turn increases with increase of the values of the Young's modulus.

KEYWORDS titanium alloys, elastic moduli, thermal conductivity, the ab-initio calculations

ACKNOWLEDGEMENTS The work was performed according to the Government research assignment for ISPMS SB RAS, project FWRW-2022-0001. Numerical calculations were performed using the SKIF Cyberia super-computer at Tomsk State University.

FOR CITATION Kasparyan S.O., Ordabaev A.E., Bakulin A.V., Kulkova S.E. Elastic and thermal properties of some ternary β -Ti based alloys. *Nanosystems: Phys. Chem. Math.*, 2025, **16** (2), 225–234.

1. Introduction

Due to the combination of biocompatibility and unique mechanical properties, such as shape memory effect and the ability to achieve a low Young's modulus (E), β -Ti based alloys are considered promising for use in medicine [1–3]. Currently, the most commonly used material for orthopedic and dental implants is commercially pure (CP) titanium or an alloy of the composition Ti-6Al-4V [3–6]. At the same time, titanium remains a universal structural material and is widely used in the aerospace, automotive, and shipbuilding industries, in particular, for aircraft skins, various fasteners, chassis parts, rocket engines, etc. Due to its high strength and heat resistance, titanium and its alloys can withstand significant loads. Since titanium does not react with salt water, materials based on it are widely used in shipbuilding. In addition, titanium demonstrates excellent corrosion resistance. This property explains the popularity titanium has gained in the chemical process and power generation industry where harsh environments are usual. It is used to manufacture key equipment for the chemical and petrochemical industries. However, the addition of alloying impurities can significantly affect its mechanical and physicochemical properties.

It is known that the addition of bioinert β -stabilizing elements such as Mo, Nb, Ta, etc. extends the temperature range of β -Ti stability [7], and the addition of Zr and some s, p -elements (e.g. Sn, In) leads to a decrease in Young's modulus. Recently, a “cluster plus glue atom” model [8] was proposed to search for new low-modulus ternary titanium alloys, where the alloying atom (X) is located in the center of the titanium cluster, with 8 atoms on the first and 6 atoms on the second coordination sphere, and additional element (Y) plays the role of “glue atom”. It is believed that they should weakly interact with the Ti atoms. Within this model, a theoretical study of the elastic moduli of a number of ternary titanium alloys was carried out [9], and three types of clusters with the number of Y atoms equal to 1, 3 and 4 were considered. The authors showed that in the case of $TaNb_3Ti_{11}$, the Young's modulus exhibits the lowest value of ~ 7 GPa. In work [10], calculations of the electronic structure and elastic properties of a number of ordered XY_3Ti_{11} alloys were also carried out using the model [8] and it was found that all the alloys considered have Young's modulus values lower than CP titanium, and for five alloys it is even lower than 45 GPa. However, in both works [9, 10], only transition metals were used as X and Y elements.

The aim of this work is to study the elastic moduli of four series of titanium alloys of the XY_3Ti_{11} composition with In and Sn both at the X and Y positions, which will allow us to identify their role in reducing the Young's modulus. Besides such series of ternary Ti-based alloys are very convenient models for study not only elastic properties but also

for calculation of thermal properties, which are less studied by DFT methods [11, 12]. Thus, we calculate the Debye temperature, acoustic Grüneisen parameter and thermal conductivity of the alloys and reveal their trends in dependence on the alloy composition.

2. Computational details

The electronic structure and elastic properties of ternary titanium alloys were calculated using the projector augmented wave method [13, 14] within the VASP code [15, 16] with a generalized gradient approximation for the exchange-correlation functional in the form of PBE–GGA [17]. The maximum energy of plane waves from the basis set was 300 eV. Integration over the Brillouin zone was performed using a $12 \times 12 \times 12$ Monkhorst–Pack k -point grid [18]. Full optimization of the atomic structure of the alloys included both the relaxation of atomic positions and a change in the cell volume. Convergence was considered achieved if the difference in the total energies of two successive iterations did not exceed 10^{-6} eV. The convergence criterion for the forces acting on the atoms was 10^{-3} eV/Å.

The elastic constants were estimated using the finite difference method, based on the analysis of the change in the total energy of the system during deformation. The bulk modulus was calculated using the following formula:

$$B = (C_{11} + 2C_{12})/3. \quad (1)$$

To estimate the stability of the alloys, the Born criteria [19] $C_{44} > 0$, $C_{11} - C_{12} = 2C' > 0$, and $C_{11} + 2C_{12} > 0$ were used. The shear moduli (G) and Young's moduli (E), as well as Poisson's ratio (ν) were calculated within the Voigt–Reuss–Hill model [20], which averages the values of elastic moduli calculated using the Voigt (V) [21] and Reuss (R) [22] methods:

$$G = \frac{G_V + G_R}{2}, \quad E = \frac{9BG}{3B + G}, \quad \nu = \frac{3B - 2G}{2(3B + G)}, \quad (2)$$

$$G_V = \frac{C_{11} - C_{12} + 3C_{44}}{5}, \quad G_R = \frac{5(C_{11} - C_{12})C_{44}}{4C_{44} + 3(C_{11} - C_{12})}. \quad (3)$$

Note that for cubic systems $B = B_V = B_R$.

3. Results and discussion

3.1. Elastic properties

Tables 1 and 2 present the calculated elastic constants and moduli for the studied series of alloys. All considered alloys in accordance with above-mentioned Born criteria [19] are stable. However, the minimum values of C' are observed in the following systems: InHf₃Ti₁₁ (first series), SnHf₃Ti₁₁ (second series), CrIn₃Ti₁₁ (third series), and WSn₃Ti₁₁ (fourth series), which indicates their proximity to the critical threshold of mechanical stability. It is seen that the constant C_{11} , which characterizes the interaction between the elements X and Y with the titanium atoms in the second coordination spheres, demonstrates a tendency to increase with the number of electrons in the d -band of the transition element. In the studied systems the values of the constant C_{44} are significantly lower than the other elastic constants, which causes a positive value of the difference ($C_{11} - C_{44}$), known as the Cauchy pressure. A positive value of this parameter is traditionally associated with the metallic bond.

Comparison of the systems with Sn and In at the X-position revealed a slight increase in the C_{11} and C_{12} values in Sn-containing alloys, while C_{44} demonstrates a weakly expressed growth in In-containing alloys. The lowest C' values are in the alloys with Zr and Hf, which is consistent with the previously noted trend. In the systems with In and Sn at the Y-position, a correlation was observed between the changes in the C' and C_{44} constants, with the latter having values significantly higher than in the alloys of the first two series. In general, the C_{11} constants are lower in the last two series, which indicates a decrease in the interatomic interaction in these alloys with an increase in the concentration of s, p -elements.

The results of elastic moduli calculations demonstrate the following trend: $B > E > G$ is observed for almost all alloy series (Fig. 1). The shear modulus is characterized by comparatively low values. The lowest values of Young's modulus in each series were: 37.3 GPa for InHf₃Ti₁₁, 36.5 GPa for SnHf₃Ti₁₁, 65.7 GPa for CrIn₃Ti₁₁ and 52.4 GPa for WSn₃Ti₁₁ (Fig. 1). At the same time, low values of Young's modulus correspond to low values of elastic constant C_{11} (shown by bold in Tables 1 and 2). It should be noted that the values of Young's modulus for the studied alloys are lower than for pure titanium and Ti-6Al-4V alloy (105 – 120 GPa [23, 24]). However, these results were obtained for α -phase. Of particular interest are InHf₃Ti₁₁ and SnHf₃Ti₁₁ alloys, demonstrating the lowest values of Young's modulus, which makes them promising for further research in the context of biomedical application. In addition, a relationship was found between the increase in the number of valence d -electrons and the growth of the bulk modulus B in the In(Sn)Y₃Ti₁₁ alloy series. In general, the alloys with In and Sn elements at the X-position exhibit close values of all moduli (Table 1). Young's modulus in the series of alloys with In and Sn at the Y-position (Table 2) demonstrates a tendency to decrease in value with an increase in the number of electrons in the d -band of the X-element. High values of Young's modulus in the series of alloys with Sn correlate with high values of the shear modulus in the case of Zr and Hf.

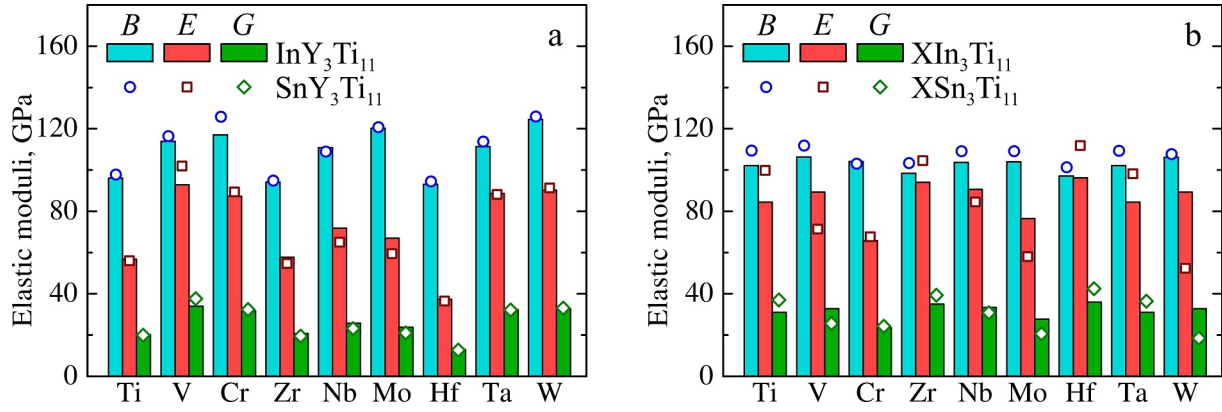


FIG. 1. Theoretical elastic moduli in dependence on the number of valence d -electrons in alloys In(Sn)Y₃Ti₁₁ (a) and XIn(Sn)₃Ti₁₁ (b) with metals of IVB–VIB groups

TABLE 1. Elastic constant and moduli (in GPa) for series of alloys InY₃Ti₁₁ and SnY₃Ti₁₁

Alloy	C_{11}	C_{12}	C_{44}	B	G	E	Alloy	C_{11}	C_{12}	C_{44}	B	G	E
InTi ₃ Ti ₁₁	110.5	88.8	30.7	96.1	20.2	56.7	SnTi ₃ Ti ₁₁	111.1	91.2	31.6	97.8	19.9	56.0
InV ₃ Ti ₁₁	157.7	92.1	34.8	113.9	34.0	92.8	SnV ₃ Ti ₁₁	164.4	92.5	38.8	116.4	37.6	101.9
InCr ₃ Ti ₁₁	174.0	88.5	25.9	117.0	31.7	87.3	SnCr ₃ Ti ₁₁	185.9	95.8	25.9	125.8	32.4	89.4
InZr ₃ Ti ₁₁	109.0	86.7	31.2	94.1	20.7	57.7	SnZr ₃ Ti ₁₁	109.8	87.5	28.3	94.9	19.5	54.7
InNb ₃ Ti ₁₁	140.5	96.0	28.4	110.8	25.8	71.8	SnNb ₃ Ti ₁₁	135.7	95.5	25.6	108.9	23.2	65.0
InMo ₃ Ti ₁₁	155.7	102.4	22.0	120.2	23.8	66.9	SnMo ₃ Ti ₁₁	148.7	106.6	21.0	120.7	21.0	59.5
InHf ₃ Ti ₁₁	96.3	91.3	32.5	93.0	13.0	37.3	SnHf ₃ Ti ₁₁	97.8	92.9	31.6	94.5	12.7	36.5
InTa ₃ Ti ₁₁	140.5	96.6	42.1	111.3	32.4	88.6	SnTa ₃ Ti ₁₁	142.5	99.4	42.1	113.8	32.2	88.2
InW ₃ Ti ₁₁	163.7	104.9	35.1	124.5	32.7	90.2	SnW ₃ Ti ₁₁	163.6	107.0	36.8	125.9	33.1	91.3

TABLE 2. Elastic constant and moduli (in GPa) for series of alloys XIn₃Ti₁₁ and XSn₃Ti₁₁

Alloy	C_{11}	C_{12}	C_{44}	B	G	E	Alloy	C_{11}	C_{12}	C_{44}	B	G	E
TiIn ₃ Ti ₁₁	116.8	94.8	60.0	102.1	31.0	84.4	TiSn ₃ Ti ₁₁	132.7	97.8	60.9	109.4	37.0	99.8
VIn ₃ Ti ₁₁	121.4	98.7	64.4	106.3	32.8	89.3	VSn ₃ Ti ₁₁	121.5	106.9	55.1	111.8	25.6	71.4
CrIn ₃ Ti ₁₁	113.1	99.8	50.9	104.2	23.6	65.7	CrSn ₃ Ti ₁₁	113.2	97.8	50.0	103.0	24.3	67.7
ZrIn ₃ Ti ₁₁	119.4	87.9	59.3	98.4	35.0	94.0	ZrSn ₃ Ti ₁₁	130.0	89.9	61.6	103.3	39.3	104.6
NbIn ₃ Ti ₁₁	122.1	94.5	59.6	103.7	33.4	90.6	NbSn ₃ Ti ₁₁	126.6	100.4	54.0	109.1	30.8	84.5
MoIn ₃ Ti ₁₁	118.1	97.0	51.7	104.0	27.7	76.4	MoSn ₃ Ti ₁₁	117.2	105.1	43.6	109.1	20.6	58.0
HfIn ₃ Ti ₁₁	118.5	86.4	61.4	97.1	36.0	96.2	HfSn ₃ Ti ₁₁	131.1	86.4	65.1	101.3	42.5	111.8
TaIn ₃ Ti ₁₁	116.8	94.8	60.0	102.1	31.0	84.4	TaSn ₃ Ti ₁₁	132.4	97.8	59.4	109.3	36.4	98.2
WIn ₃ Ti ₁₁	121.4	98.7	64.4	106.2	32.8	89.3	WSn ₃ Ti ₁₁	111.6	105.7	48.3	107.7	18.5	52.4

There are several approaches to estimate the ductile/brittle behavior of materials. In [25] the ratio of the shear modulus to the bulk modulus is used for these purposes: the values $G/B < 0.5$ correspond to ductile behavior, and $G/B > 0.5$ to brittle behavior. As can be seen from Fig. 2a, the G/B values for all series of alloys are below 0.5. The second approach [25] is that in ductile materials, the Poisson's ratio (ν) should be greater than $1/3$. From Fig. 2b, it is seen that ν is generally greater than this value, with the exception of the $\text{HfSn}_3\text{Ti}_{11}$ alloy, while the ν values for $\text{HfIn}_3\text{Ti}_{11}$ and $\text{ZrSn}_3\text{Ti}_{11}$ correspond to the critical value. In addition, the values of Poisson's ratio are used to analyze the nature of the chemical bond in the systems. Thus, the value $\nu \approx 0.25$ indicates an ionic bond, which corresponds exactly to brittle fracture, while high values ν indicate a strong metallic bond and good toughness.

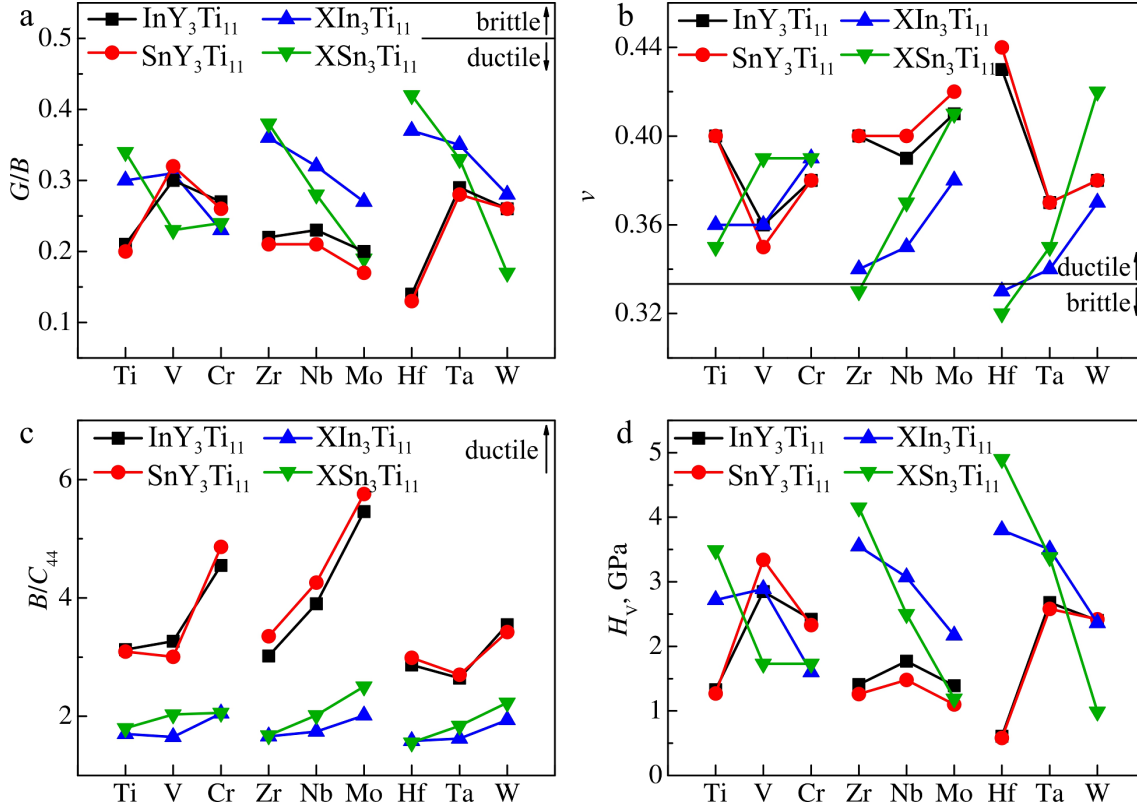


FIG. 2. Pugh's ratio G/B (a), Poisson's coefficient ν (b), B/C_{44} (c), and H_V for the alloys $\text{In(Sn)Y}_3\text{Ti}_{11}$ and $\text{XIn(Sn)}_3\text{Ti}_{11}$

In addition, an increase in the ratio of the bulk modulus to the C_{44} constant [25] can also correlate with a decrease in the brittleness of the material. It is seen from Fig. 2c that in general these values are greater than ~ 1.5 , while the values for the $\text{InY}_3\text{Ti}_{11}$ and $\text{SnY}_3\text{Ti}_{11}$ alloy series are higher than for alloys with simple metals in the Y-position. The Vickers hardness of the alloys was also estimated using the following empirical relationship [26]:

$$H_V = 0.92 (G/B)^{1.137} G^{0.708}. \quad (4)$$

Vickers hardness is used to evaluate the ability of materials to resist deformation under compressive stress. Several empirical formulas were proposed for its calculation, as shown in our earlier work [27]. Fig. 2d demonstrates that the microhardness in $\text{XSn}_3\text{Ti}_{11}$ alloys with metals of IVB group is increased from 3.5 to 4.9 GPa in the set of isoelectronic elements. These values are significantly higher than that of 1.8 GPa for Ti-6Al-4V. High microhardness values are observed for $\text{In(Sn)Y}_3\text{Ti}_{11}$ alloys with V and $\text{XIn}_3\text{Ti}_{11}$ alloys with V, Nb, Ta (Table 3). In addition, other parameters that are also used to describe brittle/ductile behavior were also calculated, in particular, the fracture toughness (K_{IC}) and the brittleness index (M_{dt}). Fracture toughness characterizes the resistance to crack propagation, and the brittleness index reflects the damage resistance and can be determined using H_V and K_{IC} [28, 29], and the large value of the M_{dt} means a weak damage tolerance. The K_{IC} and M_{dt} were obtained from the following expressions:

$$K_{IC} = V_0^{1/6} G \left(\frac{B}{G} \right)^{1/2}, \quad (5)$$

$$M_{dt} = \frac{H_V}{K_{IC}}, \quad (6)$$

TABLE 3. Calculated values of Vickers microhardness H_V (in GPa), fracture toughness K_{IC} (in $\text{MPa}\cdot\text{m}^{1/2}$), and brittleness index M_{dt} (in $\mu\text{m}^{-1/2}$)

Alloy	H_V	K_{IC}	M_{dt}	Alloys	H_V	K_{IC}	M_{dt}	Alloy	H_V	K_{IC}	M_{dt}
InTi ₃ Ti ₁₁	1.33	0.71	1.87	SnTi ₃ Ti ₁₁	1.27	0.71	1.78	TiIn ₃ Ti ₁₁	2.72	0.92	2.97
InV ₃ Ti ₁₁	2.85	1.00	2.86	SnV ₃ Ti ₁₁	3.34	1.07	3.12	VIn ₃ Ti ₁₁	2.89	0.96	3.01
InCr ₃ Ti ₁₁	2.42	0.99	2.44	SnCr ₃ Ti ₁₁	2.33	1.03	2.25	CrIn ₃ Ti ₁₁	1.60	0.80	1.99
InZr ₃ Ti ₁₁	1.41	0.72	1.96	SnZr ₃ Ti ₁₁	1.26	1.10	1.14	ZrIn ₃ Ti ₁₁	3.55	0.96	3.70
InNb ₃ Ti ₁₁	1.77	0.87	2.04	SnNb ₃ Ti ₁₁	1.48	1.28	1.16	NbIn ₃ Ti ₁₁	3.07	0.96	3.20
InMo ₃ Ti ₁₁	1.39	0.86	1.61	SnMo ₃ Ti ₁₁	1.10	0.81	1.36	MoIn ₃ Ti ₁₁	2.17	0.87	2.48
InHf ₃ Ti ₁₁	0.61	0.57	1.08	SnHf ₃ Ti ₁₁	0.58	0.56	1.03	HfIn ₃ Ti ₁₁	3.80	0.97	3.93
InTa ₃ Ti ₁₁	2.68	0.97	2.75	SnTa ₃ Ti ₁₁	2.58	0.98	2.63	TaIn ₃ Ti ₁₁	3.50	0.98	3.57
InW ₃ Ti ₁₁	2.40	1.03	2.33	SnW ₃ Ti ₁₁	2.42	1.05	2.32	WIn ₃ Ti ₁₁	2.36	0.89	2.64

where V_0 is the cell volume per atom (in m^3). The obtained values of these parameters are given in Table 3.

It is seen from Table 3 that for alloys with In and Sn in the X-position the scatter in the K_{IC} parameter depending on the transition metal (Y) is larger ($0.56 - 1.28 \text{ MPa}\cdot\text{m}^{1/2}$) than that in the series of alloys with simple elements in the Y-position ($0.72 - 1.04 \text{ MPa}\cdot\text{m}^{1/2}$), and the influence of Sn on this scatter is more significant than that of In. The values of the K_{IC} parameter in the considered series of alloys are significantly lower than the values obtained for c-CrH ($3.42 \text{ MPa}\cdot\text{m}^{1/2}$ [11]), AlN ($2.79 \text{ MPa}\cdot\text{m}^{1/2}$ [30]), c-BN ($5 \text{ MPa}\cdot\text{m}^{1/2}$ [30]) or for $\text{V}(\text{Nb})_5\text{Si}_3\text{B}$ compounds ($\sim 4.0 - 4.70 \text{ MPa}\cdot\text{m}^{1/2}$ [12]). At the same time, the values of the brittleness index for the studied alloys are significantly lower than for the compounds indicated above. In the series with In and Sn in the X-position, the lowest M_{dt} value corresponds to alloys with Hf, and the highest – to those with V (Table 3). With increasing concentration of simple metals, the brittleness index increases, and the maximum values of 3.93 and $4.58 \mu\text{m}^{-1/2}$ were obtained for alloys with Hf in the X-position. That is, a decrease in the hafnium concentration leads to a decrease in the damage resistance of the alloys.

3.2. Thermal properties

It is known that the free energy is significantly affected by lattice vibrations, which can be characterized in terms of the Debye temperature Θ_D and the Grüneisen constant γ_a [31]. In addition, the bond strength between atoms can also correlate with the Debye temperature: a strong bond strength corresponds to a high Debye temperature [32]. The Debye temperature of alloys can be calculated using the formula from [33]:

$$\Theta_D = \frac{h}{k_B} \left[\frac{3n}{4\pi} \left(\frac{N_A \rho}{M} \right) \right]^{1/3} v_m, \quad (7)$$

where h and k_B are the Planck and Boltzmann constants, N_A is the Avogadro constant, n is the number of atoms in the alloy, ρ is the density of the substance, M is its molecular weight, v_m is the average sound velocity, which can be calculated using the following formula from [34]:

$$v_m = \left[\frac{1}{3} \left(\frac{2}{v_t^3} + \frac{1}{v_l^3} \right) \right]^{-1/3}, \quad (8)$$

where v_t and v_l are the transverse and longitudinal sound velocities, respectively, which are obtained from the following expressions:

$$v_l = \left(\frac{B + 4G/3}{\rho} \right)^{1/2}, \quad (9)$$

$$v_t = \left(\frac{G}{\rho} \right)^{1/2}. \quad (10)$$

It is known that in order to study the thermal expansion or thermal conductivity of crystals, it is necessary to use a nonharmonic approximation to describe the interaction of atoms. For these purposes, it is necessary to know the acoustic Grüneisen parameter γ_a , which was calculated as in [35]:

$$\gamma_a = \frac{3}{2} \left(\frac{3v_l^2 - 4v_t^2}{v_l^2 + 2v_t^2} \right). \quad (11)$$

Table 4 presents the values of the density (ρ) of the alloys, which was estimated as the mass of atoms in the computational cell divided by its volume, the sound velocities (longitudinal v_l , transverse v_t and average v_m), the acoustic Grüneisen parameter γ_a , and the Debye temperature Θ_D for two series of alloys with In at the X and Y positions that is with increase of In concentration. Since there are no corresponding experimental data on the Debye temperature for the studied alloys, we estimated it for the Ti-6Al-4V alloy (Ti-10.2Al-3.6V at. %) in the β phase, while the elastic constants were calculated using the EMTO-CPA method [36], which takes into account the disordering effect. The obtained value of Θ_D according to formula (7) is 315.6 K, which agrees well with the experimental value of 326.0 K [37]. The values of Θ_D in dependence on elastic anisotropy are 264.2 – 278.2 K [23]. The estimation for β -Ti in the used model with a vacancy (i.e. Ti also occupies X and Y positions in the computational cell) gives the value 251.8 K that is smaller in comparison with the previous cases. That is, the decrease of the Debye temperature means a decrease in the bond strength and a lower hardness. The smallest Θ_D in alloy with Hf in the Y-position (Table 4), indicating the lowering of bond strength, that correlates with the lowest Young's modulus (Table 1) and hardness (Fig. 2d) as well as with the largest γ_a . In the case of alloy with Hf in the X-position, an increase in Θ_D and, consequently, the bond strength and H_V is observed. It should be noted that a correlation between the Debye temperature and Young's modulus takes place for all studied series of alloys. The obtained Debye temperatures of the alloys are subsequently used to calculate their lattice thermal conductivity.

TABLE 4. Density ρ (in g/cm^3), sound velocities (longitudinal v_l , transverse v_t and average v_m in m/s), acoustic Grüneisen parameter γ_a , and Debye temperature Θ_D (in K)

Alloy	ρ	v_l	v_t	v_m	γ_a	Θ_D	Alloy	ρ	v_l	v_t	v_m	γ_a	Θ_D
InTi ₃ Ti ₁₁	4.877	5023	2037	2306	2.64	263.2	TiIn ₃ Ti ₁₁	5.458	5125	2382	2682	2.24	301.6
InV ₃ Ti ₁₁	5.176	5547	2563	2888	2.26	334.8	VIn ₃ Ti ₁₁	5.545	5201	2433	2739	2.22	309.2
InCr ₃ Ti ₁₁	5.379	5512	2448	2762	2.38	324.0	CrIn ₃ Ti ₁₁	5.580	4929	2054	2324	2.57	262.8
InZr ₃ Ti ₁₁	5.332	4777	1968	2227	2.60	248.8	ZrIn ₃ Ti ₁₁	5.608	5086	2499	2806	2.06	313.5
InNb ₃ Ti ₁₁	5.621	5082	2141	2421	2.53	274.8	NbIn ₃ Ti ₁₁	5.707	5097	2420	2722	2.17	305.8
InMo ₃ Ti ₁₁	5.905	5070	2006	2273	2.71	261.3	MoIn ₃ Ti ₁₁	5.778	4939	2190	2472	2.38	278.5
InHf ₃ Ti ₁₁	6.900	3999	1373	1561	3.07	174.8	HfIn ₃ Ti ₁₁	6.138	4861	2422	2718	2.01	304.0
InTa ₃ Ti ₁₁	7.207	4629	2120	2389	2.28	270.8	TaIn ₃ Ti ₁₁	6.241	4894	2387	2682	2.08	301.4
InW ₃ Ti ₁₁	7.511	4730	2086	2355	2.40	269.9	WIn ₃ Ti ₁₁	6.316	4756	2144	2418	2.33	272.6

It is known that the acoustic Grüneisen parameter γ_a is related to scattering between phonons. The larger γ_a means the more inharmonic the phonons behavior, which in turn leads to lower thermal conductivity. The values of γ_a were calculated using formula (11) and the Leontiev formula [38], which used not only the average value of the sound velocities, but also density of material and bulk modulus. In the case of the test alloy Ti-6Al-4V, almost the same values of γ_a equal ~ 2.50 were obtained. However, the experimental value from paper [37] is more than two times smaller (1.100), since the so-called thermodynamic Grüneisen parameter is usually measured in experiment. As noted earlier in [39], the acoustic Grüneisen parameter can differ significantly from the thermodynamic parameter (γ_D), for example, for rare earth elements the difference in these coefficients reaches an average of two times. Our calculation of the acoustic Grüneisen parameters for Nb, Ta and other metals shows a similar trend. It is seen from Table 4 that an increase in γ_a in the InY₃Ti₁₁ alloy series is observed in the case of $4d$ -metals, as well as Ti and Hf in the Y-position. In the case of Sn in the Y-position, large γ_a values are characteristic of VIB metals.

A few words should be added about the sound velocities which are used for calculation of both characteristics Θ_D and γ_a . It is well known that the sound velocities in crystal with cubic symmetry are determined by elastic constants (Table 1) or their combinations depending on the direction of propagation. Since standard formulas for calculating the longitudinal and transverse sound velocities (Table 5) were used [40], they are not given. The longitudinal sound velocity along the [100] direction is related to the elastic constant C_{11} , which increases with the number of d -electrons of the transition metals, therefore we observe an increase in the [100] v_l in the series InTi₃Ti₁₁–InV₃Ti₁₁–InCr₃Ti₁₁ (Table 5) and in the case of metals isoelectronic to the Y-element. The transverse two modes are related to elastic constant C_{44} , which is significantly lower than C_{11} , therefore the values of v_{t1} and v_{t2} are equal and almost two times smaller than the value of the v_l . In the case of the [110] direction, the value of v_l is the highest, and the transverse velocities are different in accordance with their determination. Finally, in the case of the [111] direction, the longitudinal sound velocity reaches a maximum for VB elements for InY₃Ti₁₁ (Table 5). Replacing In with Sn does not lead to significant changes in the values of sound velocities. An increase in the concentration of simple metals leads to a decrease in [100] v_l and an increase in the transverse modes also (Table 6).

TABLE 5. The anisotropic sound velocities (in m/s) in alloys $\text{InY}_3\text{Ti}_{11}$

Alloy	$[100]v_l$	$[010]v_{t1}$	$[001]v_{t2}$	$[110]v_l$	$[1-10]v_{t1}$	$[001]v_{t2}$	$[111]v_l$	$[11-2]v_{t1}$	$[1-10]v_{t2}$
$\text{InTi}_3\text{Ti}_{11}$	4760	2510	2510	5171	1490	2510	5300	1892	1892
$\text{InV}_3\text{Ti}_{11}$	5519	2594	2594	5554	2518	2594	5566	2543	2543
$\text{InCr}_3\text{Ti}_{11}$	5752	2218	2218	5476	2832	2218	5381	2643	2643
$\text{InZr}_3\text{Ti}_{11}$	4521	2418	2418	4919	1446	2418	5044	1828	1828
$\text{InNb}_3\text{Ti}_{11}$	5000	2248	2248	5107	1990	2248	5143	2080	2080
$\text{InMo}_3\text{Ti}_{11}$	5134	1931	1931	5057	2124	1931	5031	2062	2062
$\text{InHf}_3\text{Ti}_{11}$	3736	2169	2169	4278	600	2169	4444	1344	1344
$\text{InTa}_3\text{Ti}_{11}$	4415	2416	2416	4721	1744	2416	4819	1994	1994
$\text{InW}_3\text{Ti}_{11}$	4668	2162	2162	4749	1978	2162	4775	2041	2041

TABLE 6. The anisotropic sound velocities (in m/s) in alloys $\text{XIn}_3\text{Ti}_{11}$

Alloy	$[100]v_l$	$[010]v_{t1}$	$[001]v_{t2}$	$[110]v_l$	$[1-10]v_{t1}$	$[001]v_{t2}$	$[111]v_l$	$[11-2]v_{t1}$	$[1-10]v_{t2}$
$\text{TiIn}_3\text{Ti}_{11}$	4625	3315	3315	5511	1419	3315	5776	2238	2238
$\text{VIn}_3\text{Ti}_{11}$	4679	3407	3407	5608	1433	3407	5885	2288	2288
$\text{CrIn}_3\text{Ti}_{11}$	4502	3020	3020	5310	1092	3020	5553	1958	1958
$\text{ZrIn}_3\text{Ti}_{11}$	4615	3252	3252	5391	1677	3252	5626	2324	2324
$\text{NbIn}_3\text{Ti}_{11}$	4625	3231	3231	5424	1555	3231	5665	2257	2257
$\text{MoIn}_3\text{Ti}_{11}$	4521	2990	2990	5249	1353	2990	5470	2050	2050
$\text{HfIn}_3\text{Ti}_{11}$	4393	3162	3162	5165	1617	3162	5398	2253	2253
$\text{TaIn}_3\text{Ti}_{11}$	4420	3174	3174	5218	1544	3174	5458	2225	2225
$\text{WIn}_3\text{Ti}_{11}$	4343	2918	2918	5059	1333	2918	5277	2005	2005

Thermal conductivity (k_{ph}) reflects atomic interaction within crystal at a certain temperature. The calculation of the lattice thermal conductivity of the alloys was carried out within the Slack's model [41] using the empirical formula:

$$k_{ph} = \frac{AV_0M_a\Theta_D^3}{T\gamma_a^2n^{2/3}}, \quad (12)$$

where V_0 is the volume per atom, M_a is the average atomic mass per atom, T is the temperature, n is the number of atoms in the computational cell, A is a coefficient depending on the acoustic Grüneisen parameter γ_a . The coefficient A can be calculated as follows:

$$A = \frac{2.43 \cdot 10^{-8}}{1 - 0.514/\gamma_a + 0.228/\gamma_a^2}. \quad (13)$$

Figure 3 shows the temperature dependences of k_{ph} . The highest values of the thermal conductivity in each series of alloys, for example, calculated for a temperature of 300 K are 1.64 W/(m·K) for $\text{InV}_3\text{Ti}_{11}$, 2.18 W/(m·K) for $\text{SnV}_3\text{Ti}_{11}$, 2.15 W/(m·K) for $\text{HfIn}_3\text{Ti}_{11}$, and 3.15 W/(m·K) for $\text{HfSn}_3\text{Ti}_{11}$. The lowest values of k_{ph} at the same temperature are: 0.18 W/(m·K) for $\text{InHf}_3\text{Ti}_{11}$, 0.17 W/(m·K) for $\text{SnHf}_3\text{Ti}_{11}$, 0.71 W/(m·K) for $\text{CrIn}_3\text{Ti}_{11}$, and 0.37 W/(m·K) for $\text{WSn}_3\text{Ti}_{11}$. In general, there is a correlation between the values of thermal conductivity and Debye temperature. This is especially pronounced for the alloys of the first two series, i.e. for In and Sn in the X-position. At the same time, in alloys with a large concentration of simple metals (In and Sn in the Y-position) compared to transition metals (in the X-position), this trend may be imperfect, since close values of Θ_D were obtained for several alloys. As can be seen from Fig. 3, the thermal conductivity decreases sharply with increasing temperature, and at $T > 600$ K the decrease in the thermal conductivity slows down.

The theoretical lower limit of the thermal conductivity is known as intrinsic minimum lattice thermal conductivity k_{\min} of a crystal. It can be calculated using two models: Clarke's model [42, 43] and Cahill's model [44]. In the Clarke's

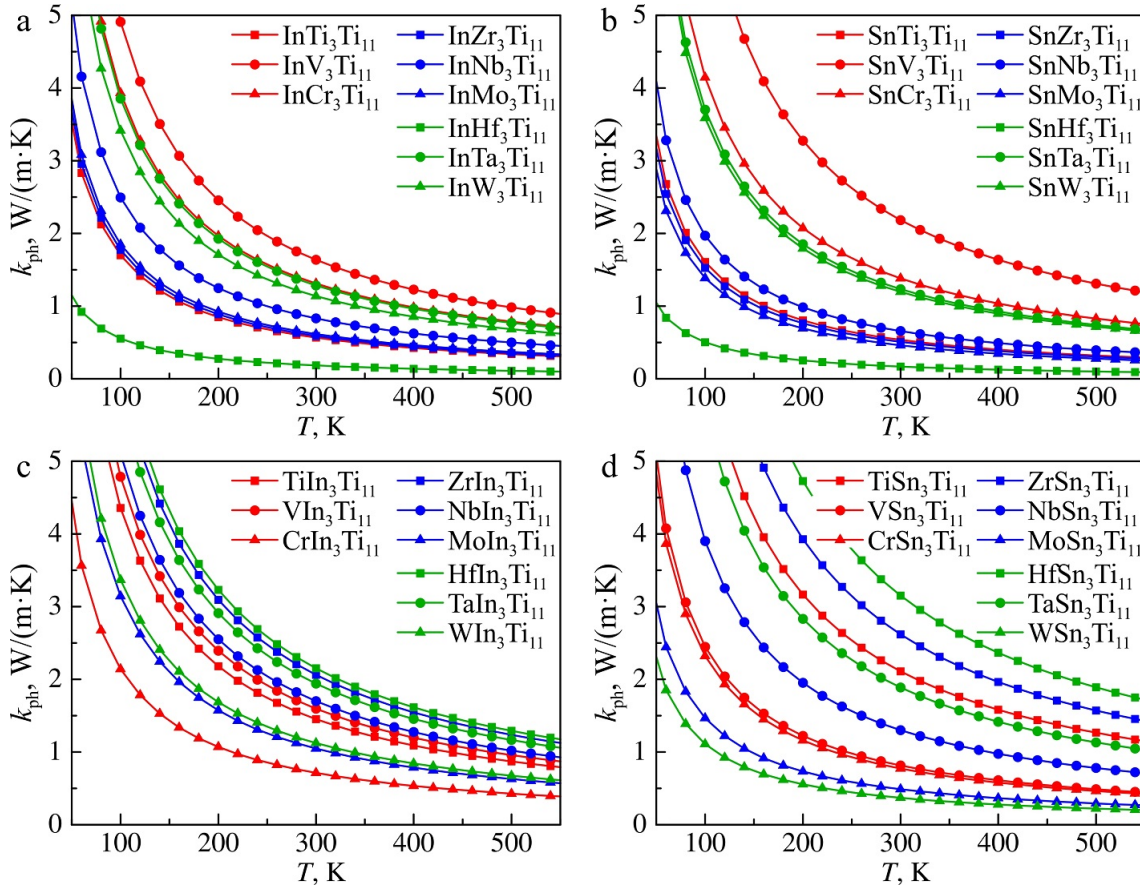


FIG. 3. Calculated lattice thermal conductivities k_{ph} in the temperature ranging from 50 to 550 K for four series of alloys: $\text{InY}_3\text{Ti}_{11}$ (a), $\text{SnY}_3\text{Ti}_{11}$ (b), $\text{XIn}_3\text{Ti}_{11}$ (c), $\text{XSn}_3\text{Ti}_{11}$ (d), where X and Y are elements of IVB–VIB groups

model,

$$k_{\min} = 0.87k_B M_a^{-2/3} E^{1/2} \rho^{1/6}, \quad (14)$$

$$M_a = \frac{M}{mN_a}, \quad (15)$$

where M_a is the average atomic mass, M is the molar mass, and m is the total number of atoms.

In Cahill's model k_{\min} is expressed as

$$k_{\min} = \frac{k_B}{2.48} n^{2/3} (v_l + 2v_t). \quad (16)$$

It is seen from Table 7 that the highest values of k_{\min} in each series are observed for the $\text{InV}_3\text{Ti}_{11}$, $\text{SnV}_3\text{Ti}_{11}$, $\text{VIn}_3\text{Ti}_{11}$, and $\text{ZrSn}_3\text{Ti}_{11}$ alloys. The k_{\min} values calculated using Clarke's model are somewhat lower than the values obtained by Cahill's model, which is due to the fact that Clarke's model does not take into account the contribution of the phonon spectrum [45]. In addition, the k_{ph} results calculated using Slack's model at high temperatures (Fig. 3) are close to those obtained using Clarke's formula. It is seen that for all alloys there is a correlation between the high k_{\min} value and the Debye temperature (Table 4). In the case of $\text{VIn}_3\text{Ti}_{11}$ and $\text{ZrIn}_3\text{Ti}_{11}$, practically the same thermal conductivity values were obtained, and the difference in the Debye temperature values is insignificant, it is approximately 4.3 K. Besides, smaller γ_a values also indicate higher thermal conductivity but this trend is imperfect with increase of s , p -element concentration.

4. Conclusion

The elastic and some thermal properties of ternary titanium alloys of the composition $\text{InY}_3\text{Ti}_{11}$, $\text{SnY}_3\text{Ti}_{11}$, $\text{XIn}_3\text{Ti}_{11}$, and $\text{XSn}_3\text{Ti}_{11}$, where X and Y are transition metals of IVB–VIB groups, are calculated using the projector augmented wave method within the density functional theory. It is shown that the values of Young's modulus for almost all alloys are lower than those of pure titanium and the Ti-6Al-4V alloy used for practical applications. The minimum values of Young's modulus (~ 37 GPa) are obtained for the alloys with Hf in the Y-position, which demonstrate a weaker interaction of the X and Y atoms with the titanium atoms located on the second coordination sphere. This trend (low C_{11} corresponds to

TABLE 7. Calculated values of k_{\min} (in W/(m·K)) for series of alloys $\text{In}(\text{Sn})\text{Y}_3\text{Ti}_{11}$ and $\text{XIn}(\text{Sn})_3\text{Ti}_{11}$

Alloy	k_{\min}^{Clarke}	k_{\min}^{Cahill}	Alloys	k_{\min}^{Clarke}	k_{\min}^{Cahill}	Alloy	k_{\min}^{Clarke}	k_{\min}^{Cahill}	Alloys	k_{\min}^{Clarke}	k_{\min}^{Cahill}
$\text{InTi}_3\text{Ti}_{11}$	0.60	0.74	$\text{SnTi}_3\text{Ti}_{11}$	0.60	0.74	$\text{TiIn}_3\text{Ti}_{11}$	0.67	0.78	$\text{TiSn}_3\text{Ti}_{11}$	0.69	0.80
$\text{InV}_3\text{Ti}_{11}$	0.77	0.90	$\text{SnV}_3\text{Ti}_{11}$	0.79	0.92	$\text{VIn}_3\text{Ti}_{11}$	0.69	0.80	$\text{VSn}_3\text{Ti}_{11}$	0.61	0.75
$\text{InCr}_3\text{Ti}_{11}$	0.76	0.90	$\text{SnCr}_3\text{Ti}_{11}$	0.74	0.89	$\text{CrIn}_3\text{Ti}_{11}$	0.59	0.72	$\text{CrSn}_3\text{Ti}_{11}$	0.60	0.73
$\text{InZr}_3\text{Ti}_{11}$	0.55	0.68	$\text{SnZr}_3\text{Ti}_{11}$	0.54	0.67	$\text{ZrIn}_3\text{Ti}_{11}$	0.69	0.79	$\text{ZrSn}_3\text{Ti}_{11}$	0.72	0.82
$\text{InNb}_3\text{Ti}_{11}$	0.62	0.76	$\text{SnNb}_3\text{Ti}_{11}$	0.59	0.73	$\text{NbIn}_3\text{Ti}_{11}$	0.68	0.79	$\text{NbSn}_3\text{Ti}_{11}$	0.65	0.77
$\text{InMo}_3\text{Ti}_{11}$	0.60	0.75	$\text{SnMo}_3\text{Ti}_{11}$	0.57	0.73	$\text{MoIn}_3\text{Ti}_{11}$	0.62	0.74	$\text{MoSn}_3\text{Ti}_{11}$	0.54	0.68
$\text{InHf}_3\text{Ti}_{11}$	0.39	0.53	$\text{SnHf}_3\text{Ti}_{11}$	0.39	0.53	$\text{HfIn}_3\text{Ti}_{11}$	0.67	0.76	$\text{HfSn}_3\text{Ti}_{11}$	0.72	0.81
$\text{InTa}_3\text{Ti}_{11}$	0.61	0.71	$\text{SnTa}_3\text{Ti}_{11}$	0.61	0.71	$\text{TaIn}_3\text{Ti}_{11}$	0.67	0.77	$\text{TaSn}_3\text{Ti}_{11}$	0.67	0.78
$\text{InW}_3\text{Ti}_{11}$	0.62	0.73	$\text{SnW}_3\text{Ti}_{11}$	0.61	0.73	$\text{WIn}_3\text{Ti}_{11}$	0.61	0.72	$\text{WSn}_3\text{Ti}_{11}$	0.49	0.63

a lower value of E) becomes less perfect with an increase in the concentration of the s, p -element. The trends in the change of the shear modulus and Young's modulus in the studied alloys with an increase in the number of d -electrons of the transition metal are similar, and their behavior demonstrates a non-monotonic character. The decrease of Young's modulus in the series of alloys with In and Sn in the Y-position with an increase in the number of d -electrons of the X-element is also observed.

The studied ternary alloys mainly have a ductile fracture character according to three empirical criteria, although with an increase in the concentration of s, p -elements, the ionic contribution increases, which leads to an increase in the brittleness and microhardness of the alloys. In addition, with an increase in the concentration of simple metals, the brittleness index also increases and the maximum values of 3.93 and 4.58 $\mu\text{m}^{-1/2}$ were obtained for alloys with Hf in the X-position. That is, in alloys with a lower hafnium concentration, there is a decrease in the fracture (damage) resistance.

The Debye temperature was estimated for all considered ternary alloys and it was found that its lower values correlate with low values of the Young's modulus. The calculation of thermal conductivity showed that it correlates with the Debye temperature (large Θ_D corresponds to alloys with higher thermal conductivity and larger Young's moduli). In alloys with simple metals in the Y-position, i.e. with their high concentration, this trend can be imperfect. In general, the influence of s, p -elements on elastic and thermal characteristics is less pronounced compared to transition metals, regardless of the X or Y position they occupy, and reflects mainly the size effect, whereas the influence of transition metals depends significantly on the number of d -electrons of alloying elements.

References

- [1] Gunther V.E., Kotenko V.V., Mirgazitov M.Z., Polenichkin V.K., Vityugov I.A., Itin V.I., Ziganshin R.V., Temerhanov F.T. *Shape memory alloys in medicine*. TSU Publ., Tomsk, 1986, 208 p. (in Russian)
- [2] Long M., Rack H.J. Titanium alloys in total joint replacement – a materials science perspective. *Biomater.*, 1998, **19**, P. 1622–1639.
- [3] Niinomi M. Recent research and development in titanium alloys for biomedical applications and healthcare goods. *Sci. Technol. Adv. Mater.*, 2003, **4**, P. 445–454.
- [4] Niinomi M. Mechanical biocompatibilities of titanium alloys for biomedical applications. *J. Mech. Behav. Biomed. Mater.*, 2008, **1**, P. 30–42.
- [5] Zhang L.C., Chen L.Y. A review on biomedical titanium alloys: recent progress and prospect. *Adv. Eng. Mater.*, 2019, **21**, 1801215.
- [6] Mohammed M.T., Khan Z.A., Siddiquee A.N. Beta titanium alloys: the lowest elastic modulus for biomedical applications: a review. *Int. J. Mater. Metall. Eng.*, 2014, **8** (8), P. 822–827.
- [7] Yu Z. *Titanium alloys for biomedical development and applications. Design, microstructure, properties, and application*. Elsevier, Amsterdam, 2022, 232 p.
- [8] Hao C.P., Wang Q., Ma R.T., Wang Y.M., Qiang J.B., Dong C. Cluster-plus-glue-atom model in bcc solid solution alloys. *Acta Phys. Sin.*, 2011, **60** (11), 116101.
- [9] Yan X., Cao W., Li H. Novel biomedical Ti-based alloys with low Young's modulus: a first-principles study. *J. Mater. Eng. Perform.*, 2024, **33**, P. 6835–6842.
- [10] Kasparyan S.O., Bakulin A.V., Kulkova S.E. Mechanical properties of ternary $\text{XY}_3\text{Ti}_{11}$ alloys. *Izvestiya vuzov. Fizika*, 2024, **67**, P. 77–85. (in Russian)
- [11] Bai H., Duan Y., Qi H., Peng M., Li M., Zheng S. Anisotropic elastic and thermal properties and damage tolerance of CrH: A first-principles calculation. *Vacuum*, 2024, **222**, 112962.
- [12] Sun Y., Yang A., Duan Y., Shen L., Peng M., Qi H. Electronic, elastic, and thermal properties, fracture toughness, and damage tolerance of $\text{TM}_5\text{Si}_3\text{B}$ (TM = V and Nb) MAB phases. *Int. J. Refract. Met. Hard Mater.*, 2022, **103**, 105781.
- [13] Blöchl P.E. Projector augmented-wave method. *Phys. Rev. B*, 1994, **50** (24), P. 17953–17979.
- [14] Kresse G., Joubert D. From ultrasoft pseudopotentials to the projector augmented-wave method. *Phys. Rev. B*, 1999, **59** (3), P. 1758–1775.
- [15] Kresse G., Hafner J. Ab initio molecular-dynamics simulation of the liquid-metal–amorphous-semiconductor transition in germanium. *Phys. Rev. B*, 1994, **49** (20), P. 14251–14269.

- [16] Kresse G., Furthmüller J. Efficiency of ab-initio total energy calculations for metals and semiconductors using a plane-wave basis set. *Comput. Mater. Sci.*, 1996, **6**, P. 15–50.
- [17] Perdew J.P., Burke K., Ernzerhof M. Generalized gradient approximation made simple. *Phys. Rev. Lett.*, 1996, **77** (18), P. 3865–3868.
- [18] Monkhorst H.J., Pack J.D. Special points for Brillouin-zone integrations. *Phys. Rev. B*, 1976, **13** (12), P. 5188–5192.
- [19] Born M., Huang K. *Dynamic theory of crystal lattices*. Oxford University Press, London, 1954, 420 p.
- [20] Hill R. The elastic behaviour of a crystalline aggregate. *Proc. Phys. Soc. London, Sect. A*, 1952, **65**, P. 349–354.
- [21] Voigt W. Bestimmung der Elastizitätskonstanten von Eisenglanz. *Ann. Phys.*, 1907, **327** (1), P. 129–140.
- [22] Reuss A. Berechnung der Fließgrenze von Mischkristallen auf Grund der Plastizitätsbedingung für Einkristalle. *Z. Angew. Math. Mech.*, 1929, **9** (1), P. 49–58.
- [23] Ledbetter H., Ogi H., Kai S., Kim S., Hirao M. Elastic constants of body-centered-cubic titanium monocrystals. *J. Appl. Phys.*, 2004, **95** (9), P. 4642–4644.
- [24] Zhang Z., Li B., Chen L., Qin F., Hou Y. Measurement of elastic constants of additive manufactured Ti-6Al-4V by non-contact multi-mode laser ultrasonic system. *J. Mater. Eng. Perform.*, 2022, **31**, P. 7328–7336.
- [25] Pugh S.F. Relations between the elastic moduli and the plastic properties of polycrystalline pure metals. *The London, Edinburgh, and Dublin Philosophical Magazine and Journal of Science*, 1954, **45** (367), P. 823–843.
- [26] Tian Y., Xu B., Zhao Z. Microscopic theory of hardness and design of novel superhard crystals. *Int. J. Refract. Met. Hard Mater.*, 2012, **33**, P. 93–106.
- [27] Bakulin A.V., Kulkova S.E. Effect of impurities on the formation energy of point defects in the γ -TiAl alloy. *J. Exp. Theor. Phys.*, 2018, **127** (6), P. 1046–1058.
- [28] Niu H., Niu S., Oganov A.R. Simple and accurate model of fracture toughness of solids. *J. Appl. Phys.*, 2019, **125**, 065105.
- [29] Gong X., Sun C.C. A new tablet brittleness index. *Eur. J. Pharm. Biopharm.*, 2015, **93**, P. 260–266.
- [30] Munro R.G., Freiman S.W., Baker T.L. *Fracture toughness data for brittle materials*. NIST Publ., Gaithersburg, 1998, 153 p.
- [31] Moruzzi V.L., Janak J.F., Schwarz K. Calculated thermal properties of metals. *Phys. Rev. B*, 1988, **37** (2), P. 790–799.
- [32] Liu X., Fu J. First principle study on electronic structure, elastic properties and Debye temperature of pure and doped KCaF₃. *Vacuum*, 2020, **178**, 109504.
- [33] Music D., Houben A., Dronskowski R., Schneider J.M. Ab initio study of ductility in M₂AlC (M = Ti, V, Cr). *Phys. Rev. B*, 2007, **75**, 174102.
- [34] Anderson O.L. A simplified method for calculating the Debye temperature from elastic constants. *J. Phys. Chem. Solids*, 1963, **24**, P. 909–917.
- [35] Anderson O.L. The high-temperature acoustic Grüneisen parameter in the earth's interior. *Physics of the Earth and Planetary Interiors*, 1979, **18**, P. 221–231.
- [36] Vitos L. *Computational quantum mechanics for materials engineers: the EMTO method and applications*. Springer, London, 2007, 236 p.
- [37] Kerley G.I. *Equations of state for titanium and Ti₆Al₄V alloy*. Sandia National Lab., Oak Ridge, 2003, 35 p.
- [38] Leont'ev K.L. On the relationship between elastic and thermal properties of substances. *Sov. Phys. Acoust.*, 1981, **27**, P. 309–316.
- [39] Belomestnykh V.N. The acoustical Grüneisen constants of solids. *Tech. Phys. Lett.*, 2004, **30** (2), P. 91–93.
- [40] Kittel C. *Introduction to solid state physics*, 8th ed. John Wiley & Sons, Hoboken, 2005, 681 p.
- [41] Shindé S.L., Goela J.S. *High thermal conductivity materials*. Springer, New York, 2006, 271 p.
- [42] Hoel H., Nyberg H. An extension of Clarke's model with stochastic amplitude flip processes. *IEEE Trans. Commun.*, 2014, **62** (7), P. 2378–2389.
- [43] Clarke D.R., Levi C.G. Materials design for the next generation thermal barrier coatings. *Annu. Rev. Mater. Res.*, 2003, **33**, P. 383–417.
- [44] Cahill D.G., Watson S.K., Pohl R.O. Lower limit to the thermal conductivity of disordered crystals. *Phys. Rev. B*, 1992, **46** (10), P. 6131–6140.
- [45] Duan Y.H., Sun Y., Lu L. Thermodynamic properties and thermal conductivities of TiAl₃-type intermetallics in Al–Pt–Ti system. *Comput. Mater. Sci.*, 2013, **68**, P. 229–233.

Submitted 3 April 2025; revised 7 April 2025; accepted 8 April 2025

Information about the authors:

Sergey O. Kasparyan – Institute of Strength Physics and Materials Science of the Siberian Branch of the Russian Academy of Sciences, Akademicheskii, 2/4, Tomsk, 634055, Russia; National Research Tomsk State University, Lenina, 36, Tomsk, 634050, Russia; ORCID 0000-0002-0234-884X; ks-fff-isopams@mail.ru

Adil E. Ordabaev – National Research Tomsk State University, Lenina, 36, Tomsk, 634050, Russia; ORCID 0009-0008-4124-450X; adil.ordabaev04@gmail.com

Alexander V. Bakulin – Institute of Strength Physics and Materials Science of the Siberian Branch of the Russian Academy of Sciences, Akademicheskii, 2/4, Tomsk, 634055, Russia; ORCID 0000-0001-5099-3942; bakulin@ispms.ru

Svetlana E. Kulkova – Institute of Strength Physics and Materials Science of the Siberian Branch of the Russian Academy of Sciences, Akademicheskii, 2/4, Tomsk, 634055, Russia; ORCID 0000-0002-7155-3492; kulkova@ispms.ru

Conflict of interest: the authors declare no conflict of interest.

Phase formation in the $\text{Na}_2\text{O}-\text{Bi}_2\text{O}_3-\text{Fe}_2\text{O}_3-\text{MoO}_3-(\text{H}_2\text{O})$ system

Makariy S. Lomakin^{1,2,a}¹Ioffe Institute, St. Petersburg, Russia²Branch of Petersburg Nuclear Physics Institute named by B.P. Konstantinov of National Research Centre “Kurchatov Institute” – Institute of Silicate Chemistry, St. Petersburg, Russia^alomakinmakariy@gmail.com

ABSTRACT The effect of the hydrothermal fluid pH on the chemical and phase composition, as well as the size parameters and morphology of crystallites and particles of hydrothermal synthesis products formed in the $\text{Na}_2\text{O}-\text{Bi}_2\text{O}_3-\text{Fe}_2\text{O}_3-\text{MoO}_3$ system at $T = 170$ °C and $P < 7$ MPa has been studied. It has been established that in the acidic pH region, the bulk chemical composition of the hydrothermal synthesis products is depleted relative to the nominal composition specified for the synthesis in iron oxide, while in the alkaline pH region, it is depleted in molybdenum oxide and, to a lesser extent, in bismuth oxide, while the best correspondence between the nominal and bulk composition observed at pH = 2. It is shown that in the pH range from 2 to 6 new compounds of variable composition ($\text{Na}_{0.19-0.47}\text{Bi}_{0.42-0.85}\text{Fe}_{0.14-0.31}\text{MoO}_y$) with a scheelite-like structure (sp. gr. $I\bar{4}$, No. 82) are formed, which have not been previously described in the scientific literature. These compounds with the smallest mean crystallite size (~ 25 nm) were obtained at pH = 2, and it was shown that under these conditions polycrystalline plate-like particles (thickness (h) $\sim 50-150$ nm) are formed, often having a curved shape, which grow together to form agglomerates with a “flower-like” morphology. It was found that fluorite-type solid solutions ($\text{Bi}_{3.65-4.30}\text{Fe}_{0.37-0.45}\text{MoO}_z$) are formed in alkaline media (isostructured to the oxide $\delta\text{-Bi}_2\text{O}_3$ (sp. gr. $Fm\bar{3}m$, No. 225)).

KEYWORDS hydrothermal synthesis, sodium bismuth iron molybdate, scheelite-like structure, nanocrystals, fluorite-type solid solutions.

ACKNOWLEDGEMENTS XRD, SEM and EDXMA studies were performed employing the equipment of the Engineering Center of the St. Petersburg State Institute of Technology (Technical University). The author expresses his deep gratitude to Corr. Mem. RAS Victor Vladimirovich Gusarov for valuable comments and advice on improving the quality of the manuscript. The work was financially supported by the Russian Science Foundation (Project No. 24-13-00445).

FOR CITATION Lomakin M.S. Phase formation in the $\text{Na}_2\text{O}-\text{Bi}_2\text{O}_3-\text{Fe}_2\text{O}_3-\text{MoO}_3-(\text{H}_2\text{O})$ system. *Nanosystems: Phys. Chem. Math.*, 2025, **16** (2), 235–242.

1. Introduction

Multicomponent molybdates are the objects of active research, since representatives of this class of complex oxides have a wide range of physicochemical properties that are interesting for study [1]. Bismuth molybdate, Bi_2MoO_6 , is a single-layer Aurivillius phase consisting of $[\text{Bi}_2\text{O}_2]^{2+}$ layers sandwiched between $[\text{MoO}_4]^{2-}$ slabs and could be used as potential LIB anode material [2, 3] and outstanding photocatalyst [4]. Bismuth iron molybdate, $\text{Bi}_3(\text{FeO}_4)(\text{MoO}_4)_2$, has a monoclinic structure related to the scheelite (CaWO_4) structure and could be used as a good photocatalyst for water splitting and photodegradation of organic contamination [5, 6]. Sodium bismuth molybdate, $\text{NaBi}(\text{MoO}_4)_2$, as well as other related compounds of $M^I M^{III}(\text{MoO}_4)_2$ stoichiometry, has a tetragonal scheelite-like structure and could be potentially used as host crystals for active ions having luminescence properties [7–9].

Obtaining the mentioned compounds, as well as other multicomponent molybdates, using low-temperature synthesis methods in aqueous environments, including hydrothermal conditions, can ensure their formation in nanocrystalline form, which can potentially lead to the discovery of new unique properties [10]. In addition, lowering the synthesis temperature may lead to the discovery of new compounds that are unstable at elevated temperatures [11]. For example, in the $\text{Bi}_2\text{O}_3-\text{Fe}_2\text{O}_3-\text{WO}_3$ system, the formation of new compounds of variable composition with a cubic pyrochlore structure under hydrothermal conditions ($T = 90 - 200$ °C, $P \leq 7$ MPa) was established, the upper temperature limit of stability of which is ~ 725 °C [12, 13].

The relevance of the work is related to the study of phase formation in the previously unexplored $\text{Na}_2\text{O}-\text{Bi}_2\text{O}_3-\text{Fe}_2\text{O}_3-\text{MoO}_3-(\text{H}_2\text{O})$ system and the accumulation of information that can provide a basis for obtaining new multicomponent molybdates, including in the form of nanoparticles and nanocomposites with unique properties. The aim of the work is to study the influence of the hydrothermal fluid pH on the chemical and phase composition, as well as the size parameters and morphology of crystallites and particles of hydrothermal synthesis products formed in the $\text{Na}_2\text{O}-\text{Bi}_2\text{O}_3-\text{Fe}_2\text{O}_3-\text{MoO}_3$ system.

2. Materials and Methods

2.1. Synthesis section

The synthesis procedure, which is the same for all samples, is described below. Nominal composition specified for the synthesis corresponded to the following atomic ratios: (1) $\text{Bi}_{0.50}\text{Fe}_{0.37}\text{MoO}_{4.31}$ and (2) $\text{Bi}_{0.84}\text{Fe}_{0.56}\text{MoO}_{5.10}$. To obtain a sample, 2 mmol of crystalline hydrate of bismuth (III) nitrate, $\text{Bi}(\text{NO}_3)_3 \cdot 5\text{H}_2\text{O}$ (puriss. spec.), and (1) 1.48 or (2) 1.33 mmol of crystalline hydrate of iron (III) nitrate, $\text{Fe}(\text{NO}_3)_3 \cdot 9\text{H}_2\text{O}$ (pur.), were dissolved in 5 ml of 6 M HNO_3 (puriss. spec.), after which 25 ml of distilled water was added to the resulting solution. Next, (1) 4 or (2) 2.38 mmol of sodium molybdate (VI) crystalline hydrate, $\text{Na}_2\text{MoO}_4 \cdot 2\text{H}_2\text{O}$ (puriss. spec.), was dissolved in 20 ml of distilled water and the resulting solution was added dropwise into the acidic solution of bismuth and iron nitrates stirred with a magnetic stirrer at 800 rpm (~ 30 mL of distilled water was then added there and used to rinse the beaker that had contained the sodium molybdate solution). After stirring the obtained suspension for 1 h, a solution of 2 M NaOH was added to it dropwise until reaching pH of a certain value (1 (no NaOH), 2, 4, 6, 8, 10). The amorphous precursor suspension obtained this way, was additionally stirred at 1000 rpm for ~ 1 h and then transferred into Teflon chambers ($\sim 80\%$ filling) and placed in steel autoclaves, which were then put in a furnace heated up to $T = 170$ °C. After 66 h, the autoclaves were removed from the furnace and cooled in air. The resulting precipitates were separated from the mother liquor (it was poured out), rinsed with distilled water several times by decantation and dried at 90 °C for 24 h.

2.2. Characterization

The crystal structure of the synthesized samples was analyzed by XRD using an X-ray powder diffractometer DRON-8N (IC "Burevestnik", Russia) in the Bragg-Brentano geometry (an X-ray tube with copper anode, Ni K_β filter, Cu- K_α radiation (average wavelength $\lambda = 1.54186$ Å)), equipped with a position-sensitive (PSD) linear detector Mythen2 R 1D (DECTRIS Ltd., Switzerland) with an opening angle of 4.48° and with a single parabolically bent Göbel Mirror placed after the X-ray tube at the primary beam focus. The measurements were carried out in the range of angles $2\theta = 10^\circ - 65^\circ$ with a step of $\Delta 2\theta = 0.0142^\circ$, and the total time at the point was 8 seconds.

X-ray phase analysis of the measured XRD patterns of samples was carried out using the Crystallographica Search-Match program, version 3.1.0.2 (Oxford Cryosystems Ltd., England) using the Powder Diffraction File-2 (PDF-2) [14].

Scanning electron microscopy (SEM) images and bulk elemental composition of the samples, as well as elemental composition of particles belonging to the different morphological motifs (local analysis), were obtained on a Tescan Vega 3 SBH scanning electron microscope (Tescan Orsay Holding, Czech Republic) with an Oxford Instruments Energy Dispersive X-ray Microanalysis (EDXMA) attachment. The relative number of elements was calculated using the AZtec software. When determining the bulk composition the emission spectra were accumulated from three sites of each sample with a total area of ~ 7 mm² and a set of statistics for at least 1 million pulses at each site, then the data were averaged.

3. Results and discussions

3.1. Chemical composition

Nominal composition specified for the synthesis and the EDXMA data on the bulk chemical composition of the samples are presented in Table 1 in the form of atomic ratios. It should be noted that for the two nominal compositions studied ($\text{Bi}_{0.50}\text{Fe}_{0.37}\text{MoO}_{4.31}$ and $\text{Bi}_{0.84}\text{Fe}_{0.56}\text{MoO}_{5.10}$), a similar tendency is observed in the change in the corresponding bulk compositions with a change in the hydrothermal fluid pH. According to the presented data, the best agreement between the nominal and bulk composition is observed for the samples obtained at pH = 2, while for all other samples a noticeable depletion of the bulk composition relative to the nominal one in one or two components is clearly observed: pH = 1 and 4 in Fe_2O_3 ; pH = 6 in MoO_3 ; pH = 8 and 10 in Bi_2O_3 and MoO_3 . Thus, the observed tendency in the change in the bulk composition relative to the nominal one with a change in the hydrothermal fluid pH resembles that established earlier in the study of the Bi_2O_3 - Fe_2O_3 - WO_3 system [15]: in the acidic pH region, a depletion of the bulk chemical composition in iron oxide is observed, while in the alkaline pH region, a depletion of the bulk chemical composition in molybdenum oxide and, to a lesser extent, in bismuth oxide is observed; at pH = 2 (at pH = 2–5 in [15]), the change in the bulk composition relative to the nominal one is not as significant as at other pH values.

The change in the bulk chemical composition relative to the nominal one is due to the different solubility of the components of the amorphous precursor at different hydrothermal fluid pH values, which leads to their redistribution between the dispersed phase and the dispersion medium of the amorphous precursor suspension subjected to hydrothermal treatment. For this reason, some components may remain dissolved in the cooled mother liquor and will be removed from the system during further rinsing of the sediment.

It is important to note that in the samples obtained at pH = 2, 4 and 6, a noticeable amount of sodium is detected, while in other samples it is absent even in trace amounts.

TABLE 1. Bulk chemical composition of samples synthesized by the hydrothermal method, in rel. at. units, according to the EDXMA data

Sample			Bi/Mo		Fe/Mo		Bi/Fe		Na/Mo	
			Nom. ^a	Bulk	Nom. ^a	Bulk	Nom. ^a	Bulk	Nom. ^b	Bulk
$\text{Bi}_{0.50}\text{Fe}_{0.37}\text{MoO}_{4.31}$	pH	1	0.50	0.55	0.37	0.14	1.35	3.93	-	-
		2		0.53		0.29		1.83		0.26
		4		0.55		0.15		3.67		0.38
		6		1.05		0.36		2.92		0.23
		8		3.09		2.79		1.11		-
		10		4.67		4.59		1.02		-
		$\text{Bi}_{0.84}\text{Fe}_{0.56}\text{MoO}_{5.10}$		pH		1		0.84		0.92
2	0.75		0.54		1.39	0.24				
4	0.78		0.38		2.05	0.24				
6	1.08		0.48		2.25	0.22				
8	3.39		3.05		1.11	-				
10	4.32		4.73		0.91	-				

^aNominal composition specified for the synthesis. ^bNot specified for the synthesis.

The relative error for the Bi/Mo, Fe/Mo, Bi/Fe, and Na/Mo ratios does not exceed 7, 4, 6, and 8 %, respectively.

3.2. XRD analysis

Powder XRD patterns of samples synthesized by the hydrothermal method are shown in Fig. 1 (nominal composition – $\text{Bi}_{0.50}\text{Fe}_{0.37}\text{MoO}_{4.31}$) and Fig. 2 (nominal composition – $\text{Bi}_{0.84}\text{Fe}_{0.56}\text{MoO}_{5.10}$). The change in the bulk chemical composition of samples obtained at different hydrothermal fluid pH values, which was discussed in Section 3.1, leads to a change in their phase composition. The phase composition analysis of the samples, the results of which are presented below, was performed taking into account the data obtained using SEM and local EDXMA (for details see Section 3.3).

In the XRD patterns of the samples obtained at pH = 2 (nominal composition – $\text{Bi}_{0.84}\text{Fe}_{0.56}\text{MoO}_{5.10}$) and 4, reflections of only one phase are observed – $\text{NaBi}(\text{MoO}_4)_2$ (PDF-2 No. 88-242), which crystallizes in the tetragonal syngony and has a scheelite-like structure (sp. gr. $I\bar{4}$, No. 82). However, the bulk composition of these samples contains a noticeable amount of iron, which, apparently, cannot be attributed to the composition of the amorphous phase, since it is not observed in the samples, due to the absence of signs of an amorphous halo in the XRD patterns. Taking into account the data presented in Section 3.3, it can be concluded that these samples contain only a crystalline phase of variable composition, which is a four-component complex oxide (sodium bismuth iron molybdate) with a scheelite-like structure, apparently, not previously described in the scientific literature. It can be assumed that in the structure of these compounds, the Fe^{3+} cations are located in the same octahedrally coordinated positions as the Mo^{6+} cations, however, a detailed description of the crystal structure of the compounds obtained for the first time will be the subject of further research on this topic. It should be noted that the unit cell parameters (UCP) of the indicated compounds change with a change in their composition, and, apparently, the key factor influencing this is the amount of “large” Bi^{3+} cations, the increase of which is accompanied by an increase in UCP. The calculation of the mean crystallite sizes of the indicated compounds using the Scherrer formula was performed only for single-phase samples obtained at pH = 2 (nominal composition – $\text{Bi}_{0.84}\text{Fe}_{0.56}\text{MoO}_{5.10}$) and 4, since for other samples a superposition of the reflections of the scheelite-like phase with the reflections of the phases coexisting with it was observed. The mean crystallite sizes of the scheelite-like phase, calculated using the Scherrer formula, were: ~ 25 nm – pH = 2 (nominal composition – $\text{Bi}_{0.84}\text{Fe}_{0.56}\text{MoO}_{5.10}$); ~ 31 nm – pH = 4 (nominal composition – $\text{Bi}_{0.84}\text{Fe}_{0.56}\text{MoO}_{5.10}$); ~ 51 nm – pH = 4 (nominal composition – $\text{Bi}_{0.50}\text{Fe}_{0.37}\text{MoO}_{4.31}$).

In addition to the reflections of the above-described scheelite-like phase, the XRD pattern of the sample obtained at pH = 2 (nominal composition – $\text{Bi}_{0.50}\text{Fe}_{0.37}\text{MoO}_{4.31}$) contains reflections of the $\text{Fe}_2(\text{MoO}_4)_3$ phase (PDF-2 No. 35-183); obtained at pH = 6 (nominal composition – $\text{Bi}_{0.50}\text{Fe}_{0.37}\text{MoO}_{4.31}$) – the Bi_2MoO_6 phase (PDF-2 No. 84-787); obtained at pH = 6 (nominal composition – $\text{Bi}_{0.84}\text{Fe}_{0.56}\text{MoO}_{5.10}$) – the Bi_2MoO_6 (PDF-2 No. 84-787) and $\text{Fe}_2(\text{MoO}_4)_3$ (PDF-2 No. 35-183) phases. In the XRD patterns of the samples obtained at pH = 1, 8 and 10, reflections of the new scheelite-like phase are not observed, as well as the presence of sodium in the bulk composition of these samples is not detected. This

indicates that only the scheelite-like phase is formed with the participation of sodium, while sodium is not included in the composition of other forming oxide phases, despite the presence of this component in excess in the reaction system.

In the XRD patterns of the samples obtained at pH = 1, reflections of the $\text{Fe}_2\text{Mo}_3\text{O}_{12}$ (PDF-2 No. 80-195), $\text{Bi}_2\text{Mo}_3\text{O}_{12}$ (PDF-2 No. 21-103) and $\text{Bi}_3(\text{FeO}_4)(\text{MoO}_4)_2$ (PDF-2 No. 70-31) phases are observed. The XRD patterns of the samples obtained at pH = 8 and 10 show reflections of a bismuth oxide-enriched phase with the composition $\text{Bi}_{3.65-4.30}\text{Fe}_{0.37-0.45}\text{MoO}_z$ (for details see Section 3.3), which is isostructural to the $\delta\text{-Bi}_2\text{O}_3$ phase (sp. gr. $Fm\bar{3}m$, No. 225, PDF-2 No. 16-654), and, with the exception of the case of pH = 10 (nominal composition – $\text{Bi}_{0.50}\text{Fe}_{0.37}\text{MoO}_{4.31}$), reflections of other unknown phases are observed, which could not be identified.

It is worth mentioning that the formation in alkaline media of a three-component fluorite-type solid solutions of similar composition, has already been observed in a study of the $\text{Bi}_2\text{O}_3\text{-Fe}_2\text{O}_3\text{-WO}_3$ system [15]. However, it is important to note that the obtained samples do not contain a phase with a pyrochlore structure, the formation of which was previously observed in the $\text{Bi}_2\text{O}_3\text{-Fe}_2\text{O}_3\text{-WO}_3$ and $\text{Na}_2\text{O-Bi}_2\text{O}_3\text{-Fe}_2\text{O}_3\text{-WO}_3$ systems [12, 13], despite the use of a similar synthesis procedure and despite a similar electronic structure of the Mo^{6+} and W^{6+} cations.

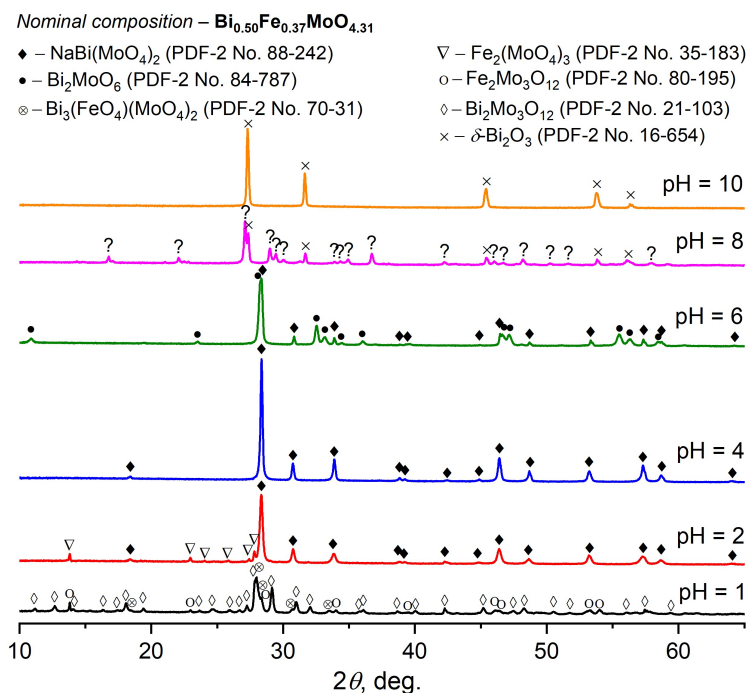


FIG. 1. Powder XRD patterns of samples synthesized by the hydrothermal method (nominal composition – $\text{Bi}_{0.50}\text{Fe}_{0.37}\text{MoO}_{4.31}$)

3.3. SEM

The SEM data for the samples synthesized by the hydrothermal method are shown in Fig. 3 and Fig. 4. In the sample obtained at pH = 2 (nominal composition – $\text{Bi}_{0.84}\text{Fe}_{0.56}\text{MoO}_{5.10}$) (Fig. 3b), large agglomerates ($\sim 5 - 20 \mu\text{m}$) are observed, the shape of which is close to spherical, composed of grown together plate-like particles (thickness (h) $\sim 50 - 150 \text{ nm}$), often having a curved shape. In the voids between the plate-like particles, smaller particles can be found, which makes it practically impossible to identify the composition of particles of different morphological motifs (plate-like and smaller particles) using local EDXMA. In the sample obtained at pH = 4 (nominal composition – $\text{Bi}_{0.84}\text{Fe}_{0.56}\text{MoO}_{5.10}$) (Fig. 3d), particles of two morphological motifs are observed: (1) conditionally spherical particles ($\sim 0.5 - 1.5 \mu\text{m}$) and (2) rod-shaped particles ($h \sim 1 \mu\text{m}$ and length (l) $\sim 10 \mu\text{m}$), as well as agglomerates of these particles (1 and 2). In the back-scattered electron (BSE) detection mode, it can be observed that the particles of the two morphological motifs have the same brightness, which indicates a fairly uniform distribution of different type atoms throughout the sample volume. In addition, local EDXMA data show that the spherical particles have the composition $\text{Na}_{0.19}\text{Bi}_{0.81}\text{Fe}_{0.31}\text{MoO}_{4.78}$, while the rod-shaped particles – $\text{Na}_{0.30}\text{Bi}_{0.85}\text{Fe}_{0.22}\text{MoO}_{4.76}$, and these atomic ratios are close to the bulk chemical composition of this sample. In the sample obtained at pH = 4 (nominal composition – $\text{Bi}_{0.50}\text{Fe}_{0.37}\text{MoO}_{4.31}$) (Fig. 3c), one can also observe particles of two morphological motifs: (3) conventionally cubic particles ($\sim 2 \mu\text{m}$), which are aggregates of smaller particles also having a cubic shape, and (4) aggregates of plate-like particles ($h \sim 150 - 200 \text{ nm}$), grown together with flat sides (“in a stack”). Studies in the BSE mode, as well as local EDXMA data, show that the compositions of particles with different morphologies are similar to each other: cubic particles – $\text{Na}_{0.30}\text{Bi}_{0.58}\text{Fe}_{0.14}\text{MoO}_{4.23}$; aggregates

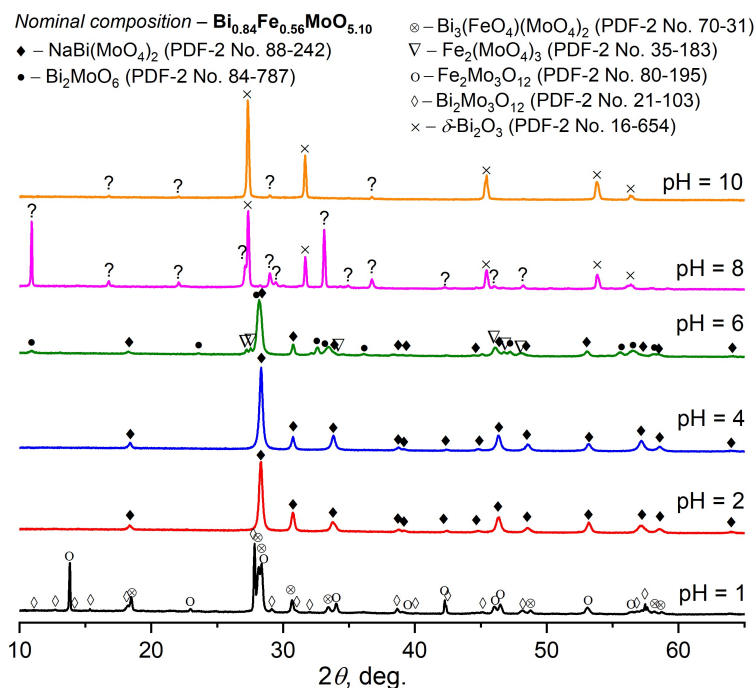


FIG. 2. Powder XRD patterns of samples synthesized by the hydrothermal method (nominal composition – $\text{Bi}_{0.84}\text{Fe}_{0.56}\text{MoO}_{5.10}$)

of plate-like particles – $\text{Na}_{0.47}\text{Bi}_{0.42}\text{Fe}_{0.15}\text{MoO}_{4.09}$, and the indicated atomic ratios are close to the bulk chemical composition of this sample. Taking into account the fact that the XRD patterns of the three described samples show reflections of only the scheelite-like phase, it can be concluded that compounds of this structural type were synthesized in the form of particles with different morphology and quantitative chemical composition, which is observed both when comparing different samples with each other, and in each of them. The formation of particles of scheelite-like compounds of two morphological motifs and with slightly different quantitative chemical compositions within a sample could be due to one of the following two reasons. The first reason may be that the reaction system has not reached a state of thermodynamic equilibrium, the achievement of which may be complicated, for example, by the fact that the reacting components are not distributed homogeneously enough throughout the volume of the reaction space, which prevents their direct contact and further interaction. This is a typical problem when using “traditional” methods of mixing the reaction system (magnetic/blade stirrer, etc.), which provide low micro-mixing quality [16]. The second reason may be related to the fact that the reaction system has reached a state of thermodynamic equilibrium, but in this region of chemical compositions at the synthesis temperature and pressure, there is a region of two-phase equilibrium in which two isostructural solid solutions with slightly different quantitative compositions coexist.

The sample obtained at pH = 2 (nominal composition – $\text{Bi}_{0.50}\text{Fe}_{0.37}\text{MoO}_{4.31}$) (Fig. 3a) contains particles of two morphological motifs: (5) large agglomerates of various shapes and sizes, composed of grown together curved plate-like particles ($h \sim 50 - 150$ nm), and (6) particles resembling a bar or beam ($h \sim 5$ μm and $l \sim 20 - 30$ μm), often collected in aggregates of various shapes. In the BSE mode, particles (5) are noticeably lighter than particles (6), while according to the local EDXMA data, particles (5) have the composition $\text{Na}_{0.25}\text{Bi}_{0.60}\text{Fe}_{0.18}\text{MoO}_{4.30}$; particles (6) have the composition $\text{Fe}_2\text{Mo}_3\text{O}_{12}$, which is close to the composition of the known compound (PDF-2 No. 35-183).

In the sample obtained at pH = 6 (nominal composition – $\text{Bi}_{0.50}\text{Fe}_{0.37}\text{MoO}_{4.31}$) (Fig. 4a), two morphological motifs are observed: (i) flat plate-like particles ($h \sim 100$ nm), growing together at right angles into large, conditionally isometric agglomerates ($\sim 2 - 5$ μm), and (ii) aggregates of conditionally isometric particles having the shape of a rectangular parallelepiped ($h \sim 0.6 - 0.8$ μm) with a square base ($\sim 2 - 3$ μm). The sample obtained at pH = 6 (nominal composition – $\text{Bi}_{0.84}\text{Fe}_{0.56}\text{MoO}_{5.10}$) (Fig. 4b) also contains particles of two morphological motifs: (i) large particles resembling an elongated spheroid ($h \sim 2 - 3$ μm and $l \sim 5 - 10$ μm), and (ii) smaller particles “scattered” over these large particles (i), and also forming separate large agglomerates of a conditionally isometric shape ($\sim 5 - 10$ μm). In these samples (pH = 6), it is practically impossible to identify the composition of particles of different morphological motifs using local EDXMA due to their close contact.

In the sample obtained at pH = 8 (nominal composition – $\text{Bi}_{0.50}\text{Fe}_{0.37}\text{MoO}_{4.31}$) (Fig. 4c), three morphological motifs are observed: (7) octahedral particles ($\sim 2 - 4$ μm), (8) rod-shaped particles ($h \sim 0.3 - 1$ μm and $l \sim 5 - 30$ μm) and (9) agglomerates of different sizes without a clearly defined morphology. In the BSE mode, particles (7) and (8)

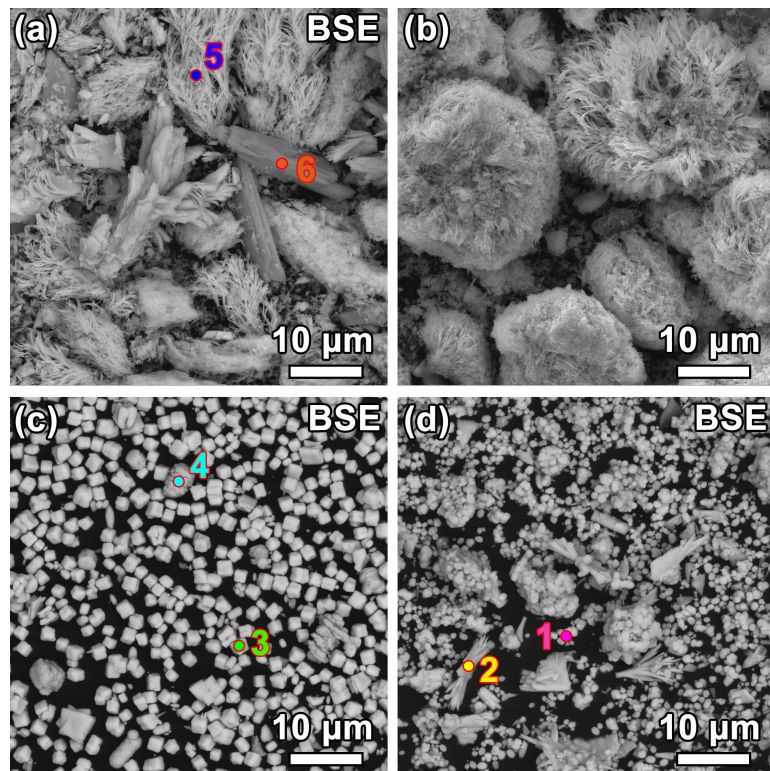


FIG. 3. SEM images of samples synthesized by the hydrothermal method: nominal composition – $\text{Bi}_{0.50}\text{Fe}_{0.37}\text{MoO}_{4.31}$ ((a) pH = 2, (c) pH = 4); nominal composition – $\text{Bi}_{0.84}\text{Fe}_{0.56}\text{MoO}_{5.10}$ ((b) pH = 2, (d) pH = 4)

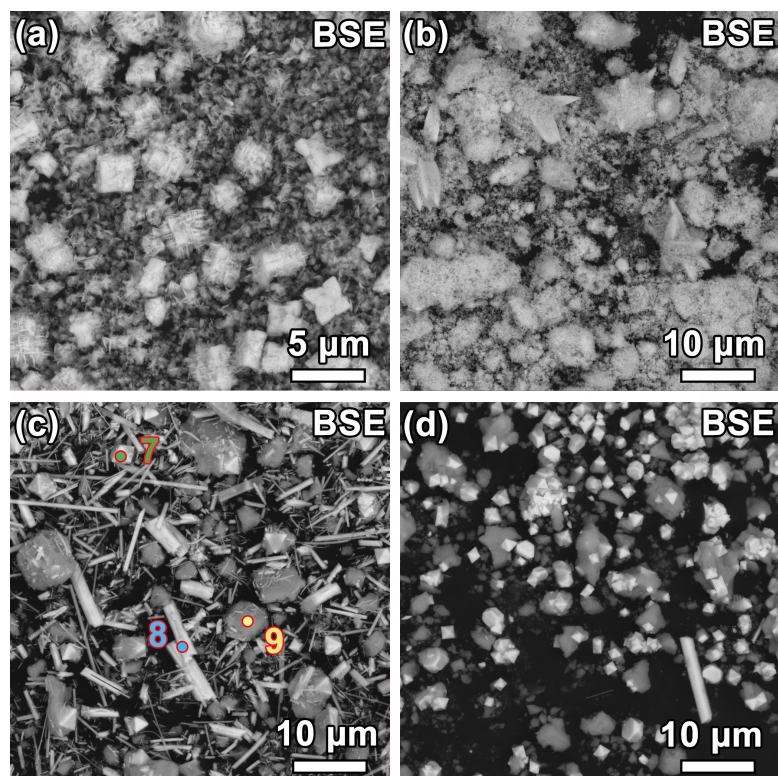


FIG. 4. SEM images of samples synthesized by the hydrothermal method: nominal composition – $\text{Bi}_{0.50}\text{Fe}_{0.37}\text{MoO}_{4.31}$ ((a) pH = 6, (c) pH = 8); nominal composition – $\text{Bi}_{0.84}\text{Fe}_{0.56}\text{MoO}_{5.10}$ ((b) pH = 6, (d) pH = 10)

are noticeably lighter than particles (9), while according to the local EDXMA data, particles (7) have the composition $\text{Bi}_{3.65}\text{Fe}_{0.45}\text{MoO}_{9.15}$; particles (8) – $\text{Bi}_{2.76}\text{Fe}_{0.31}\text{MoO}_{7.61}$; particles (9) – $\text{Bi}_{3.67}\text{Fe}_{0.45}\text{MoO}_{22.68}$. A similar tendency is observed in the case of the sample obtained at $\text{pH} = 10$ (nominal composition – $\text{Bi}_{0.84}\text{Fe}_{0.56}\text{MoO}_{5.10}$) (Fig. 4d), except that the amount of octahedral particles (7) in relation to rod-shaped particles (8) becomes significantly greater. Apparently, the octahedral particles, which have a composition highly enriched in bismuth oxide, are fluorite-type solid solutions that are isostructural to the $\delta\text{-Bi}_2\text{O}_3$ phase (sp. gr. $Fm\bar{3}m$, No. 225). However, in the crystallographic database PDF-2 it is not possible to find a known compound whose composition would be close to the composition of iron oxide-enriched particles (9), which complicates the phase analysis of these samples.

4. Conclusion

It is shown that the hydrothermal fluid pH has a key effect on the processes of phase formation in the $\text{Na}_2\text{O}-\text{Bi}_2\text{O}_3-\text{Fe}_2\text{O}_3-\text{MoO}_3$ system, determining the chemical and phase composition, as well as the size parameters and morphology of crystallites and particles of hydrothermal synthesis products ($T = 170\text{ }^\circ\text{C}$ and $P < 7\text{ MPa}$).

The discovered tendency in the change in the bulk chemical composition relative to the used nominal compositions ($\text{Bi}_{0.50}\text{Fe}_{0.37}\text{MoO}_{4.31}$ and $\text{Bi}_{0.84}\text{Fe}_{0.56}\text{MoO}_{5.10}$) with a change in the hydrothermal fluid pH resembles that established earlier in the study of the $\text{Bi}_2\text{O}_3-\text{Fe}_2\text{O}_3-\text{WO}_3$ system [15]: in the region of acidic pH, a depletion of the bulk chemical composition in iron oxide is observed, while in the region of alkaline pH, a depletion of the bulk chemical composition in molybdenum oxide and, to a lesser extent, in bismuth oxide is observed; at $\text{pH} = 2$ (at $\text{pH} = 2-5$ in [15]), the change in the bulk composition relative to the nominal one is not as significant as at other pH values.

It is shown that in the pH range from 2 to 6 new compounds of variable composition ($\text{Na}_{0.19-0.47}\text{Bi}_{0.42-0.85}\text{Fe}_{0.14-0.31}\text{MoO}_y$) with a scheelite-like structure (sp. gr. $I\bar{4}$, No. 82) are formed, which have not been previously described in the scientific literature. The discovered compounds are isostructural with the known compound $\text{NaBi}(\text{MoO}_4)_2$ (PDF-2 No. 88-242) and, apparently, are formed by isomorphic substitution of some amounts of octahedrally coordinated Mo^{6+} cations by Fe^{3+} cations. It was found that the unit cell parameters (UCP) of these compounds change with a change in their composition, and, apparently, the key influence on this is the number of “large” Bi^{3+} cations, the increase of which is accompanied by an increase in the UCP. An increase in the hydrothermal fluid pH from 2 to 4 leads to an increase in the mean crystallite sizes of the scheelite-like phase, calculated using the Scherrer formula, from ~ 25 to $\sim 30-50\text{ nm}$. The particles of these compounds are polycrystalline, and have different morphology and quantitative chemical composition, which is observed both when comparing different samples with each other, and in each of them. It is shown that the “flower-like” agglomerates of particles formed at $\text{pH} = 2$ have the most developed surface and are grown together plate-like particles ($h \sim 50-150\text{ nm}$), often having a curved shape, while with an increase in pH, the formation of “denser” aggregates with a significantly smaller number of voids is observed.

It has been shown that fluorite-type solid solutions ($\text{Bi}_{3.65-4.30}\text{Fe}_{0.37-0.45}\text{MoO}_z$) (isostructural with the oxide $\delta\text{-Bi}_2\text{O}_3$ (sp. gr. $Fm\bar{3}m$, No. 225)) are formed in the region of alkaline pH, the particles of which have a clear octahedral habit, which was previously observed in the study of the $\text{Bi}_2\text{O}_3-\text{Fe}_2\text{O}_3-\text{WO}_3$ system [15].

It was established that the obtained samples do not contain a phase with a cubic pyrochlore structure, the formation of which was previously observed in the $\text{Bi}_2\text{O}_3-\text{Fe}_2\text{O}_3-\text{WO}_3$ and $\text{Bi}_2\text{O}_3-\text{Na}_2\text{O}-\text{Fe}_2\text{O}_3-\text{WO}_3$ systems [12, 13], despite the use of a similar synthesis procedure and despite a similar electronic structure of the Mo^{6+} and W^{6+} cations.

References

- [1] Ray S.K., Hur J. Surface modifications, perspectives, and challenges of scheelite metal molybdate photocatalysts for removal of organic pollutants in wastewater. *Ceramics International*, 2020, **46**, P. 20608–20622.
- [2] Yuan S., Zhao Y., Chen W., Wu C., Wang X., Zhang L., Wang Q. Self-assembled 3D hierarchical porous Bi_2MoO_6 microspheres toward high capacity and ultra-long-life anode material for Li-ion batteries. *ACS Appl. Mater. Interfaces*, 2017, **9**, P. 21781–21790.
- [3] Zhai X., Gao J., Xue R., Xu X., Wang L., Tian Q. Facile synthesis of Bi_2MoO_6 /reduced graphene oxide composites as anode materials towards enhanced lithium storage performance. *J. Colloid Interface Sci.*, 2018, **518**, P. 242–251.
- [4] Dai Z., Qin F., Zhao H., Ding J., Liu Y., Chen R. Crystal Defect Engineering of Aurivillius Bi_2MoO_6 by Ce Doping for Increased Reactive Species Production in Photocatalysis. *ACS Catalysis*, 2016, **6**(5), P. 3180–3192.
- [5] Nie X., Wulayin W., Song T., Wu M., Qiao X. Surface, optical characteristics and photocatalytic ability of Scheelite-type monoclinic $\text{Bi}_3\text{FeMo}_2\text{O}_{12}$ nanoparticles. *Applied Surface Science*, 2016, **387**, P. 351–357.
- [6] Liu B., Yasin A.S., Musho T., Bright J., Tang H., Huang L., Wu N. Visible-Light Bismuth Iron Molybdate Photocatalyst for Artificial Nitrogen Fixation. *Journal of The Electrochemical Society*, 2019, **166**(5), P. H3091–H3096.
- [7] Pushpendra, Kunchala R.K., Achary S.N., Tyagi A.K., Naidu B.S. Rapid, Room Temperature Synthesis of Eu^{3+} Doped $\text{NaBi}(\text{MoO}_4)_2$ Nanomaterials: Structural, Optical, and Photoluminescence Properties. *Cryst. Growth Des.*, 2019, **19**, P. 3379–3388.
- [8] Gan Y., Liu W., Zhang W., Li W., Huang Y., Qiu K. Effects of Gd^{3+} codoping on the enhancement of the luminescent properties of a $\text{NaBi}(\text{MoO}_4)_2:\text{Eu}^{3+}$ red-emitting phosphors. *J. Alloys Compd.*, 2019, **784**, P. 1003–1010.
- [9] Calderón-Olvera R.M., Núñez N.O., González-Mancebo D., Monje-Moreno J.M., Muñoz-Rui M.J., Gómez-González E., Arroyo E., Torres-Herrero B., de la Fuente J.M., Ocaña M. Europium doped-double sodium bismuth molybdate nanoparticles as contrast agents for luminescence bioimaging and X-ray computed tomography. *Inorg. Chem. Front.*, 2023, **10**, P. 3202–3212.
- [10] Byrappa K., Adschiri T. Hydrothermal technology for nanotechnology. *Prog. Cryst. Growth Charact. Mater.*, 2007, **53**(2), P. 117–166.
- [11] Shandilya M., Rai R., Singh J. Review: hydrothermal technology for smart materials. *Adv. Appl. Ceram.*, 2016, **115**(6), P. 354–376.

- [12] Lomakin M.S., Proskurina O.V., Danilovich D.P., Panchuk V.V., Semenov V.G., Gusarov V.V. Hydrothermal Synthesis, Phase Formation and Crystal Chemistry of the pyrochlore/Bi₂WO₆ and pyrochlore/ α -Fe₂O₃ Composites in the Bi₂O₃-Fe₂O₃-WO₃ System. *J. Solid State Chem.*, 2020, **282**, P. 121064.
- [13] Lomakin M.S., Proskurina O.V., Levin A.A., Nevedomskiy V.N. Pyrochlore phase in the Bi₂O₃-Fe₂O₃-WO₃-(H₂O) system: its stability field in the low-temperature region of the phase diagram and thermal stability. *Nanosyst.: Phys. Chem. Math.*, 2024, **15**(2), P. 240–254.
- [14] Fawcett T.G., Kabekkodu S.N., Blanton J.R., Blanton T.N. Chemical analysis by diffraction: the Powder Diffraction File™. *Powder Diffr.*, 2017, **32**, P. 63–71.
- [15] Lomakin M.S., Proskurina O.V., Gusarov V.V. Influence of Hydrothermal Synthesis Conditions on the Composition of the Pyrochlore Phase in the Bi₂O₃-Fe₂O₃-WO₃ system. *Nanosyst.: Phys. Chem. Math.*, 2020, **11**(2), P. 246–251.
- [16] Lomakin M.S., Proskurina O.V., Abiev R.Sh., Nevedomskiy V.N., Leonov A.A., Voznesenskiy S.S., Gusarov V.V. Pyrochlore Phase in the Bi₂O₃-Fe₂O₃-WO₃-(H₂O) System: Physicochemical and Hydrodynamic Aspects of its Production Using a Microreactor with Intensively Swirled Flows. *Adv. Powder Technol.*, 2023, **34**(7), P. 104053.

Submitted 10 October 2024; accepted 24 November 2024

Information about the authors:

Makariy S. Lomakin – Ioffe Institute, 26, Politekhnikeskaya St., 194021, St. Petersburg, Russia; Branch of Petersburg Nuclear Physics Institute named by B.P. Konstantinov of National Research Centre “Kurchatov Institute” – Institute of Silicate Chemistry, 2, Makarov Emb., 199034, St. Petersburg, Russia; ORCID 0000-0001-5455-4541; lomakin-makariy@gmail.com

Conflict of interest: the authors declare no conflict of interest.

Conducting properties of single-wall carbon nanotubes in composites based on polystyrene

Marianna N. Nikolaeva¹, Elena M. Ivan'kova¹, Alexander N. Bugrov^{1,2}

¹NRC "Kurchatov Institute" – PNPI – IMC, St. Petersburg, Russian Federation

²Saint Petersburg Electrotechnical University "LETI", St. Petersburg, Russian Federation

Corresponding author: Marianna N. Nikolaeva, marianna_n@mail.ru

PACS 36.20.-r, 68.65.Pq, 71.20.Rv, 72.80.Tm, 74.78.-w

ABSTRACT Composite films were synthesized by radical copolymerization of styrene with methacrylate groups on the surface of modified single-walled carbon nanotubes. Mechanical grinding and reforming of films on the electrode led to a decrease in the electrical resistance values by two magnitude orders. This effect was observed when measuring the current-voltage characteristics in both sandwich and planar structures. This decrease in the electrical resistance of the composite films is likely due to the disintegration and reorientation of carbon nanotubes, as well as the creation of mechanical stresses in them as a result of covalent bonding to the polymer matrix, which could affect the electronic structure of carbon inclusions.

KEYWORDS single-walled carbon nanotubes, surface modification, polymer composites, electrical resistance

ACKNOWLEDGEMENTS The work was carried out on the topic of the state assignment of the Russian Federation "Polymer and composite materials for advanced technologies" (No. 124013000726-6).

FOR CITATION Nikolaeva M.N., Ivan'kova E.M., Bugrov A.N. Conducting properties of single-wall carbon nanotubes in composites based on polystyrene. *Nanosystems: Phys. Chem. Math.*, 2025, **16** (2), 243–249.

1. Introduction

Research concerning the electrical conductivity of single-walled carbon nanotubes (SWCNTs) was intensively carried out in recent decades, including for their use as fillers in polymer composites for flexible electronics and other applications [1–5]. It is known that the conductivity values for SWCNTs can vary from dielectric and semiconducting to metallic, depending on the method of their preparation, axial ratio and surface modification [6–11]. The introduction of disaggregated SWCNTs in quantities sufficient for percolation, even into high-resistivity polymers, made it possible to obtain composites with high electrical conductivity values, up to 57 S/cm [12]. Yoon H. and colleagues [13] investigated which method of dispersing millimeter-long SWCNTs was the most effective for obtaining composites with high electrical conductivity characteristics based on fluorinated rubber and polystyrene (PS). The authors used a total of 11 approaches to disperse SWCNTs in methyl isobutyl ketone, which were based on three mechanisms of action: turbulent flow (nanomizer, high-pressure jet mill), cavitation (probe sonicator) and mechanical forces (ball-mill, bead-mill, paint shaker, ball collision-mill, cone-mill, high shear batch disperser, thin-film spin mixer, rotor-mill). The comparative analysis of dispersion methods presented in [13] showed that the highest average electrical conductivity of SWCNTs in a fluorine rubber film was 33 S/cm and was achieved by grinding the filler in a turbulent solvent flow, preceding it mixing with the polymer, molding and drying of the composite film. In turn, ultrasonic and mechanical effects on the dispersion of SWCNTs in methyl isobutyl ketone made it possible to obtain polymer composites with lower electrical conductivity of 20 and 8 S/cm, respectively. For polystyrene-based samples, the trend of changes in the electrical conductivity of SWCNTs depending on the method of their dispersion remained unchanged [13]. Thus, an increase in the electrical conductivity of the composites was achieved due to the homogeneous distribution of SWCNTs during their dispersion in a turbulent flow, which allowed one to form a branched network of conducting channels of large range with a minimum number of breaks in the polymer matrix. In work [14], in order to avoid severe destruction of SWCNTs under the influence of ultrasound, the authors resorted to their mechanical grinding and found that this led to an increase in the electrical conductivity of nanotubes in films where ethyl cellulose acts as a binder. The electrical conductivity of the composite films depended on SWCNTs grinding duration (5, 15, 60 min) and their concentration relative to the binder (1:1, 1:10, 1:50). An increase in the grinding time of SWCNTs from 15 to 60 minutes had a negative effect on the electrical conductivity of the composite films, which was associated, in the authors opinion, with excessive aeration of the filler during the crushing process. A clear explanation for the higher electrical conductivity of ethylcellulose films with SWCNTs subjected to five-minute grinding in comparison with similar compositions based on uncrushed carbon filler was not given in this work. Another study [15] was devoted to comparing theoretical and experimental data on the electrical conductivity of SWCNTs with different lengths and axial ratios. Theoretical calculations showed that longer SWCNTs in polymers should have better

conductivity, while the experimentally obtained electrical conductivity values for short and long nanotubes were in the same range ($10^4 \div 10^8$ S/m).

Uniform distribution and a decrease in the aggregation degree of SWCNTs can be achieved not only by dispersion, but also by using their surface functionalization. To do this, during the oxidation process, the SWCNT framework was damaged by strong acids, oxidizing agents, ozone or plasma, which resulted in the generation of oxygen-containing functional groups, such as hydroxyl, carboxyl and ester [16, 17]. These groups were subsequently used for silanization [18], esterification [19] of SWCNTs and grafting of polymers onto them [20]. It should be noted that in works [8, 21, 22], the authors discovered growth in the number of charge carriers and an increase in the electrical conductivity of SWCNTs during their oxidation. Moreover, some articles [23, 24] talk about the manifestation of the superconductivity effect in SWCNTs, which can also make a significant contribution to reducing the electrical resistance of the composite material. Similar effects was previously observed for another allotropic modification of carbon, namely reduced graphene oxide (rGO), when its sheets were deformed and mechanical stresses were created in them during copolymerization with styrene, that led to the appearance of local areas with abnormally low electrical resistance and the manifestation of superconducting properties in the samples up to room temperatures [25–27]. In the present work, we study the influence of the SWCNT's surface functionalization process with methacrylate groups, their subsequent copolymerization with styrene, precipitation conditions, disintegration and formation of a polymer composite coating on the conductive properties of 1D carbon filler.

2. Experimental

The studied single-walled carbon nanotubes (obtained from OCSiAl) according to the manufacturer have a length of more than $5 \mu\text{m}$, an outer average diameter of 1.4 ± 0.3 nm and a specific surface area of about $400 \text{ m}^2/\text{g}$. SWCNTs taken in their original form were functionalized with methacrylate groups using the organosilicon compound 3-(trimethoxysilyl)propyl methacrylate (TMSPM) (Sigma-Aldrich, CAS number 2530-85-0, purity $>98\%$) according to the method described in detail in [28]. After removing unreacted TMSPM from the alcohol dispersion of modified SWCNTs by repeated washing with ethanol and drying the resulting powder in an air to constant weight, the fact of grafting of the organosilicon modifier to the carbon filler was confirmed using FTIR spectroscopy (Vertex 70 spectrometer, Bruker, Germany). The transmission spectrum of a KBr tablet with original SWCNTs (Fig. 1a) contained barely noticeable bands at 1730 (stretching vibrations of C=O groups), 1510 (skeletal vibrations of C=C bonds) and 1250 cm^{-1} (stretching vibrations of C–O groups, corresponding to internal defects of carbon nanotubes) [29, 30]. After modification of SWCNTs using TMSPM, bands appear in the FTIR spectrum (Fig. 1b) at 1720 (stretching vibrations of C=O groups), 1634 (C=C groups), 1270 (Si–CH₃ bonding), 1190 (Si–O–CH₃ vibrations), 1096 (Si–O–Si antisymmetric stretching) cm^{-1} , that indicates the presence of an organosilicon modifier on the surface of the carbon filler [31, 32]. Another indirect confirmation of the successful modification of the surface of carbon nanotubes was an increase in their diameter after treatment with TMSPM. It should be noted that the smallest diameter of original SWCNTs recorded using a SUPRA 55 VP scanning electron microscope (Carl Zeiss, Germany) was about 4 nm (Fig. 2a), while after their functionalization it approximately doubled (Fig. 2b).

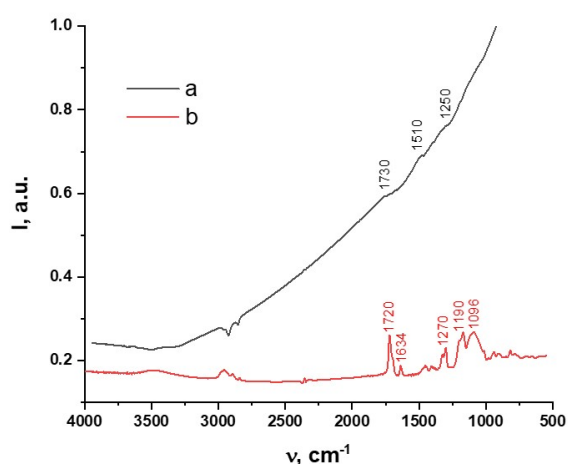


FIG. 1. FTIR spectra of SWCNTs before (a) and after (b) treatment with TMSPM

Next, the functionalized SWCNTs were dispersed in a styrene–toluene solution (1:1) and copolymerized in an inert atmosphere with the monomer for 20 hours, using azobisisobutyronitrile (1 wt. % of the polymer weight) as an initiator. The content of SWCNTs in the synthesized composite was 1 wt. %. The average molecular weight of polystyrene under the selected polymerization conditions was about 9000 Da. The resulting composite was precipitated in ethanol and, after

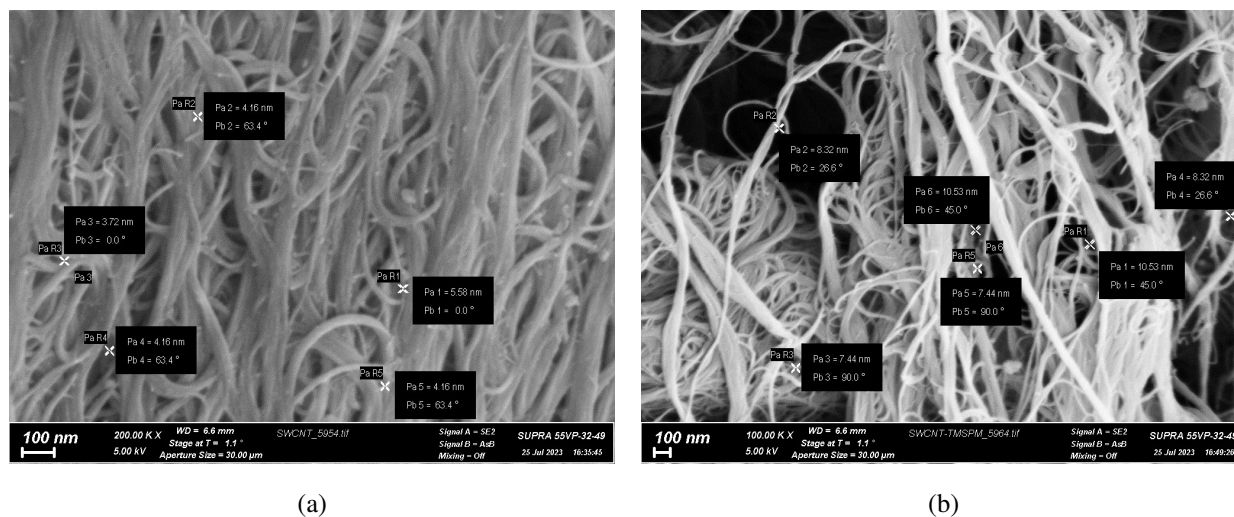


FIG. 2. SEM micrographs of original (a) and TMSPM-modified (b) SWCNTs

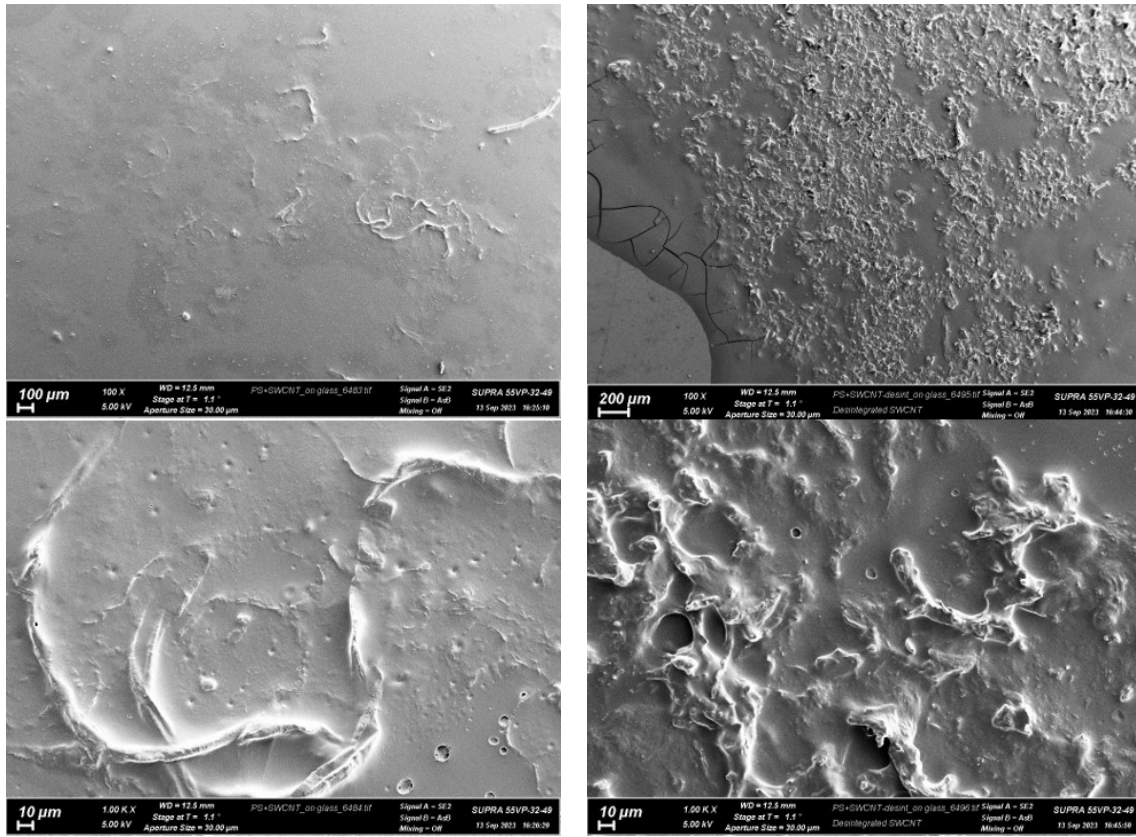
drying, divided into 2 parts. One part was left unchanged (original), the other part was mechanically crushed in a vibrator ball mill (DDR-GM 9458, 30 W, 50 Hz, Germany) for 2 hours to a powdery state.

The current-voltage characteristics of the composites were measured in two ways: 1) in the geometry of the sandwich structure; 2) in the planar geometry. To obtain current-voltage characteristics (CVCs) in metal/composite/metal sandwich structures, the samples were deposited onto copper electrodes from their 1 % solutions in benzene. The area of the copper electrodes used to measure electrical conductivity of the composites in sandwich structures was 1 cm². The thickness of the films deposited on the electrodes for CVCs measuring was from 2 to 10 μm, and the temperature dependencies of the electrical resistance were obtained for the samples of 2 and 3 μm. The thickness of the composite coating was estimated using a Solver P-47 PRO (NT-MDT) scanning probe microscope. CVCs and temperature dependencies of the electrical resistance in metal electrode/composite/metal electrode sandwich structures were obtained by 4-probe method as in [25, 33]. The probe contacts were soldered into the current electrodes. In this case, the voltage drops across the electrodes at the maximum current used in the experiment was less than the sensitivity of the voltmeter, i.e. 100 nV. The following devices were used in electrical measurements: universal voltmeter V7-78/1, multimeter RS-232C, combined digital device Shch-300, DC power supply B5-90.

To measure CVCs in planar structures, the composites were deposited on glass substrate from a mixture of benzene/petroleum ether solvents taken in a ratio of 1:1 by volume. To prepare solutions, chemical pure benzene (chemical pure, ECOS-1, Russia) and petroleum ether 40 – 70 (chemical pure, ECOS-1, Russia) were used. Previously, it was shown [33] that this ratio allowed the maximum separation of rGO and polystyrene and promoted the maximum enlargement of carbon clusters on the polymer surface. To obtain sufficiently large SWCNT structures on the polystyrene surface deposited from a mixture of benzene and petroleum ether, solutions were prepared with a composite content of about 30 wt. %. For the film obtained from a non-disintegrated composite, the length of SWCNT formations emerging on the polystyrene surface reached 500 μm (Fig. 3a). At the same time, on the surface of the film formed on a glass substrate from the composite crushed to a powder state, SWCNT aggregates with a size of 20 – 30 μm were observed (Fig. 3b). Such sizes of inclusions made it possible to measure their electrical resistance on the surface of the polymer using the copper electrodes with an area of 10 μm².

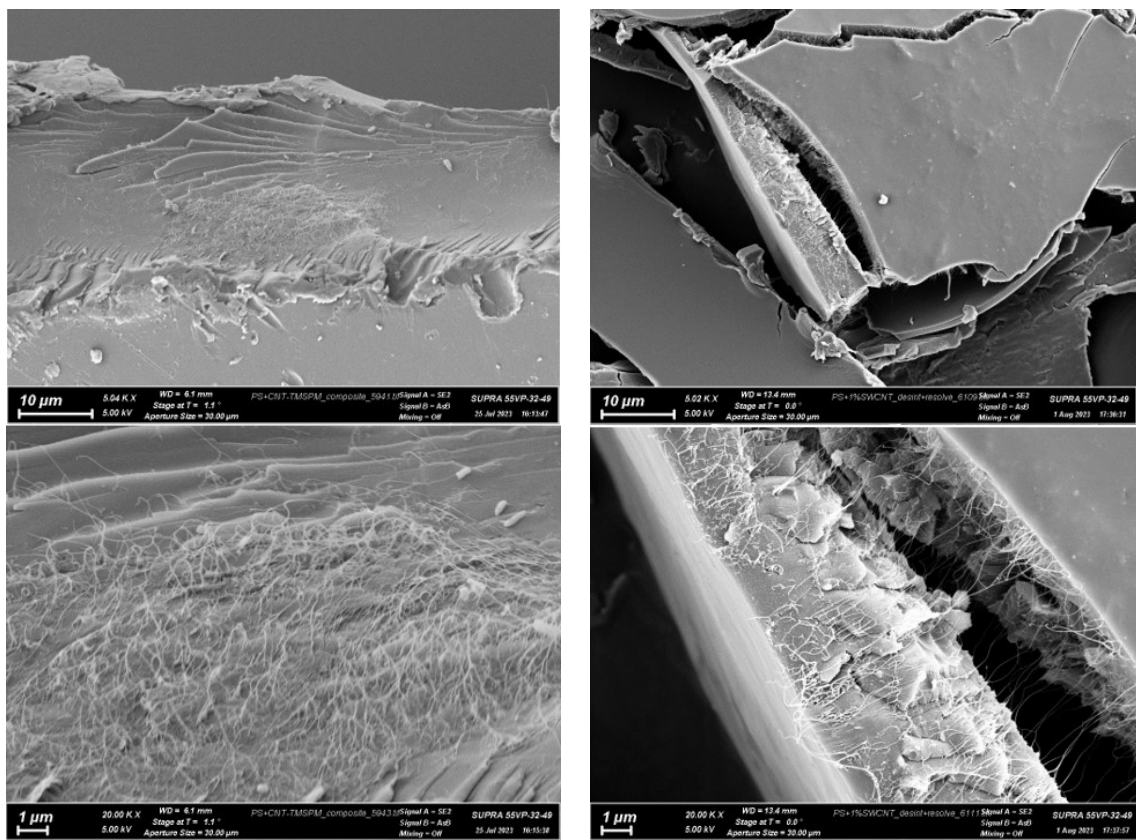
3. Results and discussion

Since PS is a dielectric, it is an ideal matrix for studying the electrical conductivity of a component with lower resistance, such as SWCNTs. Composite coatings of uncrushed and disintegrated PS films with SWCNTs formed on a glass substrate using a mixed solvent were heterogeneous in their electroconductive properties. Low electrical resistance was observed only in some small (up to hundreds of micrometers) areas of composites, while most of their surface remained high-resisted or has electroconductivity corresponding to semiconductors. When the electrodes were separated by more than 1 cm, the electrical resistance of the composite film exceeded 30 MΩ, since the low concentration of SWCNTs (1 wt. %) in the PS did not allow the formation of extended electroconductive channels in the near-surface layer of the dielectric matrix. The metallic type of conductivity was recorded only for individual areas of the composite film (Fig. 4), where the SWCNTs came out onto the PS surface. The length of such areas corresponded to the sizes of the agglomerates observed in the SEM micrographs of cross-sections of the composite films (Fig. 3c). It is obvious that the structural features of the aggregates and the relative arrangement of the SWCNTs in the PS film formed using a mixed solvent of benzene/petroleum ether determine the electrical resistance values of its areas. Low values of electrical



(a)

(b)



(c)

(d)

FIG. 3. SEM micrographs obtained at different magnifications of the surface of the films formed from the original (a, c) and disintegrated (b, d) composites on the glass substrate (a, b), as well as images of their transverse cleavages (c, d)

resistance at the distance between electrodes, down to $50\ \mu\text{m}$, were recorded in planar structures both for films formed from uncrushed composite and those obtained from the pre-disintegrated sample (Fig. 4). It is shown that the absolute values of electrical resistance of agglomerates from disintegrated SWCNTs in the PS matrix can be even lower than that of metal. It would be logical to expect better electrical conductivity in the case of the composite films with uncrushed SWCNTs, when their structure was not damaged and there were fewer edge defects, which should obviously appear when the nanotubes were disintegrated. However, in the case of disintegrated SWCNTs, the electrical resistance in planar structures was 2 orders of magnitude lower than that of the composite films based on uncrushed ones. Apparently, the reduction in the electrical resistance of the films was facilitated by the special self-organization of individual SWCNT fragments into aggregates that acted as conducting channels in the dielectric matrix.

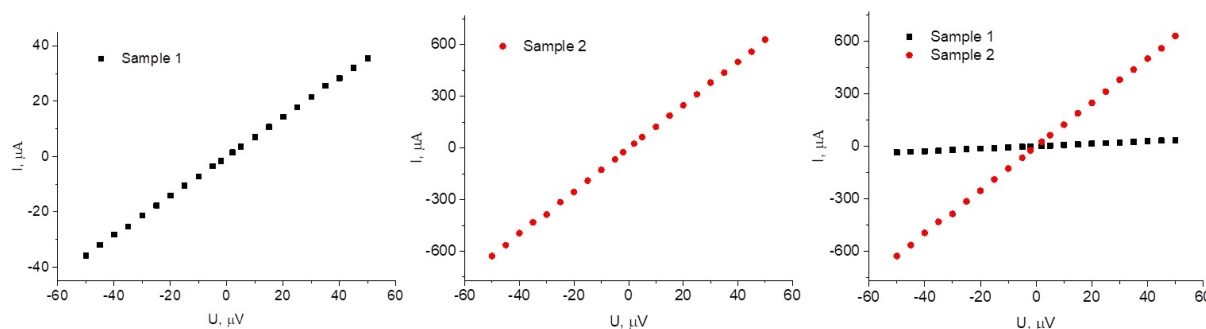


FIG. 4. CVCs at 298 K in planar-structures of composite films based on PS with original (sample 1, $R = 1.4\ \Omega$) and disintegrated SWCNTs (sample 2, $R = 0.08\ \Omega$); distance between electrodes $50\ \mu\text{m}$

To measure the electrical conductivity of the composites in sandwich structures, the films with a thickness from 2 to $10\ \mu\text{m}$ were formed on the copper electrodes from benzene. In this case, SWCNTs covalently bonded to PS were uniformly distributed and did not form large aggregates in the polymer matrix (Fig. 3b). The electrically conductive properties of the composite films were determined by their thickness depending on the length of the SWCNTs. The films obtained from the pre-disintegrated PS samples with SWCNTs showed low electrical resistance values at a thickness of up to several micrometers (Fig. 5), and over $5\ \mu\text{m}$ they became completely insulating. This can be explained by the fact that during grinding, the length of some part of individual SWCNTs was shortened, and they ceased to provide electrical conductivity at a film thickness much greater than their linear dimensions. Thus, for disintegrated SWCNTs in sandwich structures, low electrical resistance was maintained only at small film thicknesses, comparable to the sizes of the conducting channels they form (Fig. 3d). For the films based on PS with uncrushed SWCNTs, the electrical conductivity was maintained even at a thickness of $10\ \mu\text{m}$. However, if we compare thin films obtained from uncrushed and disintegrated composites, the absolute values of electrical conductivity for the latter will be significantly higher (comparison of sample 1 and 2 in Fig. 5).

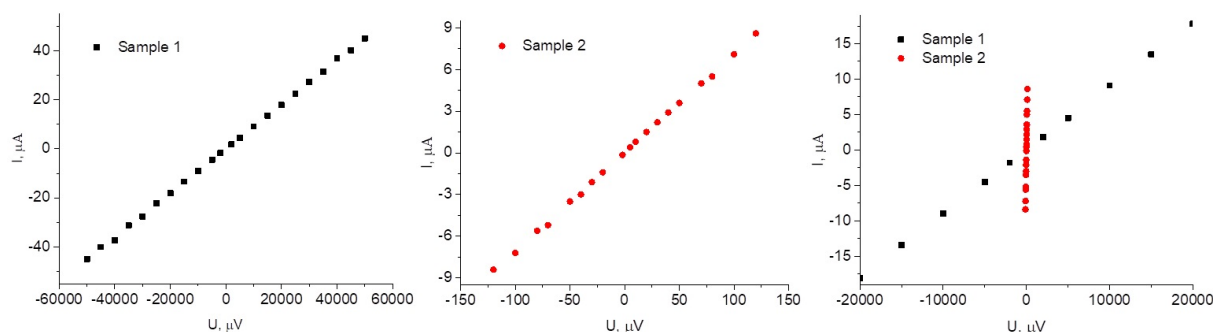


FIG. 5. CVCs at 298 K in sandwich-structures of composite films based on PS with original (sample 1, $R = 1.4\ \text{k}\Omega$) and disintegrated SWCNTs (sample 2, $R = 14\ \Omega$); distance between the electrodes $2\ \mu\text{m}$

The metallic nature of the electrical conductivity of SWCNTs in PS films formed from the original and disintegrated parts of the polymer composite was also confirmed by the temperature dependencies of the resistance (Fig. 6). Thus, at 298 K the electrical resistance of the SWCNTs was $220\ \text{k}\Omega$, at 280 K it was already $650\ \text{k}\Omega$, and at 273 K it was $1\ \text{M}\Omega$. In addition, the electrical resistance of the films obtained from the disintegrated PS composites with SWCNTs dropped by approximately 100 times when the temperature was reduced from room to liquid nitrogen temperature (Fig. 6, sample 2). For the samples 2 and 3 at low temperatures, electrical resistance of copper level was observed in the experiment.

Therefore, for clarity, a comparative analysis of the temperature dependences of the resistance of the PS samples with the original and disintegrated SWCNTs was carried out with a film thickness of $3\ \mu\text{m}$ (Fig. 6).

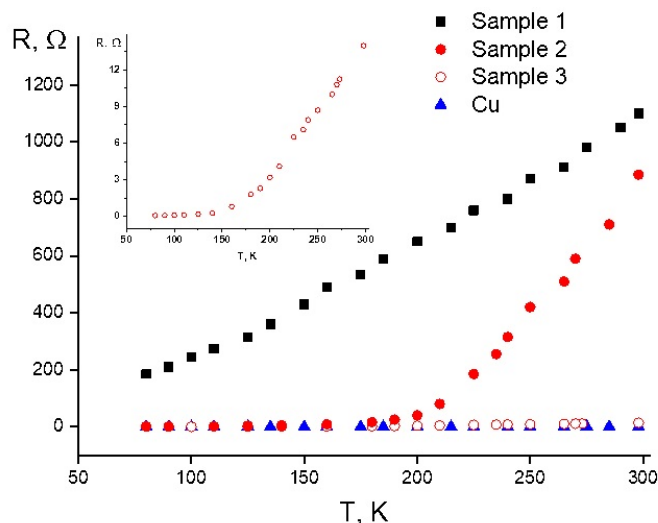


FIG. 6. Temperature dependencies of the electrical resistance of the composite films based on PS with original (sample 1, film thickness $3\ \mu\text{m}$) and disintegrated SWCNTs (sample 2, film thickness $3\ \mu\text{m}$; sample 3, film thickness $2\ \mu\text{m}$) measured in planar structures in comparison with copper

4. Conclusions

For the films deposited from solutions of original and disintegrated polymer composite obtained by radical polymerization of styrene with SWCNTs, the current-voltage characteristics and the temperature dependencies of the resistance have been measured. The obtained data have demonstrated a decrease in resistance and a metallic type of conductivity in certain areas of the nanotube aggregates' surface. It has been determined that the grinding of SWCNTs leads to a decrease in their resistance in planar structures in separate areas by two orders of magnitude compared to original ones. Also, when using thin films of the composite with a thickness of up to $2\ \mu\text{m}$ in sandwich structures, the electrical resistance values of the disintegrated polymer composite turned out to be lower by two orders of magnitude comparing to original composite.

Thus, we can conclude that mechanical grinding of the composite material leads to the fragmentation of SWCNTs, and, consequently, to a change in the arrangement of the carbon filler in the network of conducting channels. We believe that, to varying degrees, both of these factors may contribute to the decrease in a local conductivity of the composite material based on polystyrene and SWCNTs observed in this work.

References

- [1] Badamshina E.R., Gafurova M.P., Estrin Ya.I. Modification of carbon nanotubes and synthesis of polymeric composites involving the nanotubes. *Russian Chemical Reviews*, 2010, **79** (11), P. 945–979.
- [2] Kamalov A.M., Kodolova-Chukhontseva V.V., Dresvyanina E.N., Maslennikova T.P., Dobrovolskaya I.P., Ivan'kova E.M., Popova E.N., Smirnova V.E., Yudin V.E. Effect of nanotubes on the electrical and mechanical properties of chitosan films. *Technical Physics*, 2022, **3**, P. 340–346.
- [3] Lee D.K., Yoo J., Kim H., Kang B.H., Park S.H. Electrical and Thermal Properties of Carbon Nanotube Polymer Composites with Various Aspect Ratios. *Materials (Basel)*, 2022, **15** (4), 1356.
- [4] Castellino M., Rovere M., Shahzad M.I., Tagliaferro A. Conductivity in carbon nanotube polymer composites: A comparison between model and experiment. *Composites Part A: Applied Science and Manufacturing*, 2016, **87**, P. 237–242.
- [5] Sánchez-Romate X.F., Jiménez-Suárez A., Ureña A. Electrical Properties of Carbon Nanotubes. In: Abraham J., Thomas S., Kalarikkal N. (eds) *Handbook of Carbon Nanotubes*. Springer, 2022.
- [6] Cees Dekker. How we made the carbon nanotube transistor. *Nature electronics*, 2018, **1**, 518.
- [7] Rakov E.G. Carbon nanotubes in new materials. *Russian Chemical Reviews*, 2013, **82** (1), P. 27–47.
- [8] Stando G., Han S., Kumanek B., Łukowiec D., Janas D. Tuning wettability and electrical conductivity of single-walled carbon nanotubes by the modified Hummers method. *Sci. Rep.*, 2022, **12**, 4358.
- [9] Rdest M., Janas D. Enhancing Electrical Conductivity of Composites of Single-Walled Carbon Nanotubes and Ethyl Cellulose with Water Vapor. *Materials*, 2020, **13** (24), 5764.
- [10] Abdulhameed A., Wahab N.Z.A., Mohtar M.N., Hamidon M.N., Shafie S., Halin I.A. Methods and applications of electrical conductivity enhancement of materials using carbon nanotubes. *J. Electron. Mater.*, 2021, **50**, P. 3207–3221.
- [11] Charoenpakdee J., Suntijitruang O., Boonchui S. Chirality effects on an electron transport in single-walled carbon nanotube. *Sci. Rep.*, 2020, **10** (1), 18949.
- [12] Sekitani T., Noguchi Y., Hata K., Fukushima T., Aida T., Someya T. A rubberlike stretchable active matrix using elastic conductors. *Science*, 2008, **321**, P. 1468–1472.

- [13] Yoon H., Yamashita M., Ata S., Futaba D.N., Yamada T., Hata K.. Controlling exfoliation in order to minimize damage during dispersion of long SWCNT for advanced composites. *Sci. Rep.*, 2014, **4**, 3907.
- [14] Kumanek B., Wasiak T., Stando G., Stando P., Łukowiec D., Janas D. Simple method to improve electrical conductivity of films made from single-walled carbon nanotubes. *Nanomaterials*, 2019, **9** (8), 1113.
- [15] Elaskalany M., Behdian K. Effect of carbon nanotube type and length on the electrical conductivity of carbon nanotube polymer nanocomposites. *Mater. Res. Express*, 2023, **10** (10), 105010.
- [16] In-Yup J., Wook C.D., Ashok K.N., Jong-Beom B. Functionalization of carbon nanotubes. Carbon nanotubes – polymer nanocomposites. 2011, Edited by S.Y. Rijeka, Croatia: Intech., P. 91–110.
- [17] Mann F.A., Galonska P., Herrmann N., Kruss S. Quantum defects as versatile anchors for carbon nanotube functionalization. *Nat. Protoc.*, 2022, **17**, P. 727–747.
- [18] Manoharan G., Bösel P., Thien J., Holtmannspötter M., Meingast L., Schmidt M., Eickmeier H., Haase M., Maultzsch J., Steinhart M., Wollschläger J., Palma M., Meyer C. Click-Functionalization of silanized carbon nanotubes: From inorganic heterostructures to biosensing nanohybrids. *Molecules*, 2023, **28** (5), 2161.
- [19] Hamon M., Hui H., Bhowmik P., Itkis H.M.E., Haddon R.C. Ester-functionalized soluble single-walled carbon nanotubes. *Appl. Phys. A*, 2002, **74**, P. 333–338.
- [20] Díez-Pascual A.M. Chemical functionalization of carbon nanotubes with polymers: A brief overview. *Macromol.*, 2021, **1** (2), P. 64–83.
- [21] Roch A., Greifzu M., Roch Talens, E., Stepien, L., Roch T., Hege J., Van Nong N., Schmiel T., Dani I., Leyens C., Jost O., Leson A. Ambient effects on the electrical conductivity of carbon nanotubes. *Carbon*, 2015, **95**, P. 347–353.
- [22] Yeontack R., Yin L., Yu C. Dramatic electrical conductivity improvement of carbon nanotube networks by simultaneous de-bundling and hole-doping with chlorosulfonic acid. *J. of Materials Chemistry*, 2012, **10** (14).
- [23] Ferrier M., Kasumov A., Deblock R., Guéron S., Bouchiat H., Junji Haruyama. Superconductivity in carbon nanotubes, disorder-induced superconductivity in ropes of carbon nanotubes. In: *Carbon Nanotubes*, 2009, **10** (4), P. 252–267.
- [24] Yang Y., Fedorov G., Zhang J., Tselev A., Shafranuk S., Barbara P. The search for superconductivity at van Hove singularities in carbon nanotubes. *Superconductor Science and Technology*, 2012, **25** (12).
- [25] Ionov A.N. Josephson-Like behaviour of the current-voltage characteristics of multi-graphene flakes embedded in polystyrene. *J. Low Temp. Phys.*, 2016, **185** (5–6), P. 515–521.
- [26] Ionov A.N., Volkov M.P., Nikolaeva M.N., Smyslov R.Y. Bugrov A.N. The magnetization of a composite based on reduced graphene oxide and polystyrene. *Nanomaterials*, 2021, **11** (2), 403.
- [27] Ionov A.N., Volkov M.P. Magnetization of needle graphene embedded in polystyrene matrix. *Tech. Phys. Lett.*, 2022, **48** (8), P. 44–46.
- [28] Nikolaeva M.N., Anan'eva T.D., Bugrov A.N., Dideikin A.T., Ivankova E.M. Correlation between structure and resistance of composites based on polystyrene and multilayered graphene oxide. *Nanosystems: Physics, Chemistry, Mathematics*, 2017, **8** (2), P. 266–271.
- [29] Nawaz M.A.H., Rauf S., Catanante G., Nawaz M.H., Nunes G., Marty J.L., Hayat A. One step assembly of thin films of carbon nanotubes on screen printed interface for electrochemical aptasensing of breast cancer biomarker. *Sensors*, 2016, **16** (10), 1651.
- [30] Ionov A.N., Volkov M.P. Nikolaeva M.N., Smyslov R.Y. Bugrov A.N. Magnetization of ultraviolet-reduced graphene oxide flakes in composites based on polystyrene. *Materials*, 2021, **14** (10), 2519.
- [31] Melgoza M.L., Ramírez-Bon R. Europium ions as a spectroscopic probe in the study of PMMA-SiO₂ hybrid microstructure with variable coupling agent. *J. of Sol-Gel Science and Technology*, 2021, **107** (10), P. 46–56.
- [32] Bugrov A.N., Zavialova A.Y., Smyslov R.Y., Anan'eva T.D., Vlasova E.N., Mokeev M.V., Kryukov A.E., Kopitsa G.P., Pipich V. Luminescence of Eu³⁺ ions in hybrid polymer- inorganic composites based on poly(methyl methacrylate) and zirconia nanoparticles. *Luminescence*, 2018, **33** (5), P. 837–849.
- [33] Nikolaeva M.N., Bugrov A.N., Anan'eva T.D. Gushchina E.V., Dunaevskii M.S., Dideikin A.T. Resistance of reduced graphene oxide on polystyrene surface. *Nanosystems: Physics, Chemistry, Mathematics*, 2018, **9** (4), P. 496–499.

Submitted 5 November 2023; revised 1 April 2024; accepted 24 February 2025

Information about the authors:

Marianna N. Nikolaeva – NRC “Kurchatov Institute” – PNPI – IMC, Bolshoy pr. 31, 199004 St. Petersburg, Russia; ORCID 0000-0002-5034-7665; Marianna_n@mail.ru

Elena M. Ivan'kova – NRC “Kurchatov Institute” – PNPI – IMC, Bolshoy pr. 31, 199004 St. Petersburg, Russia; ORCID 0000-0002-4823-0695; ivelen@mail.ru

Alexander N. Bugrov – NRC “Kurchatov Institute” – PNPI – IMC, Bolshoy pr. 31, 199004 St. Petersburg, Russia; Saint Petersburg Electrotechnical University “LETI”, Professora Popova 5, 197376 St. Petersburg, Russia; ORCID 0000-0003-1052-4919; alexander.n.bugrov@gmail.com

Conflict of interest: the authors declare no conflict of interest.



NANOSYSTEMS:

PHYSICS, CHEMISTRY, MATHEMATICS

INFORMATION FOR AUTHORS

The journal publishes research articles and reviews, and also short scientific papers (letters) which are unpublished and have not been accepted for publication in other magazines. Articles should be submitted in English. All articles are reviewed, then if necessary come back to the author to completion.

The journal is indexed in Web of Science Core Collection (Emerging Sources Citation Index), Chemical Abstract Service of the American Chemical Society, Zentralblatt MATH and in Russian Scientific Citation Index.

Author should submit the following materials:

1. Article file in English, containing article title, the initials and the surname of the authors, Institute (University), postal address, the electronic address, the summary, keywords, MSC or PACS index, article text, the list of references.
2. Files with illustrations, files with tables.
3. The covering letter in English containing the article information (article name, MSC or PACS index, keywords, the summary, the literature) and about all authors (the surname, names, the full name of places of work, the mailing address with the postal code, contact phone number with a city code, the electronic address).
4. The expert judgement on possibility of publication of the article in open press (for authors from Russia).

Authors can submit a paper and the corresponding files to the following addresses: nanojournal.ifmo@gmail.com, popov1955@gmail.com.

Text requirements

Articles should be prepared with using of text editors MS Word or LaTeX (preferable). It is necessary to submit source file (LaTeX) and a pdf copy. In the name of files the English alphabet is used. The recommended size of short communications (letters) is 4-6 pages, research articles– 6-15 pages, reviews – 30 pages.

Recommendations for text in MS Word:

Formulas should be written using Math Type. Figures and tables with captions should be inserted in the text. Additionally, authors present separate files for all figures and Word files of tables.

Recommendations for text in LaTeX:

Please, use standard LaTeX without macros and additional style files. The list of references should be included in the main LaTeX file. Source LaTeX file of the paper with the corresponding pdf file and files of figures should be submitted.

References in the article text are given in square brackets. The list of references should be prepared in accordance with the following samples:

- [1] Surname N. *Book Title*. Nauka Publishing House, Saint Petersburg, 2000, 281 pp.
- [2] Surname N., Surname N. Paper title. *Journal Name*, 2010, **1** (5), P. 17-23.
- [3] Surname N., Surname N. Lecture title. In: Abstracts/Proceedings of the Conference, Place and Date, 2000, P. 17-23.
- [4] Surname N., Surname N. Paper title, 2000, URL: <http://books.ifmo.ru/ntv>.
- [5] Surname N., Surname N. Patent Name. Patent No. 11111, 2010, Bul. No. 33, 5 pp.
- [6] Surname N., Surname N. Thesis Title. Thesis for full doctor degree in math. and physics, Saint Petersburg, 2000, 105 pp.

Requirements to illustrations

Illustrations should be submitted as separate black-and-white files. Formats of files – jpeg, eps, tiff.



NANOSYSTEMS:

PHYSICS, CHEMISTRY, MATHEMATICS

Журнал зарегистрирован

Федеральной службой по надзору в сфере связи, информационных технологий и массовых коммуникаций
(свидетельство ПИ № ФС 77 - 49048 от 22.03.2012 г.)
ISSN 2220-8054

Учредитель: федеральное государственное автономное образовательное учреждение высшего образования
«Национальный исследовательский университет ИТМО»

Издатель: федеральное государственное автономное образовательное учреждение высшего образования
«Национальный исследовательский университет ИТМО»

Отпечатано в Учреждении «Университетские телекоммуникации»
Адрес: 197101, Санкт-Петербург, Кронверкский пр., 49

Подписка на журнал НФХМ

На второе полугодие 2025 года подписка осуществляется через
ОАО «АРЗИ», подписной индекс Э57385